Fabrication techniques to produce micro and macro porous MAX-phase Ti2AlC ceramic

Thomas, Tony

Award date:
2015

Awarding institution:
University of Bath

Fabrication techniques to produce macro and micro porous Max-phase Ti_2AlC ceramic

Tony Thomas

A thesis submitted for the degree of Doctor of Philosophy

University of Bath

Department of Mechanical Engineering

October 2014

Acknowledgement

I would like to take this opportunity to thank my supervisors Professor Chris Bowen and Dr. Irene Turner. I am delighted to extend my remarkable appreciation to Professor Chris Bowen for guiding me throughout the time of this research and constantly supporting me with many invaluable suggestions and insight into this research, which led to the completion of my intended research project. Thank you Sir, for accepting me as your research student and for being a great source of inspiration and motivation for this project. And also thank you for funding me now and then for this project. It was an immense pleasure working with you.

I would like to thank Dr. Irene Turner for her suggestions on fabricating porous ceramics and providing practical recommendations for producing porous ceramic material. I also thank Mr. Kenneth Schneider and Dr. Petra Cameron for collaborating their work on Microbial Fuel Cell and help me characterise the porous ceramic as an electrode material.

I thank University of Bath for their financial and material support for this project. I am extremely grateful to Mr. Frank Hammet, Mrs. Clare Ball and Mr. Mathew Ball of Department of Mechanical Engineering for their technical support on daily basis, without their support, this wouldn't have been possible. I would also like to thank Dr. John Mitchel and Mrs. Ursula potter of Microscopic Analysis Suite for training me and helping me with image characterisation and analysis techniques and Mr. Harry Bones for helping me with the XRD analysis. I thank Mr. Ian Trussler for providing technical assistance for the tube furnace and replacing the gas cylinders for a smooth functioning of the project.

I would like to express my sincere appreciation to my colleagues and friends Ms. Vana Adamaki, Mr. Mike Bertin and Mr. Daniel Zabek for helping me with technical ideas and sharing witty humours throughout this research period. I thank my good friends Gaodi, Masulova, Anish and Rose for being there for me as a moral support all the time and supporting me in various aspect of life throughout my student life. I love you guys.

Finally and most importantly I take this opportunity to extend my everlasting gratitude towards my parents Mr. P. A. Thomas and Mrs. Pilomena Thomas for their financial support, love and care throughout my student life. I also thank my sister Mrs. Teena Job and my Brother-in-law Mr. Sudeep Job for constantly helping me and guiding me with non- academic difficulties. I love you all.

Fabrication techniques to produce micro and macro porous MAX-phase Ti_2AlC ceramic

Tony Thomas

University of Bath

Abstract

MAX-phase ceramics are a class of ductile ceramic material group with the general molecular formula $\mathbf{M_{n+1}AX_n}$ (n = 1, 2, 3….), where **M** is an early transition element, **A** is an element from the 'A' group of the periodic table and **X** is either nitrogen or carbon. One advantage of these materials is that they maintain their strength at high temperatures. In addition these ceramic materials possess the best properties of both ceramics and metals. Some of their important characteristics are low density, high stiffness, machinability, excellent thermal and electrical conductivity and they even exhibit some plasticity at elevated temperature. These amazing combinations of properties have made researchers foresee the technological importance of these materials as a structural ceramic for high temperature application. Since this ceramic is relatively new to the market, only a handful of work has been undertaken on this material and its applications are limited to heating elements. In addition, analysis of the thermodynamic data on this material is incomplete. This PhD work addresses this issue and conducts a complete thermodynamic analysis involved in the formation mechanism of the ternary titanium carbide MAX-phase Ti_2AlC ceramic, using Self-propagating High temperature Synthesis (SHS) form of combustion synthesis process, based on the following exothermic reaction:

$$(2+x)\,Ti + (y)\,Al + C \rightarrow Ti_2AlC + (x)\,Ti + (y)\,Al \qquad (i)$$

Where x and y = 0.1. 0.2, 0.3…

A thermodynamic model has been formulated to predict the temperature evolution during the reaction (i), for the formation of Ti_2AlC using SHS process. In addition the effect of particle size in the elemental reaction has been studied on the formation mechanism of Ti_2AlC and methods to control the porosity by fine tuning the particle size has been recognized.

Manufacturing processes such as Self-propagating High temperature Synthesis (SHS), foam replication and freeze casting have been developed in this thesis to produce micro and macro porous Ti_2AlC ceramic mainly for electrode applications. A systematic material development technique to produce macro porous Ti_2AlC ceramic, using a foam replication technique has been established in this research work. The material fabricated by this technique has a uniform pore size (up to 5mm), with open interconnected pores and is ideal for a flow battery application which requires a multifunctional electrode material which is highly porous to allow the flow of electrolyte through it, is corrosion resistant and at the same time being electrically conductive. The mechanical properties of the ceramic produced by this method has been characterised and steps to mitigate the cracks and defects formed during the fabrication process to obtain structurally stable macro porous Ti_2AlC ceramic has been reported in this work. This research demonstrates that one of the applications of macro porous Ti_2AlC ceramic formed using foam replication technique is as an electrode material in a photo-Microbial Fuel Cell (p-MFC).

Graded porosity micro porous Ti_2AlC ceramics have also been fabricated using a freeze casting technique, with camphene as the freezing vehicle. A systematic material development process has been tailored for this particular material. A ceramic material with gradient pore size ranging from 27-305µm has been fabricated using this technique. This type of ceramic is a good candidate as an electrode material in micro-redox battery and for sensing applications. A variety of processing parameters such as solid loading (amount of ceramic content in the material), freezing temperature and mould material which affect the pore formation and pore size have been studied in this research project and the range of porosities achieved by controlling these parameters have been reported.

Table of Contents

List of Figures

List of Tables

Chapter 1. Introduction

This research work will mainly focus on the fabrication techniques to produce macro to micro porous MAX-phase electrically conductive Ti_2AlC ceramic. The processes include Self-propagating High temperature Synthesis (SHS), foam replication and freeze casting techniques. The following chapter will explain the structure of MAX-phase ceramics and also the intrinsic and extrinsic properties of the Ti_2AlC ceramic, which is the material under investigation. It will provide an initial introduction of the SHS process and the evolution of this process as a solid-state combustion reaction. The research also includes the understanding of the thermodynamics involved in the formation mechanism of Ti_2AlC by SHS process from the elemental powders based on the following reaction:

$$2Ti + Al + C \rightarrow 2Ti_2AlC \qquad (Reac.\ 1)$$

Hence this chapter will explain the basic thermodynamic model that will be adapted to study the thermodynamics involved in Reaction 1. Finally some of the material characterisation techniques frequently used in this research will be briefly explained.

1.1 MAX-phase ceramics

MAX-phase ceramics are a new class of ceramic materials which are also known as the 'nano-lamellar' ceramics [1]. The ceramics are considered nano-lamellar since, when the crystal structure of this material is observed at a nano-scale, a succession of planes can be seen in which the dominant atomic bond is an alternating strong metal and weaker non-metal bond. This results in a material made of strong planes (Ti-Al) with a weak link (Ti-C) to each other in their perpendicular direction as shown in figure 1 [1].

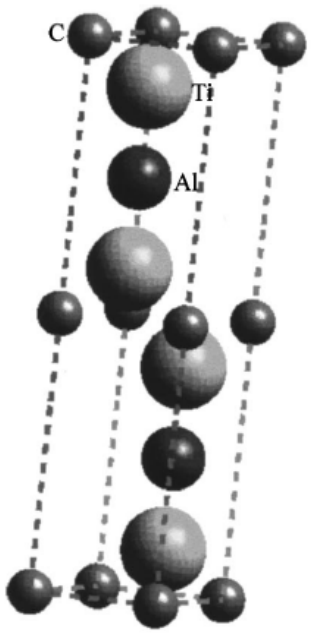

Figure 1. Crystal structure of Ti_2AlC [1]

These materials are well known with the general molecular formula $M_{n+1}AX_n$ (n = 1, 2 or 3) [1, 2, 3, 4]. The name MAX-phase describes the elements from transition metal M, A represents the group 13 or 14 elements such as Al, Si, B, Ga, Ge, Sn, Pb and Si and X is either carbon or nitrogen as seen in figure 2. Depending of the value of n, their stoichiometry varies leading to M_2AX, M_3AX_2 and M_4AX_3 which are generally known as 211, 312 and 413 phases respectively based on the number of 'A' monolayers inserted per 'M' layer. The A/M ratios for 211, 312 and 413 phases are 0.5, 0.33 and 0.25 respectively. MAX-phases with higher n value resulting in 514 [2] and 615 [3] phases have been reported. These materials are nano-laminated ternary carbides or nitrides and exist in more than 60 known phases and there are some reports [4] that for 211 phases more than 50 M_2AX compounds have been found. Their initial discovery and crystallographic analysis was initiated by Nowotny in the early 1960's [1]. The study of these materials has been boosted recently due to their unique properties and interest in these materials emerged when Ti_3SiC_2 was reported [4] to exhibit both metallic and ceramic-like properties. This was contrary to the understanding that carbides and ceramics are predominantly brittle with poor machinability.

Due to their particular chemical bonds, these materials exhibit very unusual combinations of properties reflecting those of both metals and ceramics [4]. Their electrical, chemical and thermal properties are very similar to those of corresponding nitrides/carbides. They have good electrical conductivity, high thermal diffusivity and good oxidation resistance. However they have an unusual combination of mechanical properties. They have a high bulk modulus (186GPa) and can retain their properties at high temperature [2]. They exhibit a good resistance against thermal shock, are machinable and deform plastically like metals at elevated temperatures. These properties have made these materials popular among the material scientists who are trying to use MAX-phase ceramics as replacements for other materials used in high temperature applications [1].

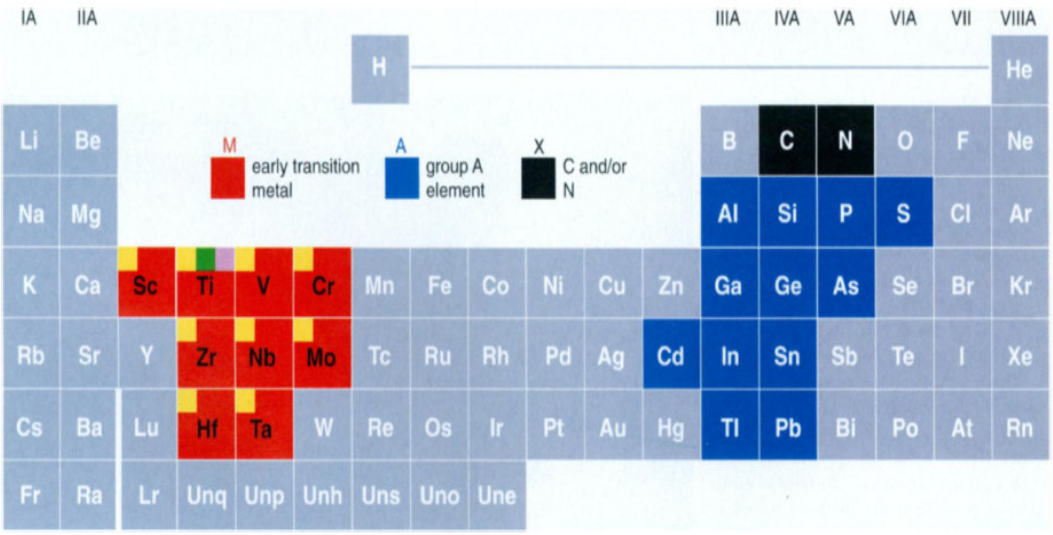

Figure 2. Periodic table showing the elements which combine together to form the MAX-phase family [1]

1.2 Crystal structure of MAX-phase material

To comprehend the behaviour of any material, it is important to study and understand its structure at the atomic and crystallographic scale and the way the material is formed. The important properties of the material depend on the nature of the bond between each element responsible for the formation of the material.

As it is known [5], the study of MAX-phase ceramics has grown largely due to its unusual combination of metallic and ceramic properties. Barsoum [1] in a review of MAX-phase stated that the mechanical response of MAX-phase is **schizoid** in nature, .i.e. there is an inherent dilemma of the material to behave like a metal or ceramic. MAX-phase ceramics, like metals, are electrically and thermally conductive, exhibit plastic deformation at high temperatures, is machinable and is resistant to both physical and thermal shock. As with all ceramics, it is refractory and is relatively light and stiff (high Young's modulus). The thermal expansion of these materials is also closer to a typical ceramic rather than a metal. Hence there is significant interest in these materials due to their novel combination of properties. To understand why the material exhibits such unusual properties, one should look at how the crystalline solids in these materials deform.

This section will analyse the material starting with the arrangement of atoms in the Ti-Al-C system MAX-phases since the Ti_2AlC ceramic is the material of interest in this PhD. Ti-Al-C materials share similar structures with other MAX-phases such as Cr_2AlC. Therefore the study of one material can also be closely related to other materials in this family. The Ti-Al-C family is chosen since among all the ternary carbides reported to date, two materials in this system, namely Ti_2AlC and Ti_3AlC_2, are the lightest and most oxidation resistant [4, 5]. Ti_2AlC ceramics upon heating forms a thin layer of αAl_2O_3 at around 800^oC and as the temperature climbs to 1000^oC, due to the outward diffusion of Ti from the aluminium oxide results in the formation of rutile TiO_2 and provides protection from further oxidation since the density of Al_2O_3 scale is high and impedes the diffusion of oxygen through the oxide scale on to the MAX-phase.

Ti_2AlC and Ti_3AlC_2 have a similar crystal structure [5]. They crystallize in the $P6_3/mmc$ space groups [6, 7]. Ti_2AlC has a structure similar to Cr_2AlC and the lattice parameters are a = 0.304 nm and c = 1.360 nm. The Ti_3AlC_2 phase has a Ti_3SiC_2 structure with the parameters a = 0.3075 nm c = 1.858 nm. These materials are formed as a result of alternative stacking of edge shared Ti-C octahedral and a 2-D close packed Al plane. The only difference in the crystal structure between Ti_2AlC and Ti_3AlC_2 is the number of Ti layers stacked by each Al plane. From the chemical composition, Ti_2AlC has two Ti layers stacked by every Al plane and Ti_3AlC_2 has three Ti layers stacked by every Al plane as seen in figure 3, which shows the 211 and 312 structures. These structural properties are shared by the other MAX-phases. Hence the early transition metal atom, 'M', and the 'X' that is the carbon or nitrogen form octahedral edge sharing (MX) bonds are inter-weaved by pure 'A' element layer (figure 3). Therefore three different stacking arrangements of the MX block with the 'A' element layers, results in the MAX-phases falling into three subgroups namely M_2AX, M_3AX_2 and M_4AX_3 [8]. Figure 3 shows the orientation of elements in the crystal structure of M_2AX, M_3AX_2 and M_4AX_3 MAX-phase material which were explained in section 1.1.

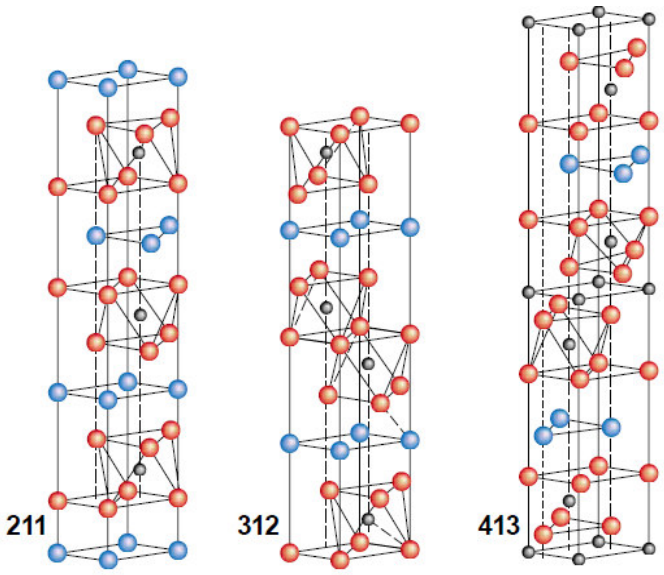

Figure 3. Crystal structure of Max-phase ceramics [1]

As a result of the structure, the chemical bonding is anisotropic in Ti_2AlC. It has a metallic bonding between Al and Ti which are parallel to the basal plane. There also exist a strong directional ionic and covalent bonds between the Ti-Al and Ti-C atoms. Consequently the chemical bonding in these materials is metal – covalent – ionic in nature and the anisotropic bonding nature relates to the mechanical and physical properties of these layered machinable ceramics. Ti_2AlC has a low density of 4.1 g/cm^3 and a high electrical conductivity of $3x10^6\Omega^{-1}m^{-1}$. Due to the nature of the bonding the bulk modulus of Ti_2AlC (186GPa) is much lower than the bulk modulus of binary TiC (240 GPa) [9]. It has a brittle to ductile transition temperature of aproximately 1050^{o}C [10] and its stiffness is not strongly affected at room temperature. Barsoum et al. [11] has found that the shear modulus of Ti_2AlC at 1000^{o}C is 88% of its shear modulus at room temperature. Barsoum [1] highlights that the presence of a number of basal plane dislocations explain why these phases have good damage and fracture tolerance. These basal dislocations are confined only to the basal plane and are arranged in arrays or kink bands. These kink bands restrict the propagation of cracks along the basal plane, making these materials more fracture resistant with a fracture toughness of 6.5MPa.$m^{1/2}$ [12]. This effect of kink banding resisting crack propagation in Ti_3SiC_2, MAX-phase can be seen in figure 4.

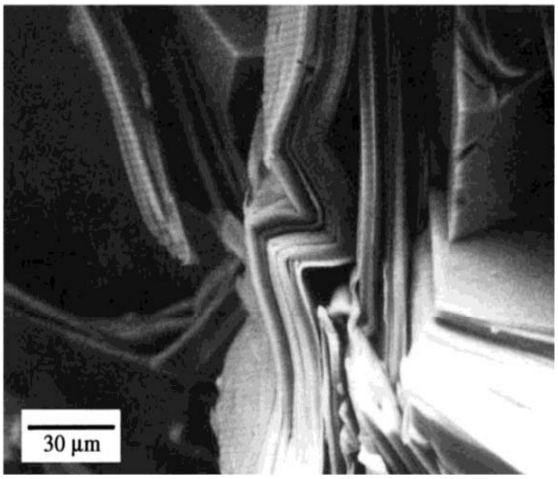

Figure 4. Kinking effect in Ti_3SiC_2 [12]

In this PhD, porous Ti_2AlC MAX-phase ceramics will be produced by Self-Propagating High Temperature Synthesis (SHS) to understand the formation mechanism of the material and also the thermodynamic of the combustion mechanism; therefore the next section will describe the history and development of SHS.

1.3 History of Self-propagating High temperature Synthesis (SHS)

SHS is a novel technique developed for the production of engineering ceramics and other advanced materials. This process is advantageous since it is low cost and energy efficient compared to the classic solid-state sintering process. SHS involves the combustion of a compact powder mixture in air or inert atmosphere which provides sufficient heat (via an exothermic reaction such as reaction 1) energy from the chemical reaction to make the reaction self-sustaining without any further addition of external energy. The SHS process is schematically shown in figure 5. The reaction takes place in the form of a combustion wave propagating through the entire reaction mixture converting it into the desired product.

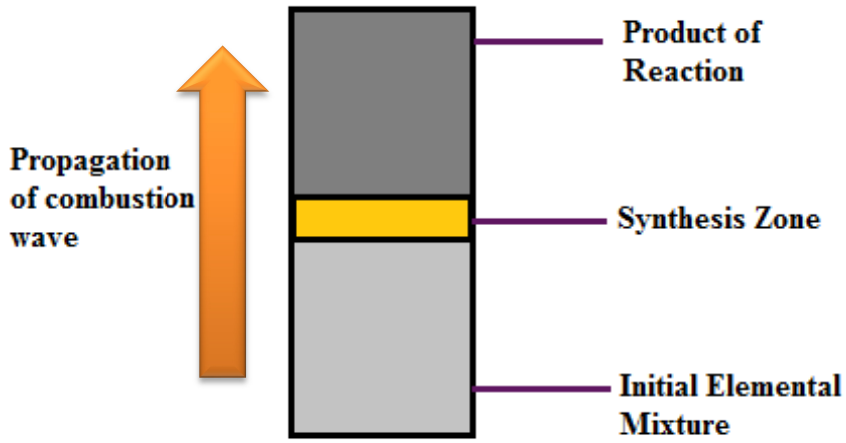

Figure 5. Schematic representation of SHS process

The discovery of this process dates back to the 19th century but became popular when scientists, Borovinskaya, Shkiro and Merzhanov were searching for a new pattern of combustion [13]. They made a scientific discovery which was coined as the 'solid flame phenomenon'. The reaction was observed between titanium and boron yielding titanium di-boride. The fact that these products retained their original shape with a hard and dense body was of interest and soon they realised the potential of such a simple method and began to research its potential for producing high value ceramic products. The term 'solid flame' means that the compound involved in this type of phenomenon retains its solid state even at maximum combustion temperature. i.e. throughout the entire duration of the reaction. It was found that the products obtained from this type of reaction made good refractory compounds. These developments led to the birth of a new production technique, especially for refractory compounds, known as the self-sustaining high temperature synthesis, widely known as SHS. Since then many countries such as the Russia, USA and Japan have conducted extensive research to explore its capability and limitations in different fields. By 1976, 30 different Russian groups were engaged in researching the SHS process and the ceramics that could be produced using this method. The SHS process has been recognised as the outstanding achievement of the Academy of Science of the USSR. In 1980, many plans were undertaken to integrate SHS technology into industrial production [14].

The earliest work on combustion synthesis ever recorded was in 1825, when Berzelius found zirconium oxide could be made by heating amorphous zirconium metal and the reaction could be ignited below room temperature [15]. It was Goldschmidt in 1885 who suggested that aluminium metal can reduce most metal oxides at high temperature which is commonly known as thermite reaction in which Al metal is oxidised by another metal oxide mostly Fe_2O_3 [16]. The reaction was a solid-solid, non-catalytic, self-propagating thermite reaction and Schmidt stated that: "in a thermite reaction, a metallic compound is reduced by one of several metals or metallic alloys in such a way that when the mixture is ignited at one place, the reaction continues on its own accord" [16].

Since then many research groups and institutes has been carrying out various experiments to study this technology in more detail. The major researchers are based in the USA and Japan. The latter of these, in Japan, successfully used SHS to produce many materials and even pioneered the art of depositing corrosion resistant coating on pipes and to weld ceramics on metals. A two year DARPA research program [17] led to the much further research in this area. This includes the important contribution of Holt and Munir [18] to knowledge and understanding of SHS for manufacturing a range of ceramic systems.

SHS falls under the non-linear chemical phenomenon and as a result the end product not only represents the result of the combustion but is also the reason for the combustion to take place. The study of SHS gave rise to a new branch of research known as the structural macro-kinetics [19]. This deals with the study of both structural and phase transitions during heat and mass transfers during the chemical reaction. The SHS process was designed to study powdered mixtures of metals (Ti, Nb, Hf, Zr, Cr, W, V etc) with non-metals such as B, Si, S, C combined with intermetallic mixtures of Ni, Ti, Co, Al etc [14].

SHS is also known as a chemical synthesis process as it is mainly used in synthesizing different systems of chemical compounds such as solid solutions of binary compound, binary compounds and solid solutions of chemical elements, high temperature and high pressure phases, nonstoichiometric phases in addition to others. In 1995, more than 500 compounds were synthesized by SHS [14]. These included oxides (cuprates, niobates, tanthalates, ferrites etc), refractory compounds (nitrides, borides, silicides, and carbides), and intermetallic compounds such as aluminides, chalcogenides, phoshides, hydrides and many others [14].

1.4 Thermodynamics of Combustion reaction [20], [21], [22]

In order to clearly understand and control the SHS process, one should understand the thermodynamics involved in the process. In this way it is possible to study the different parameters involved in the process and the effect of the process on these parameters. There are a number of reports in the literature explaining the study on the formation of Ti_2AlC with different elemental reactions [23 - 27] but the thermodynamics of the SHS process is poorly explained. As a result, there is limited literature on the necessary thermodynamic data of Ti_2AlC. Hence there is a need for the development of a thermodynamic model to predict the temperatures associated with the formation of Ti_2AlC by SHS process. Hence the following methodology has been adapted as the back bone of the theoretical modelling technique.

Combustion reactions may be divided into many categories: explosives, propellants and pyrotechnics. One common characteristic of these reactions is the production of a large quantity of heat and gas. This project is interested in the study of pyrotechnics which ideally do not produce gas. Generally pyrotechnic combustions are mixtures which are not explosive by nature and are simply designed to burn. Their burning rate varies from below 1 mm/s to more than 1000 mm/s. SHS falls under the banner of a pyrotechnic reaction [20]. It is important to understand the thermodynamics of the reactions because the control of temperature and combustion wave propagation of the reacting material is essential to ensure high quality of the products and control the structure and phase composition of the final material. It also helps in assessing the stability and feasibility of synthesising a compound**.**

The combustion temperature in the SHS process is mainly associated with the change in enthalpy between the reactants and the products. During SHS, four temperatures are most important:

(i) **Initial temperature T_o**:- This is the average temperature of the reactant before initiating the propagation mode.

(ii) **Ignition temperature T_{ig}:-** This is the temperature at which the reaction is activated without further external heat supply.

(iii) **Adiabatic combustion temperature T_{ad}:-** The maximum temperature achieved normally under adiabatic condition.

(iv) **Actual combustion temperature T_c:-** Maximum temperature achieved under non-adiabatic condition.

Consider a SHS between solid reactants, **M** and **X**, so that $\mathbf{M_{(s)} + X_{(S)} \rightarrow MX_{(S)}}$. The reactants need to be heated to an ignition temperature to initiate the SHS reaction. Hence the reaction needs to be heated from T_o to T_{ig}. Therefore, the amount of heat, H(R) needed is given by:

$$H(R) = \int_{T_o}^{T_{ig}} \sum n_i C_p(R_i) dT + \sum_{T_0 - T_{ig}} n_i L(R_i) \qquad (1)$$

Where $L(R_i)$, $C_p(R_i)$ are the heat capacity and the enthalpy of the phase transformation. Since the SHS reaction is initiated at T_{ig}, there is no influence of the heat on unreacted layer, the heat of reaction $\Delta H(T_{ig})$ is given by:

$$\Delta H(T_{ig}) = -[H(P) + H(R)] \qquad (2)$$

Where H(P) is the adiabatic heat for the formation of products under adiabatic conditions, H(R) is the heat needed to rise the temperature of the reactants from $T_o - T_{ig}$. Hence the adiabatic temperature T_{ad} achievable is dependent on H(P). The adiabatic temperature will be $T_{ad}(T_o)$ as shown in figure 6, as it is the heat absorbed by the products under this condition.

The amount of heat, H(P), required to increase the temperature of the products from T_{ig} to T_{ad} is given by:

$$H(P) = \int_{T_{ig}}^{T_{ad}(T_0)} \sum n_j C_p(P_j) dT + \sum_{T_{ig} - T_{ad}(T_0)} n_j L(P_j) \quad (3)$$

Where $L(P_j)$ and $C_p(P_j)$ are the heat capacity and the enthalpy of phase transformation.

It can be seen in figure 6, that pre-heating from T_o to T_1, will decrease H(R) and increase the H(P) from T_{ad} to $T_{ad}(T_1)$. Whereas an increase from T_o to T_{ig} will reduce H(R) to zero and all of $\Delta H(T_{ig})$ will be left to be utilized by the products.

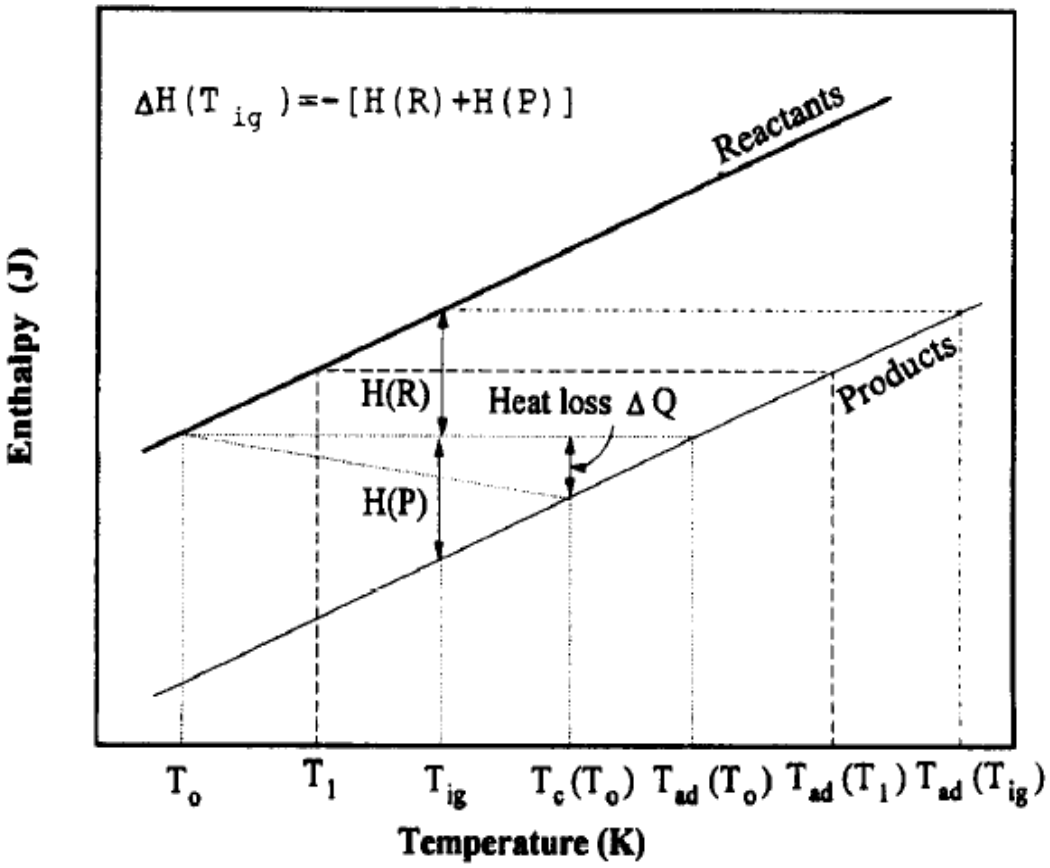

Figure 6. Schematic representation of the enthalpy-temperature plot for reactants and products considering no phase change [20]

$\Delta H(T_{ig})$ at room temperature can be calculated using the following equation:

$$\Delta H = \Delta H_{298} + \int_{298}^{T_{ad}} \left[\sum n_j C_p(P_J) - \sum n_j C_p(R_i)\right] dT + \left[\sum_{298-T_{ig}} n_j L(P_j) - \sum_{298-T_{ig}} n_i L(R_i)\right] \quad (4)$$

Where $\Delta H_{(298)}$ is the enthalpy of the reaction at 298K. Substituting eq (1), eq (3) and eq (4) into eq (2) and rearranging gives:

$$\Delta H + \int_{298}^{T_{ad(298)}} \sum n_j C_p(P_j) dT + \sum_{298-T_{ad(298)}} n_j L(P_j) = 0 \quad (5)$$

This equation indicates that T_{ad} has a roughly linear relationship with $\boldsymbol{\Delta H_{(298)} / \sum n_j (C_p(P_{j(298)}))}$ at T_o = 298K, considering no phase change, as shown in figure 6.

For the reaction to be self-sustaining it has been shown that $T_{ad} \geq 1800K$ [21]. The actual combustion temperature, T_c, is usually less than the maximum adiabatic combustion temperature T_{ad} due to heat losses to the surrounding environment. This can be seen in figure 6, where T_c and the related heat loss are shown by ΔQ**.**

In this project the calculation of T_{ad} will be performed with the help of mathematical models developed as shown above and the theoretical and experimental effects will be studied.

1.5 Characterisation of the ceramic products

In order to establish the phases and compounds present in the products after they are processed, it is necessary to perform analysis using a number of standard techniques. The most commonly used are Scanning Electron Microscopy (SEM), X-Ray Diffraction (XRD) and which will now be described.

1.51 Scanning Electron Microscopy (SEM)

SEM is used to obtain images of the microstructure of the sample (micrograph) with an electron beam. The sample is placed in a vacuum chamber and beam of electrons are scanned over the surface of the material. The beam interacts with the surface elements, resulting in the emission of secondary electrons from the surface. The primary beams are reflected back (back-scattered) and the energy absorbed by the material cause ionisation resulting in the generation of X-rays. X-ray signals are detected and computed in the form of an image. The image can be scaled from millimetre to nanometre scale and this is one of the main advantages of this technique. Care should be taken that no dirt or inclusions are present during the analysis.

Figure 7 is a JEOL 6480LV SEM equipped with an Oxford instrumentation IMLA X-act, X-ray detector. This was used to take the micrographs of the sample in this project. There are four types of imaging:

SEI (**S**econdary **E**lectron **I**maging): This is useful when high resolution details of the surface features or microstructure are needed.

BET (**B**ackscattered **E**lectron **T**opographic Imaging): The signal reflected carries the topographic feature of the material.

BEC (**B**ackscattered **E**lectron **C**omposition Imaging): Signals are reflected due to increasing density or atomic number.

BES (**B**ackscattered **E**lectron **S**hadow Imaging):- Provides enhanced topographic features as a result of a pseudo lighting angle.

Figure 7. JEOL 6480LV SEM equipment used in Bath

1.52 X-Ray Diffraction (XRD)

X-ray powder diffraction analysis is a powerful method by which X-rays of known wavelength are diffracted from the samples to be identified to find the crystal structure and phase composition of the ceramic. When the X-rays are passed through the powder sample, they are diffracted by the lattice of the crystalline structures of the element giving a unique pattern of peaks as seen in figure 8, which is due to the reflections at different angle and intensity. The diffracted beams can be identified and used as a 'finger print' for the structure.

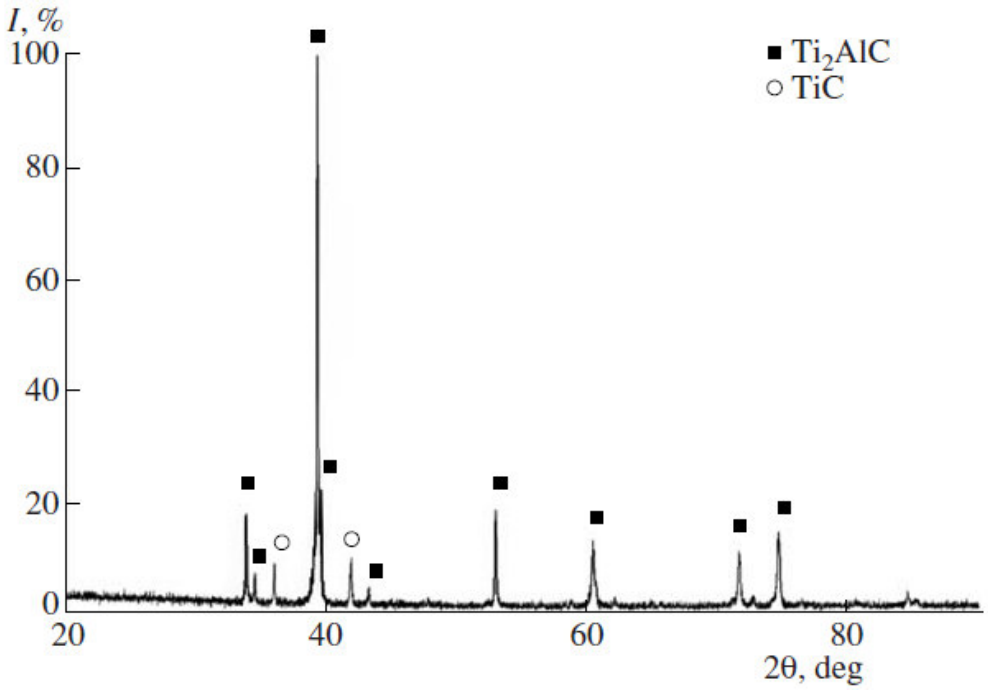

Figure 8. X-ray spectra generated from the compound's crystal structure [23]

The diffraction process obeys the Bragg relationship .i.e.

$$nl = 2dSinq$$

l = wavelength of the X-ray

d = distance between various planes of atoms in the crystal lattice

q = angle of diffraction

The X-ray detector moves around the sample collecting the reflections and measures the intensity of these peaks and their relevant positions. The highest peak is termed as the 100% peak and the intensity of rest of the peaks are measured as the percentage of the 100% peak. This is the general principle of chemical analysis using XRD technique. Xpert plus software developed by Philips was used to analyse the raw data generated by the X-ray diffraction equipment.

1.53 Density measurement using Archimedes principle

The density (apparent and bulk) and the porosity of the ceramic materials formed were calculated using the British Standards BS EN 623-2:1993. This method was standardised specially for advanced ceramic materials. Using this method the average pore size up to 200μm can be calculated. The applicable definitions for characterisation of porous materials are

(i) **Open pores**

The pores that are impregnated by the liquid in contact under vaccum

(ii) **Closed pores**

The pores that are not impregnated by the liquid in contact under vaccum or atmospheric pressure

(iii) **Bulk volume (V_b)**

Sum of the volumes of the solid material, the open and the closed pores in the sample

(iv) **True volume**

Volume of the sample, excluding any form of porosity

(v) **Apparent solid volume (V_s)**

Sum of the true volume and the volume of the closed pores

(vi) **Bulk density (ρ_b)**

The ratio of the mass of the dry porous sample to its bulk volume

(vii) **Apparent solid density (ρ_s)**

The ratio of the mass of the dry porous sample to its apparent solid volume

(viii) **Apparent porosity (π_a)**

The ratio of the total open pore volume in the porous sample to its bulk volume

.

Method of calculation

The mass of the dry test sample 'm_1' is determined and the sample is then immersed in liquid and impregnated under vaccum to find the apparent mass 'm_2', and finally the mass of the ceramic in air while still soaked with the immersion liquid 'm_3' is taken. Using these values m_1, m_2 and m_3, the test sample's bulk density, apparent solid density and apparent porosity is calculated based on the following equations:

$$\rho_b = \frac{m_1}{m_3 - m_2} * \rho_L$$

$$\rho_s = \frac{m_1}{m_1 - m_2} * \rho_L$$

$$\pi_a = \frac{m_3 - m_1}{m_3 - m_2} * 100$$

Where ρ_L is the density of the immersion liquid in kg/m^3.

The following section Chapter 2, is a detailed review on Max-phase Ti-Al-C system and methods to manufacture them

Chapter 2. Literature Review

2.1 Introduction

Before the 19th century manufacturing was carried out by individuals with a diversity of skills. This made production of artefacts such as belts, wagon wheels, shoes etc. very expensive. To reduce the cost of production, manufacturing methods were streamlined and merged to provide methods known as batch production and mass production. It was Eli Whitney in 1799 [28] who introduced the concept of uniform inter-changeability for the muskets (fire arm) as shown in figure 9.

Figure 9. Musket and their accessories [29]

This made the muskets low-cost and easy to repair. As a result, from this date onwards many inventors came up with the technologies and methods to produce everyday goods in mass and widely available at lower prices. Since the current study deals with manufacturing of MAX-phase based Ti_2AlC ceramics, a detailed review and different routes for producing the ceramic will be covered in the next section.

2.2 Review of the Ti-Al-C MAX-phase system

The most common method for producing ceramics is sintering. A simple definition of this method is to create an object from the powder state. Sintering technology has existed for thousands of years. Bricks heated in open fires were some of the first sintered products - this was done in order to increase their strength. Artefacts such as porcelain ware, glass bonded ceramic and gold platinum ornaments were sintered. During the sintering process, the small particles are fused together to form a strong bond between the particles as shown in figure 10.

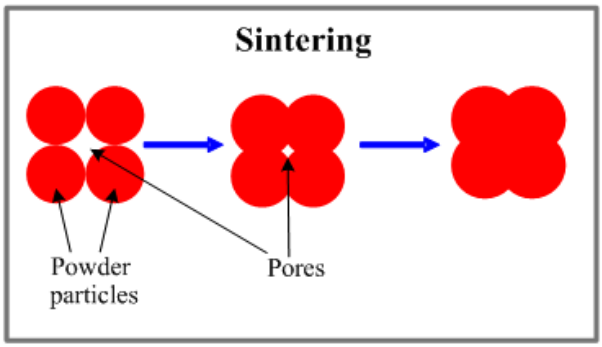

Figure 10. Schematic representation of sintering process [30]

Sintering mainly relates in the decrease of surface area and surface energy of the fine scale powders. During this process the adjacent particles partially adhere due to the diffusion and as a result the total surface area decreases. This process improves the physical and mechanical properties of the material and for advanced ceramics is typically carried out at a temperature below the melting point of the ceramic particles.

The Ti_2AlC MAX-phase compound was first synthesised by Veitschko in the 1960's [31]. The process of annealing elemental powders was used in an evacuated quartz tube at 1000^{o}C for 150 hours [31]. These unique materials were known as the H-Phases. Some reports [4, 5] claim that the two compounds in the Ti-Al-C system i.e. Ti_2AlC and Ti_3AlC_2 are the lightest and most oxidation resistant materials. In 1976 Ivchenko et al. [14] attempted to prepare Ti_2AlC by a method involving two-stages. The first step was the synthesis of powders followed by sintering of the ground powders. The sample contained a nominal amount of TiC and was recorded as having a density of 4.42 g/cm^3 and an electrical resistivity of $0.52\Omega^{-1}.m^{-1}$ [14]. It took nearly two decades to produce high purity bulk samples of Ti_2AlC [28, 32]. The work was carried out by Barsoum et al. [1] who called this material MAX ($M_{n+1}AX_n$) from the H-phase. His research group

blended the initial reactants Ti, Al_4C_3 and graphite powders by reactive hot pressing (HP) for 4 hours at 1600^oC and applied a pressure of 40MPa [28]. The alternative route was the simultaneous application of heat and isostatic pressure using hot isostatic pressing (HIP) at 1300^oC for 30 hours and 40MPa of pressure. These methods developed by Barsoum led to the synthesis of the first high-purity Ti_2AlC [32].

In 1994 Pietaka and Schuster identified a new ternary phase in this class (Ti-Al-C) Ti_3AlC_2. This was synthesised by sintering a mixture of Ti, TiAl, Al_4C_3 and C powders for 20 hours in pure hydrogen. Several combinations of powder mixtures such as Ti/Al/C, Ti/Al_4C_3/C, Ti/Al_4C_3/TiC have been examined as starting elemental mixtures. It has been reported that in most of the cases Ti_2AlC and TiC were recognised as the secondary phases [33].

Barsoum and Tzenov [34] prepared polycrystalline bulk Ti_3AlC_2 at a sintering temperature of 1400^oC for 16hrs at 70MPa by using reactive HIP of Ti, Al_4C_3 and graphite mixture. This product had Al_2O_3 as an impurity due to the presence of hygroscopic Al_4C_3. The disadvantage of the HIP processes is that it can be very time consuming, expensive and requires high energy inputs [34].

In any synthesis process the main concern is the achievement of high-purity products in a time efficient manner. Wang and Zhou [35] successfully produced high purity and dense Ti_2AlC by adopting a solid-liquid reaction carried out at 1500^oC for 5 minutes at 25MPa pressure followed by annealing for 20min at 1200^oC. The XRD analysis confirmed that the synthesised products contained no phases other than Ti_2AlC. An elemental composition of 3Ti/ 1.1Al/ 1.8C was used in this synthesis [35]. They also studied the reaction route for obtaining Ti_3AlC_2 from the elemental Ti, Al and graphite. From this investigation they proposed that the Al powder melted at 660^oC and the melt coated the Ti particles to form Ti-Al inter-metallic such as Ti_3Al and $TiAl_3$ at 740^oC. At elevated temperatures the diffusion of carbon into the Ti-Al inter-metallic led to the formation of Ti_2AlC, TiC and Ti_3AlC. Bai et al. [36] synthesised reasonably dense (up to 95% dense by applying external pressure) polycrystalline Ti_2AlC by SHS with a 'pseudo-HIP' process (means the SHS reaction was initiated using external energy source and the samples were densified after the reaction using HIP). The authors stated that the purity of the synthesised product mainly depended on the molar ratio of the raw powders. Ti_2AlC was densified by applying pressure soon after the SHS reaction.

All the above possible routes of synthesis have one thing in common, the application of pressure to make the product dense. However these techniques are not always efficient and may not be suitable for mass production of mechanical parts with complex shapes. There are obvious advantages if it is possible to sinter bulk Ti_3AlC_2 and Ti_2AlC using 'pressureless sintering'.

Pressureless-sintering (PS) is a traditional powder metallurgy processing method involving the sintering of the product from a green compact of powders without any additional pressure. Combustion synthesis is a type of PS reactive sintering but associated with an uncontrolled densification effect. Hashimoto et al. [37] conducted many trials to sinter Ti_2AlC using the PS method. Several oxides such as TiO_2, MgO and Al_2O_3 at 5wt% were mixed as additives in the Ti_2AlC powder. The product without additives was 94.2% dense while 5wt% Al_2O_3 was recorded as being 96.6% dense [37].

Published literature indicates that it is difficult to synthesise Ti_3AlC_2 via PS because of the weak bonding between TiC and the interleaved Al atomic plane of Ti_3AlC_2. In addition it decomposes at high temperature i.e. the Al atom has the potential to migrate out of the structure at elevated temperatures. Lu and Zhou [38] developed a technique to suppress this decomposition mechanism. The basic idea evolved from earlier work where the decomposition of Si_3N_4 during sintering was achieved by using high N_2 pressure or incorporating a Si_3N_4 bed [38, 39, 40]. Si, Ti_3AlC_2 and Al_4C_3 were used for this purpose. By placing the Ti_3AlC_2 compacts in Al_4C_3 powder, Ti_3AlC_2 was synthesised at 1450^{o}C for 150 minutes. Interestingly, no additives or pressure were used. The final product had a relative density of 96.2%.

The above methods give an insight into the preparation of ceramics using the sintering processes. They also indicate the importance of sintering temperatures and the role of the additives in producing dense and pure products. Another route of obtaining MAX-phase is through SHS which is a form of combustion synthesis process (described in section 1.3). Unlike sintering it has the advantage of using a self-sustaining reaction due to the exothermic nature of the reactants. As a result it is time efficient and requires low energy. Some research has been conducted into the synthesizing of Ti_2AlC and Ti_3AlC_2 using the SHS process [35].

Lopacinski et al. [41] conducted SHS using a direct reaction between Ti, Al and C. The reaction was highly unstable and resulted in the formation of binary carbides such as

Al_4C_3 and TiC in the partially molten state. Later when the team tried using TiAl as the source of aluminium, the combustion temperature significantly reduced and resulted in the formation of a ternary titanium aluminium carbide phase [41]. Zou et al. [42] reported that to obtain Ti_2AlC as the main phase from the combustion process, the carbon level should be deficient with respect to the ratio 3Ti/ 1.5Al/ C or 2Ti/ Al/ 0.7C. By following this protocol, single phase Ti_2AlC_{1-x} was successfully synthesised by carrying out SHS on the Ti-Al-C system.

Yen and Shen [43] carried out a series of investigations to synthesize Ti_2AlC and Ti_3AlC_2 using the SHS process. Compacts containing Ti, Al, C and TiC powder were used. The reaction successfully yielded 85wt% of Ti_3AlC_2 when 20mol% of TiC was used in the sample compared to 61wt% produced using an elemental mixture [43]. The authors also conducted a systematic study of forming Ti_2AlC by SHS. They used three different reactant mixtures including (i) Ti/ Al/ C, (ii) Ti/ Al/ C/ TiC and (iii) Ti/ Al/ C / Al_4C_3. The degree of phase conversion and the result of adding additives such as TiC and Al_4C_3 were studied. The additives resulted in a decrease in the combustion temperature corresponding to a reduced flame-front propagation velocity. Only the use of TiC as the additive enhanced the formation mechanism of Ti_2AlC to 90wt%. Samples with Al_4C_3, resulted in less Ti_2AlC compared with the samples containing TiC. This is due to the reduction in the exothermicity during the reaction. They also noted that, due to the formation of liquid Ti-Al and substantial growth of Ti_3AlC_2 grains, the sample underwent permanent deformation during the manufacturing process.

From this review it is evident that little work has been conducted on the Ti_2AlC phase, particularly manufacturing using SHS and using the material for making porous ceramic which will be explained in section 2.4. Hence to address the lack of knowledge in the literature, the proposed research will focus on updating the thermodynamic data on this material in addition to establishing a methodology for manufacturing porous Ti_2AlC ceramic. The potential applications of MAX-phase ceramics, and porous structures of this material, will now be described.

2.3 Applications

From the mechanical and chemical properties of the material, it is evident that MAX-phase ceramics have the potential for high temperature applications since the materials can withstand mechanical loads at elevated temperatures with minimal signs for fatigue failure [44].

El-Raghy explained [32] the importance of this material in jet engine application seen in figure 11. An increase in operating temperature of a jet engine by increased by $1^{o}C$ makes a tremendous impact on the fuel efficiency and has the potential to save around 1 billion $ every year. It also increases the efficiency of the vehicle fleet by three miles per gallons. These predictions are based on simple thermodynamic fact that efficiency of the engine .i.e. the fuel consumed is directly proportional to its operating temperature.

Figure 11. A typical jet engine in which majority of the parts are made of Ti metal which can be replaced by MAX-phase materials which has better thermal conductivity and thermal shock resistance [45]

The search for a light, thermally conductive material to replace the turbine blades continues since with better cooling the thermal load formed in the blade in use can be minimised and mitigate the catastrophic failure that causes the turbine blade to fracture and the debris formed blow up the whole engine. The turbine blades of the jet engines which rotates at high temperature and speed is susceptible to elongation due to the centrifugal force and ceramics offer a solution to developing a material capable of withstanding high temperature with high co-efficient of thermal expansion. However, due to its brittle nature they are susceptible to a catastrophic failure mechanism. Recently Gilbert and Bloyer from the Laurence Berkley National Laboratory showed [44] that the MAX-phase made from the combination of Ti-Si-C is fatigue resistant at high temperature up to temperature in excess of 1300°C. The reason for this is the presence of ligaments made of Ti-Si-C that hold the fracture surfaces of the crack together, thereby enhancing the resistance to crack propagation. Figure 12 shows the temperature dependence of compressive strength of Ti_2AlC.

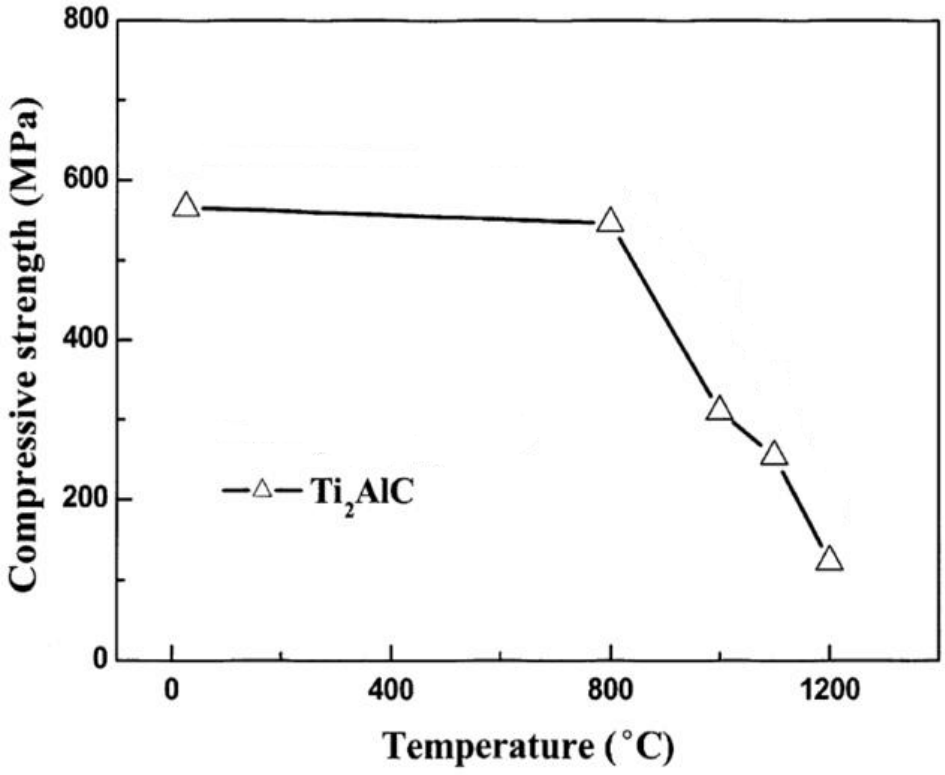

Figure 12. Compressive strength of Ti_2AlC at various operating temperatures [13]

One of the other potential applications of MAX-phase ceramics is as an anti-corrosive coating product. Barsoum et al. of Drexel University demonstrated [46] that Ti_3SiC_2 can be sprayed by plasma in a vacuum or by high velocity oxy-fuel in air onto a metallic substrate. MAX-phase Ti_3SiC_2 has been shown to be three times more thermally conductive, harder and significantly more wear resistant than graphite can replace graphite to some extent and reduce the carbon foot print.

Researchers in Australia and England [46] have found that Ti_3SiC_2 MAX-phase material exhibits self-lubricating properties. These compounds are therefore potential materials for applications such as bearings which require lubrication when operating at elevated temperature.

As these materials are very good conductors of heat and electricity, they also hold promising applications as heating elements and electrodes [5], as seen in figure 13. The 211 Max-phase based on Ti_2AlC ceramic was initially developed for high temperature structural industrial application.

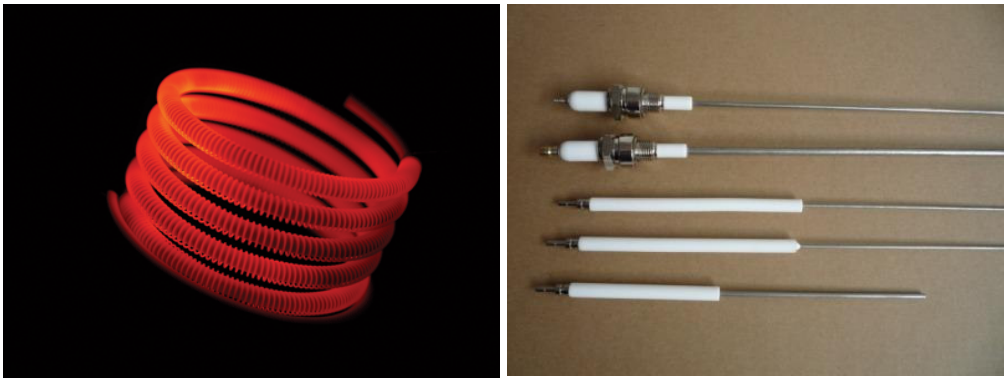

Figure 13. Ceramic heating coil in the left [47] and electrodes [48]

There is a report [36] on Ti_2AlC which tested the material for corrosion resistance to liquid metals. For example resistance to molten lead (Pb) at 650^{o}C and 800^{o}C was characterised to examine the ability of the material to act as a structural material in a lead cooled reactor. The material was less reacted than lead (Pb) and was considered to be an attractive material for nuclear applications.

Researchers [36] have also conducted ballistic impact experiments to examine the high strain rate deformation behaviour of Ti_3SiC_2. The result shows good response relative to its density with a bending strength of 660MPa and a flexural strength of 6.2MPa.m$^{0.5.}$ Hence it can also be used as light weight armour material and can be combined with other metal layers to enhance the mechanical resistance properties.

It can be seen above that the majority of the work to date has examined dense MAX-phase ceramic materials for a variety of applications to exploit its high thermal and electrical conductivity, high toughness, temperature and corrosion resistance. This PhD will consider application of porous MAX-phase ceramics. Therefore the following section will discuss porous ceramics.

2.4 Porous ceramics

2.41 Introduction

In recent years, with the evolution of new technologies and needs, there has been a growing demand for porous ceramics. Hence their manufacturing methods are being widely studied and the subject of extensive research. Some of their useful applications are in the field of filter manufacturing [49], where these porous structures are used in the filtration of high pressure gas at high temperature and are used as an aid to remove the pollutants. In the field of petroleum treatment, porous ceramics are used in recovering hydrogen from the crude oil [49]. They are also used as a substrate for catalysts in the filtration process [49]. Other applications are as thermal insulators in filter membrane for separating metallic impurities from molten metals such as steel, iron and aluminium [49]. Today, porous ceramic structures made from different materials based on their application are used extensively in the biomedical field. For example, porous hydroxyapatite is used for bone replacement and also as a drug delivery system [50]. There porous calcium phosphate materials can be used to replicate bone architecture and allow the growth of osseous tissue on an artificial substrate, thereby forming an artificial living bone structure [50].

Porous ceramics are mainly classified based on the pore size (nano to millimetres) and pore structure such as closed cell structure, open cell and membranes as seen in figure 14.

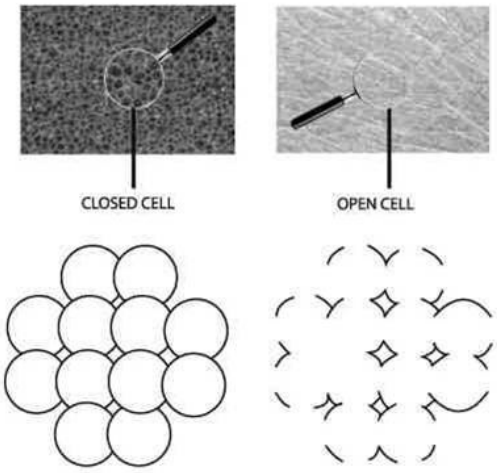

Figure 14. Microscopic cell structures of open and closed cell foam structures [51]

Highly porous ceramics are also known as *reticulated ceramics* and the degree of porosity is very high (70 – 90%). However in an open cell structure the pores are interconnected and this result in voids of size ranging from 10μm – 5mm. These porous ceramics are generally produced by replicating polymer foam [52]. Generally the ceramics produced by this method have low strength and toughness, for example a solid HA/TCP compound has a bending strength of 55MPa, but when it is formed into a porous ceramic (60% porous) its bending strength is 13MPa [53].

Depending on the pore size, membranes are classified as filtration membranes [Pore Size (PS) > 104nm], ultra-filtration membranes (PS, 2 -100nm), micro filtration membranes (PS between 102-104nm) and reverse osmosis membranes (PS 1nm or less) [54]. There have been reports [58] on developing ceramics with a combination of closed and open porosity, functionally gradient porosity and continuous pores. These combinations result in complex structures but allow tailoring of properties and performance. Some of the novel porous manufacturing methods use natural templates such as wood or coral skeleton [59]. This results in novel cellular ceramics with micro, meso and pseudo morphs of the initial template ranging from nanometre to millimetres [59]. All these techniques are directly influenced by the processing route used for the manufacturing. These manufacturing techniques can be tailored according to the potential application where one can easily tune the required porosity, pore size distribution, pore morphology etc.

Currently, porous ceramics are attracting attention in the field of electrodes, solid oxide fuel cells, bone replacement and tissue engineering, chemical sensors, solar cells and many others [60]. Some of the most popular techniques used in their production and the current research work are discussed below. Clearly in some cases the potential to create an electrically conductive porous ceramic based on MAX-phase ceramic properties would be advantageous.

2.42 Replica technique

The replica technique, shown in figure 15, is based on the immersion of a cellular substrate or template in a ceramic slip or suspension to produce a porous ceramic with the same features as the original template material. Templates made of natural cellular structure and artificial structures are used as sacrificial scaffolds in the replication technique [61]. As such they are removed by a 'burn-out' process as part of the sintering process (explained in detail in chapter 6).

Figure 15 shows a schematic representation of replica technique. A detailed explanation and commonly adopted composition of slip used in this technique is explained below.

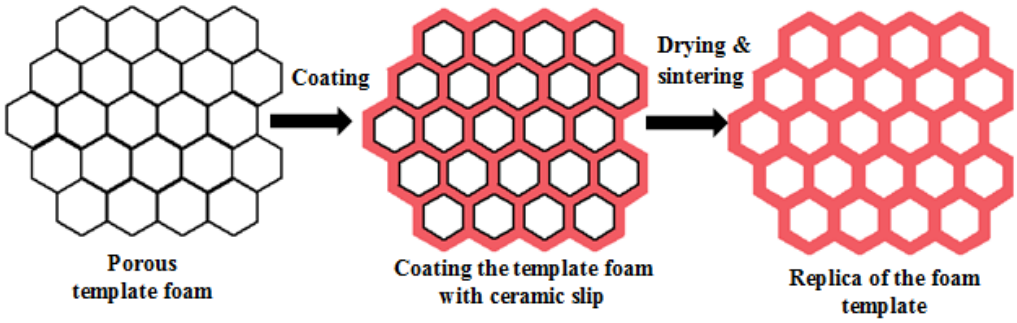

Figure 15. Schematic of replica technique

1. Synthetic template

The replica technique was invented in the early 1960's and considered to be the first method used in the manufacturing of macro porous ceramics. Schwartzwalder and Somers [62] first used this method to produce cellular ceramic structures of varying porosity, size and chemical composition using polymeric sponges [62]. Subsequently this technique proved popular and is used extensively in many industries to produce ceramic filters to filter molten metal and for other applications [63] due to the simplicity of the method.

In the replica technique a polymeric sponge (usually polyurethane foam) of the desired pores per inch (ppi) and pore size is dipped into a ceramic slip. This result in the ceramic slip coating the sponge. Excess material is squeezed out using a roller or blown out with air to enable a thin uniform coating of slip on the struts of cellular structure. The slip or slurry should be sufficiently fluid to remove the excess slip as well as sufficiently viscous to adhere to the template and avoid any dripping. It has been found

that the slip should have a viscosity ranging from 10-30 Pa.s at a shear rate of 5/s down to 1-6 Pa.s at a shear rate of 100/s [64]. This type of slip behaviour is achieved using a binder or additives such as carboxymethyl cellulose, polyethylene oxide, clay, colloidal silica and thixotropic in combination with a dispersant [65].

The coated polymeric structure is dried at room temperature and pressure and pyrolysed by heating between 300^{o}C to 800^{o}C. The heating rate should be lower than 1^{o}C/min in order to ensure gradual decomposition and diffusion of the material thereby avoiding building up of pressure within the struts [66]. In order to prevent the struts from cracking additional binders and plasticizers are added to the initial slip. Potassium, colloidal aluminium and orthophosphate are typical binders used [61]. Magnesium orthoborate, sodium silicates, polyvinylbutyl with polyethylene glycol are some of the plasticizers used [64, 65, 66]. The polymer template is removed by pyrolysis at elevated temperature. The porous ceramic structure is densified by sintering in a suitable atmosphere and at a specific temperature dependent on the ceramic material used.

Porous ceramics made using this method can have a total open porosity within the range of 40%-95%. Such ceramics are characterized by a reticulate structure of interconnected pores with a pore size varying from 3mm to 200μm. Figure 16 is a scanning electron micrograph (SEM) of an alumina based open cell structure ceramic produced by the foam replica method.

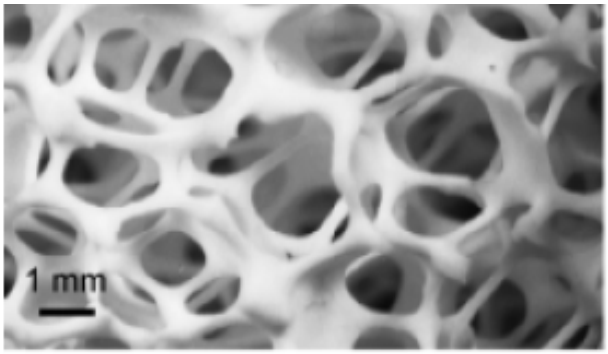

Figure 16. SEM image of alumina based open cell structure [61]

The open porous nature of the ceramic enables the permeation of gases and fluids through the pores thereby making the reticulated structure appropriate for filtration applications [67]. The main advantage of this processing technique, apart from its simplicity, is that the ratio of the open to closed pores in the final porous product can be adjusted by controlling slip viscosity and shear thinning behaviour. As with many other techniques there are drawbacks. The struts of the reticulated structure can be susceptible to cracking during the pyrolysis phase where the polymer foam is burnt-out. This can decrease the mechanical strength of the ceramic material [61]. Figure 17 illustrates how compressive strength of the open cell structured porous ceramic product is directly related to the density.

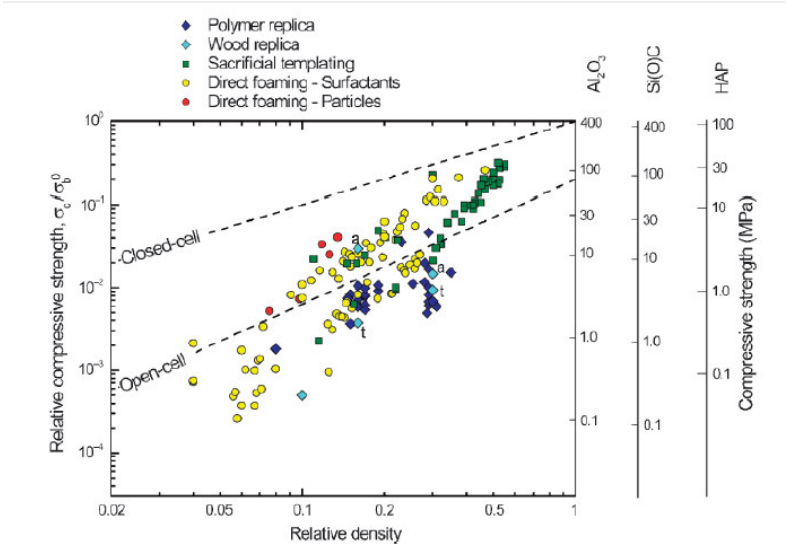

Figure 17. Compressive strength achievable by various replica techniques [61]

In order to overcome the problem of cracking, attempts have been made to improve the wetting of the slip by using additives [63], using a recoating step to fill the cracks [65] and introducing fibres to increase the integrity of the material. Porous ceramics derived from pre-ceramic polymers are found to have more crack free struts due to their partial melting of cross-linked polymer during pre-heating. Pre-ceramic polymers are those which are composed of a main chain of inorganic elements group with organic appendages. These organic appendages are shed to leave an amorphous network of inorganic elements which upon heat treatment transform into a crystalline ceramic [68].

2. Natural templates

Apart from synthetic foams, natural cellular structures have been used as suitable templates for producing porous ceramics by the replica approach. The natural replica templates available have interesting cellular structures mainly due to their intricate microstructures and pore morphology which is difficult to reproduce artificially [61].

White et al. in 1970 [69] used a method known as “replamine-foam” to reproduce the cellular structure of coral and other marine skeletons. The wax was initially impregnated under vacuum to create a positive form of coral structure. After the wax hardened the calcium carbonate which formed the skeleton of the coral was leached out of the structure using a strong acid. This artificially formed wax skeleton was later impregnated in a ceramic suspension to produce a macroporous ceramic. The organic (wax) skeleton was removed by pyrolysis [75]. This technique was successfully used to produce lead zirconate titanate (PZT) macroporous ceramic with desired piezoelectric properties. It has also been used to produce some macroporous hydroxyapatite scaffolds [64, 70]. To improve the mechanical properties of the macroporous hydroxyapatite scaffolds made from coral, a sol-gel approach has also been employed. Figure 18 shows an SEM of porous hydroxyapatite obtained from coral.

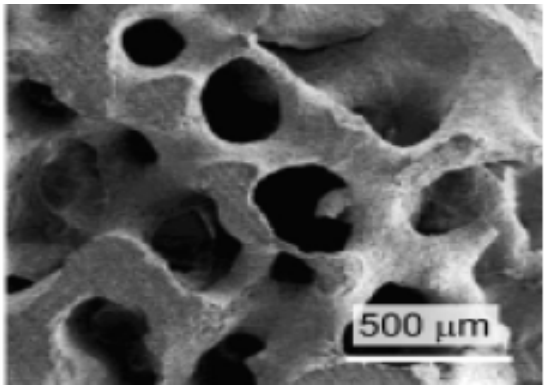

Figure 18. Macroporous hydroxyapatite derived from coral template [61]

Based on the “replamine-foam” technique many researchers have conducted studies on how the wood cellular structure is a useful template for producing porous ceramics. Figure 19 is a typical example to show the pore structure and scale obtained when wood is used as the template.

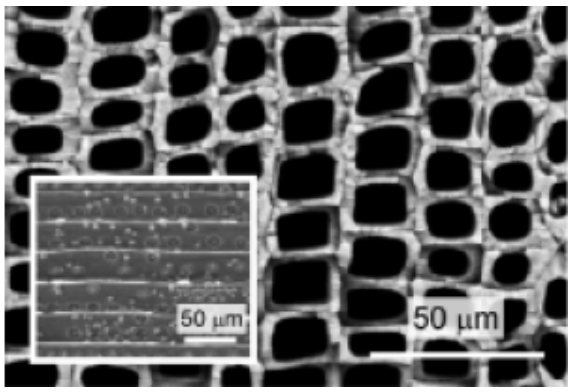

Figure 19. SEM of SiC macroporous ceramic obtained by the infiltration of wood template under the influence of Si gas [71]

Wood is a potentially useful template due to the oriented vessels in the structure of wood. This feature makes it suitable for the production of porous ceramics with highly anisotropic aligned pores which can be achieved only with this replication process [72]. Ota et al. [73] were the first to use wood as biomorphic template to produce cellular structured ceramic. The approach is relatively simple, as shown in figure 20.

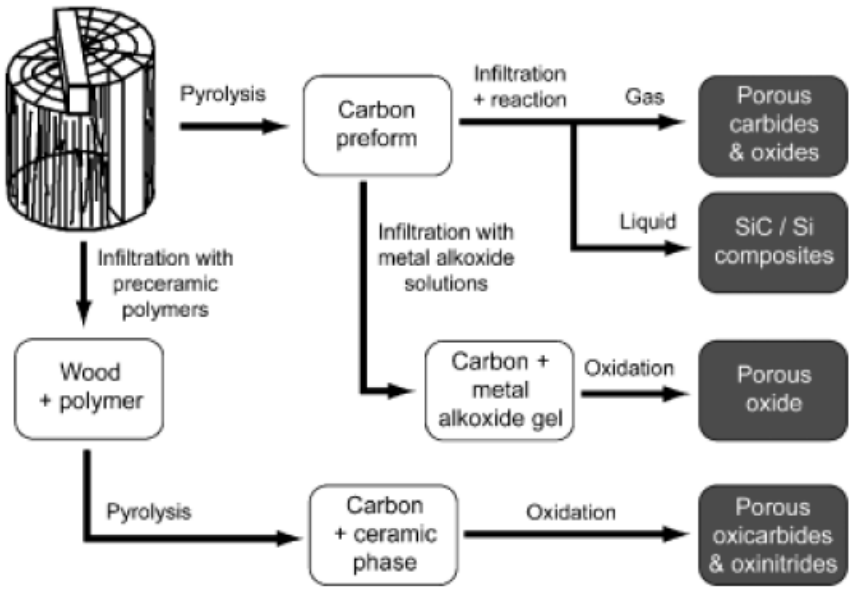

Figure 20. Schematic of the route used to transform a wood template into a porous ceramic [73]

The aim of their work was to form a carbon cellular pre-foam obtained by heat treating the wood in an inert atmosphere at a temperature of between 600°C – 1800°C. This pre-foam was infiltrated with liquid or gases at a high temperature to obtain the porous ceramic. Another approach is to infiltrate the carbon pre-foam with a liquid sol at room temperature and subsequently oxidize the material to produce a cellular ceramic [73].

The methods outlined above are the most common ones used as replica techniques to manufacture macroporous ceramics with tailored properties; other approaches are briefly outlined below.

2.43 Sacrificial template method

This method is employed when there is a need to prepare a *biphasic* composite which consists of a continuous matrix of ceramic with isolated pores. These particles are dispersed in a sacrificial phase which is homogeneously distributed throughout the matrix and is later extracted to generate pores with a microstructure as shown in the figure 21.

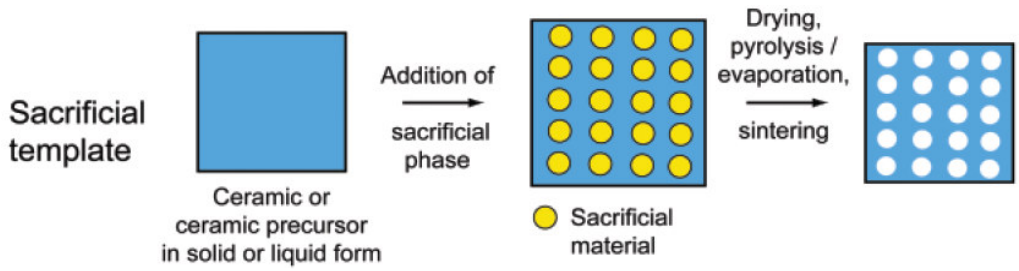

Figure 21. Schematic representation of sacrificial template technique [61]

Here the porous material is obtained by removal of the sacrificial porosifier. Common methods to produce biphasic compounds are:

(i) forming a two phase suspension followed by wet colloidal routes such as slip, tape or direct casting [74],

(ii) pressing a powder mixture of the two components [75],

(iii) impregnating previously consolidated pre-foam of the sacrificial material with preceramic polymer or ceramic suspension [76].

Both natural and synthetic materials are used as the sacrificial material to burn-out and generate the pores. These materials are often extracted using a thermal treatment known as pyrolysis at a temperature between 200^{o}C – 600^{o}C [75]. As with the foam replication technique, the heat treatment process and the gases released during the processing are the main disadvantages of using an organic sacrificial material. As an example, the heat treatment employed by Cycrafeldt and Ferrira [74] for the removal of sacrificial material from an alumina sample of 5cm x 10cm x 23cm having 50% porosity required a heat treatment of three weeks.

A chemical process, rather than thermal pyrolysis, involving salts, ceramics and other metallic sacrificial materials can be used to extract material from the microstructure to create porosity. Imhof et al. [78] used a salt based material (NaCl is the most commonly used material) which was extracted by repeated washing of the composite with water. Metallic and ceramic particles are often removed by acidic leaching [77]. In all of the above processes, care should be taken that the continuous matrix phase is partially consolidated before the sacrificial material is extracted. If not, the pores will collapse during the extraction process. To consolidate the matrix some setting agents and binders are often used [77].

Another alternative to create porosity is to use a volatile oil as a sacrificial phase. The oil can be used as either an aqueous or non-aqueous emulsion for fabricating porous ceramics [77]. The emulsion template method has been advocated in combination with sol-gel reactants to fabricate materials with high porosities of up to 90% [77]. This incorporation of a third phase allows the fabrication of porous ceramics with control over the pore distribution [78]. Some of the advantages of this method are:

(i) easy incorporation of the template into the continuous mixture phase by agitating the mix,

(ii) easy removal of the template,

(iii) degree of control of the pore size from 1 - 700μm [61], when immiscible liquids having a low interfacial energy are used.

Sacrificial template techniques can also be used in combination with chemical composition methods. Here, starch components are used as sacrificial templates in combination with different oxides to fabricate macroporous ceramics. Starch particles of various sizes ranging from 2-100μm are readily available and make the process simple. Above all, this technique can be applied to any material readily dispersed in an aqueous suspension [70]. Figure 22 shows the level of porosity that can be attained with this method and is compared to the replica process described in section 2.42. It is possible to achieve a porosity of 20 – 90% and a pore size ranging from 1 - 700μm.

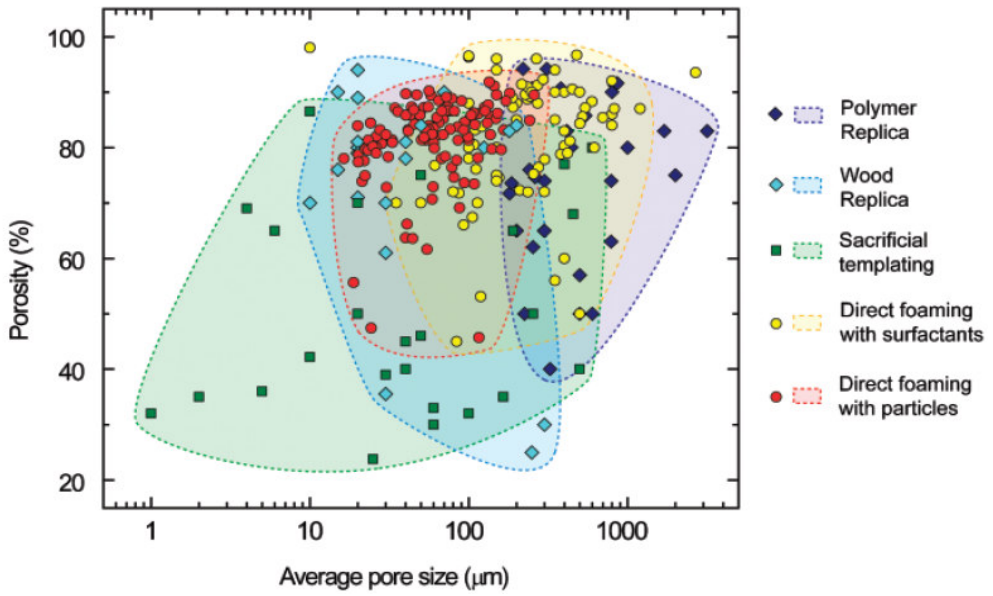

Figure 22. Porosity and typical pore size that can be achieved by different processes [65]

There are some reports [80, 81] on the production of foams by using a freeze casting method (which is explained in section 2.5), where water or a high melting point oil is used as a sacrificial material. Using this technique a highly oriented porous structures can be obtained by controlling the growth of ice crystals through unidirectional freezing of a suspension as shown in figure 23.

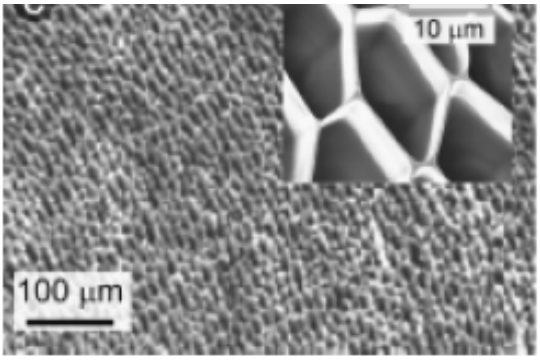

Figure 23. SiO_2 structure obtained through unidirectional freeze-drying of silica gel [80]

Using these methods the final ceramic is the negative of the actual template. One advantage of this approach is that, unlike the positive replica methods, the removal of the template does not leave any flaws or defect in the ceramic struts. As a result, the components produced using this method have higher mechanical strength than the components produced using the positive replica technique [81].

This PhD will also consider the fabrication of micro porous MAX-phase ceramics by a freeze casting method. Therefore the following section will discuss the concept of freeze casting and the parameters one should know to exploit the processing technique according to the requirements.

2.5 Review on freeze casting technique

Freeze casting involves the generation of porous structures by the solidification of a freezing solvent [82]. Water is the most common freezing solvent used [83]. The process involves preparation of the slurry of the desired material which is a mixture of freezing solvent, binder and the required ceramic powder. Once the slurry is poured into the mould it solidifies and the freezing vehicle sublimes from a solid to a gas under room temperature and pressure. The remaining ceramic porous body is then sintered to consolidate and densify the porous sample, leaving a porous structure throughout the sample which is the replica of the frozen solvent crystals. Fukasawa's [84] work on freeze casting alumina opened the gateway to exploit this technique for different materials and since then the efforts have been made to develop a greater understanding of this process.

The pore channels are formed when the particles are suspended in the slurry and are rejected by the propagating solidification front of the freezing solvent crystals [85]. The solidification is initiated by the appearance of solid nuclei in the slurry close to the mould wall where there is a large temperature gradient. With time the nuclei increase in size and grow parallel to the heat flow but in the opposite direction. Many porous materials can be processed by freeze casting which explain that the underlying processing techniques are not entirely dependent on the material, but rather rely on the physical interaction of the material particle with the chemical solvents used. Materials ranging from polymers, ceramics and metals can be used in this technique but the processing is predominantly dedicated to forming ceramic materials; these include biomedical grade ceramics such as hydroxyapatite (HAP) [86, 87], bio glass [88, 89], titania [90], zirconia and yttria stabilized zirconia [91, 92], HAP-TCP [81] and alumina [93, 94]. Organic and inorganic composites including HAP/gelatine [95], HAP/collagen [96], poly(a-hydroxyl acid)/bio-glass [97] can also be processed by mixing a water soluble polymer with ceramic powder [82].

2.51 Processing steps

The processing can be divided into four basic steps as seen in figure 24, and other processing steps may be included based on the freezing solvent used namely water, camphene or tert-butyl alcohol [82].

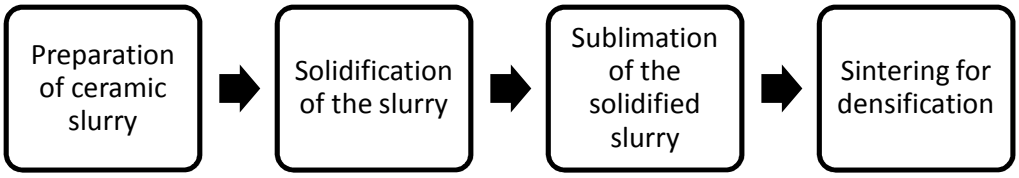

Figure 24. Basic four steps involved in freezing casting

2.51a Preparation of ceramic slurry

Here the ceramic powder under consideration is uniformly dispersed in the solvent, which is a mixture of freezing vehicle, binder, dispersant and plasticizers. The temperature of the slurry during preparation is usually the melting point of the freezing solvent. For example 45-60^{o}C if camphene is used. The *solid loading*, i.e. amount of ceramic, is chosen based on the porosity required and also to avoid any porosity and density gradient in the final product [83]. Dispersant or anti-settling agents are used to homogeneously suspend the ceramic particles in the solvent. Binders are used to strengthen the green samples after sublimation of the freezing vehicle. Finally the slurry is poured into the mould of desired shape to solidify.

2.51b Solidification of the slurry

This is the most important stage in this process as the characteristics of the pore are determined in this stage. During this stage continuous crystals or dendrites are formed as seen in figure 25.

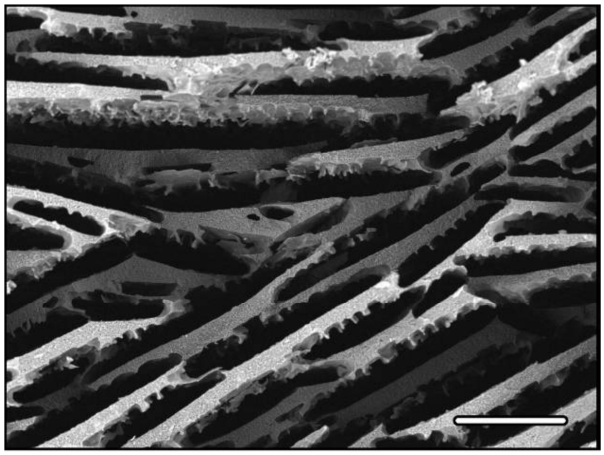

(a)

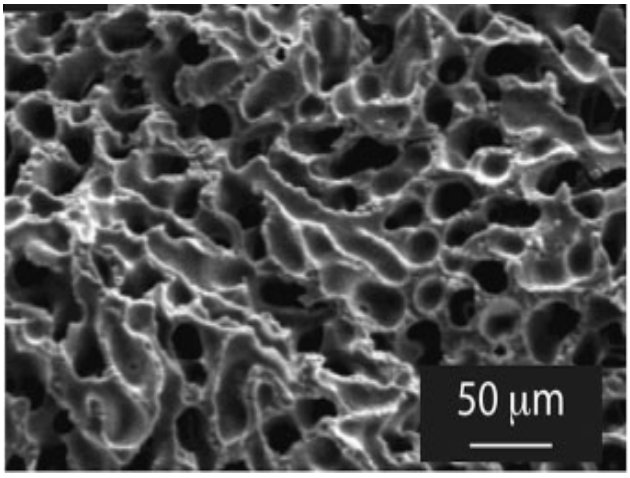

(b)

Figure 25. (a) Water crystals formed during freeze casting of alumina [98], (b) camphene dendrites formed during freeze casting of alumina [99]

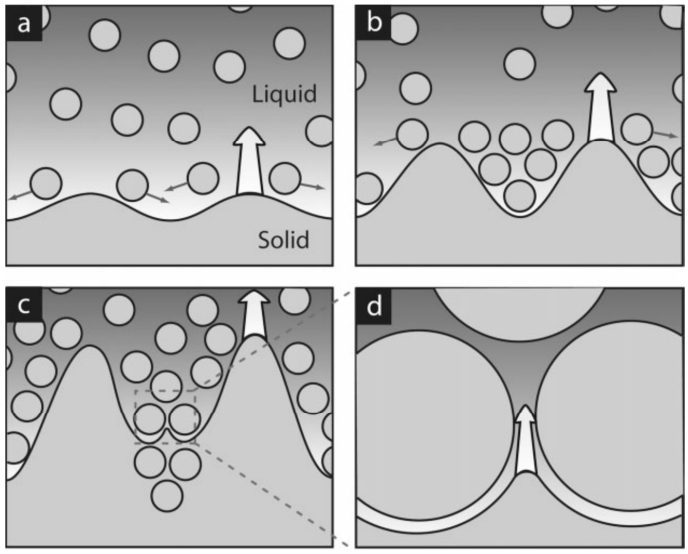

Figure 26. (a) Solidification front growing into the slurry with ceramic particles. The particle moving in-between the growing dendrite crystals, (c) particles entrapped between the dendrite crystals, (d) dendrite growing into the inter-particle gap [83]

These dendrites grow into the slurry by entrapping the ceramic particle in between the crystals as seen in figure 26. Depending on the pore morphology, isotropic or anisotropic cooling is introduced for homogeneous and directional cooling [100]. The solidification temperature mainly depends on the freezing vehicle used. For example, if water is used a low temperature below $0^{o}C$ is required and when camphene is used the slurry solidifies at room temperature as the camphene remain solid up to a temperature of $45^{o}C$ [100].

2.51c Sublimation of the solidified slurry

After the sample is solidified, it is removed from the mould and left for sublimation at a temperature and pressure conditions depending on the physical properties of the solvent. At this stage the solvent is sublimed from solid to gas and leaves behind pores in the green sample. The pores obtained in the green sample are a direct replica of the solid solvent. When camphene is used, a low vapour pressure of 1.3kPa is sufficient for sublimation (room temperature and pressure 20-$25^{o}C$) [83]. However, when water is used a conventional freeze dryer is used to sublime the water. Therefore camphene as the solvent makes the process effortless as no other specific equipment is required.

2.51d Sintering for densification

The samples are sintered using conventional sintering techniques after the freezing agent is completely sublimed. The sintering temperature depends on the densification temperature of the ceramic.

2.52 Structure and orientation of the pores

The structures of the pores mainly depend on the solvent used and the solidification condition. The solidification is often directional and leads to homogeneous nucleation of dendrites upon cooling as seen in figure 27 [101]. When water is used as a solvent, lamellar channels are obtained as seen in figure 25a. In the case of camphene as a solvent, a clear dendrite structure is obtained as seen in figure 27, and when tert-butyl alcohol is used as a solvent, a prismatic channel is obtained [102].

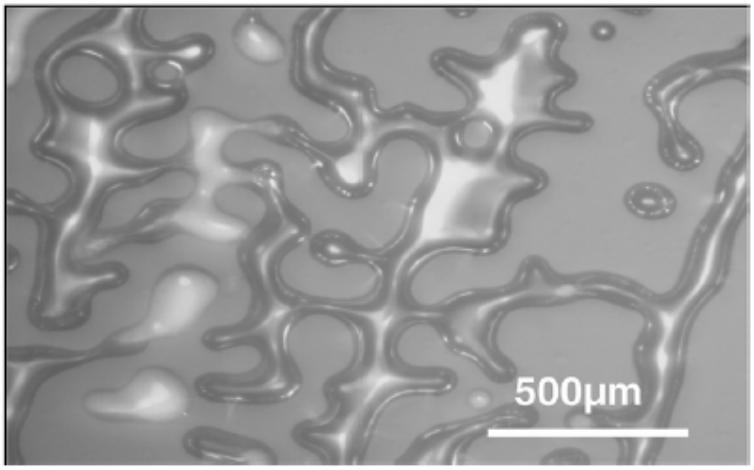

Figure 27. Directional dendrites formed after the solidification of the camphene [81]

A thermal gradient can be introduced to vary the cooling rate and achieve anisotropy in the ceramic sample. Macchetta et al. [81], has reported a graded porosity during the freeze casting of porous hydroxyapatite, using camphene as the freezing vehicle. They were able to produce large primary dendrites at a lower heat transfer rate. The heat transfer mechanism in freeze casting can be related to the equation 2.1, based on the Fourier heat conduction law i.e.

$$\frac{\Delta Q}{\Delta t} = -kA\frac{\Delta T}{\Delta x} \qquad Eqn.\ 2.1$$

Where ΔT is the temperature difference in the system, ΔQ/Δt is the heat transfer rate, k is the heat transfer co-efficient, A is the cross sectional surface area and Δx is the distance between the temperature difference. Roy et al. [103] studied the kinetics of the dendrite growth in pure metals and silicon system. They used the free dendrite model formulated by Di. Venuti [104]. According to this model, the dendrite tip radius decreases and the tip velocity (solidification front) increases with super cooling. This means that with high heat transfer rate a finer pore structure can be achieved. Koch et al. [105] in his work on freeze casting alumina found that larger pores are produced further from the cooling surface which experiences lower cooling rate [106]. Hou et al. [107] in his work on freeze casting β-Si-Al using camphene highlighted that heat transfer rate is not the only factor which determine pore size. His study was to understand the relationship between solid loading and pore size. The result showed that the pore size is inversely proportional to the solid loading which is also explained in Koch et al.'s work [105].

In this PhD, effort has been made to fabricate porous Ti_2AlC ceramic as no effort has been made to fabricate gradient porous Ti_2AlC ceramic. Hence the characteristic feature of the freeze casting technique (gradient porosity) was adopted based on Maccheta et al.'s [81] work. The gradient porous Ti_2AlC ceramic will be first of its kind and one of the potential applications can be in the field of solid-state electrodes in redox battery since it can take advantage of the resistance of the material to corrosion and its high electrical conductivity.

2.53 Summary

MAX-phase ceramics are an interesting class of materials that combine metallic and ceramic properties, e.g. they are electrically conducting but are corrosion resistant, and have high melting points and high stiffness. The majority of work to date has concentrated on manufacture of dense MAX-phase ceramics. In this PhD porous MAX-phase materials are examined, in particular the Ti_2AlC system since this material can offer multi-functional features such as corrosion resistance, electrically ($3x10^6\Omega^{-1}m^{-1}$) and thermally conductive and also high stiffness (186GPa) with low density ($4.1g/cm^3$) [9].

This thesis will therefore:

(i) conduct thermodynamic analysis of SHS processing of Ti_2AlC to produce porous structures,

(ii) understand the influence of SHS reactant composition (particle size, stoichiometry etc.) on the phase composition and microstructure,

(iii) develop foam replication methods to fabricate macro-porous Ti_2AlC,

(iv) develop freeze casting methods to fabricate micro-porous Ti_2AlC,

(v) demonstrate the applicability of porous Ti_2AlC in an application that requires high open porosity, sufficient mechanical strength and high electrical conductivity.

The next Chapter 3 describes efforts to use SHS to produce Ti_2AlC ceramic. Details on the thermodynamic modelling are covered, which was formulated to understand the thermodynamic mechanism and predict the combustion temperatures involved in the formation of Ti_2AlC using SHS process.

Chapter 3. SHS to produce Ti_2AlC ceramics

The objective of this chapter is to understand the formation of Ti_2AlC using self-propagating high temperature (SHS) and to explore the processing parameters involved in the synthesis of Ti_2AlC ceramic from the elemental reaction 3.1 ($2Ti + Al + C \rightarrow Ti_2AlC$), using SHS. The parameters are the thermodynamics of the reaction, addition of diluents to control the exothermic reaction, the effect of reactant particle size on the formation of Ti_2AlC and also the effect of different carbon sources (e.g. graphite or carbon black) in the elemental reaction mixture in forming the final MAX-phase product. By understanding the effect of these parameters on the reaction mechanism, it is possible to tune the process according to the requirements. For example, in order to form intermetallic compounds, for controlling the porosity without applying external pressure or improving the purity of the final product in terms of phase composition.

3.1 Thermodynamic modelling to predict the T_{ad} of SHS reaction

3.11 Introduction

As discussed in Chapter 1, section 1.4, the T_{ad} is the maximum combustion temperature achieved under adiabatic conditions in the SHS reaction; although in reality some heat will always be lost. For example, for the ZrB_2 system the calculated T_{ad} was 2235K while that experimentally measured was 1850K [108]. Once the T_{ad} is known, it is possible to predict the nature of the reaction, for example if the reaction is self-sustaining and whether or not liquid phases can be produced if the melting point of the reactants or products is exceeded. In addition to determining whether SHS is feasible a detailed thermodynamic analysis allows the understanding on the effect of (i) pre-heating of the reactants or (ii) the addition of diluents such as excess Al or Ti on the combustion temperature to be examined. Nevertheless, the precise value of T_{ad} is a measure of the exothermicity of the SHS reactions and an indicator of whether SHS is possible. For example it has been reported that a $T_{ad} \geq 1800K$ is necessary for SHS reaction to be self-sustaining [109].

The reactions of the Ti-Al-C system have been studied experimentally in detail by Hendaoui et al. [23-27] where excess reactants such as Al were used to reduce the combustion temperature and pre-heating can be used to increase the combustion temperature. However, while there has been experimental work to examine the manufacture of Ti_2AlC there has been no detailed thermodynamic analysis of the SHS reactions to date. This thermodynamic analysis to be considered in this chapter is novel as previously no effort has been made to evaluate the adiabatic combustion temperature of Ti_2AlC MAX-phase material.

The thermodynamic study presented here is based on the exothermic reaction (Reac 3.1), using available data on Ti_2AlC. Eqn. 3.1 is the basic thermodynamic equation for the analysis to form the MAX-phase Ti_2AlC by SHS. Further work will study how the thermodynamic model was formulated to predict the T_{ad} for the following reaction.

$$2Ti + Al + C \rightarrow Ti_2AlC \qquad (Reac.3.1)$$

Before the modelling is explained it is necessary to define the adiabatic combustion temperature T_{ad}.

3.12 Adiabatic combustion temperature T_{ad}

The T_{ad} is the maximum temperature attained in an exothermic reaction subjected to the SHS process. Alexander G. Merzhanov [110] have shown an empirical relationship which states that the reaction can be self-propagating only if $T_{ad} \geq 1800K$. There is another empirical relationship to examine whether the reaction can be self-propagating or not which takes into account all of the important parameters in SHS apart from the density ρ and the thermal conductivity k [111]. It is claimed that the effect of ρ and k should be considered when very high density or very high thermally conductive reactants are used [64]. The author [111] claims that SHS will occur if:

$$\frac{(T_{ad} - T_{ig})}{(T_{ig} - T_{start})} \geq \frac{\hat{C}_p(reactants)}{\hat{C}_p(products)}$$

Where T_{ad} is the adiabatic combustion temperature, T_{ig} is the ignition temperature at which the SHS is initiated, T_{start} is the initial temperature of the reactants, usually at room temperature, $\hat{C}_p$(reactants) is the average specific heat between T_{start} and T_{ig}, and $\hat{C}_p$(products) is the average specific heat between T_{ad} and T_{ig} [111]. The T_{ad} is calculated by considering that the enthalpy from the reaction is utilised to convert reactants into products with no heat loss to the surrounding environment.

3.13 Modelling

From Chapter 1, section 1.4, the thermodynamic equation to calculate the adiabatic combustion temperature T_{ad} of the reaction 3.1 is given by:

$$-\Delta H_r = \int_{298}^{T_{ad}} C_p(Ti_2AlC)dT \quad (Eqn.\,3.1)$$

Where ΔH_r^{298} is the enthalpy of the reaction (*Reac 3.1*), and 298K is the initial temperature of the reactants in this case. The T_{ad} is calculated by considering that the exothermic enthalpy of the reaction is used to heat up the products with no loss of heat to the surrounding environment. It is this exothermic heating makes the reaction self-sustaining, generating a combustion wave which propagates through the entire reactants converting it into desired products. This enthalpy, which is used in the formation of products, can be related to the adiabatic combustion temperature (T_{ad}) by the definition of the heat capacity of the product Ti_2AlC**.** Equation 3.1 is used to calculate the adiabatic combustion temperature considering no phase change of the product, such as melting during the exothermic reaction. A limitation is that, until the maximum combustion temperature is known, it is difficult to predict whether any phase change exists.

To increase the adiabatic combustion temperature it is possible to pre-heat the reactants prior to SHS and in this case the energy supplied by initial heating of the whole reactants needs to be considered i.e.

Enthalpy of the reaction + Energy supplied by pre-heating reactants = Energy to heat products

$$-\Delta H_r^{298} + \int_{298}^{T_{start}} C_p[2Ti + Al + C]dT = \int_{T_{start}}^{T_{ad}} C_p[Ti_2AlC]dT \qquad (Eqn.\,3.2)$$

As the Ti_2AlC material is a relatively new and unexplored ceramic material, only a limited amount of thermodynamic data is available. Some data may have been derived from the theoretical predictions [76, 112] rather than direct experimental measurements on materials.

The enthalpy of formation ΔH_f of Ti_2AlC was calculated based on Density Function Theory (DFT) which is a first-principle quantum chemical method. For a given set of structural coordinates and chemical composition, an electron density and total energy are obtained. The VASP (Vienna Ab-initio Simulation Package) code was used for calculating the enthalpy of the reaction. Based on this quantum chemical method the ΔH_f of Ti_2AlC was found to be -278.60kJ/mol. Duong et al. [112] have tabulated accurate thermochemical data of Ti_2AX phases based on ab-initio calculations and have reported -64.59kJ/mol-atom (-258.36kJ/mol) for the enthalpy of formation at 298K. This value of ΔH_f is very close to the value calculated by DFT, which is -278.60kJ/mol. The enthalpy of formation of -258.36kJ/mol and the data in Tables 1, 2 and 3 were used for the thermodynamic analysis.

Table 1. Reactant specific heat capacities (C_p) with temperature, T (K)

$$C_p = a + bT + cT^{-2} + dT^2 \text{ (J K}^{-1}\text{ mol}^{-1}\text{)}$$

Element	a	b	c	d	Accuracy (%)	Temperature range (K)	Ref
Ti_{α}	22.11	10.5×10^{-3}	-		1.5	298-t.p.	[113]
Ti_{β}	28.93	-	-		1	t.p.-1350	[113]
$Al_{(s)}$	20.68	12.39×10^{-3}	-		1	298-933	[113]
$Al_{(l)}$	29.31	-	-		3	933-1273	[113]
$C_{(s)}$	0.108	38.97×10^{-3}	-148.184×10^{5}	-17.413×10^{-6}	3	298-2300	[109]

Table 2. Product specific heat capacities (C_p) with temperature, T(K)

$$C_p = a + bT + cT^2 + dT^3 \text{ (J K}^{-1}\text{ mol}^{-1}\text{)}$$

Compound	a	b	c	d	Temperature range (K)	Ref
Ti_2AlC	58.10	0.10	-7×10^{-5}	1.80×10^{-8}	300 - 1600	[114]

Table 3. Enthalpy of formation (ΔH_f), transformation (ΔH_t) and fusion (ΔH_m)

Element	$\Delta H_{f,298}$ (kJ/mol)	T(K), ΔH_t (kJ/mol)	Melting point (K)	ΔH_m (kJ/mol)	Reference
Ti	0	1155K $\alpha \rightarrow \beta$ 3.47	1933	18.8 ± 2	[113]
Al	0	-	932	10.5 ± 1	[113]

3.13a Calculation of ΔH_r for the reaction 3.1

Enthalpy of reaction = Enthalpy of the products – Enthalpy of the reactants

$$2Ti + Al + C \rightarrow Ti_2AlC$$

$$2*0 + 0 + 0 \rightarrow -258.36$$

Therefore ΔH_r = -258.36kJ/mole.

From Barsoum et al.'s work [114], according to the experimental data, the specific heat capacity C_p as a function of temperature for Ti_2AlC is in the form of $\mathbf{C_p = a + bT + CT^2 + DT^3}$. Where T is the temperature in Kelvin. C_p is in J/K/mole. The thermodynamic data can be found in Table 2.

Hence by integrating C_p from 298K to T_{ad}, it is possible to generate the enthalpy of reaction at different combustion temperatures. The temperature that corresponds to the calculated enthalpy of the reaction (-258.36kJ/mole) will be the adiabatic combustion temperature.

Substituting the value of C_p in equation 1:

$$-\Delta H_r = \int_{298}^{T_{ad}} C_p[58.1 + 0.01T - 0.00007T^2 + 0.000000018T^3]dT$$

$$-\Delta H_r = \{(58.1xT_{ad} + 0.1T_{ad}^2/2 - 0.00007xT_{ad}^3/3 + 0.000000018xT_{ad}^4/4) - (58.1x298 + 0.1298^2/2 - 0.00007x298^3/3 + 0.000000018x298^4/4)\}$$

This was the equation used to generate ΔH_r at different T^oK values using an Excel spread sheet.

3.13b Solving for the reactant part of equation 1

The C_p for the reactant mixture of Ti, Al and C is shown in Table 1.

Table 4. Total specific heat of the reactants for the reaction 3.1

	a	**bT**	**cT^{-2}**	**dT^2**
Total C_p (2Ti+Al+C) in cal/mole	15.516	$1.71x10^{-2}$	$-3.54x10^{-4}$	-0.00000416
Converting to J/K/mole	64.949	$7.14x10^{-2}$	$-1.48x10^{5}$	$-1.739x10^{-5}$

The above procedure was plotted on a graph as seen in figure 28, which is the 'enthalpy versus temperature' graph, which is generally used to represent the thermodynamic of a SHS reaction. The figure summarises all the calculations carried out above in graphical form. The graph illustrates the changes in the enthalpy of the reactants and products at various temperatures.

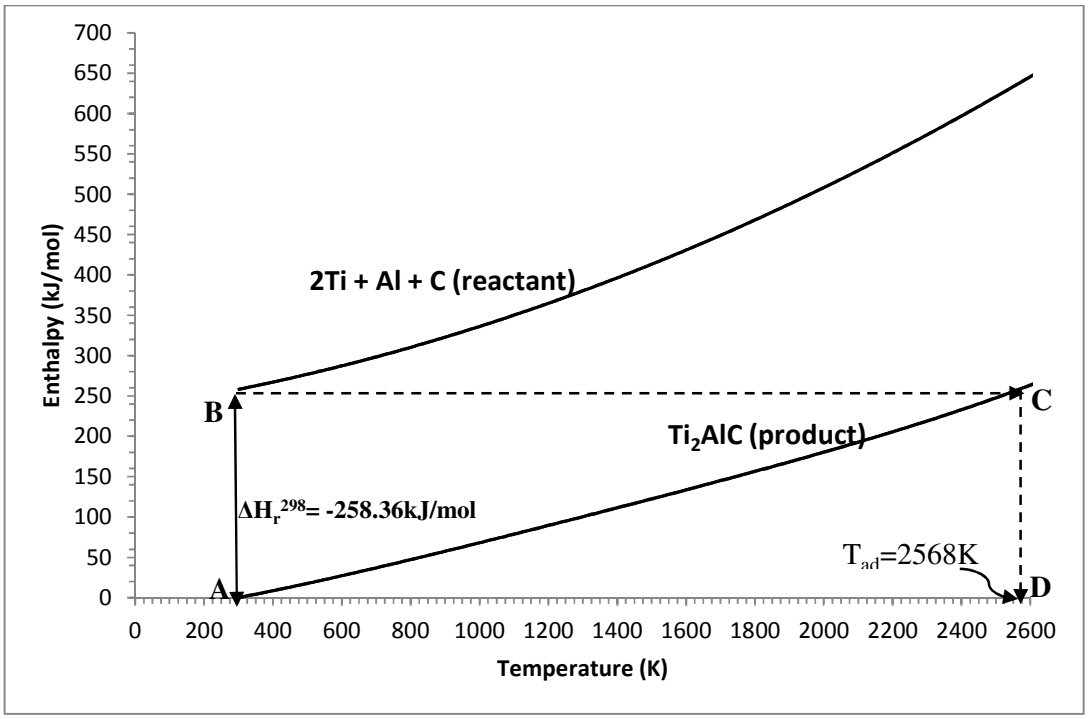

Figure 28. Enthalpy versus Temperature graph for the reaction 3.1 for the calculation of adiabatic combustion temperature

In figure 28, the vertical line (**A→B)** provides the T_{ad} from different starting temperatures and corresponds to the left hand side of the equation 3.2. The horizontal line (**B→C**) corresponds to the enthalpy of the products and the right hand side of the equation 3.2. The value of T_{ad} can be found from the vertical line down to x-axis (**C→D**). By theoretical calculation the maximum combustion temperature is found to be ~2568K. As explained earlier, for a process to undergo SHS, the $T_{ad} \geq 1800K$. Hence the reaction 3.1 is expected to undergo SHS based on the theoretical T_{ad} obtained. Combustion temperatures determined experimentally using thermocouples have been reported up to 2073-2110K [26, 115]. However in the above calculations, phase changes like melting of Al or Ti during the evolution of process is not considered. That is one of the reasons for the difference in T_{ad} value between the experimental and the theoretical calculation.

Often the heating of the reactants or products during SHS leads to a variety of phase transitions, such as melting of the reactant or products. These effects must also be considered; for example if the sample is preheated to 660°C (933K) and all the aluminium reactant melts the enthalpy of fusion of aluminium (ΔH_m) is considered as in equation 3.3.

$$-\Delta H_r^{298} + \int_{298}^{933} C_p[2Ti + Al + C]dT + \Delta H_m(Al) = \int_{298}^{T_{ad}} C_p[Ti_2AlC]dT \qquad (Eqn.3.3)$$

Since no data on the enthalpies associated with the observed phase changes in Ti_2AlC have been presented, high temperature differential thermal analysis (DTA) was undertaken using a Setsys TG-DTA on Ti_2AlC powder (Maxthal 211) using a palladium standard calibration. The results are similar to Hashimoto el al. [115] in that melting was observed with a DTA peak maximum at 1552°C with an associated enthalpy of 29.6kJ/mol as seen in figure 29; this was used in the enthalpy-temperature curves as shown in figure 30.

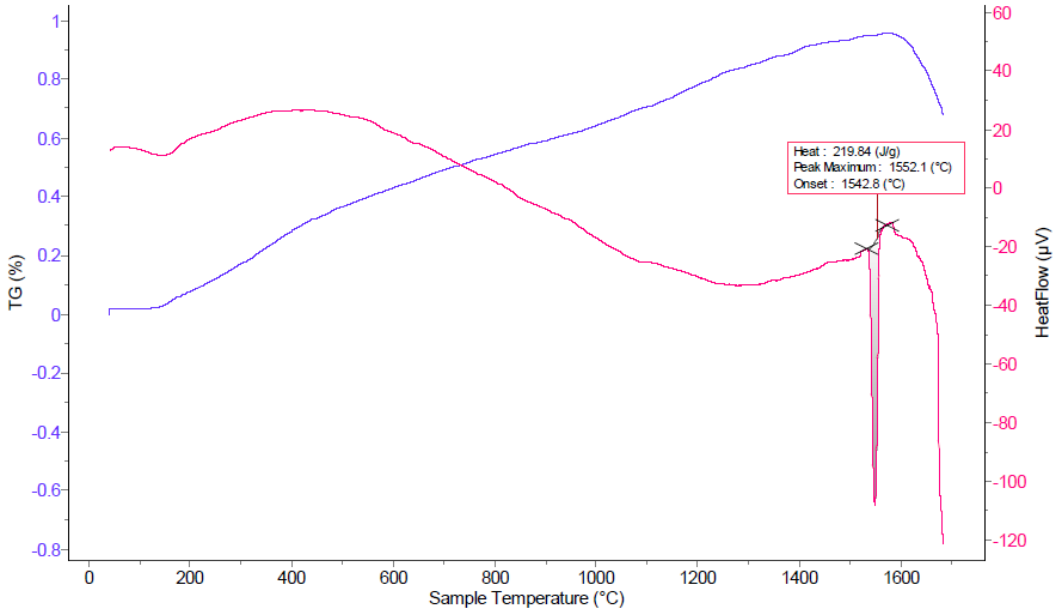

Figure 29. TG-DTA curves for Ti_2AlC powder

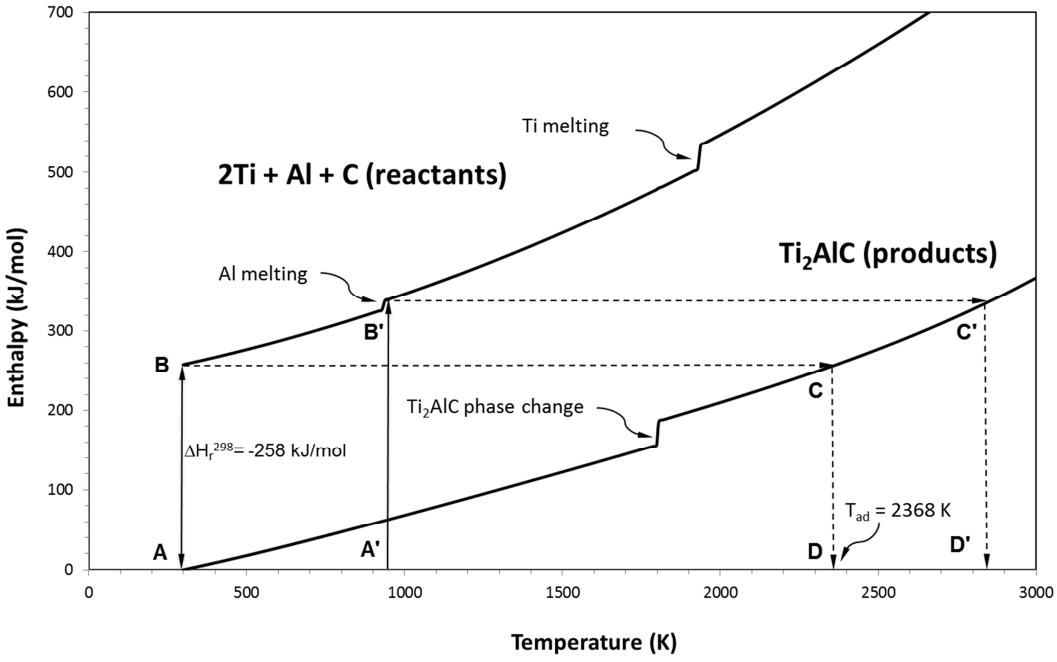

Figure 30. Thermodynamic analysis of reaction 3.1, including enthalpy of fusion of the reactants and the products

In figure 30, the vertical line **(A→B)** is the offset associated with the enthalpy of the reaction 3.1, and represents the left hand side of the equation 3.2. By creating a horizontal line **(B→C)** to the enthalpy of the products the T_{ad} value can be found from the vertical line to x-axis **(C→D),** which represents the right hand side of the equation 3.2.

According to this data, from figure 30, in equation 3.3, the adiabatic combustion temperature is 2368K. Combustion temperatures determined experimentally using thermocouples have been reported up to 2073-2110K [26, 115]. The difference between experimental and theoretical results can be accounted for by heat losses, which are assumed negligible in the adiabatic calculation and also any incomplete or side reactions producing other products [25].

3.14 Effect of diluents, on the reaction

From the thermodynamic model, it is understood which parameters cause the chemical reaction to be self-sustaining. In any conventional sintering process it is possible to control the evolution of grain size and the extent of phase transformation. Unlike sintering it is extremely difficult to do this with the SHS process due to the rapid nature of the process and the high temperatures involved. The main disadvantage of the SHS process is that the products obtained are highly porous [116]. Bowen and Derby [111] explained that it is possible to control the SHS by adding some diluents which do not take part in the reaction but lower the thermal mass and reduce the adiabatic combustion temperature T_{ad}. In simple terms, it will lower the exothermicity in the reaction and thus lower the T_{ad}.

To explore this further, reaction 3.1 was used with additional diluents such as excess Al and Ti, to see the effect on the T_{ad} as seen in reaction 3.2.

$$(2+x)Ti + (1+y)Al + C \rightarrow Ti_2AlC + yAl + xTi \qquad (Reac.3.2)$$

Where *x* and *y* are the excess Ti and Al respectively to act as diluents to tailor the combustion temperature. Excess aluminium or titanium can also be used in an attempt to create metal-ceramic composites. This is also taken into account in a similar manner such as in Eqn. 3.4,

$$-\Delta H_r^{298} = \int_{298}^{T_{ad}} C_p [Ti_2AlC + xTi + yAl]dT \qquad (Eqn.\ 3.4)$$

A graph of enthalpy vs temperature was plotted for reactions (3.2) as seen in figure 31(a) and 31(b).

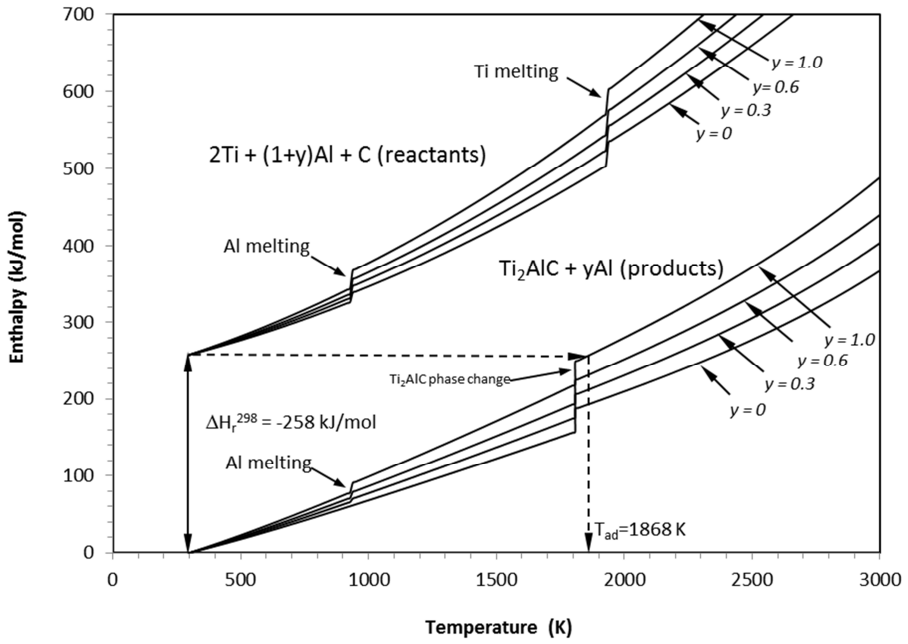

(a)

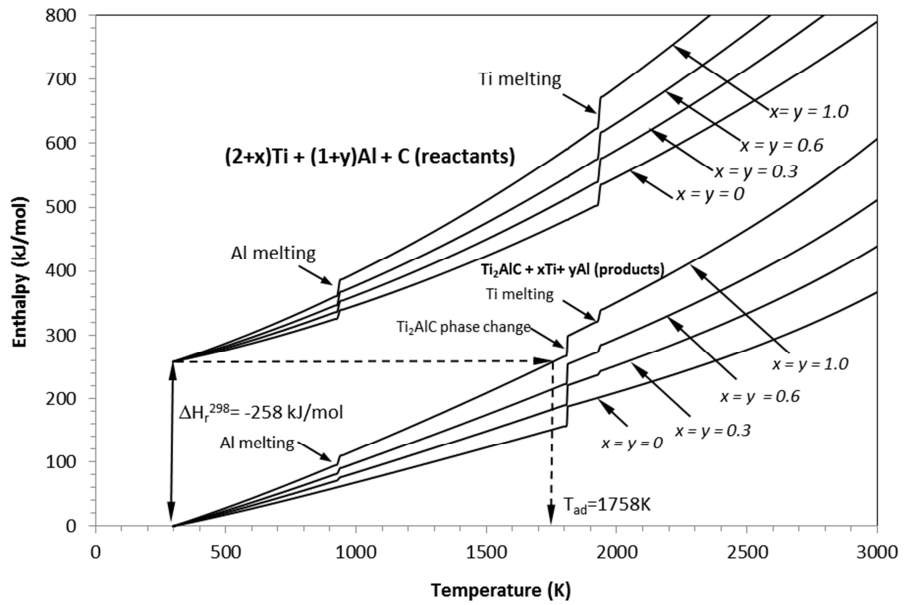

(b)

Figure 31. Graph a and b representing the thermodynamic modelling of reactions 3.2 with *y* > 0 and x and *y* >0 respectively

Figure 31a is the thermodynamic predictions when excess Al is used i.e. $y > 0$ is added to reaction 3.2, where the adiabatic combustion temperature decreases to 1868K when y = 1. Figure 31b is the thermodynamic predictions when both excess Ti and Al is used i.e. x >0 and y>0 in reaction 3.2. The T_{ad} for this reaction for when x = y = 1 is decreased even further to 1758K due to the increased thermal mass associated with the excess Al and Ti. Clearly as excess Al and Ti are added as a diluent, there is a decrease in the T_{ad} but it offers the potential to control the exothermicity of the SHS process and to form metal-ceramic composites. Hendaoui et al. [24] conducted a study on the effect of excess Al on reaction 3.2 and indicated that excess Al led to three important effects: (i) a shift in the conditions of the reaction between TiC and $TiAl_3$ yielding more Ti_2AlC compound; (ii) enhancement in the component diffusion due to the presence of more liquid phase resulting in easy ignition of the reaction; (iii) dilution of the system and hence reducing the overall exothermicity and more control over the reaction.

If the reactants are preheated prior to SHS, this additional energy is present to increase the combustion temperature. For example if the reactants of reaction 3.1 are pre-heated to 940K, the line **A'B'C'D'** can be used to calculate the new adiabatic combustion temperature as shown in figure 30; in this case the line **A'B'** corresponds the left hand side of equation 3.2 while the line **C'D'** corresponds to the right hand side of equation 3.2.

Figure 32, summarises the change in adiabatic combustion temperature with start temperature for reaction 3.1, with no excess Al or Ti.

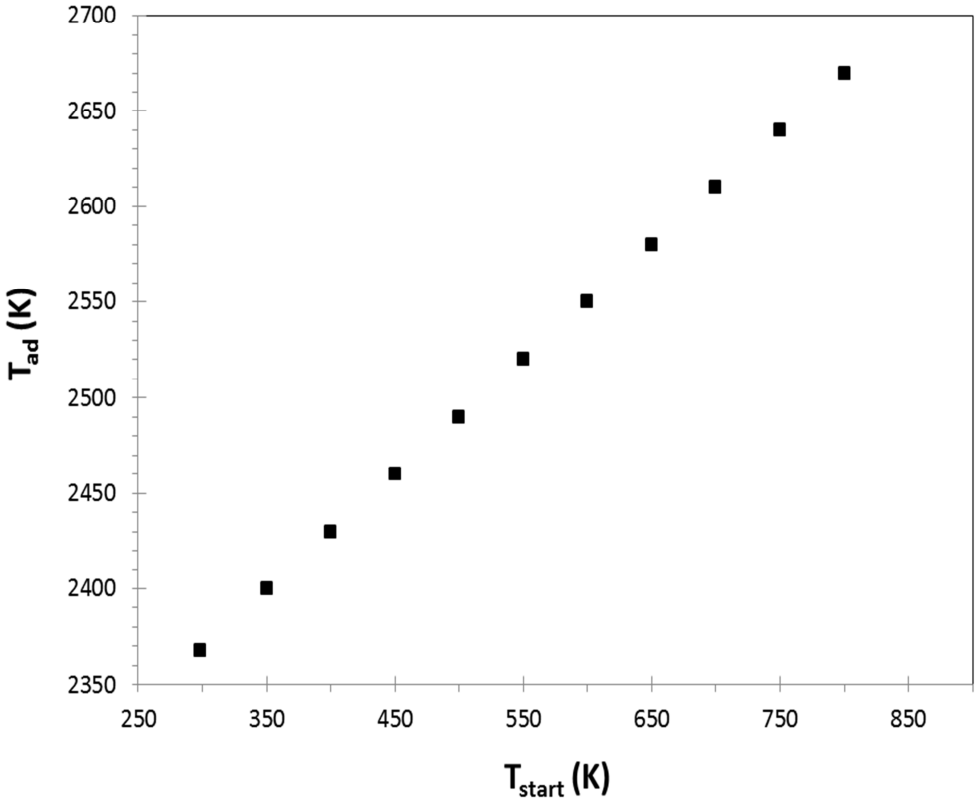

Figure 32. Effect on T_{ad} with different starting temperatures for reaction $2Ti + Al + C \rightarrow Ti_2AlC$

The next section will explain the procedure followed to experimentally measure the ignition temperature T_{ig}, which will be later used in the empirical relations to see whether the reaction to form Ti_2AlC MAX-phase material, obey the conditions to be self-sustaining or not, for example, the conditions described in section 3.12.

3.2 Thermal Explosion

3.21 Introduction

The thermal explosion mode of combustion synthesis process is very similar to SHS except for the fact that in thermal explosion the whole body of the sample is in contact with the energy source which causes the combustion of the whole sample at the same time (refer figure 33a). The temperature at which the thermal explosion initiates is termed the ignition temperature T_{ig}. This is in contrast to SHS where only a point on the sample is in contact with the energy source (tungsten wire in this case) which initiates the combustion in the sample, see figure 33b.

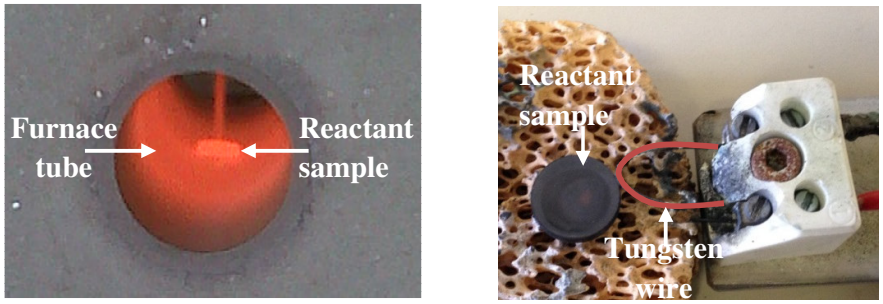

(a) **(b)**

Figure 33. Sample subjected to thermal explosion (a) and (b) sample subjected to SHS mode of combustion synthesis process

Thermal explosion experiments were conducted to observe the T_{ig} value and to examine if the material Ti_2AlC satisfies the condition to undergo SHS mode of combustion synthesis process as demonstrated in the next section 3.3 and also to study the effect of the particle size on the ignition temperature T_{ig}. As explained in Chapter 1, section 1.4, the T_{ig} is the temperature at which the reaction is activated in the sample without further external heat supply [20, 21, 22]. From the results of this study, it is possible to get a data for designing the combustion rig (construction details explained in Chapter 4, section 4.11) for conducting the SHS process. It is important to know the temperature as it is a vital data for thermodynamic modelling and it also helps in selecting the necessary ignitor element to initiate the SHS process, assuming the ignition temperature is the same for both the combustion synthesis modes (thermal explosion and SHS). The ignitor is a component in the combustion rig which supplies sufficient heat energy to the sample to initiate the combustion process.

3.22 Experimental setup

The experimental setup for thermal explosion experiment is as shown in the figure 34. It consists of a small furnace, a K type thermocouple to monitor the furnace temperature. The furnace is a basic type without any programming features. The rate of change in furnace temperature cannot be controlled. Hence the temperature increases rapidly (approx. 6.5^0C/minute).

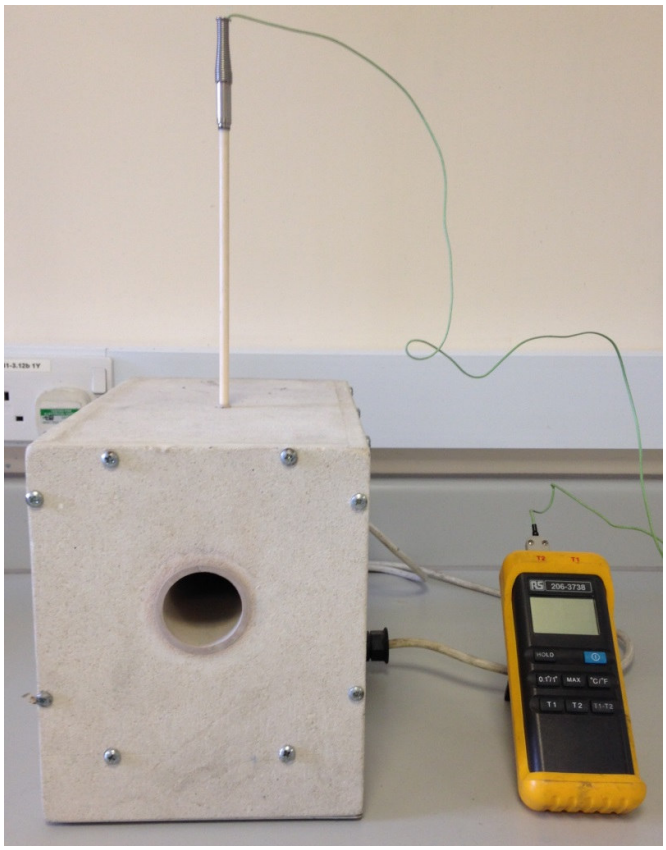

Figure 34. Experimental setup for conducting thermal explosion

The samples were prepared according to the following stoichiometric ratio:

$$2Ti + Al + C \rightarrow Ti_2AlC$$

In this experiment the particle size of Ti and Al powders were varied and the effect of particle size on the ignition temperature was monitored. The carbon source (in this case graphite of $\leq$ 20µm particle size) remained constant. Each sample weighed approximately 0.7 grams and was pressed at room temperature into compact cylindrical pellet of 13mm diameter in a uniaxial press using a pressure of 1.77kN/mm^{2}as shown in Table 5:

Table 5. Ignition temperature for different particle size

Ti 45µm Al 15 µm			
Serial Number	**Mass of the sample in grams**	**Pressing pressure in kN/mm^2**	**Ignition temperature T_{ig} in ^oC**
1	0.7008	1.77	720
2	0.7000	1.77	708
3	0.6989	1.77	708
4	0.7005	1.77	710
Ti 45 µm Al 25 µm			
1	0.7000	1.77	670
2	0.6995	1.77	668
3	0.7002	1.77	675
4	0.7010	1.77	678
Ti 45 µm Al 60 µm			
1	0.7001	1.77	685
2	0.7016	1.77	685
3	0.7020	1.77	678
4	0.7028	1.77	678
Ti 150 µm Al 15 µm			
1	0.7000	1.77	672
2	0.7014	1.77	650
3	0.7000	1.77	665
4	0.6995	1.77	663

3.23 Result and discussion

From the above Table 5, it can be observed that the particle size has no major role in the ignition temperature of the combustion process. The ignition took place around the melting point of Al which is 660^{o}C [117]. It is thought that in the mixture of Ti, Al and carbon, the molten Al acts as the combustion fuel for the ignition and this may provide a valuable insight into the reaction mechanism for Ti_2AlC formation from Ti, Al and C powders, this will be discussed in further detail in Chapter 4. Another important observation is, when the sample was placed in another programmable furnace with a lower controlled rate of change of temperature [150^{o}C/hour] the sample failed to react. This indicates that for a SHS reaction to initiate and become self-sustaining there should be a rapid increase in temperature at the heating source.

3.3 Ti_2AlC satisfying condition for SHS

As explained earlier it has been shown that it is possible to predict whether a reaction will be self-sustaining using the three conditions below,

(i) $T_{ad} \geq 1800K$ [110]

(ii) $-\Delta H_r^{298K}/C_p^{298K} \geq 2000K$ [118]

(iii) $\dfrac{(T_{ad} - T_{ig})}{(T_{ig} - T_{start})} \geq \dfrac{\hat{C}_p(\text{reactants})}{\hat{C}_p(\text{products})}$ [111]

The manufacture of Ti_2AlC by SHS has been examined by Hendaoui et al. [23,24] and the reaction is self-sustaining, therefore it is possible to assess whether these three relationships hold true for this particular MAX-phase system.

From the thermodynamic analysis, the T_{ad} is 2368K (when x = y = 0) and therefore satisfies condition (i). For condition (ii), since $\Delta H_r^{298} = -258.36 kJmol^{-1}$ and $C_p^{298} = 82.16 Jmol^{-1}K^{-1}$ (Table 2,) the ratio $-\Delta H_r^{298K}/C_p^{298K}$ = 3144K and also exceeds 2000K. Figure 35 shows the relatively linear relationship between $\Delta H_r(298)/\Sigma C_p(298)$ and T_{ad} for a range of selected compounds in the SHS literature [119]. It is interesting to note that the MAX-phase reactions considered in this work also follow this relationship.

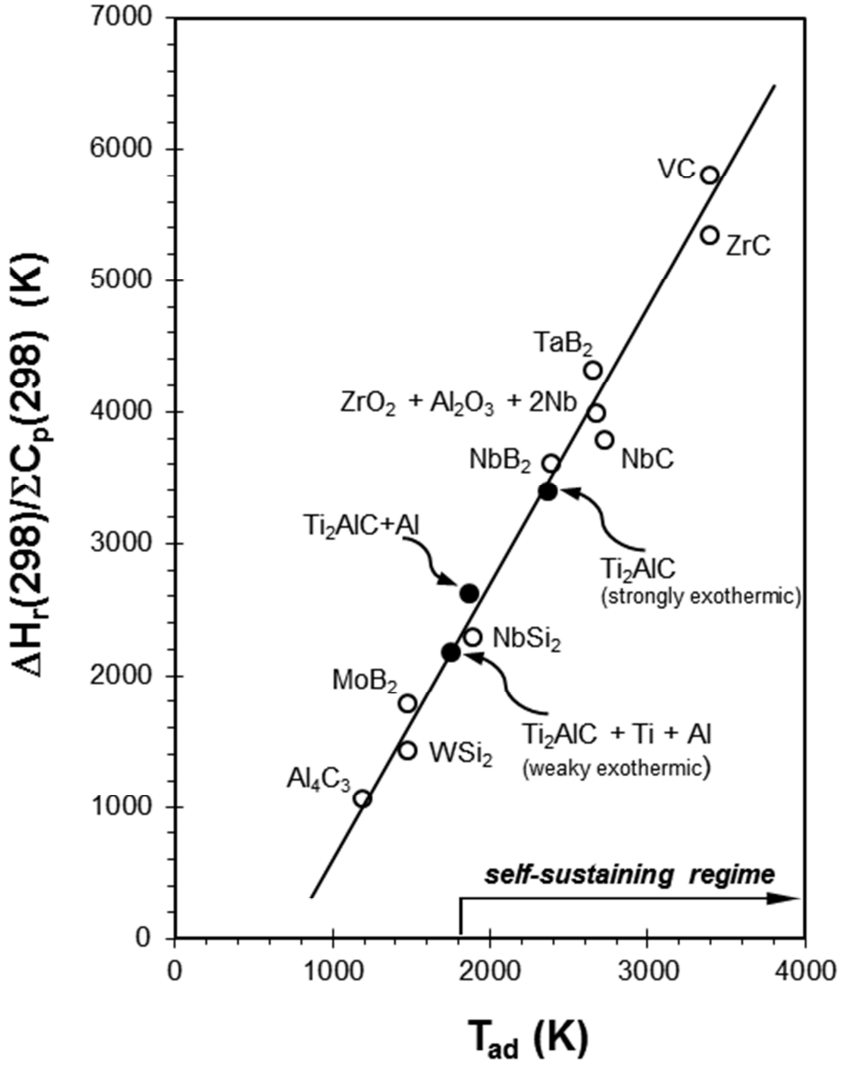

Figure 35. Relationship between $\Delta H_r(298)/\Delta C_p(298)$ and T_{ad} for selected compounds. Compounds (○) are reported in [119]. Compounds (●) are the MAX-phase reactions examined in this work

For condition (iii), T_{start}=298K,T_{ad}=2368K (figure 30), $\hat{C}_p$(reactants)=83.1Jmol^{-1}K^{-1} (Table 1,) and $\hat{C}_p$(products)=82.16Jmol^{-1}K^{-1} (Table 2). An ignition temperature (T_{ig}) of 943K, which is just above the melting point of aluminium, was experimentally determined by heating well mixed and pressed powders with a molar ratio of 2Ti:Al:C and measuring the ignition temperature using a type-K thermocouple which is explained in previous section 3.2. Based on these conditions $(T_{ad}-T_{ig})/(T_{ig}-T_{start})$=2.21 and $\hat{C}_p$(products)/ $\hat{C}_p$(reactants)=1.01 and criterion (iii) therefore correctly predicts that the reaction should be self-sustaining. For completeness, figure 30, shows the predicted T_{ad} based on an ignition temperature of 943K (line **A'B'C'D'**). These three relatively simple criteria for predicting SHS therefore work for this particular MAX-phase system and may also be applicable to the other MAX-phase family.

3.4 Summary

A detailed thermodynamic analysis was carried out to understand the thermodynamic mechanism involved in the SHS process for the formation of Ti_2AlC ceramic using elemental reaction 3.1. The thermodynamic model predicted the maximum adiabatic temperature T_{ad} of 2368K, which is close to the combustion temperatures determined experimentally using thermocouples (2073-2110K) [26, 115]. The thermodynamic data on Ti_2AlC has been updated by conducting DTA analysis and found that the enthalpy of fusion of Ti_2AlC is 29.6kJ/mol, which is used in the modelling to make it more accurate. Modelling has been carried out to understand the effect of adding diluents to reduce the exothermicity of the reaction. Based on this, thermodynamic models for reaction 3.2 was formulated and the models predicted the drop in the maximum adiabatic temperature T_{ad} with the addition of extra moles of Al and Ti, which is an useful information in controlling the porosity and fracture behaviour of the final product without the addition of external pressure for densification. Finally, the conditions to satisfy whether the reaction will be self-sustaining or not was applied to this material and most of the conditions proved positive for Ti_2AlC MAX-phase material.

One task of the PhD is to understand how the particle size of Ti, Al and carbon will affect the formation process of Ti_2AlC using SHS from the basic elemental reaction 3.1 To conduct this particular study, it is important to design a combustion rig to perform the SHS process with an inert atmosphere to prevent the oxidation of the sample product and the elements used in the combustion rig. The next Chapter will explain the study conducted to understand the effect of particle size on the formation of Ti_2AlC

ceramic by SHS process and will also explain the construction details of combustion rig used in this study to perform the SHS reaction.

Chapter 4. Study on the effect of particle size on the formation of Ti_2AlC using SHS process

4.1 Introduction

While thermal explosion requires a conventional furnace, the SHS process requires a dedicated experimental combustion rig to initiate the process. The main purpose of the combustion rig is to facilitate an inert atmosphere to prevent reactant and product oxidation and easy incorporation and ignition of the reactant sample. The reaction was initiated with an electrically heated tungsten wire under the influence of argon gas to prevent oxidation of the sample as well as the tungsten wire that was used as the ignitor.

4.11 Construction and working method

The combustion rig consists of a glass chamber which accommodates a simple electric circuit for heating the tungsten wire and a zirconia block to hold the sample as shown in the figure 36. The ends of the glass tube are covered with cork and the wire inlets are sealed with high temperature resistant sealant. This makes the chamber air tight when both the ends are closed. The entire chamber is clamped onto a ply board which is bolted to a rigid frame. This ensures the safety and prevents the whole setup from falling during the experiment or due to human handling. A power supply of 30A, 15V is used to heat the tungsten wire.

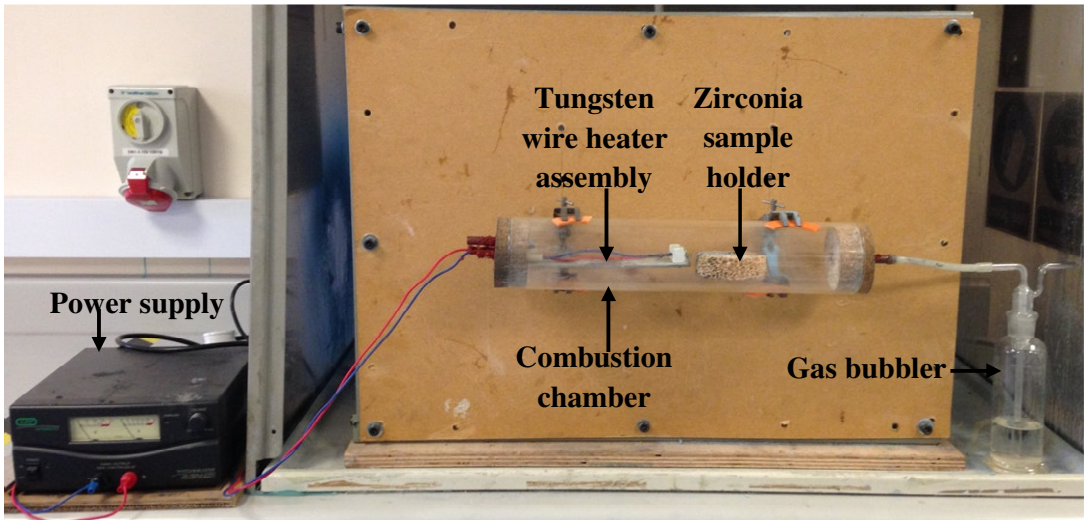

Figure 36. Combustion rig for the SHS process

Figure 37 shows the actual setup constructed to hold the electrical circuit and the connections to the tungsten wire. This was built for easy handling of the ignition components in and out of the chamber. This basic setup comprises of the combustion rig.

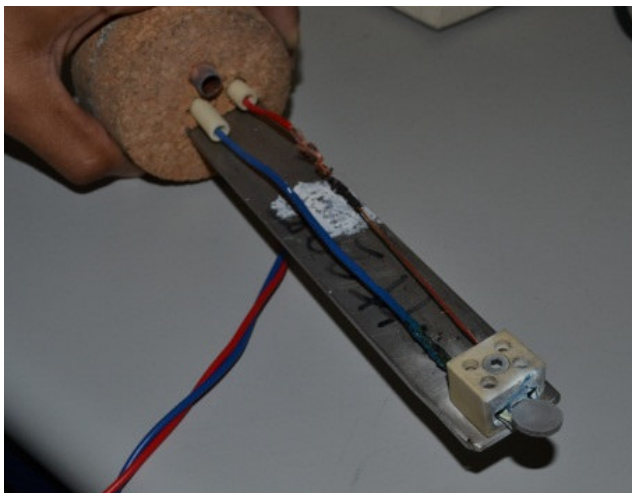

Figure 37. Actual setup of the sample and electrical circuit holder to heat the tungsten wire

4.12 Working method

It took some time to get the reaction started with this setup. Initially the sample was placed on the zirconia block and the tip of the tungsten wire was in contact with a point on the sample. This setup failed to exhibit consistent reaction ignition. The other method involved placing the sample on the wire as shown in the figure 37. This approach resulted in consistent initiation of the SHS reaction (as long as the reaction is sufficiently exothermic).

4.13 Initial experimental results

The sample was prepared according to the following stoichiometric ratio:

$$2Ti + Al + C \rightarrow Ti_2AlC$$

Ti 25µm (Aldrich), Al 15µm (Aldrich) and carbon fibre (mean diameter 3.55µm and mean length 105µm) was used. A mass of 0.8gm of the elemental powder mixture was pressed at room temperature into compact cylindrical pellet of 13mm diameter in a uniaxial press using a pressure of 1.77kN/mm^2. This optimum pressing pressure condition was chose as above this pressure, the green pellet plastically deformed and adhered to the surface of the die making it hard to retrieve the green pellets. And also, at lower pressing pressure, the pellets failed to form compact press with loosely packed particles in the pellet, making it hard to handle after pressing. The chamber was made air tight and argon is released into the glass chamber. A gas bubbler was fixed on the other end of the cork to ensure positive flow of gas in the chamber. A current of 25A constant with varying voltage up to 15V is applied to make the tungsten red hot, initiating the combustion as shown in figure 38. Once the combustion is self-sustaining, the power supply is turned off as the combustion wave propagates throughout the sample producing the final product.

Figure 38. Initiating the reaction by heating the tungsten wire

From the XRD analysis, figure 39, the material formed is $AlTi_3$ rather than the expected Ti_2AlC from reaction 3.1. This outcome is thought to be associated with the particle size of the initial reactant.

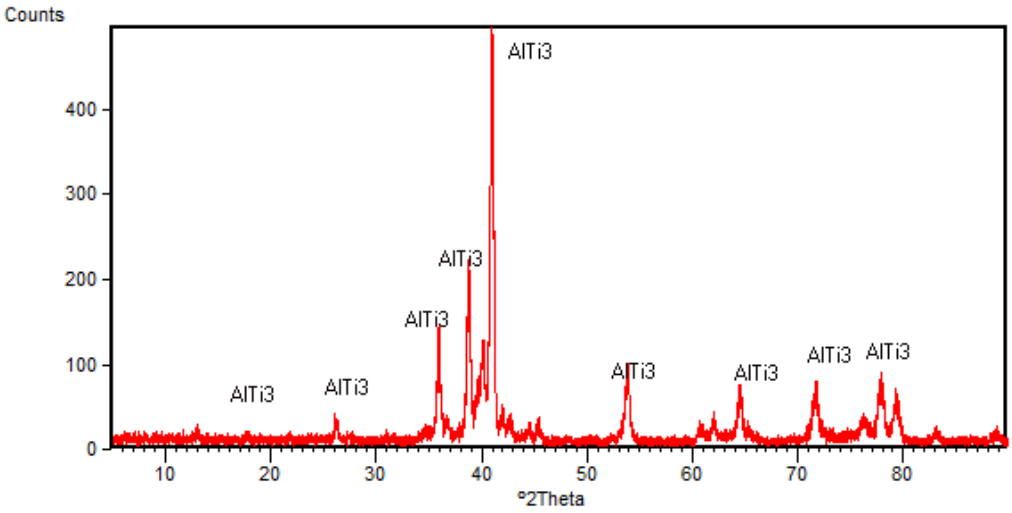

Figure 39. XRD spectra of the first sample obtained from SHS process (25µm Ti, 15µm Al, carbon fibre (mean diameter 3.55µm and mean length 105µm)) in the combustion rig

Figure 40 and 41 are the XRD data of sample ignited in in the combustion rig. As seen in figure 40, the sample was prepared with 45µm Ti and 15µm Al. The XRD confirms the existence of Ti_2AlC with a secondary phase of TiC. However when Ti of 25µm particle size was used the XRD indicates the presence of $AlTi_3$ and very little Ti_2AlC (see figure 41). It is very obvious that the formation of Ti_2AlC in dependent on the reaction temperature and the particle size. It is believed that as the particle size Ti decreases, there is a gradual fall in the exothermicity of the reaction. This affects the temperature rise and the reaction fails to produce the required product.

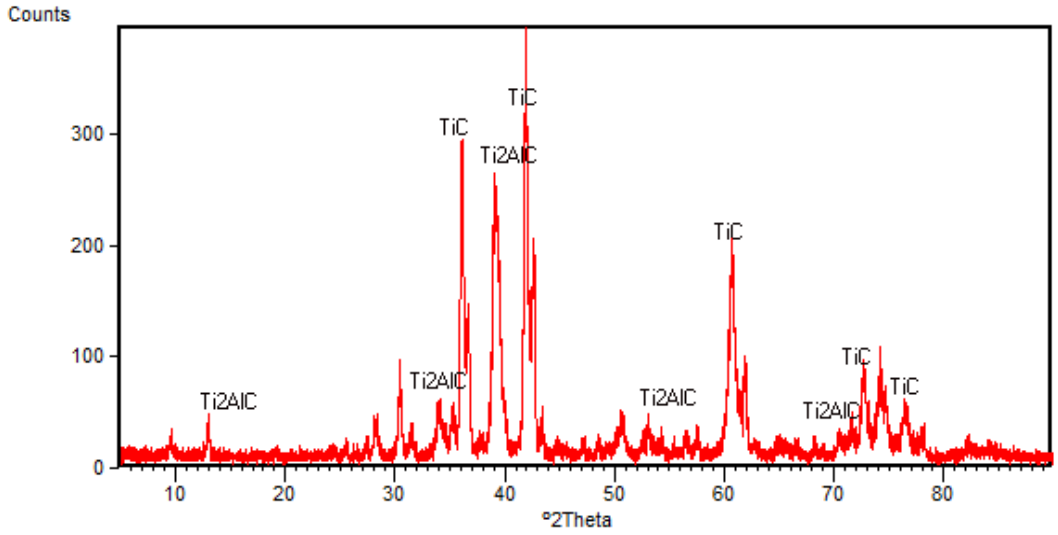

Figure 40. XRD spectra of sample prepared with 45µm Ti, 15µm Al, carbon fibre (mean diameter 3.55µm and mean length 105µm)

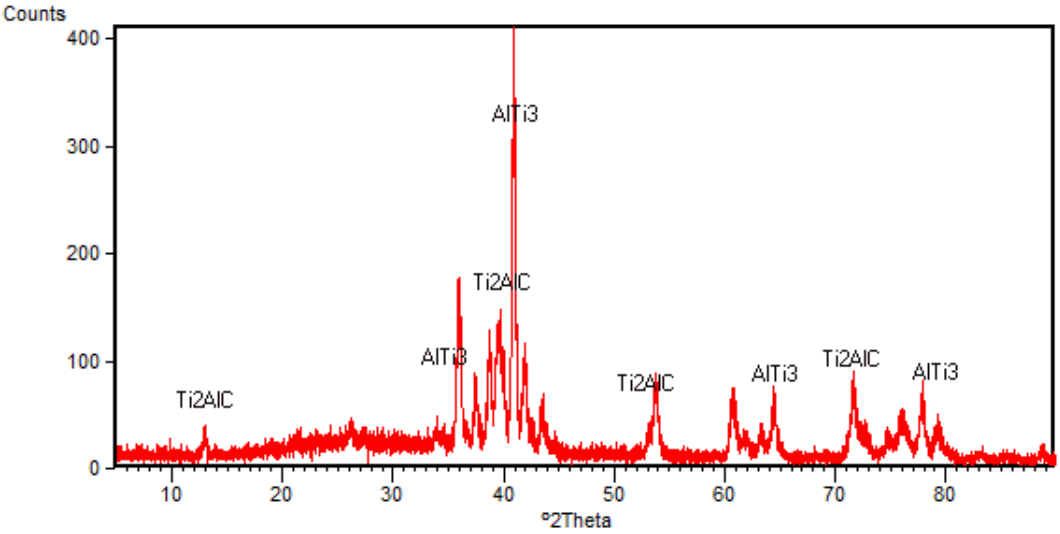

Figure 41. XRD spectra of sample prepared with 25µm Ti, 15 µm Al, carbon fibre (mean diameter 3.55µm and mean length 105µm)

In summary a combustion rig has been constructed and tested to produce ceramic by SHS process. Initial results indicate Ti_2AlC MAX-phase and $AlTi_3$ phases can be produced and the products are dependent on particle size. Further work to examine the inference of particle size and different carbon source in the elemental reaction 3.1, is discussed in the next section.

4.2 Effect of particle size on the formation of Ti_2AlC using SHS form of combustion synthesis process

4.21 Introduction

Solid-state combustion reactions for synthesising advanced materials have generated great interest in researchers [15, 16, 17, 18]. A variety of advanced materials such as Ti_2AlC, Ti_3AlC_2, Ni_3Al, Ni_2Al_3, TiAl, Zr_5Si_3 and many more can be synthesised using a solid-state combustion synthesis reaction. As explained in Chapter 1, section 1.4, combustion synthesis involves the ignition of a compact powder mixture in either air or inert atmosphere to produce sufficient heat due to the exothermic reaction so that it becomes self-sustaining in the form of combustion wave that propagates along the reactants to form the product. As a result of the high temperatures generated during the reaction, it is possible to produce products of higher purity as any low boiling point impurities present will readily volatilize.

In order to understand the application of the process, it is important to recognize the underlying process parameters such as

(i) thermodynamic mechanism,

(ii) temperature profile of the reaction,

(iii) effect of diluent on the reaction temperature and product formation,

(iv) effect of particle size,

(v) effect of particle packing density.

Chapter 3, section 3.1, provides an explanation on the study conducted to understand the thermodynamic involved in this reaction mechanism as well as the effect of diluents on the predicted combustion temperatures of the process. This chapter aims to explain the outcome of the study conducted to explore the effect of particle size and particle packing on the formation of Ti_2AlC MAX-phase ceramic.

4.22 Formation mechanism

There are various models and experimental studies explaining the evolution of compounds during SHS of Ti-Al-C based materials and the processing of Ti_2AlC [33, 120, 121]. Some models focus on the temperature range associated with the formation of Ti_2AlC and any intermediate compounds formed during the process reaction [120]. Other models [122] concentrate on the reactions involved that lead to phase changes such as

$$Al\ (s) \rightarrow Al\ (l) \text{ at } 660^0C \text{ (melting of aluminium)}$$

$$Ti\ (s) + Al\ (l) \rightarrow TiAl \text{ (melt) below } 900^0C$$

$$Ti\ (s) + C\ (s) \rightarrow TiC\ (s) \text{ above } 900^0C$$

$$TiAl \text{ (melt)} + TiC\ (s) \rightarrow Ti_2AlC \text{ at around } 1200^0C$$

during the solid-state reaction. Some mechanisms [123, 124] explain the reason for the layered structure of these ternary carbides and explain how the particle packing density affects the SHS formation mechanism of Ti_2AlC. However there are no mechanistic models or experimental studies explaining how the particle size and variation of the carbon source, such as the use of carbon black, graphite or carbon fibre used in the reaction, play an important role in reaction mechanism. In this section, we will try to understand the basic reaction mechanism involved in the formation of Ti_2AlC based on the existing experimental studies.

Yan Ming et al. [120], conducted experiments to produce a $TiAl/Ti_2AlC$ composite using 2Ti/1Al/1C elemental powders to determine the reaction temperatures associated with the phase transformation by in-situ hot pressing process. They identified the following reaction mechanism and the temperature that the reaction takes place. Three phases namely Ti, Al and $TiAl_3$ were analysed from the XRD peaks at 600^oC figure 42(ia), indicating solid-state reaction between Ti and Al ($Ti + Al \rightarrow TiAl$) before the melting point of Al which is around 660^oC. As the temperature increases towards 700^oC, Al melts and the intensity of $TiAl_3$ ($TiAl + 2Al \rightarrow TiAl_3$) phase increases. This can be seen in figure 42(ib), where XRD showed those sintered at 700^oC have some Ti_3Al and Ti_2AlC begins to form at higher temperature.

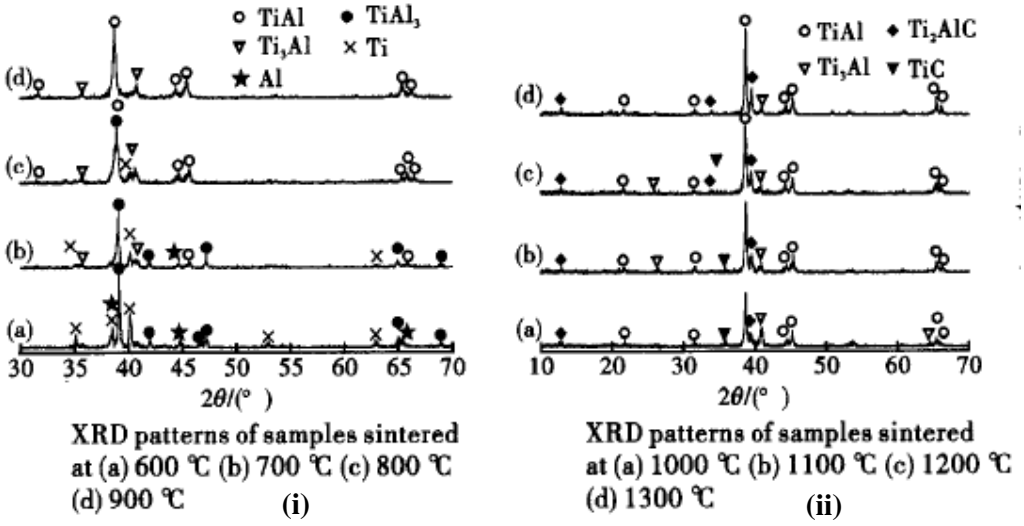

Figure 42. XRD analysis of evolution of phases during the reaction temperatures between 600°C to 1300°C [120]

At this stage, some of the partially unreacted Ti reacts to form TiAl and Ti_3Al in addition to $TiAl_3$. At 800°C, the TiAl becomes the main phase with Ti_3Al and unreacted Ti as seen in figure 42(ic). As the temperature increases to 900°C the Ti completely reacts into TiAl and Ti_3Al with higher TiAl content (see figure 42(id)). The TiC phase begins to form at a temperature range between 1000 – 1100°C (figure 42(iia), (iib)) which later results in the formation of Ti_2AlC based on the following reaction: TiAl + TiC → Ti_2AlC. At 1200°C, TiC disappears indicating the involvement of TiC in the reaction. The author reports that the peak intensity of TiAl was sharpest at this reaction temperature compared to the other competing phases and this peak decreases at an elevated temperature of 1300°C (figure 42(iid)).

From the figure 43, it is clear that TiC and $TiAl_3$ are the most stable phases and this is why, they are found as the secondary phase during the formation of Ti_2AlC.

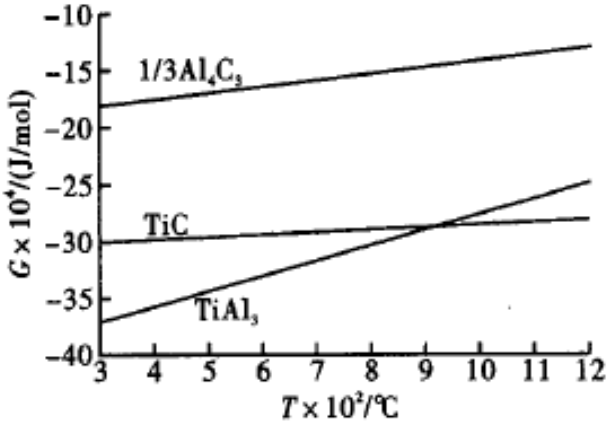

Figure 43. Gibbs free energy of formation associated with change in temperature [120]

A summary of the above explained reaction mechanism is shown schematically in figure 44.

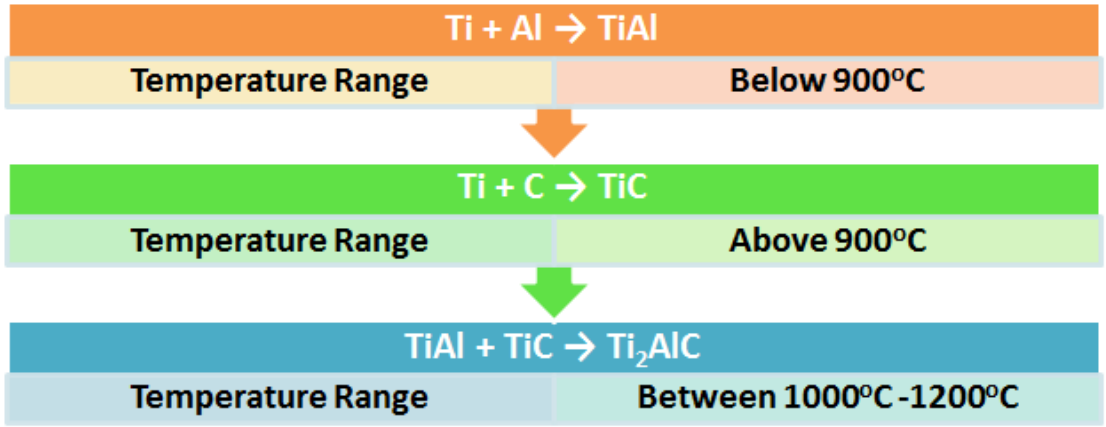

Figure 44. Reaction mechanism and the temperature associated

Zhenbin et al. [121] refers to the process as solution-precipitation as TiC dissolves into TiAl matrix resulting in the precipitation of Ti_2AlC. Pietzka et al. [28] described some interesting observations based on the thermodynamic of the reaction mechanism. They calculated the Gibbs free energy, ΔG of Ti_2AlC at two temperatures and found that ΔG^{Ti2AlC} (1000°C) = -65.9kJ/mol and ΔG^{Ti2AlC} (1300°C) = -54.8kJ/mol. As a result, it is difficult to synthesise Ti_2AlC at higher temperature. Pietzka et al. [33] also calculated the peritectic point of Ti_2AlC which is 1625±10°C and above this temperature Ti_2AlC decomposes into TiC and Al. Therefore there exists an optimum reaction temperature for forming the Ti_2AlC phase which is between 1000^0C-1200^0C.

This is the underlying formation mechanism during the synthesis of Ti_2AlC from the elemental powder mixture. We will attempt to understand how the different particle size of the elemental powder affects this formation mechanism. This will be achieved by undertaking a variety of SHS reactions with a range of reactant particle sizes.

4.23 Experimental procedure

Elemental powders of Ti 45µm (Goodfellow 99.5% purity), Ti 25µm (Pi KEM Ltd, 99.9% purity), Al 15, 20, 60µm (Goodfellow 99.9% purity), carbon fibre (mean diameter 3.55µm, mean length 104.14µm), graphite ≤20µm (Aldrich) and lamp black ≤30µm (Inoxia Ltd) were used as different reactants for the study. To undertake the SHS reaction each powder was mixed according to the stoichiometric ratio 2Ti:1Al:1C in a mortar for 10 – 15 minutes using a mortar and pestle. The combination of above mentioned elements of various particle sizes were mixed to obtain the following chemical reaction

$$2Ti + Al + C \rightarrow Ti_2AlC \quad (Reac\ 4.2)$$

A mass of 0.8gm of the elemental powder mixture was pressed at room temperature into compact cylindrical pellet of 13mm diameter in a uniaxial press using a pressure of 1.77kN/mm^2. The thickness of the pellet varies with different particle size used as seen in Table 6 and is related to degree of packing of the particulates. The shape and size of the reactant particles used can be seen in figure 45.

Table 6. Combination of particle size mixed and their apparent green density

Element, particle size(μm) and carbon source	Diameter of the tablet pressed in mm	Mean thickness mm	Green density in g/cm^3
Ti45, Al15 , Carbon fibre carbon fibre (mean diameter 3.55μm and mean length 105μm)	13	2.07	29.07
Ti45, Al25 , Carbon fibre carbon fibre (mean diameter 3.55μm and mean length 105μm)	13	2.12	28.47
Ti45, Al60, Carbon fibre carbon fibre (mean diameter 3.55μm and mean length 105μm)	13	1.99	30.29
Ti25, Al15, Graphite ≤20μm	13	1.79	33.61
Ti25, Al25, Graphite ≤20μm	13	1.74	34.71
Ti25, Al60, Graphite ≤20μm	13	1.78	33.92
Ti45, Al15, Graphite ≤20μm	13	1.68	35.80
Ti45, Al25, Graphite ≤20μm	13	1.71	35.18
Ti45, Al60, Graphite ≤20μm	13	1.67	36.02
Ti25, Al15, Lamp black ≤30μm	13	1.99	30.24
Ti25, Al25, Lamp black ≤30μm	13	2.01	29.99
Ti25, Al60, Lamp black ≤30μm	13	1.97	30.59
Ti25, Al25(0.3 mol excess), Carbon fibre carbon fibre (mean diameter 3.55μm and mean length 105μm)	13	2.08	29.02
Ti25, Al25, Carbon fibre carbon fibre (mean diameter 3.55μm and mean length 105μm)	13	2.14	28.12

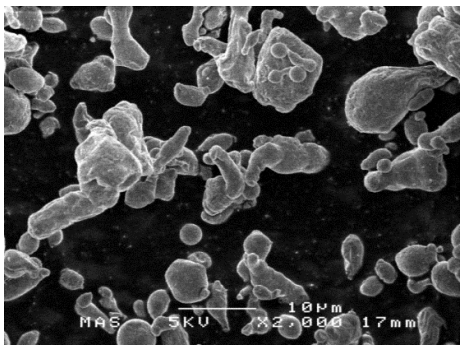

(a) Al 15µm particle size

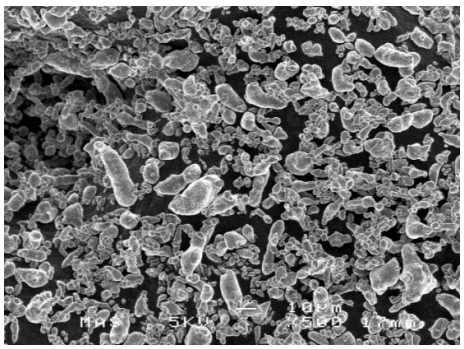

(b) Al 25µm particle size

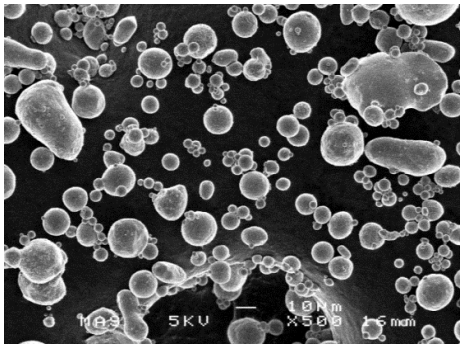

(c) Al 60µm particle size

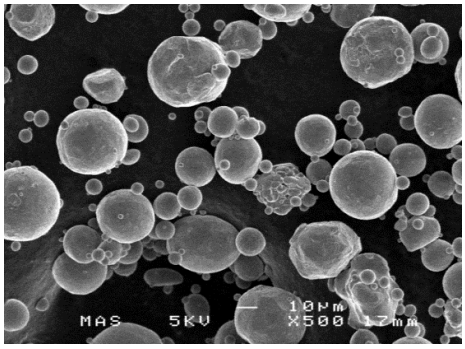

(d) Ti 45µm particle size

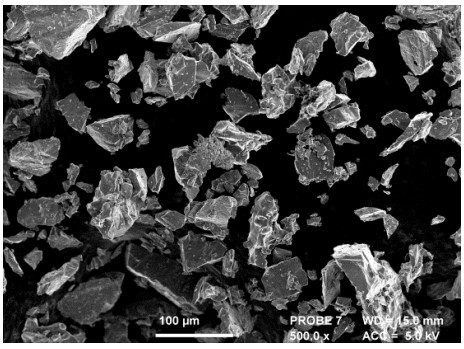

(e) Ti 25µm particle size

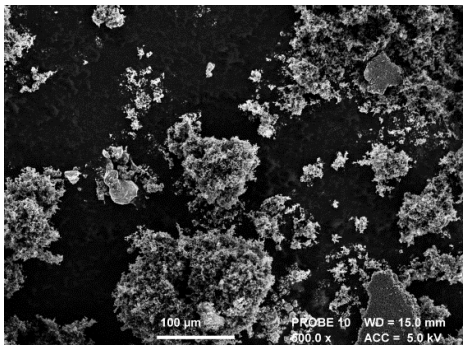

(f) Lamp black ≤30µm particle size

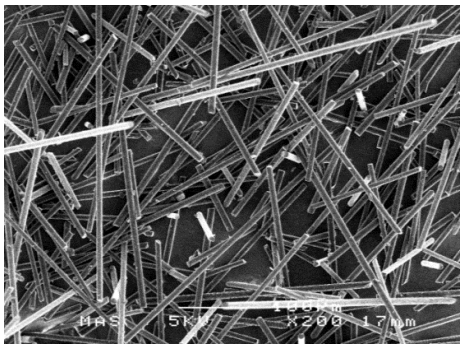

(g) Carbon fibre

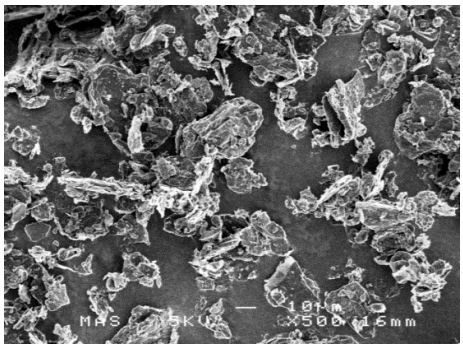

(h) Graphite ≤ 20µm particle size

Figure 45. FESM images of the different Ti, Al, carbon particles used in this study

The compact cylindrical pellet was loaded into a custom built combustion rig (construction and working explained in Chapter 4 section 4.11) and ignited using a resistively heated 'U' shaped tungsten wire of 0.5mm diameter by passing 30A of electric current in an argon atmosphere at a pressure of 2 bar. The phases formed were analysed using XRD (Cu K_α target) and the microstructure of the elemental powder and the green compact pellets were examined under a field emission scanning microscope (FESM). The microstructure of the elemental powder and the green compact mixture was examined to get a clear idea of the particle shape and how they are packed when pressed into a pellet. The density and porosity was measured according to the BS EN623-2:1993 standards (as discussed in Chapter 1, Section 1.53).

4.24 Experimental Results

Table 6 shows the combination of different particle sizes of the elemental powders mixed with different carbon source and their cold-pressed green density. This green density was examined since it provides an insight into the packing density, as each pellet was mixed under same conditions (temperature, pressure). The pellets were subjected to SHS mode of combustion synthesis and the compounds detected from XRD for the respective combination of particle sizes is provided in Table 7. The XRD analysis can be seen in figures 46, 47 and 48.

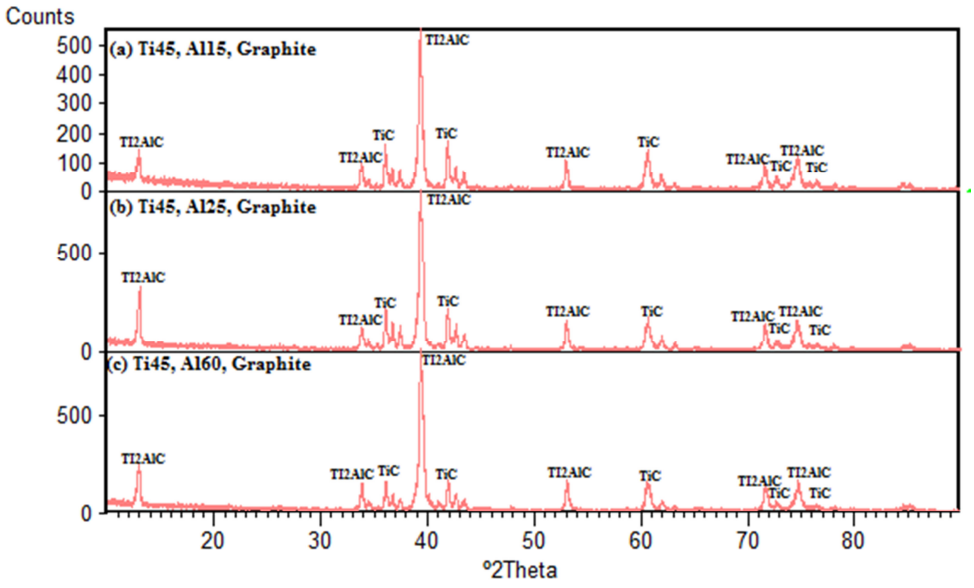

(i)

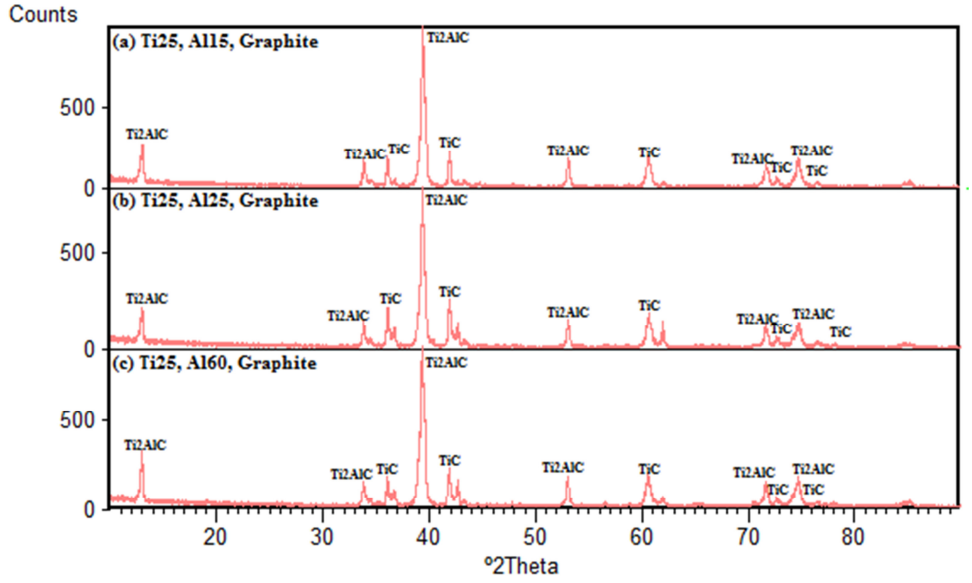

(ii)

Figure 46. XRD spectra (i) Ti 45 (ii) Ti 25, with different size of Al particle and graphite as the carbon source

Figure 46i, shows the phase analysis of products formed when 45µm Ti is stochiometrically mixed with 15, 25, 60µm Al and graphite as the carbon source. Figure 46ii shows the phase analysis when 25µm Ti is stochiometrically mixed with 15, 25, 60µm Al and graphite as the carbon source. The XRD patterns are very similar in all the case and consistanly form Ti_2AlC with a small amount of TiC.

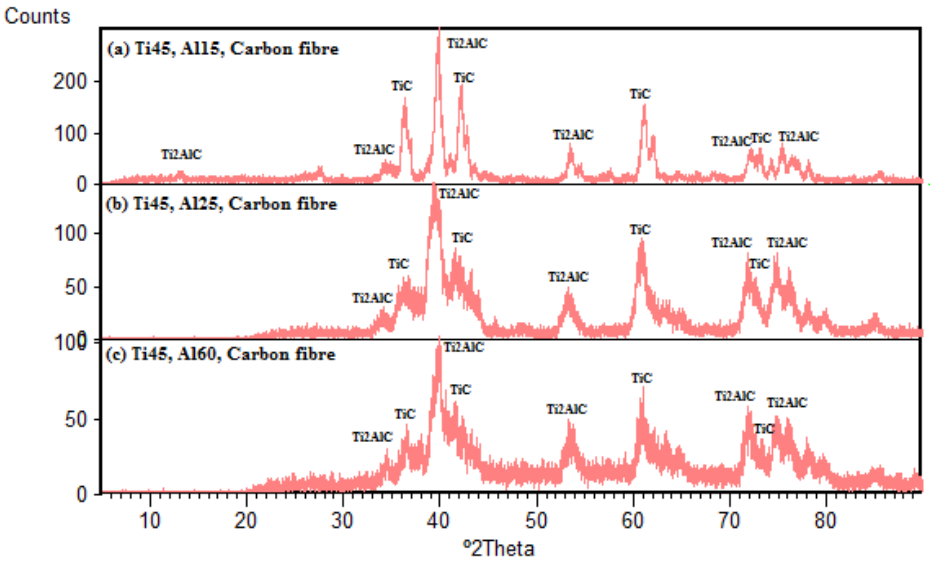

(i)

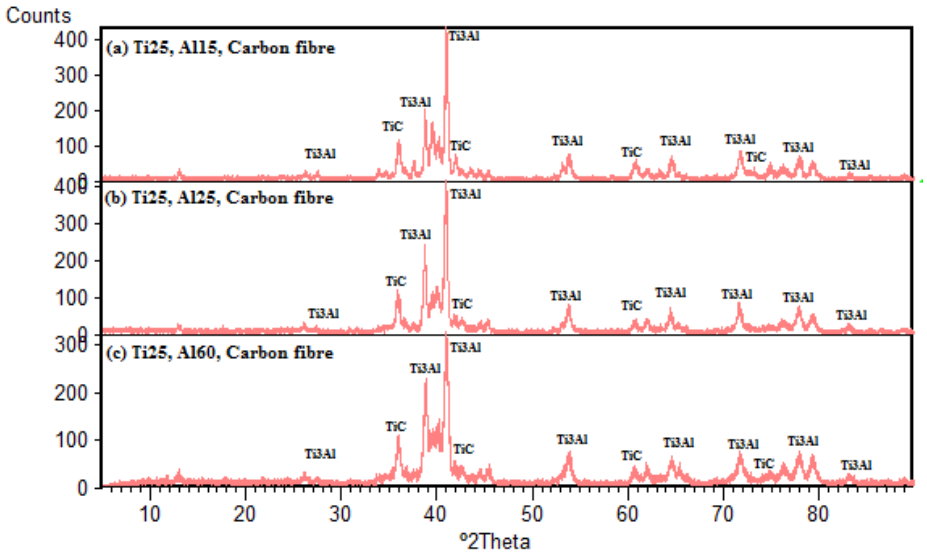

(ii)

Figure 47. XRD spectra (i) Ti 45 (ii) Ti 25, with different size of Al particle and carbon fibre as the carbon source

Figure 47i shows the phase analysis of products formed when 45µm Ti, is stochiometrically mixed with 15, 25, 60µm Al and carbon fibre as the carbon source. Figure 47ii shows the phase analysis of products formed when 25µm Ti, is stochiometrically mixed with 15, 25, 60µm Al and carbon fibre as the carbon source.

In this case we see that the products formed when 45µm Ti are Ti_2AlC and also large amount of TiC indicated by the higher intensity peaks seen at 37, 42 and 61^o (figure 47i) compared to the XRD pattern seen in figure 46. However, when 25µm Ti is used irrespective of the Al particle size it forms Ti_3Al which is an intermetallic product formed during the formation of Ti_2AlC [120] with TiC (figure 47ii). This clearly indicates that the reaction was incomplete, hence failed to form the MAX-phase as would be expected from chemical reaction *4.2*.

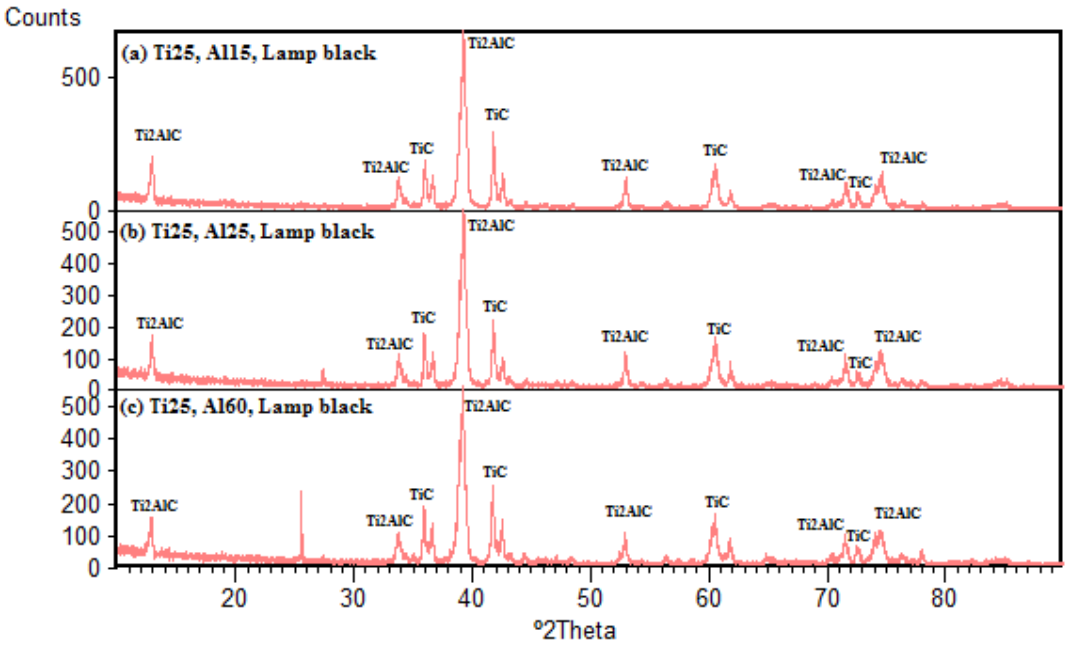

Figure 48. XRD spectra of the compounds formed when 25µm Ti is stochiometrically mixed with different size of Al particles and lamp black as the carbon source

Figure 48, is the crystallographic analysis of products formed when 25µm Ti is used with 15, 25, 60µm Al and lamp black as the carbon source. With this elemental powder combination it forms Ti_2AlC and the XRD pattern is similar to the one seen in figure 46. Reactant mixtures with 45µm Ti and lamp black was not used as it failed to form tablets upon cold pressing due to the coarse nature of the powder.

Table 7. Compounds formed by SHS from various combinations of elemental particle sizes and carbon source

Ti particle size (µm)	Al particle size (µm)	Carbon source	Compounds formed from SHS
45	15	Carbon fibre	Ti_2AlC, TiC
45	25	Carbon fibre	Ti_2AlC, TiC
45	60	Carbon fibre	Ti_2AlC, TiC
25	15	Graphite	Ti_2AlC, TiC
25	25	Graphite	Ti_2AlC, TiC
25	60	Graphite	Ti_2AlC, TiC
45	15	Graphite	Ti_2AlC, TiC
45	25	Graphite	Ti_2AlC, TiC
45	60	Graphite	Ti_2AlC, TiC
25	15	Lamp black	Ti_2AlC, TiC
25	25	Lamp black	Ti_2AlC, TiC
25	60	Lamp black	Ti_2AlC, TiC
25	15	Carbon fibre	Ti_3Al, TiC
25	25	Carbon fibre	Ti_3Al, TiC
25	60	Carbon fibre	Ti_3Al, TiC

It can be observed that, irrespective of the particle size of both the Ti and Al, when graphite and lamp black is used as the carbon source, the final products consistently formed are Ti_2AlC and TiC; this can be seen from examination of Table 7 and figures 46, 47 and 48. However, when carbon fibre is used the nature of the products formed is more complex. As the particle size of the titanium decreases from 45µm to 25µm, Ti_2AlC does not form. Instead Ti_3Al is formed (refer figure 47i and 47ii) which is an intermediate compound formed during the formation of Ti_2AlC; as described in figure 42. As the source of carbon is changed from carbon black, graphite to carbon fibre, there is a decrease in green density of the sample (refer graph in figure 49) due to the decrease in surface area of the carbon (when carbon fibre) particle. The outcome is an increase in porosity of the green body, resulting is poor particle-particle contact within the sample that leads to an incomplete reaction. In this case, only sufficient heat energy to form Ti_3Al is released from the reaction or this heat energy did not sustain long enough for the formation of other intermediate compounds such as TiAl and TiC which in turn reacts to form Ti_2AlC. Examination of the green density in figure 49, the cold-pressed pellets made with carbon fibre (black in colour bars in figure 49) has the lowest green density compared to the reactant pellets formed using graphite and lamp black with similar particle size of Ti and Al.

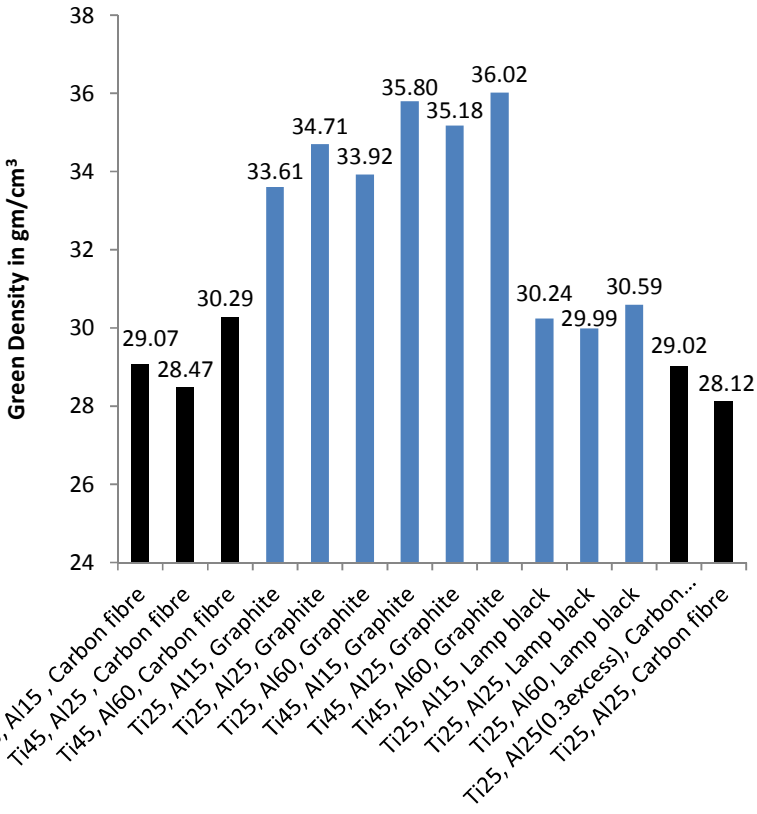

Figure 49. Green density of the pellets pressed using various combinations of particle sizes and carbon source

Figure 50, is the FESM images showing how the particles are packed when pressed into pellets.

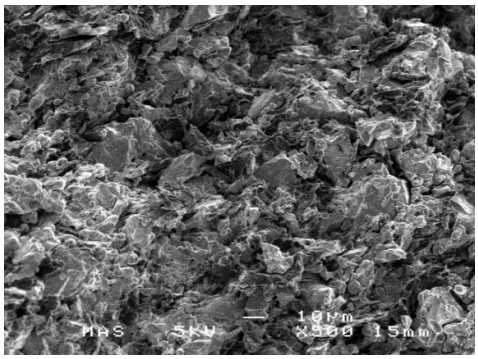

(a) Ti 25µm, Al 15µm, Graphite

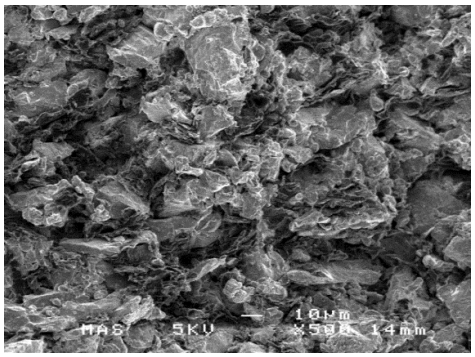

(b) Ti 25µm, Al 25µm, Graphite

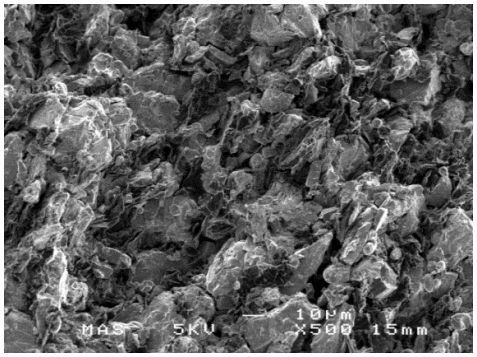

(c) Ti 25µm, Al 60µm, Graphite

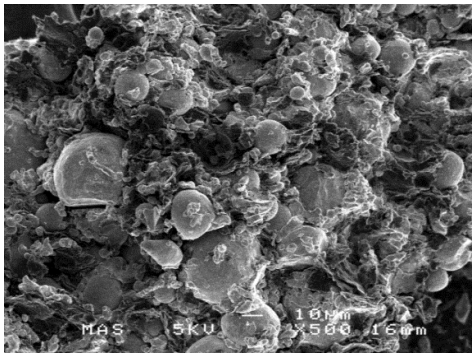

(d) Ti 45µm, Al 15µm, Graphite

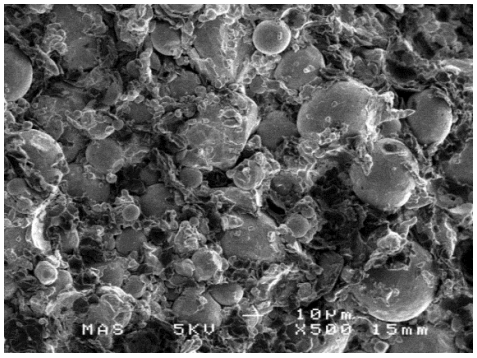

(e) Ti 45µm, Al 25µm, Graphite

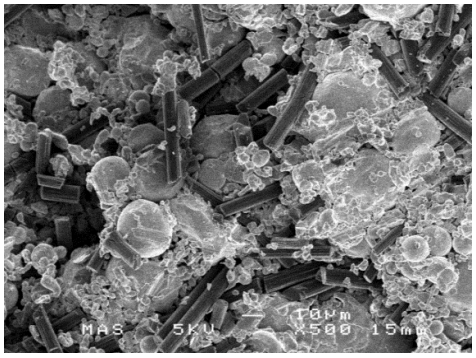

(f) Ti 45µm, Al 15µm, Carbon fibre

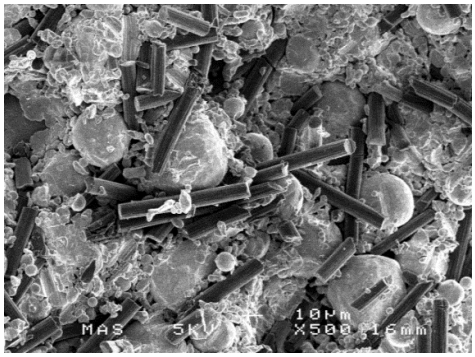

(g) Ti 45µm, Al 25µm, Carbon fibre

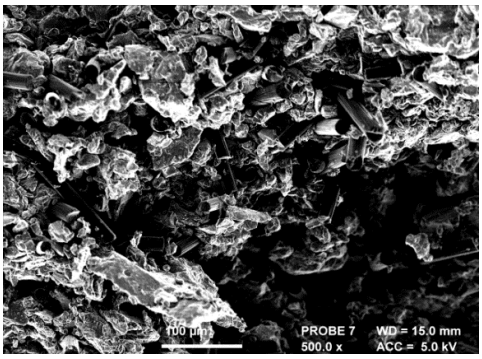

(h) Ti 25µm, Al 25µm, Carbon fibre

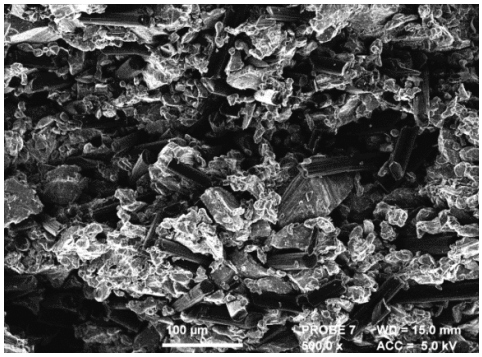

(i) Ti 25µm, (0.3 mol excess) Al 25µm, Carbon fibre

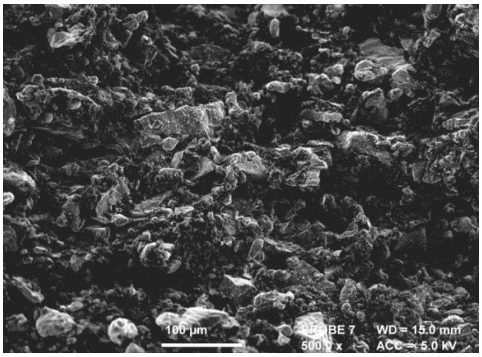

(j) Ti 25µm, Al 25µm, Lamp black

Figure 50. FESM images showing how the particles are packed when pressed into pellets

It can be seen that the elemental particles are of different shape and size and hence while pressed into pellets they tend to form different types of particle to particle surface contact. For example, there will be a point contact in the case of spherical particle, line contact in the case of elongated particles and multiple point contact when there is a contrast between particle sizes. This greatly affects the packing density (figure 49), which in turn affects the reaction process and thermal conductivity and cumulatively affect the propagation of combustion wave.

The formation mechanism in the case of pellets made with 25µm Ti, 15 & 25µm Al and carbon fibre (figure 47ii) can be explained with the schematic representation in figure 51.

In the case of carbon fibre as a carbon source, due to the shape and size of the carbon (figure 45g), there is a greater degree of metal (Ti) to metal (Al) contact as seen in the particle arrangement representation in figure 51a. As a result the green pellet has a metallic appearance (figure 54a) due to poor dispersion of carbon fibre particles. When this pellet is heated, due to high metal (Ti) to metal (Al) contact, the thermal conductivity is high. Hence as the combustion initiates, the propagating combustion wave moves across the pellet rapidly as shown in figure 51b. This rapid propagation of combustion wave and poor dispersion of carbon particles, doesn't favour the completion of the final reaction step .i.e. $Ti_3Al + TiC \rightarrow Ti_2AlC$; rather only favour the completion of initial reactions such as $3Ti + Al \rightarrow Ti_3Al$ and $Ti + C \rightarrow TiC$. Hence the XRD of the product formed by this composition identifies Ti_3Al and TiC (figure 47ii).

Therefore, when there is a rapid heating, there is a sudden increase in temperature and as explained by Pietzka et al. [33], it is very difficult to synthesise Ti_2AlC at higher temperature and hence the formation is more favourable during the cooling down stage as TiC dissolves into Ti-Al matrix (Ti_3Al in this case) resulting in the precipitation of Ti_2AlC [121]. However in this case, the cooling of the sample after the completion of the combustion reaction is also rapid and does not provide enough time for the final reaction between Ti_3Al and TiC to form Ti_2AlC ($Ti_3Al + TiC \rightarrow Ti_2AlC$) . Hence there is no sufficient temperature sustained for the precipitation reaction. Therefore the pellet pressed with 25µm Ti, 15 & 25µm Al and carbon fibre (figure 47ii) does not form Ti_2AlC.

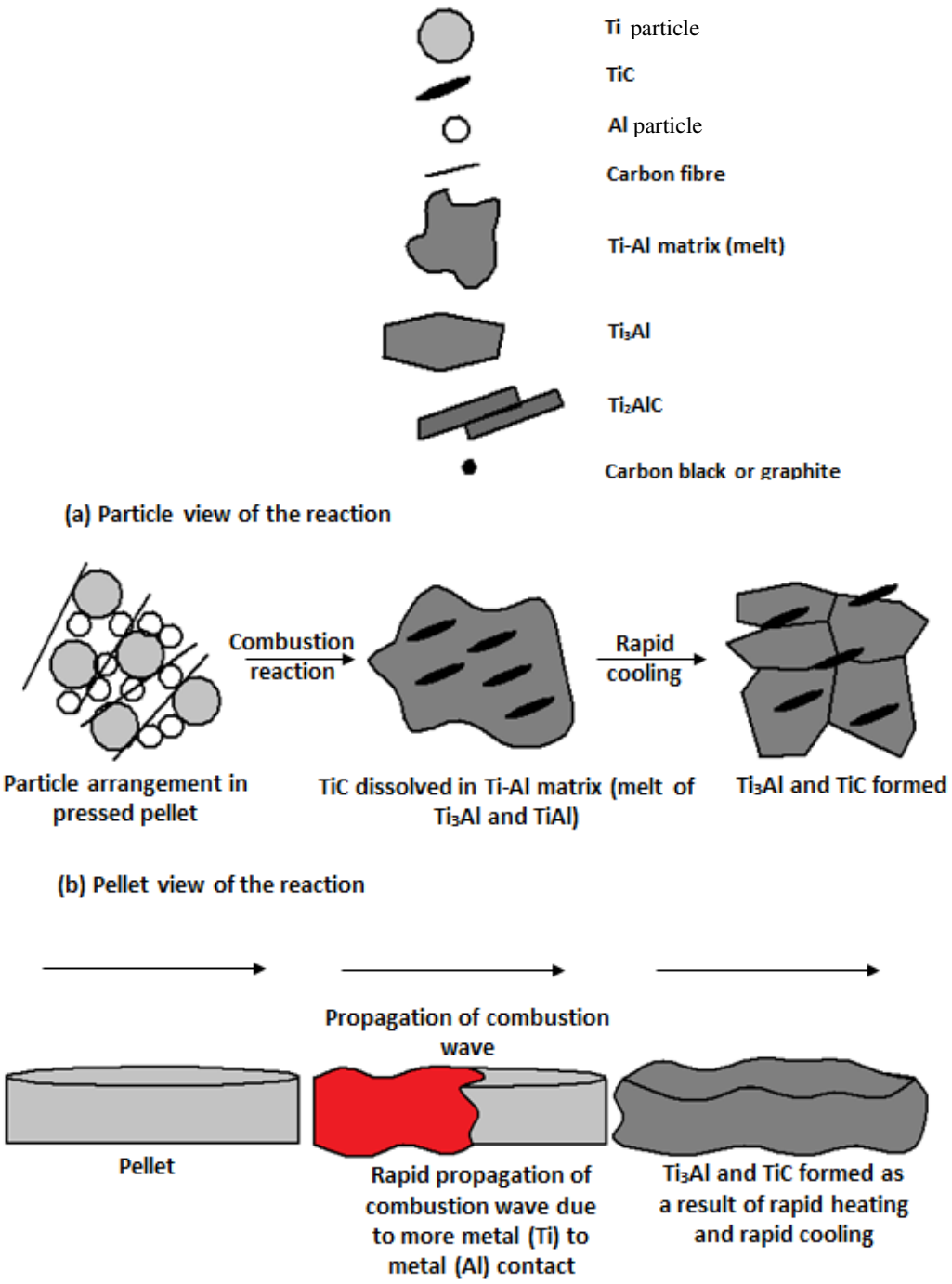

Figure 51. Schematic representation of the combustion process showing the effect of carbon fibre on the final product

However, when lamp black or graphite is used as the carbon source, due to the particle size and geometry (figure 45f and 45h), the carbon particles are in intimate contact with the Ti and Al particles upon mixing as seen in the particle arrangement in the schematic representation in figure 52a. As a result of this, the green pellets obtained after pressing are black in colour (figure 54b and 54C) in contrary to the pellets obtained using carbon fibre as carbon source which looks metallic (figure 54a).

Hence in this case, there is a poor metal (Ti) to metal contact (Al) as carbon particles are located between the metal-metal substrate as seen in the particle arrangement in figure 52a and also in FESM images in figure 50a, b, c, d, e and j. This results in a poor thermal conductivity, affecting the propagation of the combustion wave upon reaction. To be more specific, it slows down the propagating combustion wave as represented in figure 52b. The slow propagation of combustion wave ensures completion of all the reaction mechanism which is:

$$3Ti + Al \rightarrow Ti_3Al$$

$$Ti + C \rightarrow TiC$$

$$Ti_3Al + TiC \rightarrow 2Ti_2AlC$$

Or

$$Ti + Al \rightarrow TiAl$$

$$Ti + C \rightarrow TiC$$

$$TiAl + TiC \rightarrow Ti_2AlC$$

leading to the formation of Ti_2AlC MAX-phase ceramic upon cooling due to the precipitation reaction [121].

Therefore a slow cooling down stage is required for the formation of Ti_2AlC, which is more likely to occur in the case of pellets made with graphite and lamp black as seen in the schematic in figure 52a,b. The pellet continuing to be red hot even after the completion of the reaction is the sign for slow cooling as seen in figure 53b.

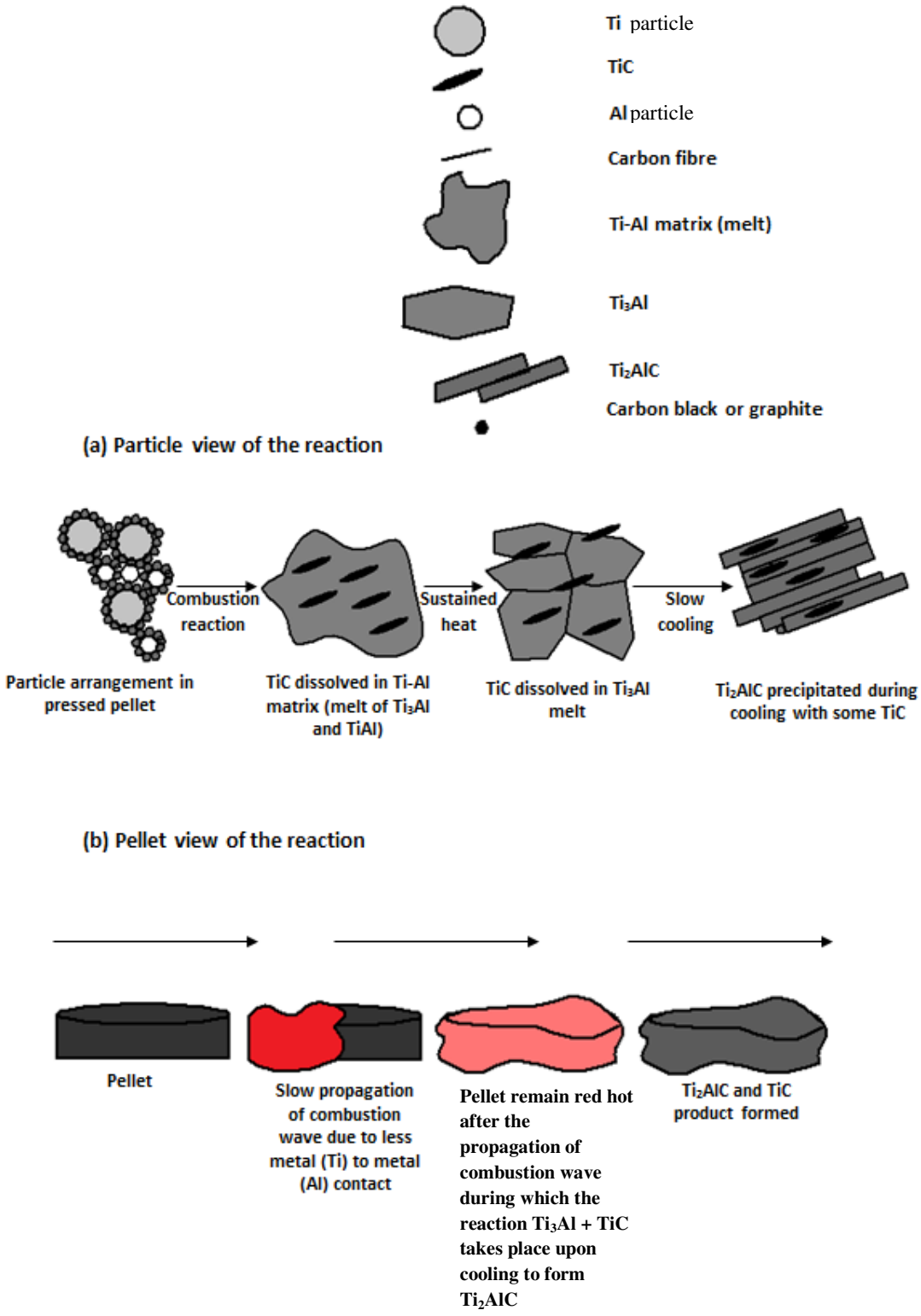

Figure 52. Schematic representation of the combustion process showing the effect of carbon fibre on the final product formed

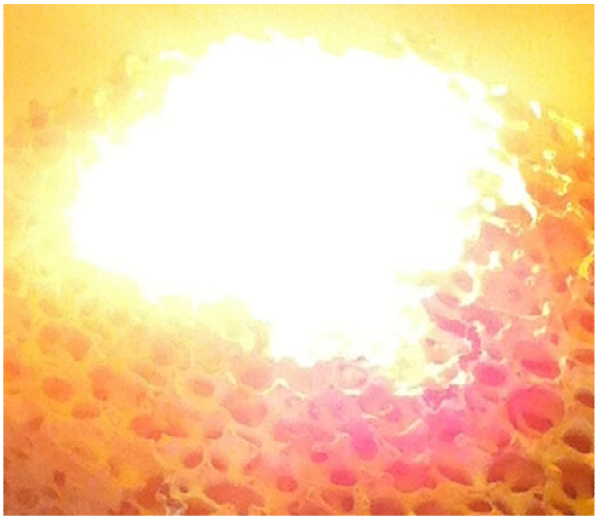

(a)

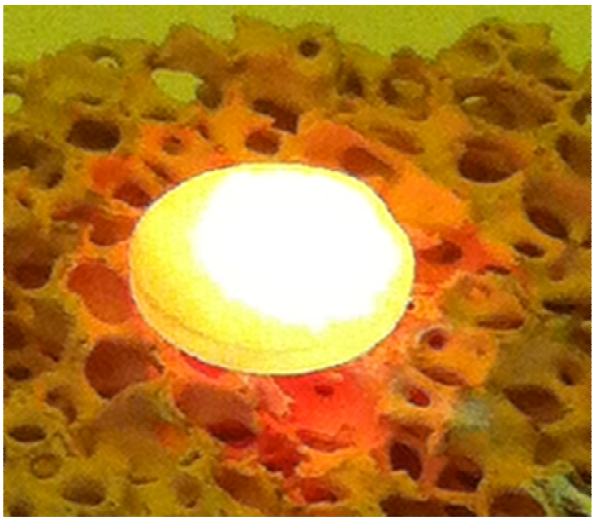

(b)

Figure 53. a) Image showing the combustion reaction, (b) image showing the red hot sample after the completion of the reaction

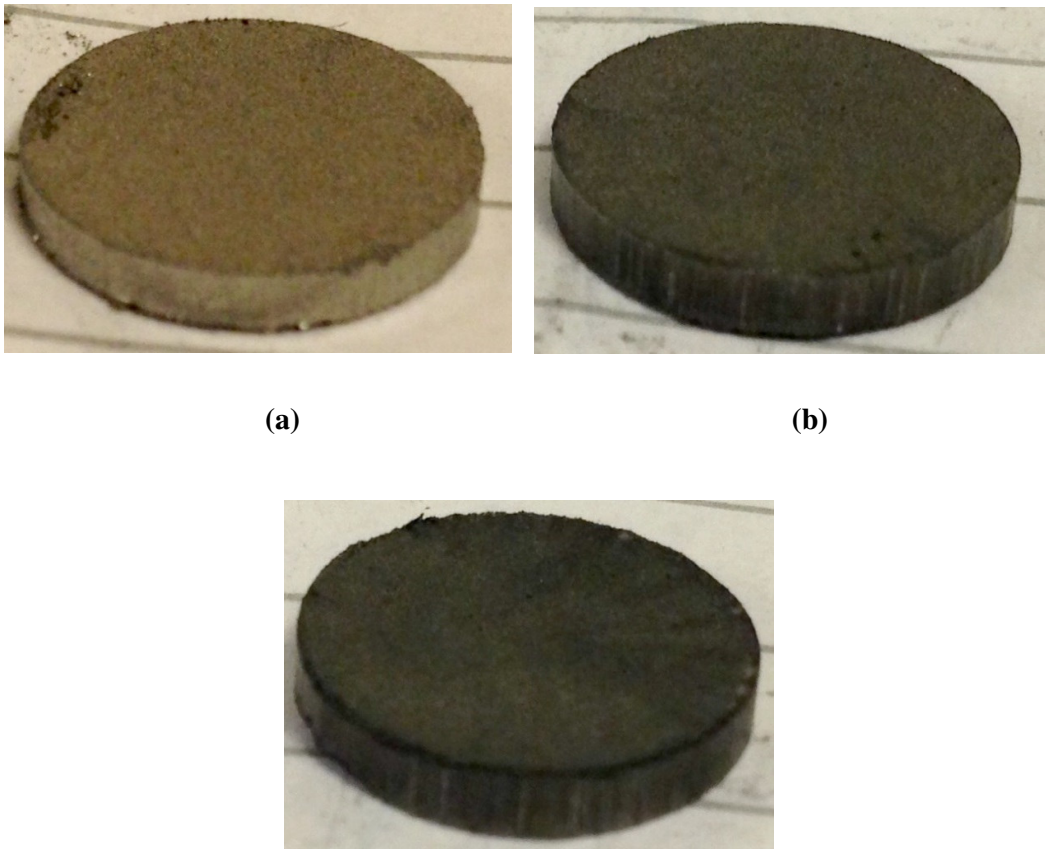

(a) **(b)**

(c)

Figure 54. Colour of the green pellets (13mm diameter and approx. 2mm thick) made according to 2Ti/Al/C ratio with different carbon source. (a) Carbon fibre (metallic in colour), (b) graphite (black in colour) and (c) lamp black (black in colour)

To examine this theory .i.e. slow propagation of combustion wave associated with slow cooling favours the formation of Ti_2AlC, the Al content in the elemental reaction mixture was increased in the pellet made with 25µm Ti, 25µm Al and carbon fibre. The effect of diluents like Al and Ti on the combustion reaction was studied in section 3.14 and it was found that they decrease the exothermicity of the reaction. The addition of excess aluminium also served to increase the green density due to the presence of the ductile aluminium phase (see Table 6 and figure 49).

Figure 55 is the XRD showing the evolution of compounds when excess Al (*y* in reaction 4.2a) is added in the basic elemental reaction *3.4*.

$$2Ti + (1 + y)\,Al + C \rightarrow Ti_2AlC + yAl \qquad (4.2a)$$

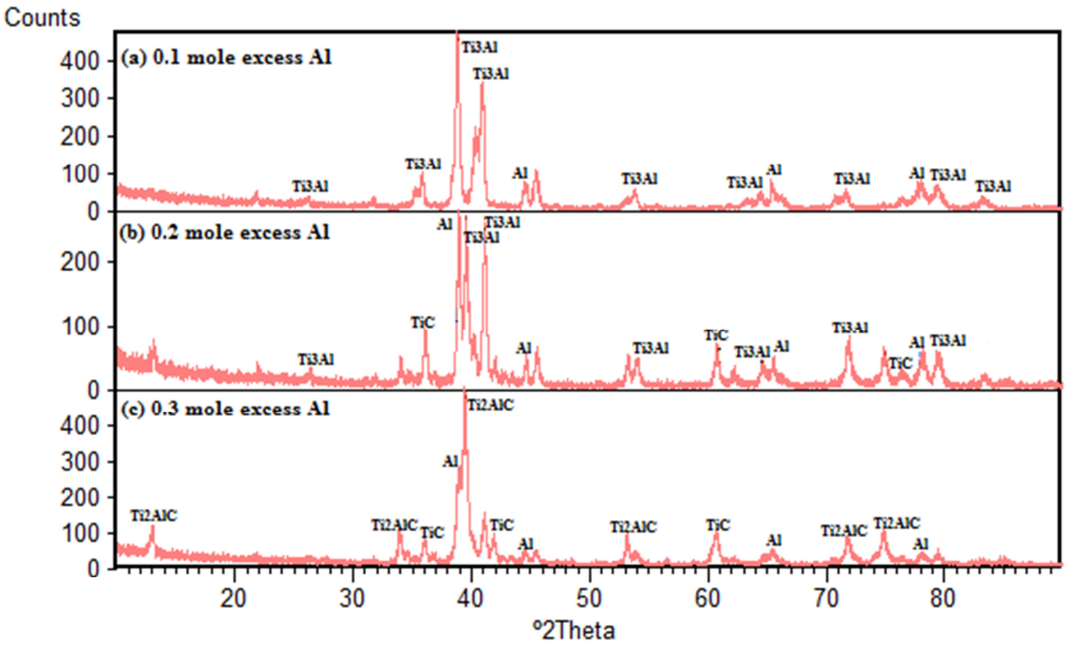

Figure 55. XRD spectra showing the evolution of compounds when excess Al is added in reaction *4.2a*

As seen in figure 55, as the Al content is increased the exothermicity of the reaction decreases, slowing down the propagating combustion wave. Here the y value in reaction 4.2a was increased from 0.1mole by 0.1 steps. And at 0.3 mole excess Al the final product formed was Ti_2AlC (figure 55c) and supports the theory that slow propagation of combustion wave associated with slow cooling of the sample upon the completion of the reaction favours the formation of Ti_2AlC ceramic by SHS reaction.

Figure 56 shows the porosity (6-7 samples per batch) of Ti_2AlC formed with different combination of elemental particle sizes and carbon source. As you can see Ti_2AlC prepared with graphite as the carbon source is less porous compared to the other samples which indirectly means the exothermicity of the reaction can be controlled by the carbon source used. i.e. when carbon fibre is used more heat energy is required to initiate the reaction which adds up to the combustion temperature and thus increasing the adiabatic combustion temperature (refer graph in figure 30, section 3.13). The rise in the final combustion temperature increases the porosity of the reacted pellets as seen in figure 56.

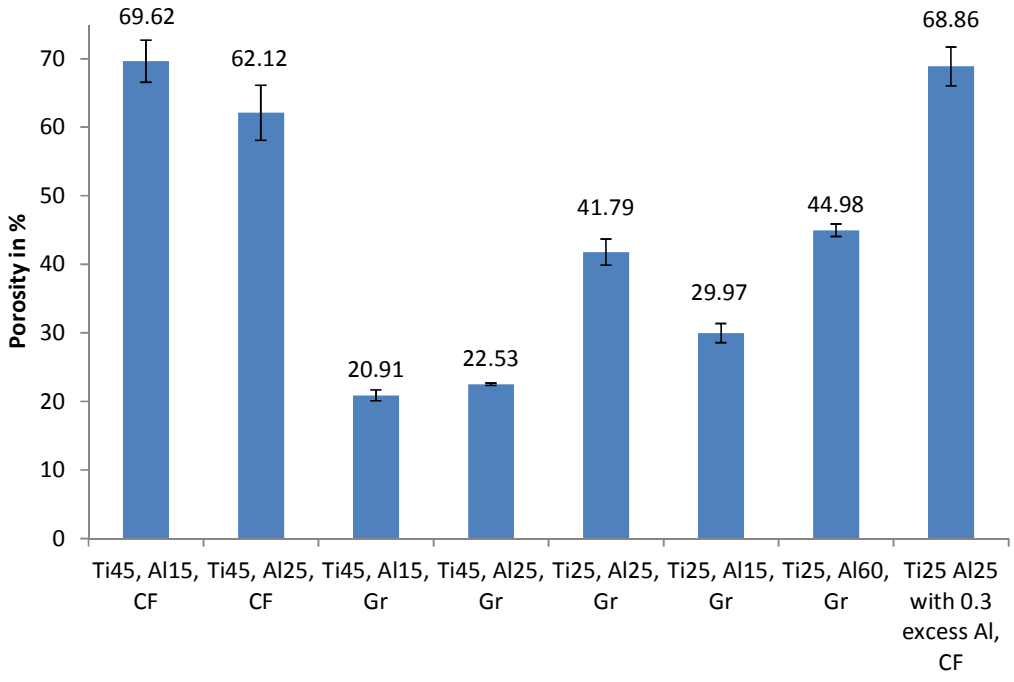

Figure 56. Porosity of the Ti_2AlC samples formed by SHS process from different combinations of particle sizes and carbon source

This data is very useful as it is a direct correlation to the exothermicity of the reaction and also helps in choosing particle size and carbon source for forming Ti_2AlC with desired porosity range which is a key factor in fabricating solid state electrodes.

4.25 Summary

It can be concluded that particle size of Al has no effect on the final products formed as it melts at around 660^0C irrespective of the particle size and is the enabler for the further proceeding in the reaction. The particle size of Ti has no influence on the final product formed. However, the shape and size of the particle has major influence on the packing density and it was found that more porous the green sample the more likely it will not form Ti_2AlC and is more likely to form Ti_3Al and TiC. It was observed that high metal to metal contact in the reactant pellet can induce rapid propagation of combustion wave which hinders the formation of Ti_2AlC. It was demonstrated that by lowering the combustion wave velocity and increasing the cooling time by addition of diluents such as Al, in this case, it is possible to control the combustion wave and facilitate the formation of Ti_2AlC. It was also demonstrated that the exothermicity of the reaction can be controlled even by fine tuning the carbon particle size.

Chapter 5. Optimisation of pressureless sintering parameters

The previous chapter has examined the manufacture of Ti_2AlC by SHS. Other approaches to create porous conductive ceramics were discussed in Chapter 2, section 2.4 and 2.5 that include foam replication and freeze casting. Both of these processes require the ceramic regions in the porous Ti_2AlC green body to be sintered to a high density to achieve strength and conductivity. Unwanted phases or degradation of the Ti_2AlC must also be prevented. This chapter therefore examines the sintering parameters such as sintering temperature and dwell time.

5.1 Introduction

Pure Ti_2AlC ("Maxthal 211 ceramic engineering material" from Kanthal) powder was subjected to sintering under argon at various temperatures to study the evolution of phases and microstructure of the sintered material with the change in temperature. In addition the effect of temperature on the final density and level of porosity of the sample was studied. This section of the chapter will describe the steps and the process adopted to conduct the above stated studies. Since this research involves the fabrication of macro and micro porous Ti_2AlC ceramic, to tune the pore size for optimised strength or for a potential application, it is important to know the exact sintering temperature of this material to obtain dense Ti_2AlC sample with high purity. Here the Ti_2AlC powder was subjected to five different sintering temperatures namely 1200, 1250, 1300, 1350 and 1400^oC respectively and any changes in the phases present in the final sintered body as well as the change in density at these temperatures was observed. Parameters such as the weight of the sample and pressing force to produce the green sample were kept constant for all sintering temperatures. Argon gas was used during pressureless sintering to avoid oxidation of the material.

5.2 Experiment setup

A mass of 0.8gm of the Ti_2AlC was pressed at room temperature into a compact cylindrical pellet of 13mm diameter in a uniaxial press using a pressure of 1.77kN/mm^2 for three minutes to obtain the green sample. Samples were prepared in the similar manner for all the sintering temperature conditions to be examined. In each test a minimum of six samples were prepared and were placed on a Ti_2AlC powder bed as shown in figure 57 to shield the material from any oxidation due to any small amount of oxygen in the argon protective gas.

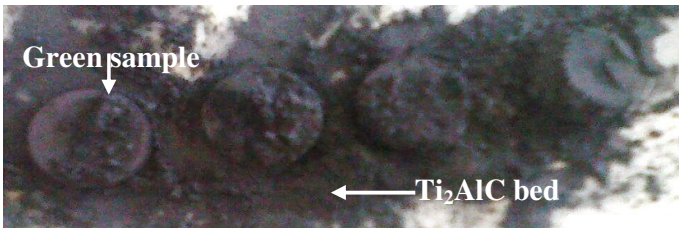

Figure 57. Samples placed in Ti_2AlC bed to prevent oxidation during sintering

The temperature of the furnace was raised to experimental temperatures (1200, 1250, 1300, 1350 and 1400^{o}C) at a rate of 150^{o}C/hour and held at the elevated temperature for three hours before the furnace was brought down to room temperature. After each batch of ceramics was sintered X-ray diffraction (XRD) and scanning electron microscopy (SEM) was performed to characterise the phase composition and microstructure of the ceramics. The density and porosity was measured according to the BS EN623-2:1993 standards (as discussed in Chapter 1, Section 1.53).

5.3 Results and discussion

Figure 58 is the XRD pattern of the 'as-received' Ti_2AlC powder that was used for the sintering study. This was done in order to ensure the phase composition of the starting powder was Ti_2AlC and provide a control over XRD pattern for easy identification of Ti_2AlC phase in the sintered body. The XRD in figure 58 shows that the main phase of the starting powder material is clearly Ti_2AlC.

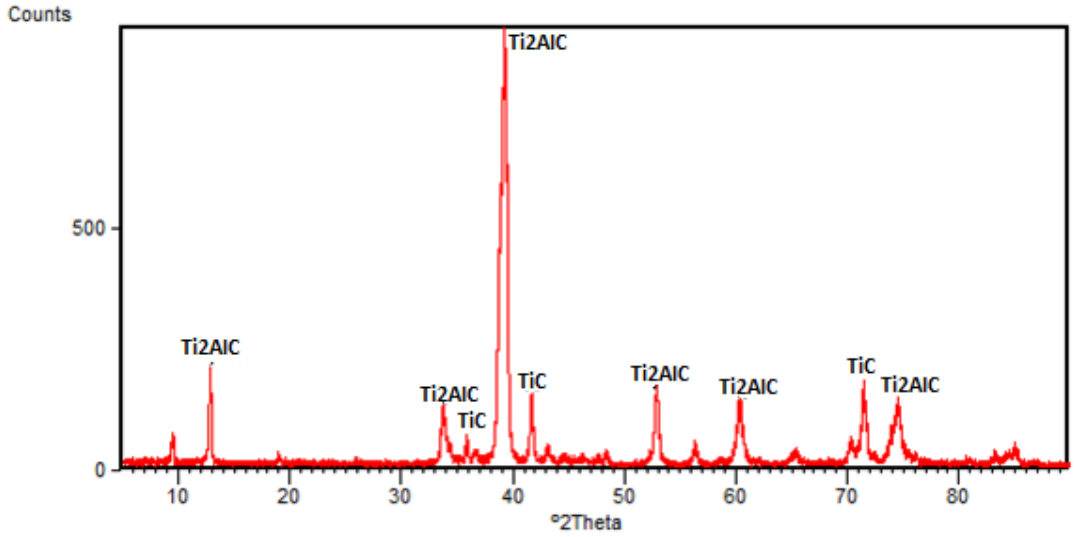

Figure 58. XRD spectra of the initial Maxthal 211 Ti_2AlC powder

Figure 59 shows the XRD of the ceramic sintered at 1200°C. At this temperature Ti_2AlC is the primary phase with low intensity peaks of other phases such as TiC as secondary phase. The inclusion of TiC was negligible but the sample failed to form single phase of Ti_2AlC. XRD is a relatively sensitive technique for phase analysis and it requires approximately 5% of the compound or the element to be identified.

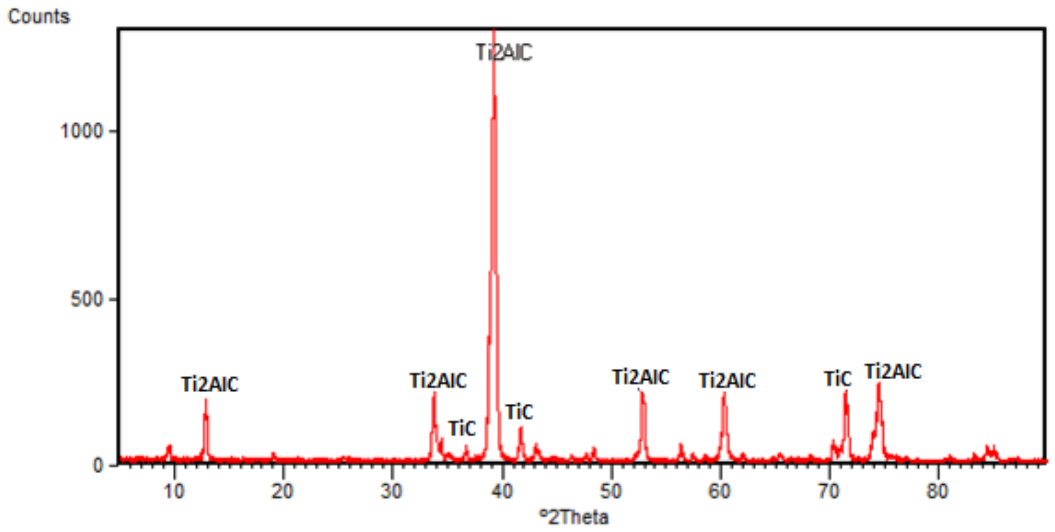

Figure 59. XRD spectra of the sample sintered at 1200°C in argon

Figure 60 shows the sample after sintering at a temperature of 1200°C. After a close inspection it could be observed that the sample has two distinct layers. One side of the sample is black and the other is grey in colour. When the electrical conductivity of the sample was tested with a simple multi-meter, only the grey coloured layer was conductive since it is Ti_2AlC. The black layer is a dense TiC which is less conducting compound [125]. Due to this reason it was decided to perform a series of sintering at various temperatures until the sample had only the Ti_2AlC phase.

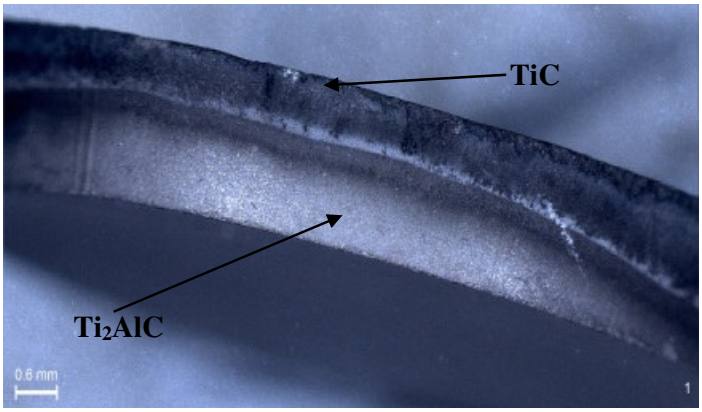

Figure 60. Optical image of the different boundary formed in the sample after sintering

On raising the sintering temperature to 1250°C there were no characteristic changes to the sample compared to 1200°C (results not shown). However, increasing the sintering temperature to 1300°C led to more diffusion of carbon resulting in the formation of more TiC with respect to Ti_2AlC (see figure 61). Two different coloured layers existed in all the sintered samples. When the samples were subjected to a sintering temperature of 1350°C under the same sintering condition, the intensity of the TiC peak reduced considerably, figure 62, when compared to samples sintered at 1300°C (figure 61). In all the above experimental studies the two common compounds in the sintered products were TiC and Ti_2AlC. From the figure 43, Chapter 4, section 4.22, it is clear that TiC is one of the most stable phases and this is why, it is found as the secondary phase during the formation of Ti_2AlC.

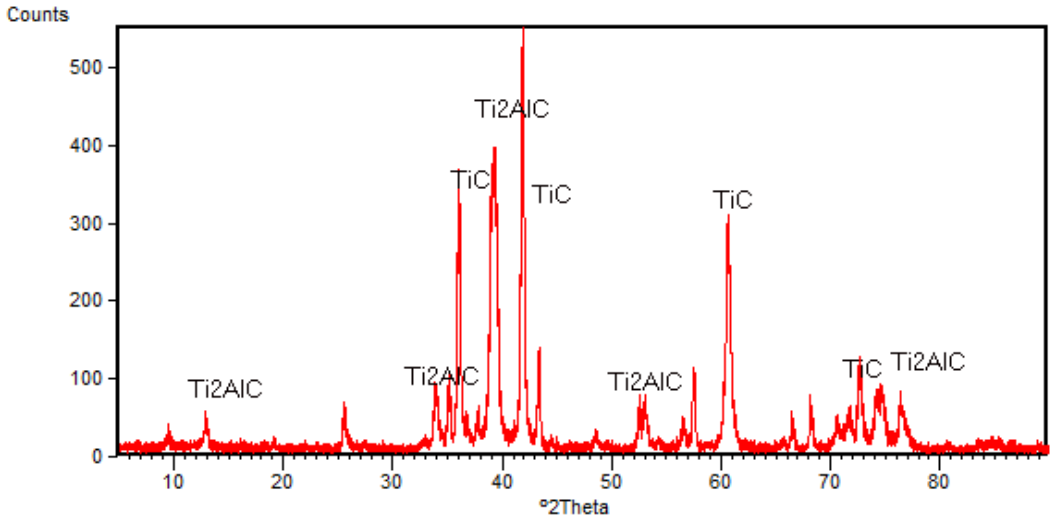

Figure 61. XRD spectra of the sample sintered at 1300°C in argon

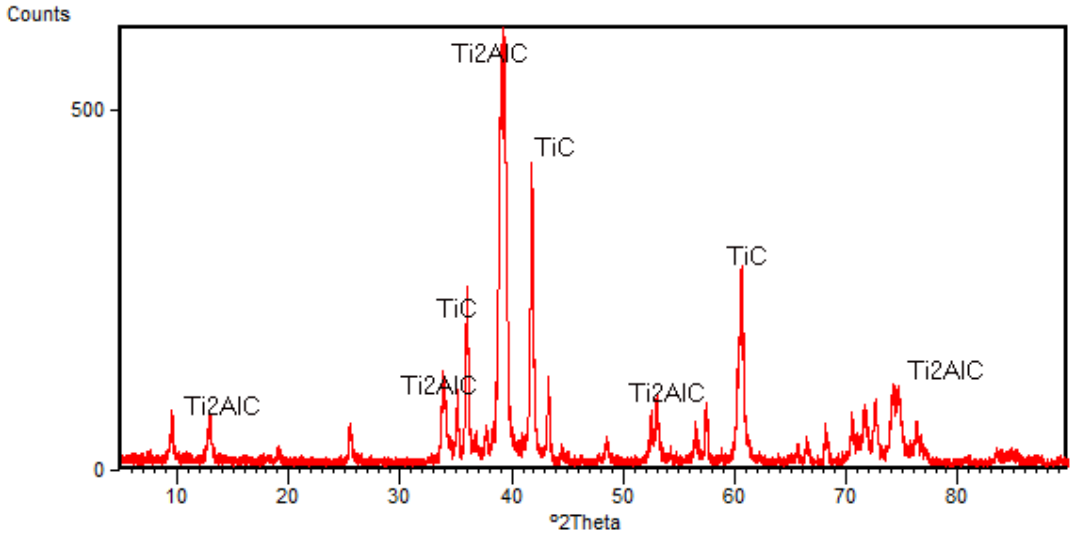

Figure 62. XRD spectra of the sample sintered at 1350°C in argon

As the intensity of the TiC peak reduced at 1350°C, it was expected to disappear or reduce at a higher sintering temperature. Therefore the next batch of samples was sintered at 1400°C and, as expected for the XRD analysis, Figure 63 was similar to the XRD pattern of the initial pure Ti_2AlC powder, figure 58. This indicated that by sintering at 1400°C it is possible to achieve sintered Ti_2AlC with lower traces of TiC.

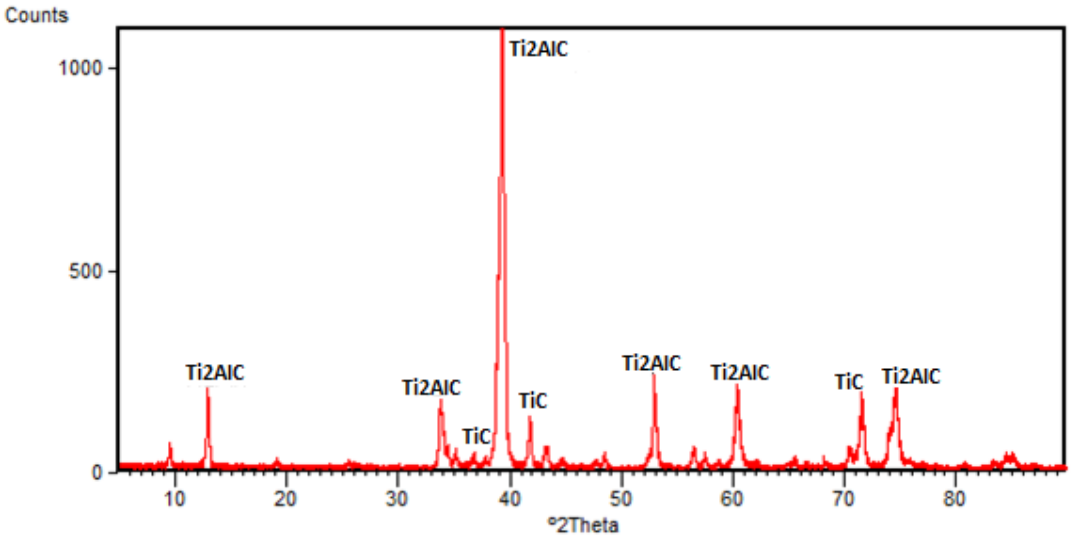

Figure 63. XRD spectra of the sample sintered at 1400°C in argon

Nevertheless a study of the effect of sintering temperature of phases present is not sufficient to establish an optimum condition to achieve bulk Ti_2AlC. The final sintered density of the ceramic plays an important role for some specific applications. For example when the material is used as a structural membrane [1] then it should possess a high density to withstand the load or force acted upon, for some applications it may be desirable to have a porous surface. Therefore the samples (a minimum of six) were characterised by the Archimedes density measurement to determine the bulk density, solid density and the level of porosity which were defined in Chapter 1, section 1.53.

Figure 64 shows the change in bulk density of the samples with sintering temperature. It is clear that as the sintering temperature is increased the density of the sample increases. For many industrial and commercial purposes, such as those discussed in Chapter 2, section 2.3, it is the high density (low porosity) that is required. In a porous green body preform it is also important that the material is sintering to high density to achieve sufficient mechanical strength e.g. to be handled or withstand a mechanical load.

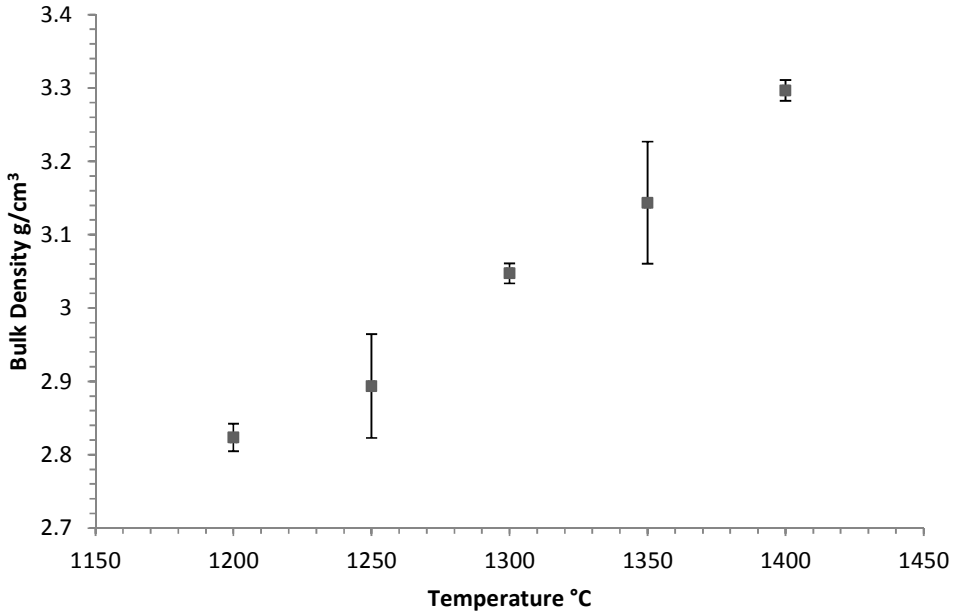

Figure 64. Variation in bulk density with sintering temperature

Figure 65 is the change in solid density of the sample with the varying sintering temperatures. It can be observed that the highest density recorded is 4.40g/cm^3 at 1300^{o}C. It should be noted that at 1300^{o}C, the sintered samples were not pure MAX-phase (refer to figure 61), and it also has the highest TiC (4.9g/cm^3) [125] peaks and this is the reason for high density. In the literature [35] it has been calculated that Ti_2AlC has a density of 4.11g/cm^3. Here in this experimental study the sample produced at 1400^{o}C has density of 3.85g/cm^3.

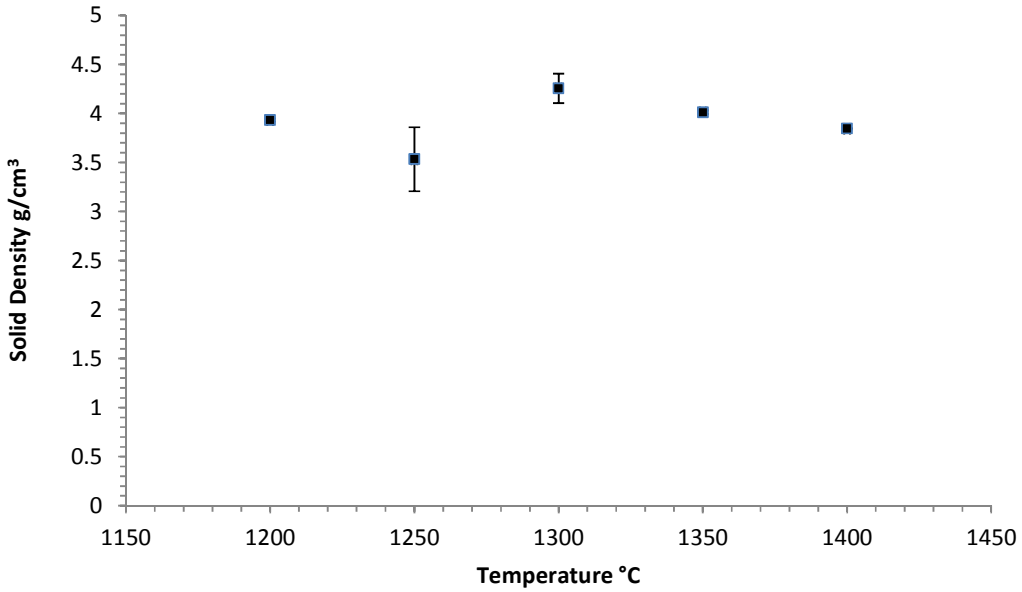

Figure 65. Variation in solid density with sintering temperature

From figure 66 it can be seen that with the increase in sintering temperature, the percentage of porosity decreases. This indicates that change in temperature can be a parameter to control the density of the sintered materials. To reduce the level of porosity further applying and external pressure while sintering has been undertaken [36], for example for hot-isostatic pressing or hot-pressing

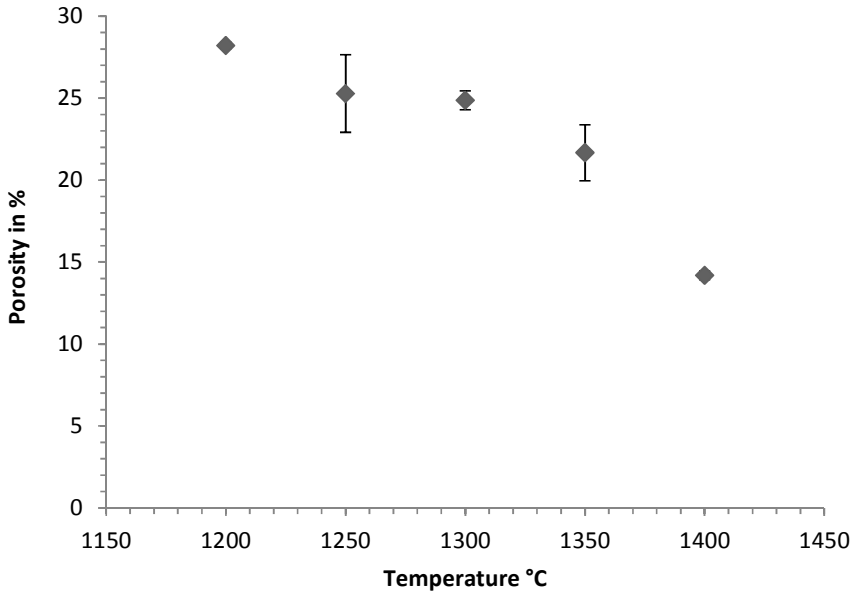

Figure 66. Variation in porosity with change in sintering temperature

Figure 67 is the SEM images showing the morphology of samples sintered at 1300^{o}C (figure 67a) and 1400^{o}C (figure 67b). In figure 67a two distinctly shaped structures can be identified. One is the spherical bright structure which is the TiC and elongated plate like structure (identified in red) which is the Ti_2AlC. When figure 67b is compared to figure 67a, the elongated plate like structures have elongated further which indicates the Ti_2AlC grain growth with increasing temperature. It can also be observed that in figure 67a there are many pore like cavities and they are less in figure 67b thus indicating the increase in density with increasing sintering temperature.

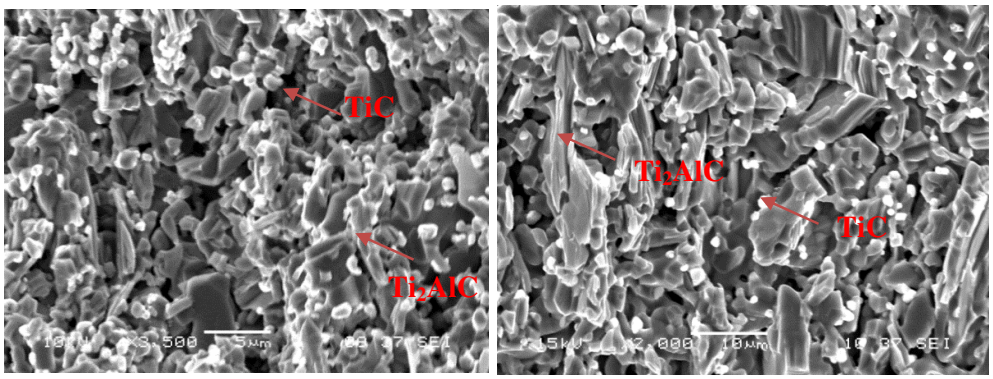

(a) **(b)**

Figure 67. (a) SEM image showing the crystal structure formed in the sample sintered at 1300°C. (b) SEM image showing the crystal structure formed in the sample sintered at 1400°C

5.4 Summary

This experiment in this chapter was conducted to optimise the sintering condition to obtain Ti_2AlC with an optimum density. This knowledge of sintering condition is applied in the development and sintering of porous Ti_2AlC ceramic which in explained in the upcoming chapters. From this study it is possible to know the sintering condition to obtain a relatively dense (85% density) pressureless sintered material for the basis of a porous ceramic. Sintering at temperature of the order of 1300 – 1350°C leads to the formation of TiC phase due to diffusion process during sintering which causes change in phase composition. Based on these results a sintering temperature of 1400°C will be used which produces a porous ceramic with ~15% porosity and a high percentage of MAX-phase. Higher densities and lower porosities can be achieved by colloidal processing techniques like slip casting and hot isostatic pressing and hot pressing processing process helps in minimising strength degrading defects [5].

Chapter 6. Fabrication of macro porous Ti_2AlC ceramic by the foam replication technique

6.1 Introduction

With the rapid development in manufacturing technology, porous ceramic materials with desired design and structures are currently generating tremendous interest in the research fraternity. The formation of porous ceramics is one such example of technological innovation that was initially developed for filtration purposes and today porous materials are used excessively. For example, porous ceramics for water purification [78], high temperature metal filters [49], biomaterials [50] and much more. Until the advent of new porous ceramic techniques the production was limited to metallic and polymeric structures, since ceramics were inherently brittle. However in present era the application of porous ceramics has increased especially where the application environment demands for high temperatures, corrosion, wear etc.

The method used in this research is the 'foam replication' which was explained in detail in Chapter 2, section 2.4. In this case, reticulated polyurethane foam of the required shape, pore distribution and pore size was impregnated with a Ti_2AlC slip, which was later dried and pyrolysed, to remove the foam, before it is finally sintered to obtain the Ti_2AlC porous ceramic. The final structure formed is an exact replica of the foam template used. Although similar methods have been widely used in the past to produce porous ceramics, this is the first time where a porous conductive Ti_2AlC ceramic has been produced using foam replication method. Research on reticulated MAX-phase ceramic shows a few studies conducted on development and application of Ti_3AlC_2 [79, 80] based ceramic an even less work has been undertaken on Ti_2AlC based porous ceramic. For example there is a report where porous Ti_2AlC was prepared by sacrificial template method where NaCl was used as the pore former [126] for controlling the volume fraction of porosity and even the pore size. This method of generating pores, using NaCl dates back to 1960 and was first reported by Polonsky [126] to fabricate aluminium open foams. There is also a report on reticulated Ti_3AlC_2 ceramic from Sun et al. [127] which was used as a substrate to deposit catalytic CeO_2 for a gas exhaust catalyst device.

The simplicity of foam replication method derives from the ease of control of the pore distribution and the pore size which directly depend on the structure of the template foam used. As with many other manufacturing processes, this does have some disadvantages. The porous ceramic obtained from this process often contains cracks on the solid parts ('struts') after sintering, which compromises the mechanical strength. The appearance of cracks is due to outgassing of the polymer during the decomposition of the polyurethane foam at elevated sintering temperature [61]. However, in this work an intermediate method to minimise this type defect is explored and has been reported in the following sections.

The motivation to use this method was the need of a highly conductive, macro porous and non-corrosive electrode for a microbial fuel cell. Details of the performance of these ceramics in a microbial fuel cell will be described in Chapter 8. Both the material and the foam replication process was adopted for this application due to the intrinsic properties of the MAX-phase ceramics, as explained in Chapter 1, section 1.1 and 1.2, its availability, and the simplicity of the process developed here. In this section the process development and materials characterisation are reported.

6.2 Material development

6.21 Slip preparation

From this section onwards the systematic development of mechanically stable porous Ti_2AlC ceramic is explained. The slip is made up of the following compounds:

(i) Ti_2AlC ("Maxthal 211 engineering ceramic material" from Kanthal),
   - Particle size distribution: 90% of the powder comprised of 20µm particles, and the rest was a mixture of 2µm and 8µm particles.

(ii) Poly(ethylenglycol) average Mn 380-420 from Sigma Aldrich

(iii) Dispex GA40 from Ciba AG

(iv) Methyl cellulose from Sigma Aldrich

(v) Distilled water with a resistivity of 18.2MΩcm

The use of the above chemicals was adopted from work of Hsu [128] for producing highly porous hydroxyapatite/tricalcium phosphate (HA/TCP) bio-ceramic. However, the precise chemical composition had to be fine-tuned for the present materials. Poly (ethylenglycol) and Dispex GA40 act as the binders and anti-settling agent respectively, which enhances the adhesive and flow character of the ceramic slip. Methyl cellulose was used as the thickening agent to increase the viscosity of the slip without affecting the solid loading (amount of ceramic content). Different compositions of these compounds were tested in producing an appropriate Ti_2AlC slip for foam replication with each successive composition leading to better porous ceramic component. Table 8 shows the three different compositions prepared in this work.

Table 8. Developing feasible composition of the slip

Composition 1	Composition 2	Composition 3
• First mix solvents in one container (has to be cylindrical) • 2mL Poly(ethylenglycol) average Mn 380-420 from Sigma Aldrich • 75gms distilled water with a resistivity of 18.2MΩcm • 1mL Dispex GA40 from Ciba AG Followed by mixing the following components in the same container and in the following order: • 2gms Methyl cellulose from Sigma Aldrich • 155gms Ti_2AlC powder ("Maxthal 211 ceramic engineering material" from Kanthal) 64gms 5mm ceramic beads were added to enhance mixing The container was subjected to milling for 24 hours	• First mix solvents in one container (has to be cylindrical): • 2mL Poly(ethylenglycol) average Mn 380-420 from Sigma Aldrich • 70gms distilled water with a resistivity of 18.2MΩcm • 1mL Dispex GA40 from Ciba AG Followed by mixing the following components in the same container and in the following order: • 3gms Methyl cellulose from Sigma Aldrich • 125gms Ti_2AlC powder ("Maxthal 211 ceramic engineering material" from Kanthal) 64gms 5mm ceramic beads were added to enhance mixing The container was subjected to milling for 24 hours	• First mix solvents in one container (has to be cylindrical): • 2mL Poly(ethylenglycol) average Mn 380-420 from Sigma Aldrich • 60gms distilled water with a resistivity of 18.2MΩcm • 1mL Dispex GA40 from Ciba AG Followed by mixing the following components in the same container and in the following order: • 3gms Methyl cellulose from Sigma Aldrich • 125gms Ti_2AlC powder ("Maxthal 211 ceramic engineering material" from Kanthal) 64gms 5mm ceramic beads were added to enhance mixing The container was subjected to milling for 36 hours

The starting composition i.e. Composition 1 in Table 8, was less viscous leading to poor binding of the slip to the polyurethane foam. Hence each different composition attempted to gradually increase the slip viscosity. Composition 3, Table 8 was employed to produce a better mechanically stable porous ceramic as this slip had better cohesive properties and a thick uniform coating was achieved throughout the foam. The processing steps followed for coating technique is as shown in figure 68 and explained in the next section.

6.22 Preparing porous ceramic using the foam replication technique

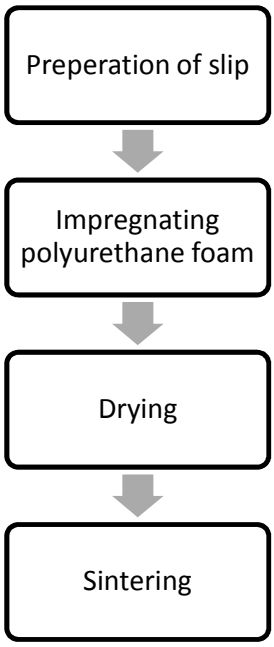

Figure 68. Basic processing steps for producing porous ceramic foam

In this work polyurethane foam ("Reticulated vitreous carbon foam" from Duocel) of 10 ppi (pores per inch) was cut into the desired shape as shown in the figure 69.

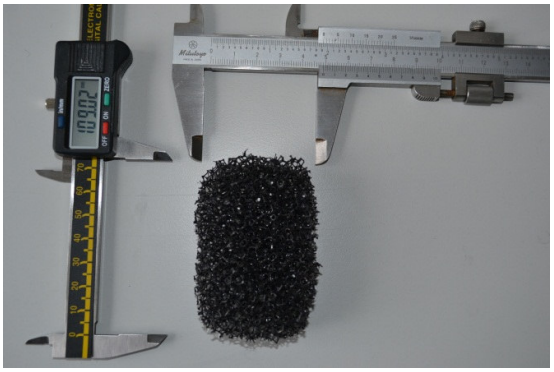

Figure 69. Foam cut into desired shape of the ceramic to be obtained

The foam was then impregnated into the prepared slip to ensure that the entire foam was coated as shown in figure 70.

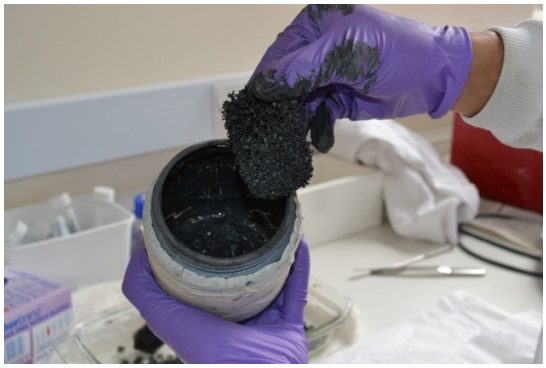

Figure 70. Foam immersed into the slip

Once the foam was impregnated care must be taken that excess slip is removed before the slip dries. A squeezing technique (figure 71) was used to remove this excess slip. Although most of the excess slip is eliminated at this stage, the pores in the foam are still clogged or closed due to the slip (figure 72).

Figure 71. Squeezing out the excess slip

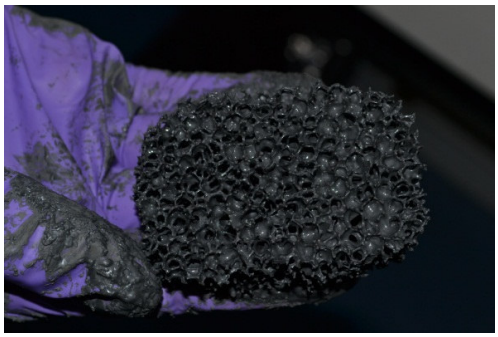

Figure 72. Pores clogged after squeezing process

Further squeezing cannot unclog these pores and therefore compressed air is used over the coated foam as shown in the figure 73. The air under high pressure serves three purposes:

(i) it helps in opening the clogged pores,
(ii) uniform coating of the slip can be ensured,
(iii) it helps in partial drying of the slip as the air is considerably warm.

Figure 73. Using compressed air to unclog the pores and remove excess slip

Figure 74 shows the impregnated foam which is now ready to be sintered. But before the foams are sintered it must be dried at least of 24 hours under room temperature and pressure.

Figure 74. Coated foam ready for sintering after drying

The impregnated foam is dried on a polyurethane foam (figure 75) to prevent the clogging of the pores in contact with the surface. While drying, due to gravity some of the slip starts flows downwards and this excess slip flows through the additional foam beneath the impregnated foam, thus preventing clogging.

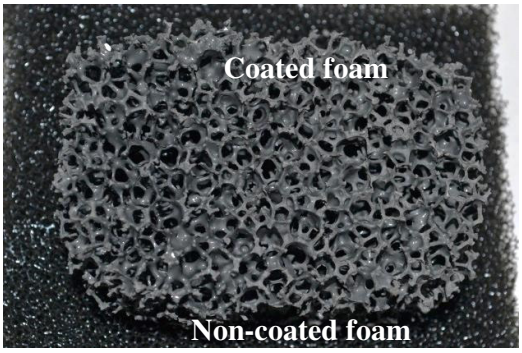

Figure 75. The coated foam placed on non-coated foam to prevent clogging of the pores while drying

The dried foam is sintered based on the optimized sintering condition established in Chapter 5 for dense Ti_2AlC tablets as seen in figure 76.

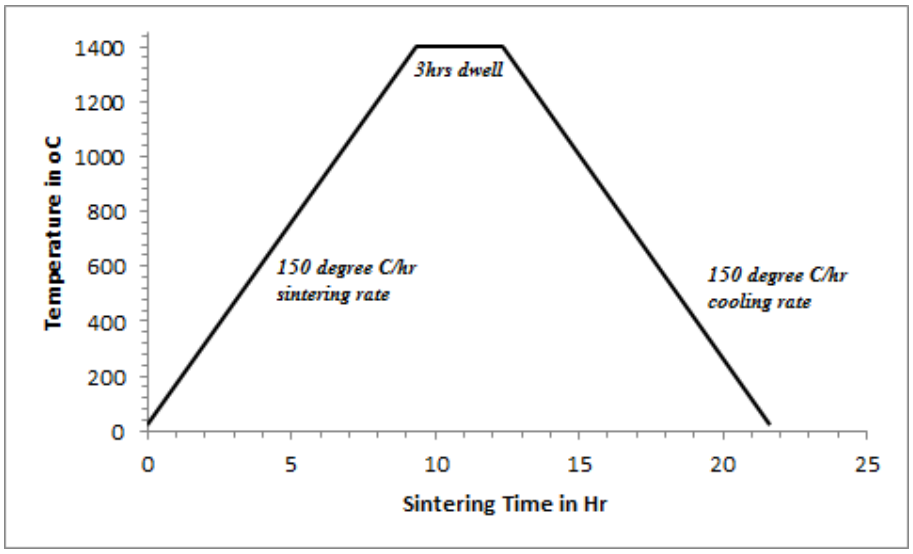

Figure 76. Optimised sintering condition to obtain dense Ti_2AlC tablet

Composition 3 was later subjected for a viscosity study to fine tune the quality of the slip in order to achieve high quality (thick and uniform) coat on polyurethane foams. The viscosity study was conducted using a Bookfield DV-II+ Pro viscometer shown in the figure 77 and is explained in the next section.

Figure 77. Brookfield DV-II+ Pro viscometer used in this study

6.23 Viscosity study

For Composition 3, while keeping other chemical quantities in Table 8 constant, only the amount of distilled water was varied to achieve an appropriate composition for a porous Ti_2AlC ceramic. The criteria to establish an optimum composition of slip are as follows:

(i) uniform coating over the polyurethane foam,
(ii) easy removal of excess slip from the foam while coating,
(iii) faster drying (under 24 hours) to minimize the processing time,
(iv) minimum loss of slip during the drying process,
(v) sufficiently thick ceramic coat to achieve a sensible mechanical strength for handling.

The viscosity reading was taken using the spindle 63 that was specific for this instrument while keeping the RPM constant to 1.5 for all the trials. Each trial was conducted for 5 minutes and the maximum viscosity was recorded in mPa.s (millipascal-second) which is the SI unit of dynamic viscosity [129]. Table 9 below provides the complete set of data on the viscosity were the quantity of distilled water is varied in Composition 3 (Table 8).

Table 9. Viscosity reading for different quantity of distilled water

Quantity of water (g)	Quantity of water as wt% of the ceramic	Milling time (hours)	Dynamic viscosity in (mPa.s)	Spindle RPM	Maximum spindle torque (%)	Quantity of ceramic in grams	Quantity of PEG as wt% of the ceramic	Quantity of methyl cellulose as wt% of the ceramic	Quantity of Dispex as wt% of the ceramic
60	48	24	332000	1.5	82.9	125	2	2.4	1.2
65	52	24	146000	1.5	35	125	2	2.4	1.2
70	56	24	75184	1.5	20.8	125	2	2.4	1.2
75	60	24	51589	1.5	12.9	125	2	2.4	1.2

6.23a Effect of slip viscosity on the foam impregnation

Table 10. Observation on impregnating the foam using various slip viscosity

Slip made with 48wt% of distilled water • From Table 9 it is evident that the slip is highly viscous and it is very difficult to achieve a uniform coat (approx.1.13mm thick) over the foam as seen in figure 78(a) and 78(b). • Due to higher coating thickness drying period is more and forms a big lump of dried mass at the bottom. • Most of the inner pores are clogged as shown in figure 78(a) as excess slip cannot be squeezed or blown out.
Slip made with 52wt% of distilled water • Although the slip is fairly viscous, it is possible to achieve uniform coating (approx. 0.77mm thick) over the foam as seen in figure 79(a) and the excess slip can be easily squeezed out. • The slip dries in 24hrs without clogging the inner pores of the foam as seen in figure 79(b).
Slip made with 56wt% of distilled water • Due to increase in distilled water content the viscosity is lesser than the previous compositions • A uniform thin layer of coating (approx. 0.57mm thick) is achieved, but is too thin as seen in figure 80(a) • Easily dries and no clogging of the pores, see Figure 80(a) and 80(b).
Slip made with 60wt% of distilled water • Very low viscosity, as a result poor adhesion of slip on to the foam but ideal as second coating slip (to be discussed in section 6.5).

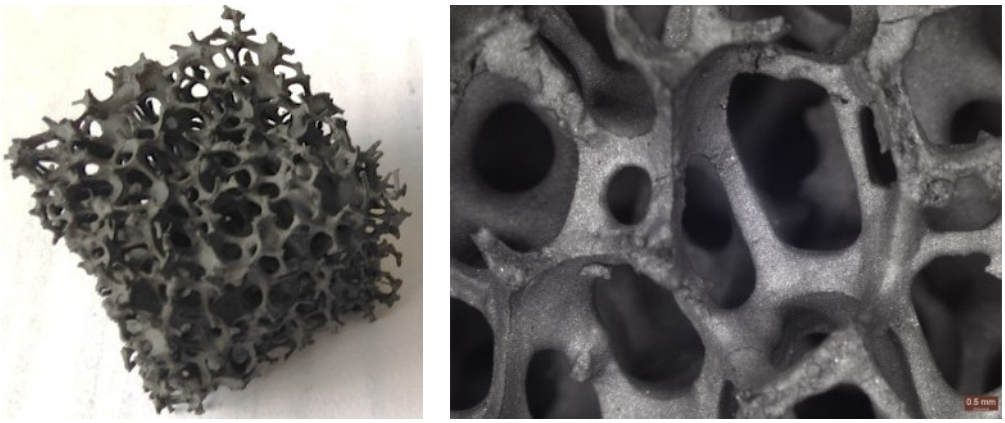

(a) **(b)**

Figure 78. Image showing the quality of coating on polyurethane foam obtained with 48wt% of distilled water. (a) coated PU foam (25x25x25mm) prior to sintering (b) optical image of coated foam prior to sintering

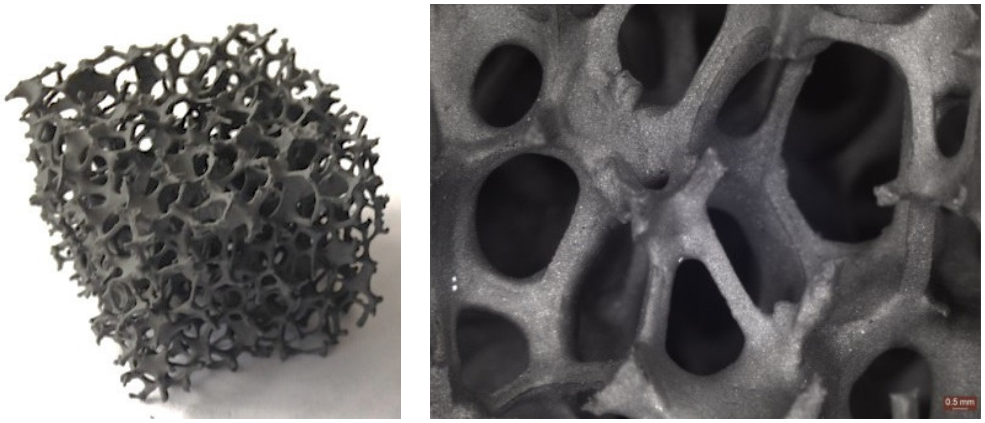

(a) **(b)**

Figure 79. Image showing the quality of coating on the polyurethane foam 25x25x25mm obtained with 52wt% of distilled water. (a) Coated PU foam (25x25x25mm) prior to sintering (b) optical image of coated foam prior to sintering

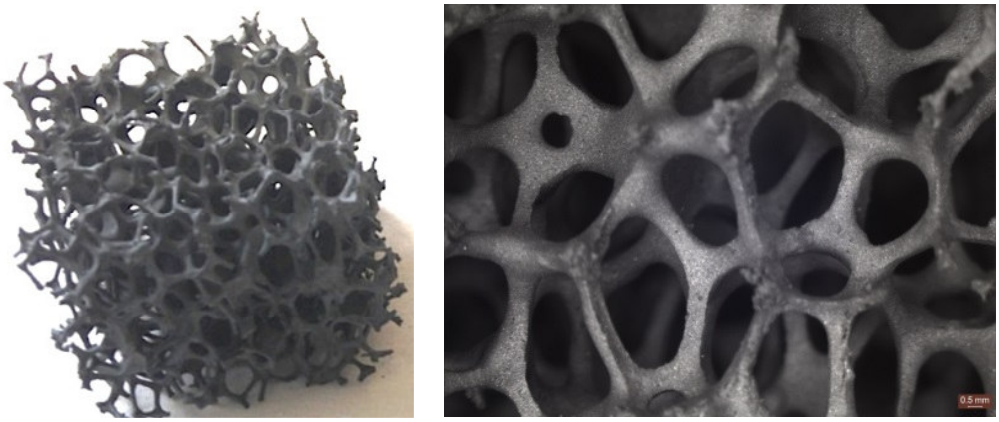

(a) **(b)**

Figure 80. Image showing the quality of coating on the 25x25x25mm polyurethane foam obtained with 56wt% of distilled water. (a) Coated PU foam (25x25x25mm) prior to sintering (b) optical image of coated foam prior to sintering

From the above observations made in Table 10, it was decided that the slip with 52wt% of distilled water will be used to produce a porous Ti_2AlC ceramic. Figure 81 shows the slip which resulted in a better porous ceramic with uniform coating and more open pore channels as the clogged slip could be easily squeezed and blown out of the pores.

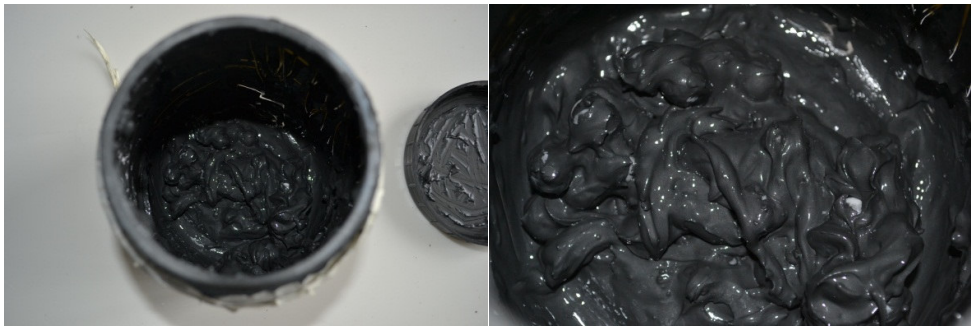

Figure 81. The latest slip developed for porous ceramic

6.3 Results and discussion

In this section the observations made after sintering the coated porous ceramic template are discussed. As discussed in section 6.21, the slip made with Composition 3 (Table 8), with 52wt% of distilled water used to coat the polyurethane foam. The samples were sintered using the temperature curve shown in figure 76.

Figure 82. Sample obtained from Composition 3, Table 5 (110x45x25mm)

When the sintered sample in figure 82 was closely observed, two colored regions are visible. This clearly states the formation of two different phases and XRD analysis in figure 83 indicates the presence of Ti_2AlC and TiC. The same issue was encountered during the sintering of dense Ti_2AlC tablets in Chapter 5, section 5.3 (figure 60). However the problem was overcome by optimizing the 1400^{o}C sintering temperature. Considering the relatively small size of the dense Ti_2AlC tablet (13mm in diameter, 2mm thick) it would be thought that the porous Ti_2AlC samples require a longer sintering period. Hence the dwelling time was increased from 3 hours to 5 hours as seen in figure 84.

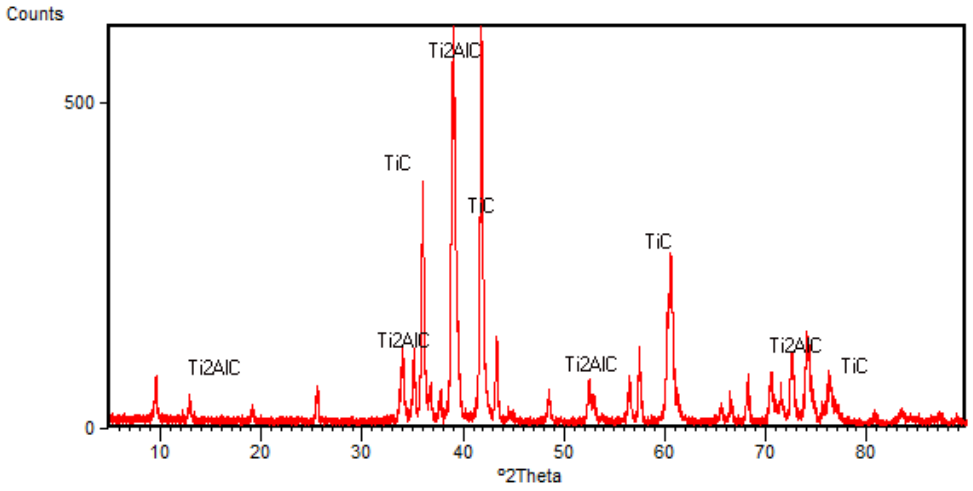

Figure 83. XRD spectra of the porous ceramic prepared using temperature curve in figure 76

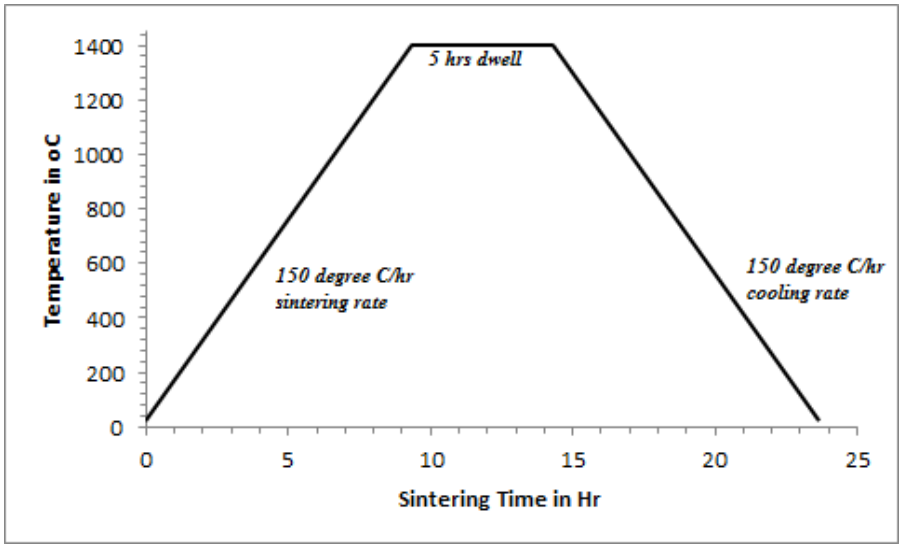

Figure 84. Optimised sintering condition for porous ceramic

This small change in the heat treatment process resulted in a Ti_2AlC porous ceramic with a smaller amount of TiC as confirmed from the XRD analysis seen in figure 85 and also by observing the single color of the sample in the figure 86.

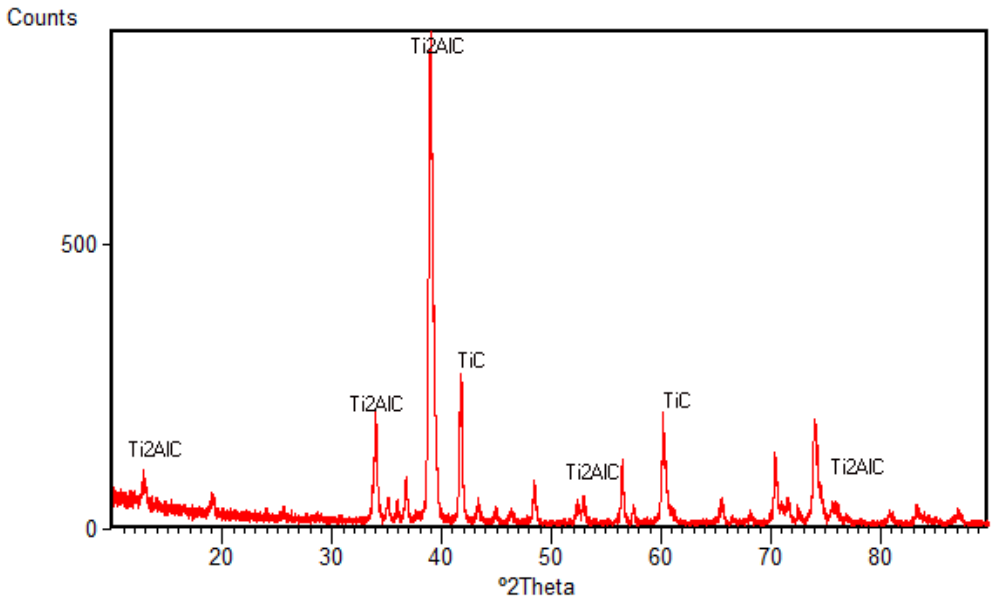

Figure 85. XRD spectra of the porous ceramic prepared using temperature curve in figure 84

Figure 86. Single phase Ti_2AlC porous ceramic obtained after optimising sintering condition (25x25x25mm)

6.4 Structural analysis

The profile of the porous ceramic samples were analysed using a JEOL 6480LV SEM equipped with an Oxford instrumentation IMLA X-act, X-ray detector.

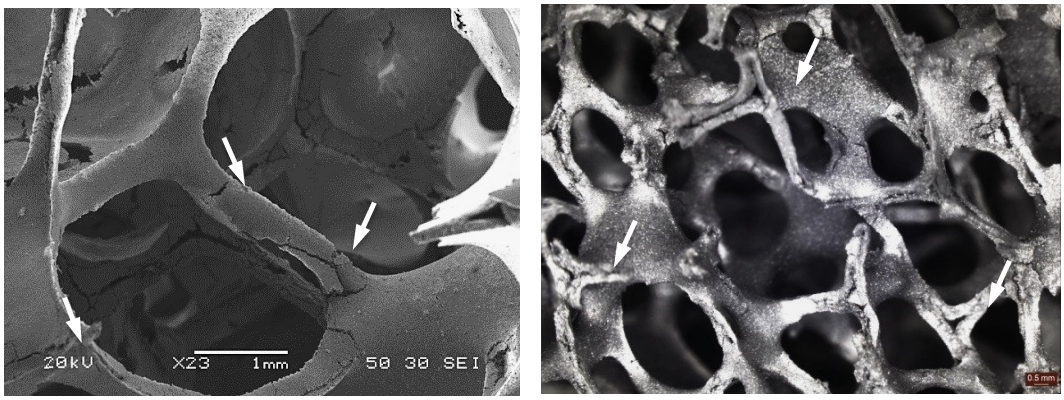

(a) **(b)**

Figure 87. (a) SEM of cracks formed along struts for samples prepared with 52wt% distilled water. (b) Optical image of hollow region in struts of the porous ceramic prepared with 52wt% of distilled water due to the decomposition of the foam during sintering

Figure 87 shows the SEM images of the struts in the sample prepared using Composition 3 in Table 8 with 52wt% of distilled water. As we can see the struts comprises of a number of defects in the form of cracks running all over the sample (indicated by arrows in figure 87(a)). This problem has been reported in papers on foam replication and the solution to overcome it, has been explained [61, 130, 131, 132]. As explained previously, the cracks are formed due to outgassing of the polymer produced during the uncontrolled decomposition of the polyurethane foam at elevated sintering temperature. In addition since the foam is burnt out it leaves behind a hollow strut throughout the sample as seen in the SEM image in figure 88.

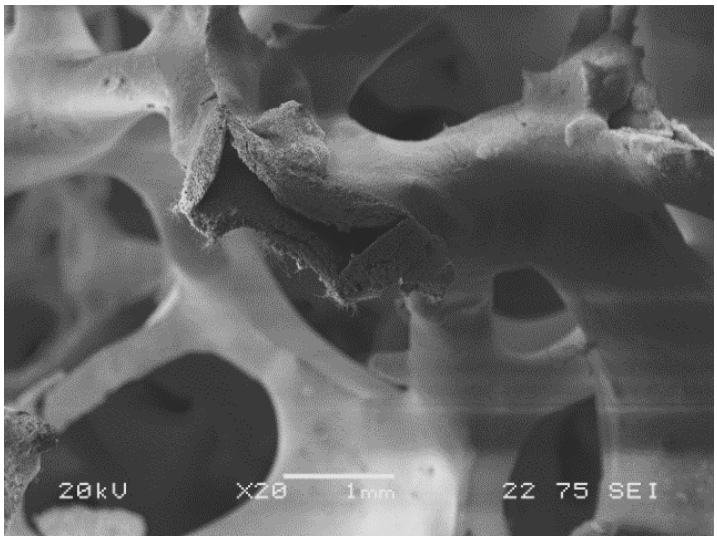

Figure 88. SEM of hollow region in struts of the porous ceramic due to the decomposition of the foam during sintering

Therefore it is important that the decomposition of the polymer foam takes place in a controlled manner. Therefore a polymer pyrolysis stage was introduced in the sintering temperature curve as seen in figure 89. This temperature curve was used in controlling the decomposition rate of the foam, so there is no sudden outgassing.

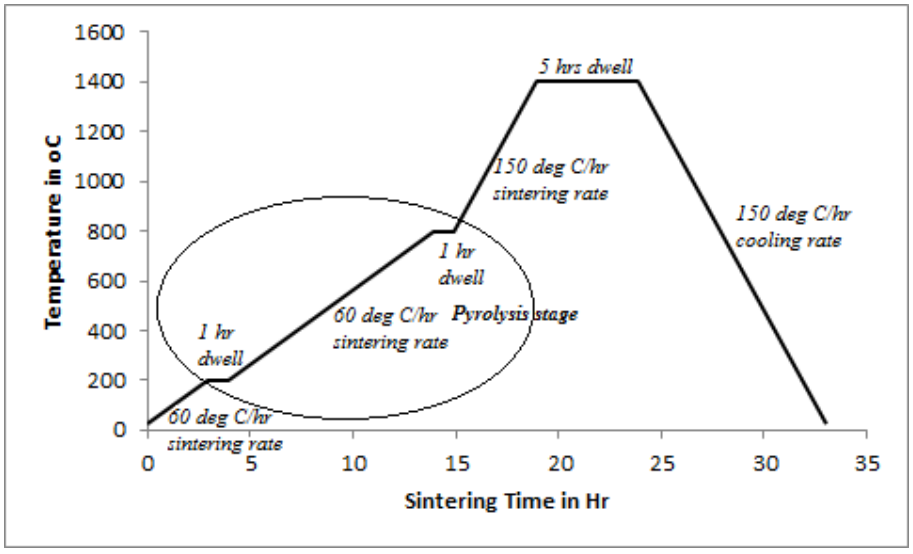

Figure 89. Optimised sintering condition introducing pyrolysis stage for minimising the defects in porous ceramic

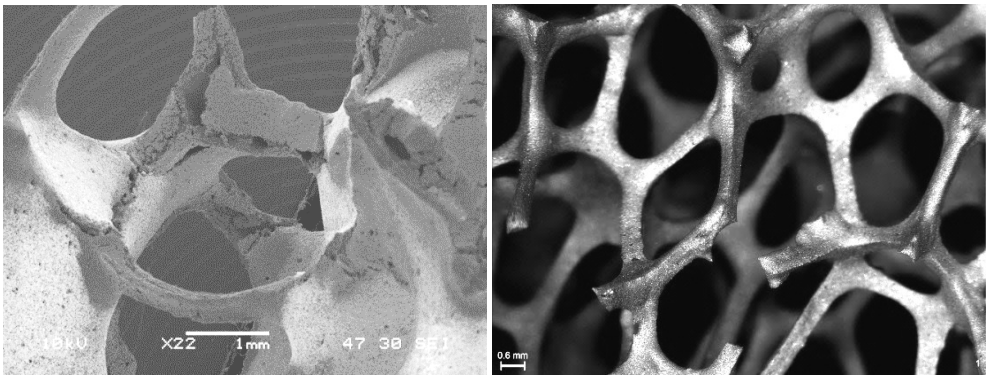

(a) **(b)**

Figure 90. (a) SEM and (b) optical image of sintered samples

Figure 90, shows the SEM image of the struts in the sample prepared from the Composition 3 with 52wt% of water but with a pyrolysis stage in the heat treatment process. Although there were defects in the region joined by struts, the strut itself had comparatively less defects compared to the samples with no pyrolysis in figure 87(a).

Compression test was carried out to see any significant improvement in the mechanical strength. The samples of 25x25x25 mm in dimension were prepared for the two different sintering conditions as shown in figure 84 and 89. A minimum of six samples were subjected to uniform, uniaxial compressive load as seen in figure 91 and the maximum load at failure was recorded.

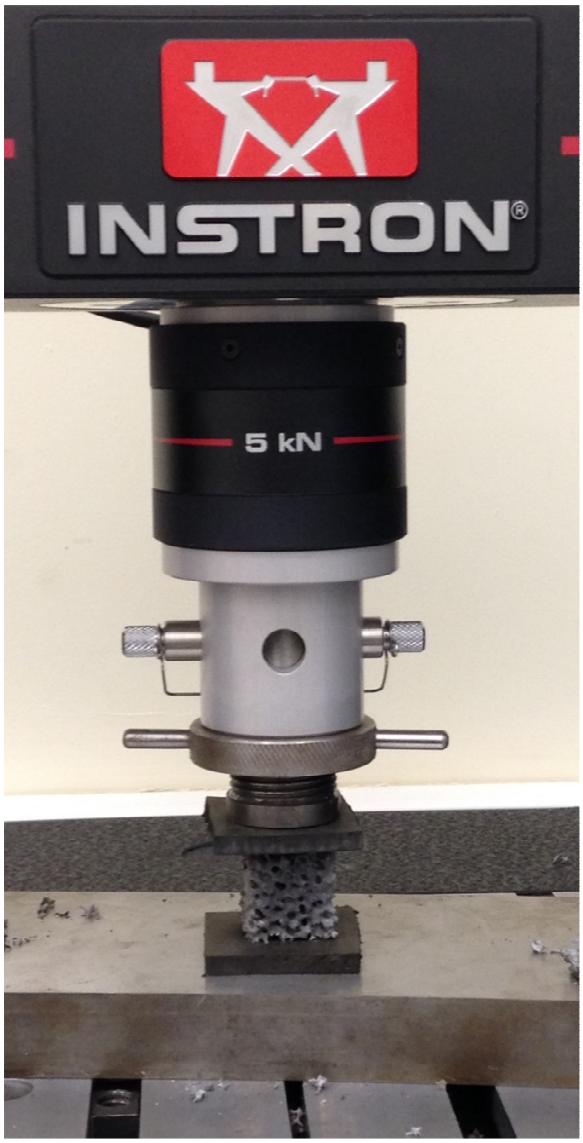

Figure 91. Compression testing conducted on the porous Ti_2AlC ceramic (sample size:25x25x25mm)

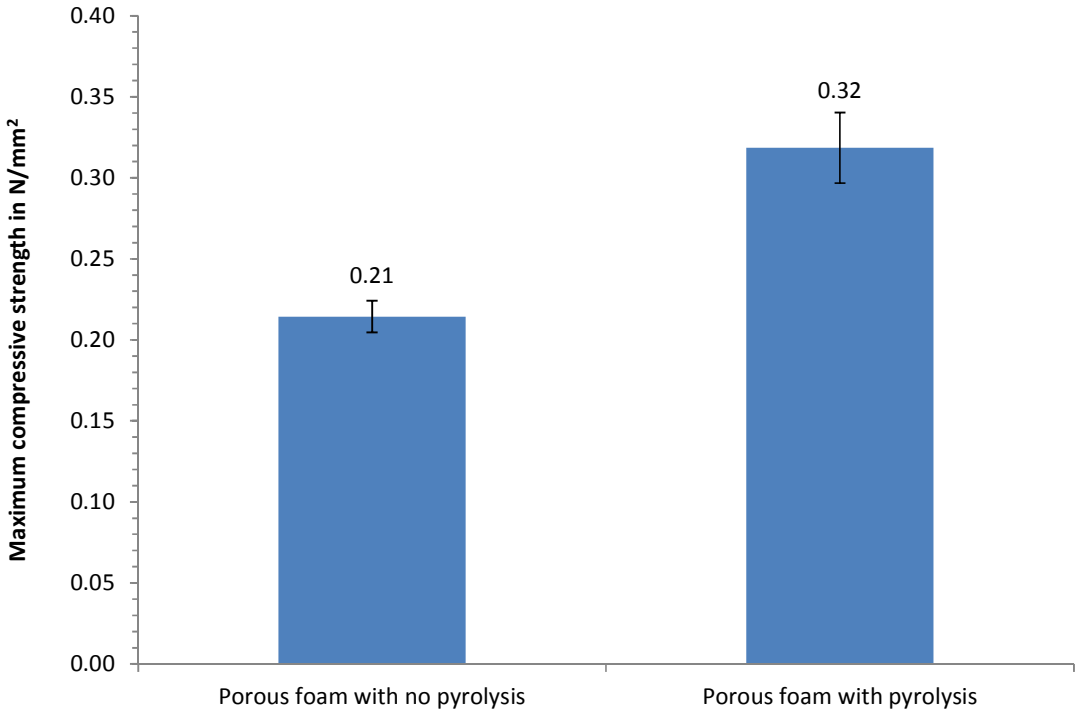

Figure 92. Compression test data conducted on porous foams

From figure 92, there is an increase in the compressive strength when pyrolysis stage was introduced in the heat treatment cycle, however the strength is still low due to defects throughout the sample. Therefore the next task was to further minimise the defects and thereby increase the compressive strength.

6.5 Coating of porous foams

In an attempt to reduce the number of defects it was decided to apply an additional ceramic coating on the ceramic before they are heat treated/sintered. The basic processing of impregnating foam, drying and sintering is described figure 68. To further reduce the defects in the final ceramic foam an additional coating of ceramic was applied to the foam before sintering or after sintering which will be now explained.

6.5a Coating of foams prior to sintering

Samples were prepared according to the processing route shown in figure 93 using a slip of lower viscosity which is 51589mPa.s (refer Table 9).

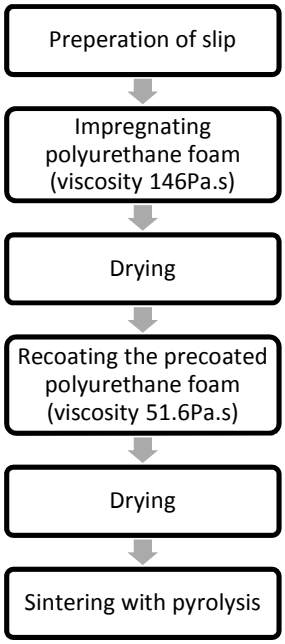

Figure 93. Processing steps to minimise defects in the porous ceramic foam by recoating the coated foam prior to sintering

As explained in section 6.23, this is the slip made with 60wt% of distilled water which is a modified composition of the Composition 3 in Table 8.

A lower viscous slip was preferred because at this stage of coating since excess slip cannot be squeezed out of the foam as it will damage the layer of the initial coating. Figure 94 and 95 shows the green sample obtained after coating of foam prior to sintering.

Figure 94. Top view of the coated samples before sintering (sample size: 25x25x25mm)

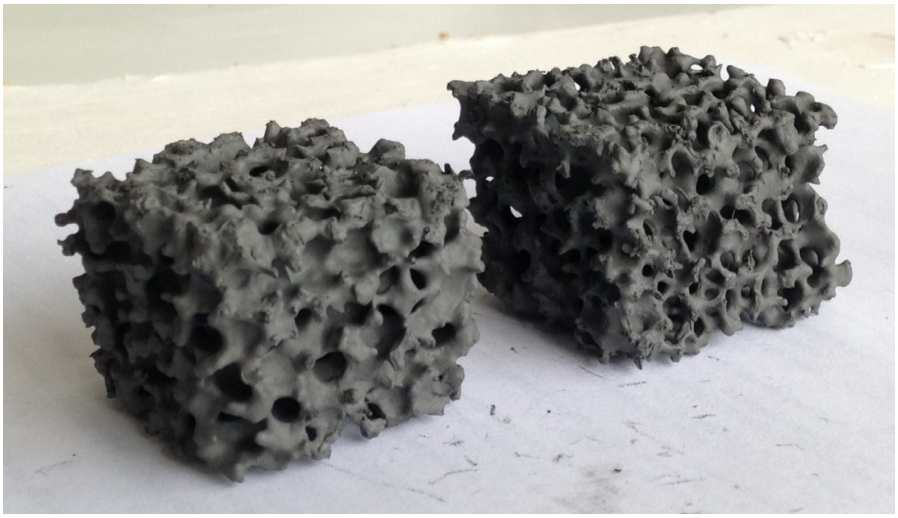

Figure 95. Isomeric view of the coated samples before sintering (sample size: 25x25x25mm)

Figures 94 and 95 show there is a thick uneven coating (approx. 2.21mm thick) on the coated samples prior to sintering. Therefore with this technique there is a reduction in the open porous channels to some extent, approximately 40% from optical microscopy. A further reduction in the slip viscosity reduces its adhesion property as discussed in Table 10.

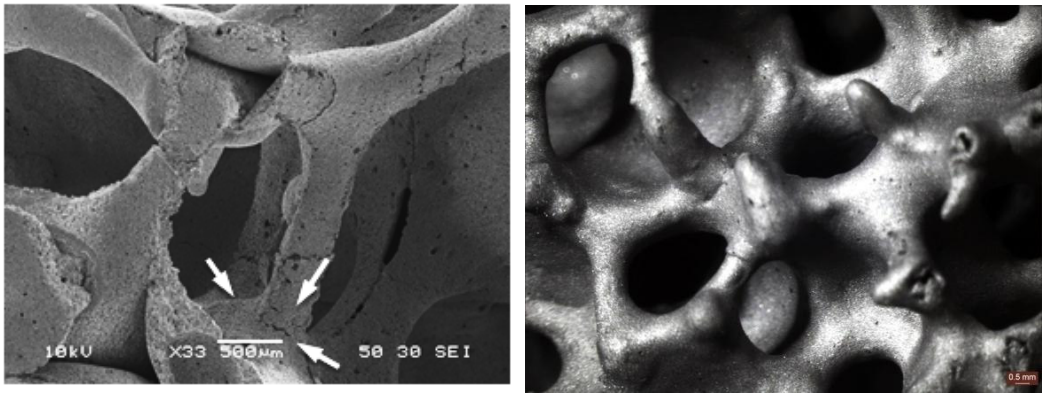

(a) **(b)**

Figure 96. (a) SEM image of defects formed on struts of sintered ceramic that was coated sample prior to sintering (b) Optical micrograph of same ceramic

Figure 96 is an SEM image of the struts of the porous ceramic. Although it is not defect free, when compared to the SEM images seen in figure 87(a) and 90(a) the defects are reduced and the ceramic struts are thicker. The intersections formed by the struts (indicated by arrows in figure 96(a)) are not damaged as seen in figure 87(a) for the foam produced with a coating. The presence of cracks is due to the polyurethane foam present in the sample while sintering and also due to the shrinkage during diffusion process upon high temperature.

Compression testing was conducted and the results show that coating of foam prior to sintering is an effective approach to minimise the defect and improve the mechanical properties. The compressive load at failure increased to an average of 6.34N/mm^2 from 0.32N/mm^2 as seen in the figure 97.

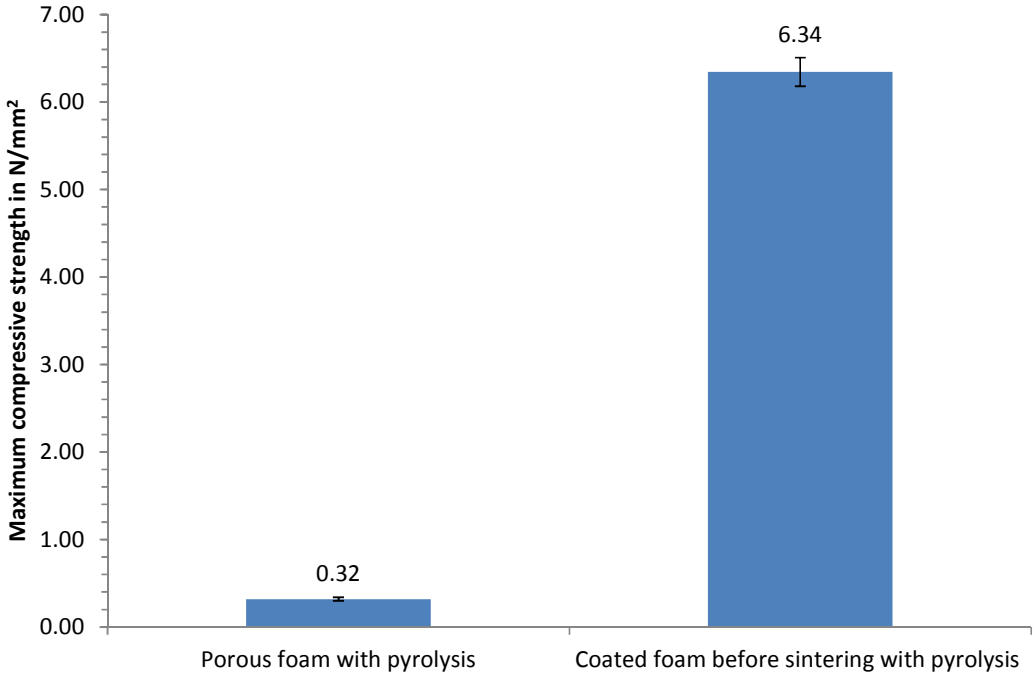

Figure 97. Compression test data conducted on porous foam with pyrolysis and coated foam before sintering with pyrolysis

6.5b Coating of foams after sintering

Since it is evident that many of the defects are formed during the decomposition of the polyurethane foam, another mechanism to reduce the size and frequency of defects is to re-coat the sintered ceramic foam after the polymeric foam has already been burnt out and the ceramic has been sintered. In this method the Ti_2AlC foam is simply used as the template.

Samples were prepared according to the processing route in figure 98. Once the Ti_2AlC foams are sintered using the thermal cycle of figure 84, it was recoated with a low viscosity slip (60wt% distilled water) of 51589 mPa.s viscosity.

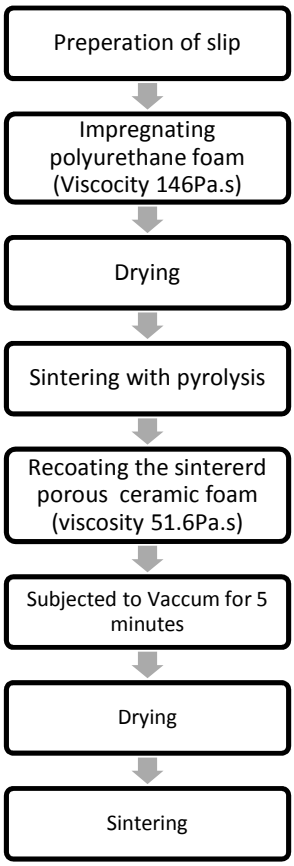

Figure 98. Processing steps to minimise defects in the porous ceramic foam by coating the Ti_2AlC foam

After coating, the samples were subjected to vacuum of 1bar pressure for 5 minutes to ensure that the recoated slip was absorbed into the cracks of the ceramic foam thus minimising the cracks and to ensure any entrapped air bubbles are removed and ensure pores are open. The samples are subsequently dried and re-sintered using temperature profile of figure 84.

When figure 99 is closely observed, majority of the pores are open unlike in the samples in figure 94 and 95. This is one of the advantages of re-coating the sample after sintering. Therefore depending on the percentage of open pore channel needed, it is possible to adopt the coating technique accordingly.

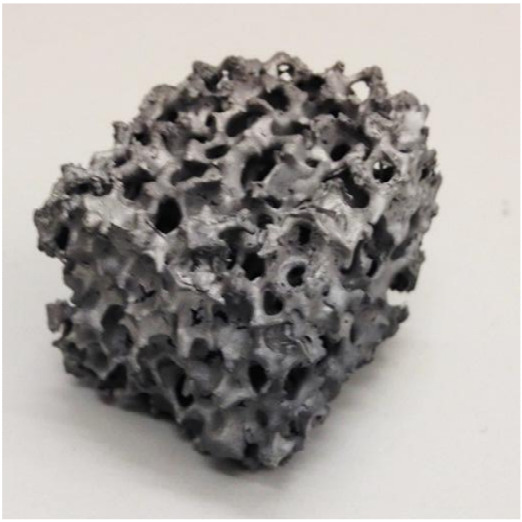

Figure 99. Sintered double coated sample

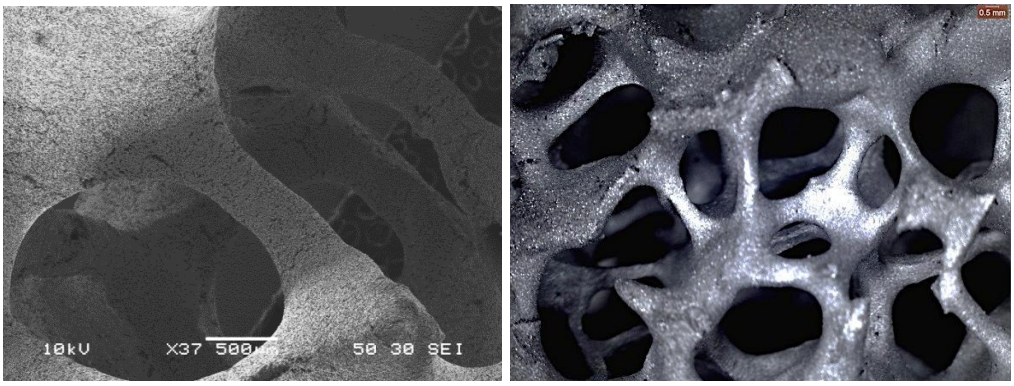

(a) **(b)**

Figure 100. SEM image of the coated foam after sintering sample. (a) Image showing individual strut surface. (b) optical image showing various strut surfaces

Figure 100 is an SEM image of the coated foam after sintering. Clearly it can be observed from the figure 100(a) that the surface of the strut is fairly smooth, compared to the other samples seen in figure 87(a) and 96(a). Some inevitable defects in the form of cracks are formed during the shrinkage of the sample during sintering process. Compression testing was carried out to see how it compares with the porous ceramic and coated foams before sintering.

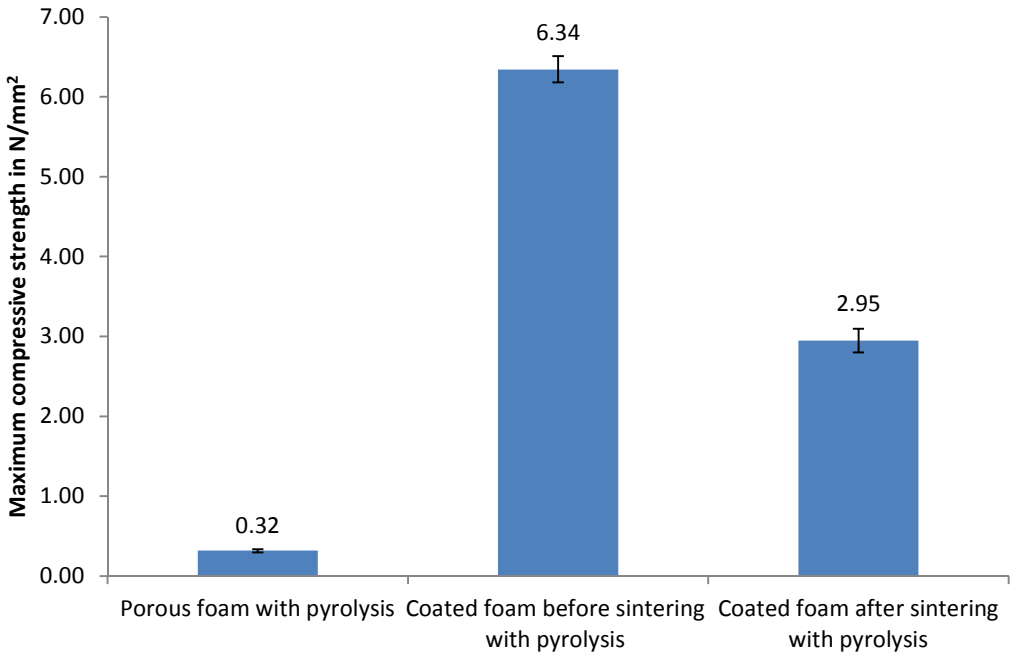

Figure 101. Summary of the compression test conducted

From the test result as seen in the figure 101, the coated foams after sintering had an average maximum compressive strength at failure of 2.95N/mm^2. The reason for the low compressive strength compared to the coated before sintering sample is the fact that, in the coated foam before sintering samples, some of the open pore channels are filled with material. This offers more resistance to load compared to the coated foam after sintering samples. Nevertheless samples prepared from both the coating techniques are structurally stable and are good candidate for porous electrode due to the inherent property of the Ti_2AlC electrically conductive ceramic.

6.6 Summary

This study demonstrates that Ti_2AlC ceramic can be used in fabricating macro porous ceramic. It also exhibits different techniques of fabrication to improve the mechanical strength of the porous ceramic component based on the application required. This is a novel method of fabricating macro porous Ti_2AlC and it is the first time macro porous Ti_2AlC has been fabricated using the foam replication technique. Both the advantages and disadvantages of this method were examined in the study and to some extent the mitigation of the formation of cracks has been stated in this study. Chapter 8 will provide an example of the application of this porous ceramic in a microbial fuel cell and its performance compared to other competitive porous electrode materials.

Chapter 7. Fabrication of micro porous Ti_2AlC MAX-phase ceramic with graded porosity by freeze casting process

7.1 Introduction

The foam replication method, as explained in Chapter 6, is a useful technique to produce macro porous ceramics (10 pores per inch between 3 - 5mm pore sizes) with constant pore size and constant pore distribution. It is an appropriate technique when interconnected open pore channels are required in the material. However, in some applications such as batteries, substrates for catalyst supports, fuel-cells or even solid-state electrodes, as in the case of Li-ion batteries [133] there is a need for a high surface-area contact with a surrounding electrolyte or produce the material in thinner sections. For these applications a conductive ceramic material with open porosity is necessary but with a high surface area; in this case a microstructure consisting of a large number of micro-pores (less than 100μm) is beneficial. To produce such micro pores on the surface as well as throughout the material, the freeze casting technique was examined and will now be described. The basic principle involved in this process, the process of pore formation and also controlling the pore size and orientation has been explained in Chapter 2, section 2.5. In essence, freeze-casting involves the solidification of a sample containing a solute, which is usually the ceramic material uniformly suspended in a solvent which is a mixture of a freezing vehicle, dispersant and a binder. The sample achieves its porous structure when the freezing vehicle solidifies under cooling, resulting in the formation of a variety of microstructures depending on the freezing solvent used; the reader is referred to Chapter 2, section 2.52. When the solidified solvent sublimes, it leaves behind pores which are the exact replica of the frozen solvent crystals.

The use of this technique dates back to 1908, when Bobertag et al. [134, 135] studied a platinum sol through a cycle of freezing and de-freezing. They concluded that the final microstructure is caused by the solvent ice crystals. In the same year Lottermoser studied the effect of freezing and de-freezing in silica and ferric oxide hydrosol and found the appearance of a honeycomb pore structure in the material [136]. The most important development on this technique was made in 1950's, when Maxwell and his group at National Advisory Committee for Aeronautics (NACA) used this technique to manufacture fully formed turbine blades [137]. They used this method to manufacture

blades with a complex shape in a single step using a high solid loading (defined here as the amount of ceramic material in the solute) slurry of TiC, Al_2O_3 and Mo metal powder in a water solvent to produce a dense article of the dimensions of the mould. Using radiography they found that a high solid loading resulted in a better quality cast but resulted in the formation of pores, termed 'air holes' [138]. To reduce the formation of the pores in the turbine blades a de-aeration stage was introduced, as seen in figure 102(b), to remove the air bubbles present in the slurry before the casting stage.

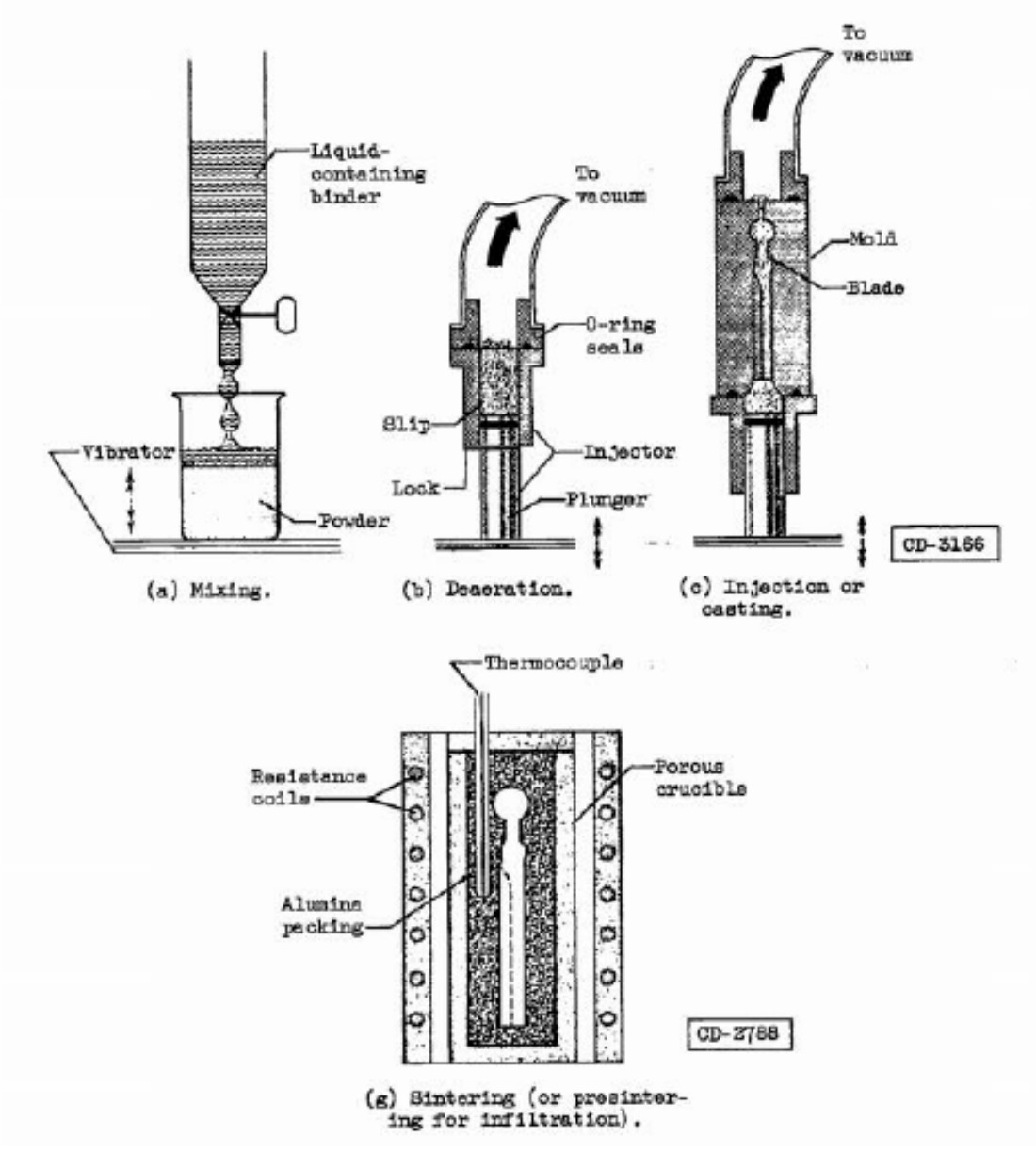

Figure 102. Processing steps followed by Maxwell for manufacturing turbine blades [138]

However, the NACA researchers found that the pore formation was unavoidable with this technique and later the potential of freeze casting to deliberately create porous microstructures was employed to manufacture filters, electrodes, catalyst supports and thermal insulation by NASA. Since then it has been a very important technique in fabricating micro to macro-porous materials and it is studied extensively today [82, 83, 137, 139].

In this present chapter, the development of a graded porous Ti_2AlC ceramic via freeze casting is explored and this approach has yet to be examined for Ti_2AlC ceramic. The effect of solid loading on the mechanical strength and porosity is reported. In addition the effect of heat transfer rate during solidification on the pore formation was studied using two different mould materials with differing thermal conductivity, namely aluminium and poly(vinyl) chloride (PVC). SEM was used to analyse the pore microstructure.

ImageJ 1.44p software was used to analyse the pore size and its distribution over the samples formed. ImageJ is a widely used java image processing software mainly used to analyse particle size and area, cell counting, pore size and distribution of pores over an area and also it can be used to examine whether the pores formed follow any particular pattern using a Fourier transform function. In this chapter, image analysis was used to analyse the size of the pores and its distribution over an area using the measure and distribution functions available in this software. Using this software the threshold of the image can be adjusted so that only the profile of the pore structure is highlighted for further analysis. As an example, figure 103(a) is the original image which will be used to analyse particles Ti. Figure 103(b) is the processed image of figure 103(a) with only the particles highlighted for further analysis using the inbuilt functions (particle distribution analysis) in the software. From this colour adjusted image, the size of the pores or particle with different level of circularity can be calculated. This simple technique has been used throughout the chapter for pore size and distribution analysis. In addition to microstructural analysis the mechanical properties were tested using a compression test and the apparent porosity was measured according to BS EN 623-2:1993 standard (refer Chapter 1 section 1.53).

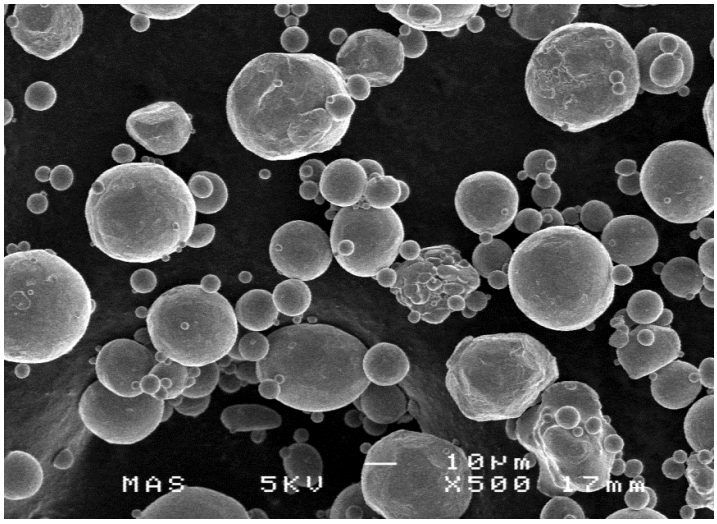

(a)

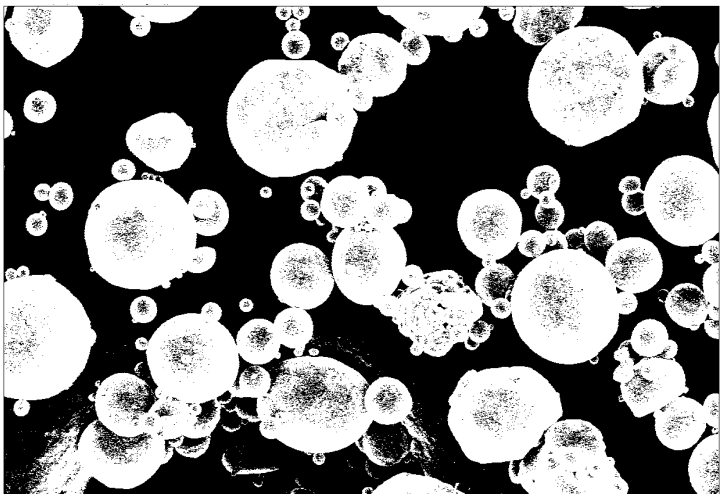

(b)

Figure 103. (a) Original image used for analysis showing Ti particles. (b) the colour threshold of the image is adjusted so that only the desired features in the image is highlighted for the size and distribution analysis using imageJ application

7.2 Material development

7.21 Material selection

The freeze casting slurry consisted of Ti_2AlC MAX-phase ceramic from Kanthal, Hallstahammar, (Sweden) as the solute. In terms of powder particle size 90% of the powder had 20µm particles and remaining was mixture of 2µm and 8µm. The solvent comprised of:

(i) Camphene ($C_{10}H_{16}$, 95% purity, Aldrich) as the freezing vehicle.
(ii) Texaphor 963 (Cognis, South Hampton, UK) with a density of 0.89-0.91g/cm^3 at 20^{o}C was used as the dispersant.
(iii) Poly(ethylene glycol) (PEG) (Sigma-Aldrich, Mn 380-420) was used as the binder.

The use of the above chemicals was adopted from Macchetta's work on "Fabrication and analysis of highly porous HA-TCP ceramic via novel freeze casting technique" [139]. Camphene was used as the freezing vehicle to avoid the need for low temperature and expensive freeze dryer equipment. Camphene is a monoterpene, which melts at 45-50^{o}C and remains solid below this temperature. Hence it solidifies at room temperature and also readily volatises at room temperature since it sublimes at ambient temperature and pressure and the gas released during this process is nontoxic and eco-friendly.

Macchetta [139] studied various binders including poly(vinyl alcohol) (PVA), poly(vinyl pyrrolidone) (PVP) and poly(ethylene glycol) (PEG). PEG was selected in this work as the binder, based on number of factors which include compatibility with the dispersant and ceramic powder, burnout features, glass transition temperature and cost. The binder is simply a long-chain polymer used to provide sufficient handling strength to the green samples by helping to hold the ceramic particles together once the camphene sublimes.

A dispersant was also used as the anti-settling agent to provide a homogeneous suspended mixture of particles in the solution by avoiding agglomeration and settling of the powder. Texaphor 963 was the dispersant used in this study which is a solution of electro-neutral salt of poly carboxylic acid with amine derivative dissolved in higher aromatics and has a density of 0.89-0.91g/cm^3 at 20^{o}C.

7.22 Material preparation

The initial chemical composition of the mixture was adopted from Macchetta et al. [81] who studied the freeze casting of HA/TCP (Hydroxyapatite/Tricalcium Phosphate) scaffolds. In their work they used 10, 20, 30vol% of solid loading mixed into solvent containing camphene. A quantity of dispersant equal to 6wt% of the ceramic powder was added to maintain a low viscosity and facilitate dendrite formation during solidification. Binder was not used in their work as the dispersant was sufficient to induce satisfactory handling strength in the green sample. However in this study, there was a need to alter the chemical composition. This is due to the higher density of the Ti_2AlC compared to the HA/TCP used by Macchetta; HA/TCP has a density between 2-3g/cm^3 [140], whereas Ti_2AlC has a density between 3.8-4.12g/cm^3 [36]. In addition the ceramic particle size of the Ti_2AlC was a mixture containing 20, 8 and 2µm with 90% of the particles with 20µm size which is different to that used by Macchetta with an average of 6µm particle size.

7.22a: Slurry preparation

In order to produce the initial slurry camphene with a 1:2wt% ratio of camphene to Ti_2AlC powder was initially melted in a conical flask by immersing in a hot water bath that was heated on a hot plate as seen in figure 104.

Figure 104. Set up used to prepare the ceramic slurry

Camphene melts at 45-50°C and the temperature of the water bath was maintained at 60°C for further mixing procedure. Ti_2AlC powder (50wt% to start with) was added to the melted camphene at 60°C, followed by the addition of the dispersant equivalent to 3wt% of the solid loading. This slurry was mixed at constant temperature of 60°C for 30 minutes using a magnetic stirrer on a hot plate as shown in figure 105. The flask was sealed with rubber cork to avoid loss of camphene during the process.

Figure 105. Slurry formed after 30 minutes of mixing

After 30 minutes of mixing at 60°C it was observed that the ceramic particle settled at the bottom of the conical flask as seen in figure 106(a).

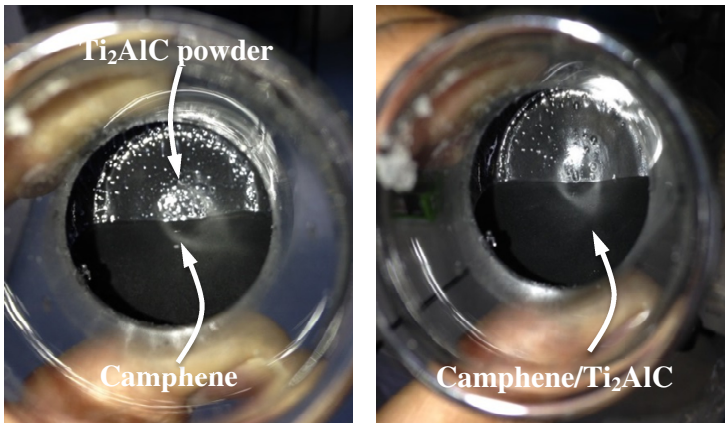

(a) **(b)**

Figure 106. (a) Ceramic particle sediment after 30 minutes of mixing due to insufficient amount of dispersant. (b) Homogenous slurry obtained after the dispersant was increased with no sedimentation (conical flask tilted approx. 45°C in this image)

The amount of dispersant was therefore increased from 3wt% to 5wt% of the solid loading and the above procedure was repeated. After 30 minutes of mixing the slurry obtained had no sedimentation and the ceramic particles were homogeneously suspended (confirmed by visual inspection) as seen in figure 106 (b).

7.22b: Sample preparation

The hot camphene based slurry was poured into the moulds (refer Appendix 1, for the design details of the mould) made of Al and PVC, as seen in figure 107, and left for 30 minutes to solidify. The solidification time was optimised by examining the freezing specimen every five minutes until it completely solidified. Two different mould materials were used to examine the effect of heat transfer rate on the pore formation which is explained in detail in section 7.33.

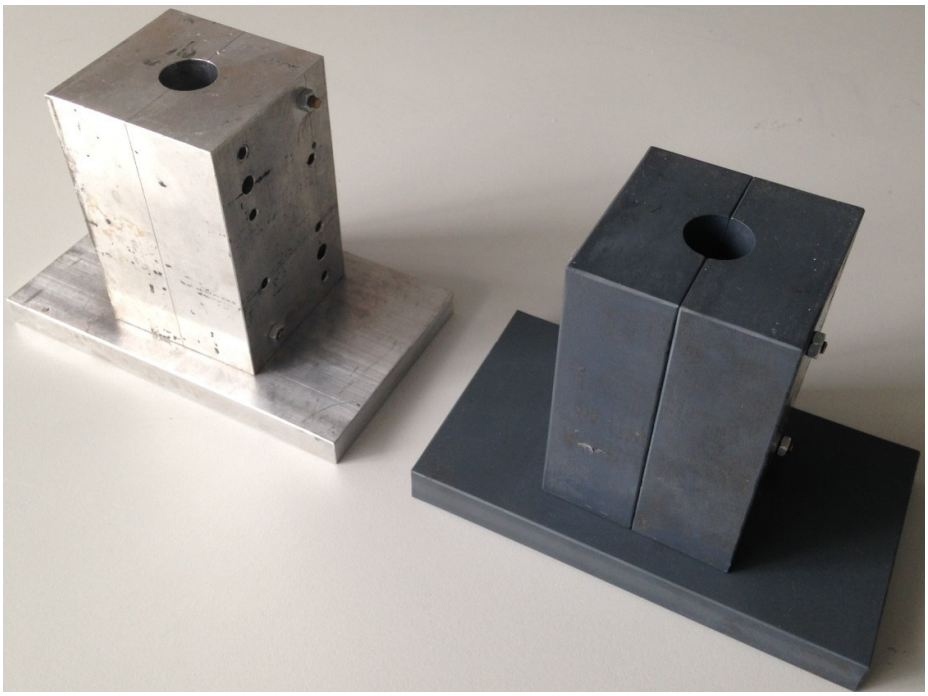

Figure 107. Moulds used in this study. Aluminium mould on the left and PVC on the right in this image (Total length of the mould 80mm with 15mm diameter)

After 30 minutes of solidification, the sample was ejected out of the mould using a wooden plunger as seen in figure 108.

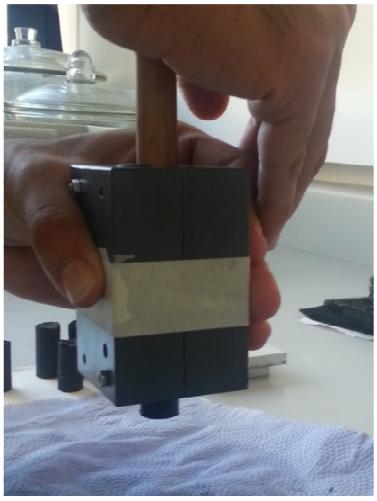

Figure 108. Ejecting the sample from the mould after solidification

The samples were left to sublime for 24 hours at atmospheric temperature and pressure. The samples prepared with this chemical composition was extremely friable after the camphene sublimed and crumbled into powder when handled (figure 109(a)).

Hence it was understood that binder was required to maintain the structural integrity of the green body after the sublimation of camphene. The above preparation procedure was repeated with an additional PEG binder (5wt% of the solid loading). As seen in figure 109(b), the samples upon sublimation collapsed but were better than the samples from the previous composition (figure 109(a)) with no binder. Further increase in binder to 10wt% of the solid loading led to the manufacture of structurally stable green samples (figure 110).

(a) **(b)**

Figure 109. Collapsed sample due to insufficient binder (a) with no binder, (b) with 3wt% binder

Figure 110. Stable green samples after sublimation of camphene (25mm long and 15mm in diameter)

A summary of the final optimised chemical compositions is shown in Table 11.

Table 11. Optimised chemical composition to fabricate freeze casted Ti_2AlC ceramic

Chemical Used	**wt% required**
Ceramic Ti_2AlC to freezing vehicle camphene ratio	1:2 wt%
Texaphor dispersant	5wt% of the ceramic content
PEG Binder	10wt% of the ceramic content

7.3 Results and discussion

7.31 Optimisation of sintering condition

The freeze cast green samples were sintered in a tube furnace at 1400^{o}C up to three hours in argon atmosphere (figure 111) using optimised densification temperature for dense Ti_2AlC ceramic which was established is previous studies explained in Chapter 5.

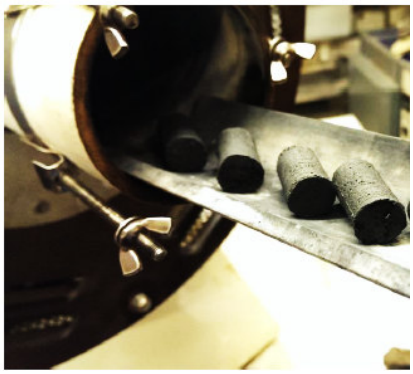

Figure 111. Green samples being loaded into the tube furnace

Since the green sample consists of a different chemical composition in terms of dispersant and binder compared to the pressed powder pellets in Chapter 5, controlled burnout of these chemicals should be accommodated in the time - temperature curve. The temperature curve in figure 112 was initially used to sinter the samples and comprises of three ramping stages. In the 1st stage the temperature was raised to 160^{o}C at 40^{o}C/hr followed by 1 hour of dwell at this temperature. This was to make sure the camphene, binder and dispersant is removed and burnt out of the sample.

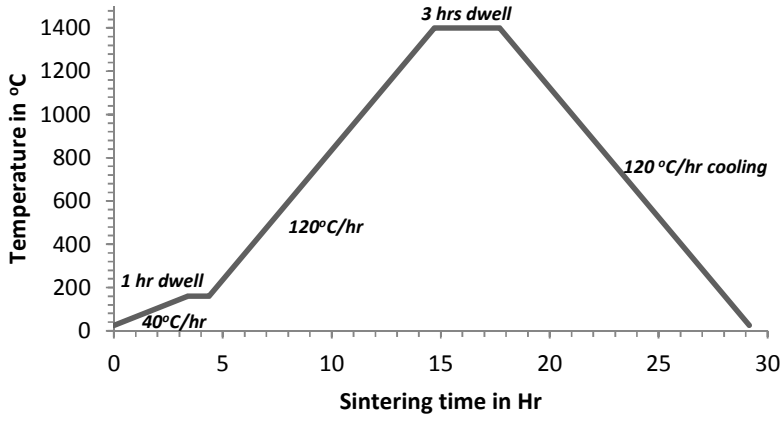

Figure 112. Initial temperature curve used to sinter the green

In the second stage the temperature is raised to 1400°C at 120°C/hr and left at this sintering temperature for 3 hours. The sample obtains its mechanical strength at this temperature due to densification (sintering) process (refer chapter 5 on optimised sintering condition). The 3rd stage involves cooling down to room temperature. However the samples obtained from this sintering curve completely melted in the alumina holder as seen in figure 113.

Figure 113. Green samples melted in the alumina holder upon sintering indicating the presence of camphene

This was thought to be due to the presence of camphene in the green sample and was confirmed by heating the green sample on a hot plate which melted at 40°C. As a result the sublimation time prior to sintering was increased to 72 hours and sintering temperature curve was slightly modified as seen in figure 114.

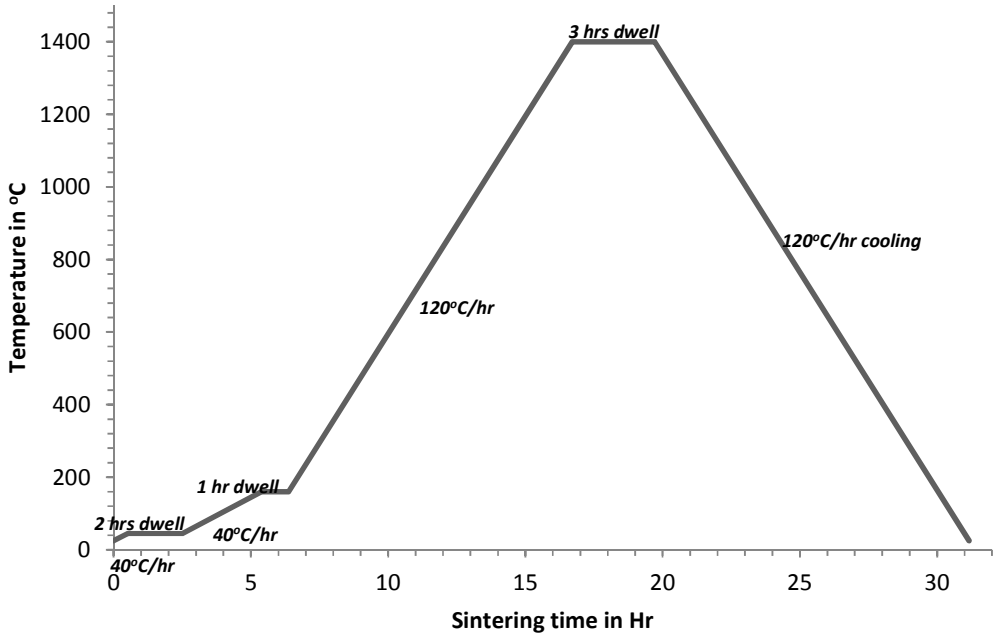

Figure 114. Optimised temperature cure to sinter micro porous Ti2AlC ceramic by freeze casting

The optimised temperature curve consists of 4 ramping stages. In the 1st stage the temperature is raised to 45°C at 40°C/hr heating rate and left for 2 hours of dwelling period. This is to ensure controlled melting of camphene if any is still present after sublimation. The 2nd stage involves raising the temperature to 160°C at 40°C/hr heating rate and left for 1 hour of dwelling period. This is to ensure that dispersant and binder is burnt-out in a controlled manner. This is followed by a densification stage and cooling similar to the initial temperature curve in figure 112. Samples obtained after sintering retained its shape and mechanically stable as seen in figure 115.

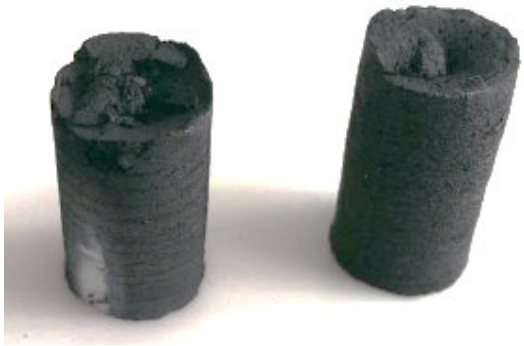

Figure 115. Samples obtained from the optimised sintering curve (25mm long and 15mm in diameter)

7.32 Study on camphene dendrite formation

7.32a Pure camphene used in this study

It is important to understand the solidification behaviour of the camphene used as it differs with the purity of camphene. Camphene used in this process is 95% pure and begins to solidify at 40°C. Upon solidification it forms dendrite type of crystal structure which is explained in detail in Chapter 2, Section 2.52. The direction of the dendrite growth can be controlled by introducing a temperature gradient and grows parallel but in opposite direction of the temperature gradient applied. The dendrite grows from a cold region and proceeds towards hotter region with the dendritic arms branching outwards [81, 141].

The solidification behaviour of the camphene was monitored using an optical microscope. A small drop of molten camphene was placed on one end of a glass slide and covered with a cover slip to avoid contamination of the heating stage used. The camphene end of the glass slide was introduced into a programmable heating stage with

the other end of the glass slide exposed to atmosphere at room temperature to create a temperature gradient. The heating stage was programmed to raise the temperature to 50^{o}C at 10^{o}C/min to melt the camphene and cooled down to room temperature at 2.5^{o}C/min. Figure 116 (a-f) shows the optical images of the dendrite structured formed by pure camphene used in this study. As seen in figure 116(f), pure camphene tends to form a dendritic structure upon solidification. The direction of solidification could be controlled by introducing a temperature gradient and grows from cold to hot region as seen in figure 116(c) and 116(d) showing highly oriented dendrite structure. The shape and size of the dendrite are non-uniform as seen in figure 116(f), and this gives the gradient porosity feature in the material. Figure 117, is the graph showing the size of the dendrites formed versus its area. It is evident that size of the dendrites fall under 150µm but majority of them are below 50µm with the total area below 500µm. The pore size and the area was analysed using imageJ application explained in section 7.1, which is commonly used in this application.

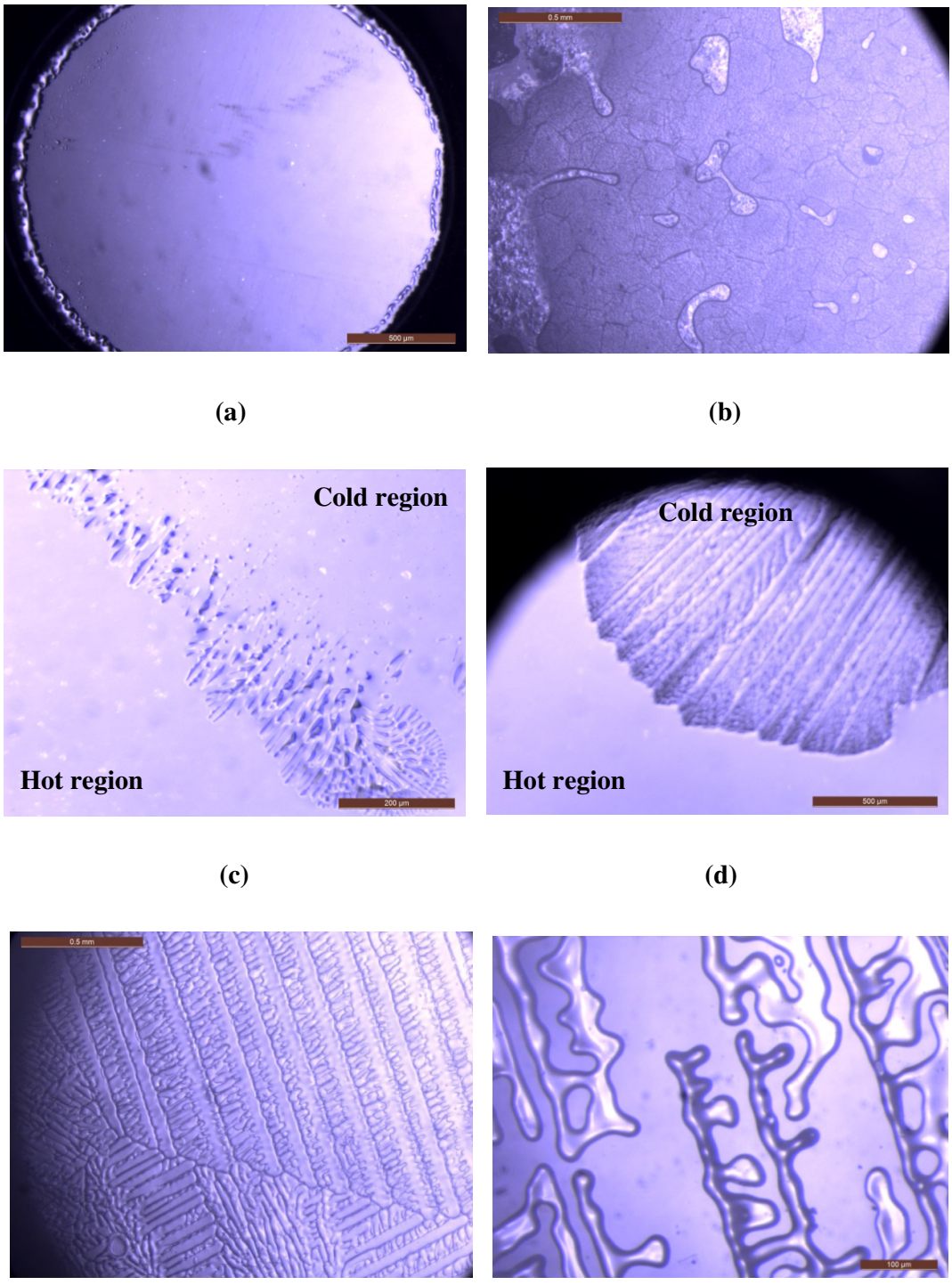

Figure 116. Optical micrograph images of camphene solidification (a) molten camphene at 50°C, (b) initiation of the dendrite at 43°C, (c) , (d) propagation of the dendrite as a result of temperature gradient, (e) highly oriented dendrite showing the primary dendrite and secondary dendrite, (f) magnified dendrite structure at 35°C upon cooling

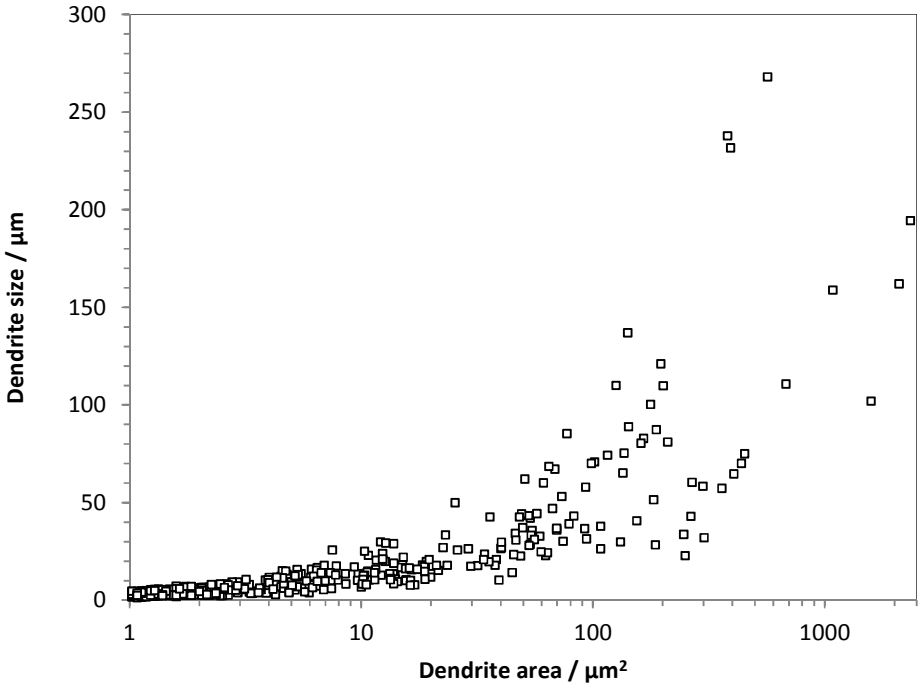

Figure 117. Graph showing the area of the pure camphene dendrite versus size of the dendrite formed upon solidification

7.32b Ti_2AlC ceramic in camphene

This optical microscopy study was conducted to observe the solidification behaviour of Ti_2AlC ceramic in camphene. For this work a 1:8wt% ratio of camphene to ceramic slurry was prepared with 5wt% and 10wt% equivalent of dispersant and binder respectively. A low concentration of ceramic was used to make the slurry translucent so that the light from the optical microscope can pass through the slide and provide a better microscope image for further analysis. A drop of this slurry was sandwiched between one end of the glass slide and cover slip. This end was introduced into the heating stage and programmed to raise the temperature to 50^{o}C at 10^{o}C/min to melt the camphene and the sample was then cooled down to room temperature at 2.5^{o}C/min.

As can be seen in figure 118, the upon solidification of the camphene there is no dendrite formation structure as seen in figure 116(f) for pure camphene, but it is more similar to a web structure enclosing the ceramic particles (observe the black in colour in the figure 118a, b, c) between the solidified camphene structure. In addition this solidified structure is finer at one end (left side of figure 118(a)) and fans out into larger circular structures (right side of figure 118(b)). It was observed that fine solid camphene dendrites were formed at the cooler end of the glass slide and a larger microstructure towards the hotter end. From this study it was evident that the pore channels are not likely to be dendritic in structure but will be more like an interconnected web (figure 118(c)) when the ceramic and other chemical aids are introduced. For high surface area applications the formation of large number of interconnected pores is beneficial.

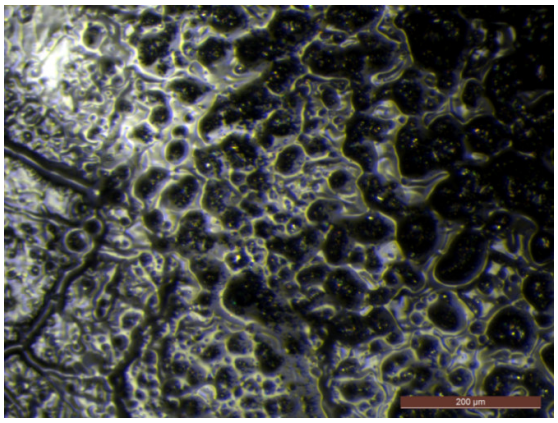

(a)

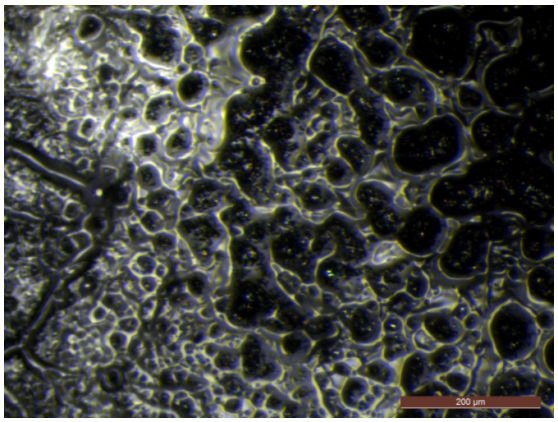

(b)

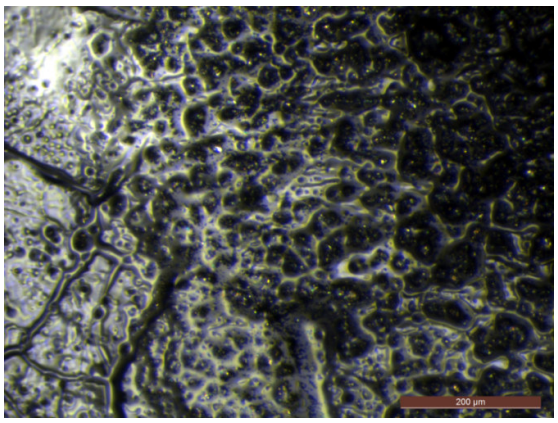

(c)

Figure 118. Camphene dendrite formed in the slurry composed of ceramic (1/8th wt% of the camphene), 5wt% dispersant and 10wt% binder. (a) solidification of the slurry, (b) propagation of the dendrite pushing the ceramic particle, (c) final solidified camphene structure formed in the slurry

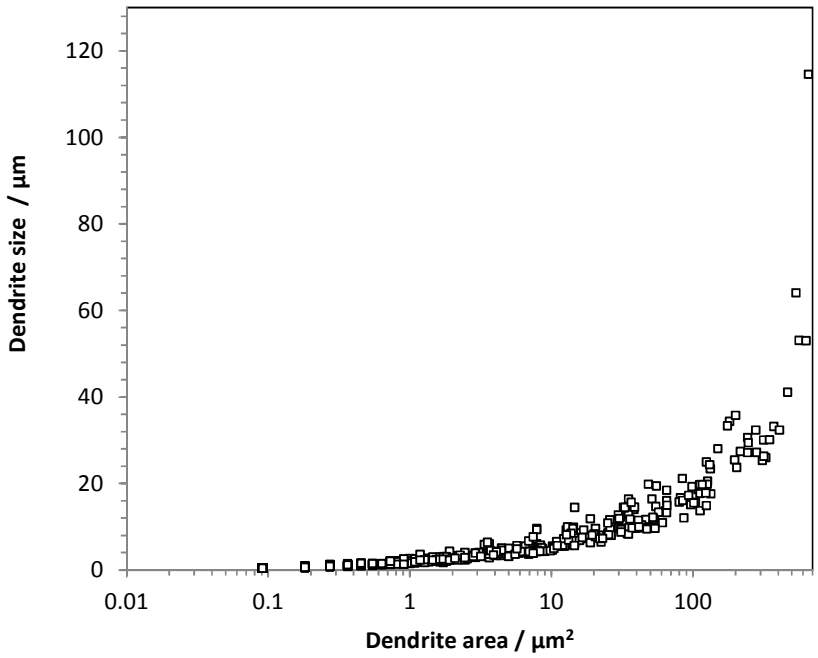

Figure 119. Graph showing the area of the camphene dendrite versus size of the dendrite formed upon solidification when ceramic, binder and dispersant is used

Figure 119 shows a graph showing the size of the dendrites formed versus the area of the dendrite when the ceramic and other chemical aids are introduced. It is evident that size of the dendrites fall below 100µm but majority of them are below 50µm with the total area below 500µm. This means that we can expect a pore size up to 100µm and an average area of the pore below 500µm in the ceramic material. However the size and area of the pores can vary with the percentage of solid loading and also the temperature gradient introduced in the mould system. The next section will explain in detail on the study conducted to observe, how the temperature gradient varies in the two mould materials (aluminium and PVC) with solidification.

7.33 Variation in temperature gradient with mould material

As discussed in Section 7.22, aluminium and PVC material were used in the construction of the moulds for casting to understand how the temperature gradient varied in both the moulds upon solidification and in turn affect the pore size and pore formation. As seen in figure 120, the moulds were wired with K-type thermocouple at three different internal sections. The thermocouple at internal lower section was in direct contact with the slurry. The thermocouple at internal mid-section was slightly above the slurry and the thermocouple at the mould opening was at room temperature. This can be used to examine the temperature gradient developed from lower mould section to the mould opening. All the six thermocouples (three in Al mould and three in PVC mould) were connected to a data-logger and the change in temperatures across the thermocouple end was monitored.

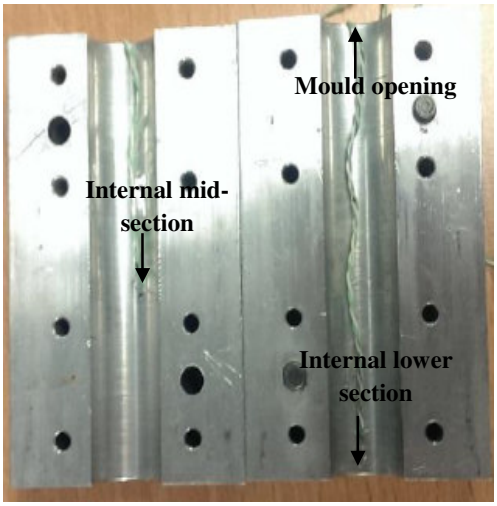

(a)

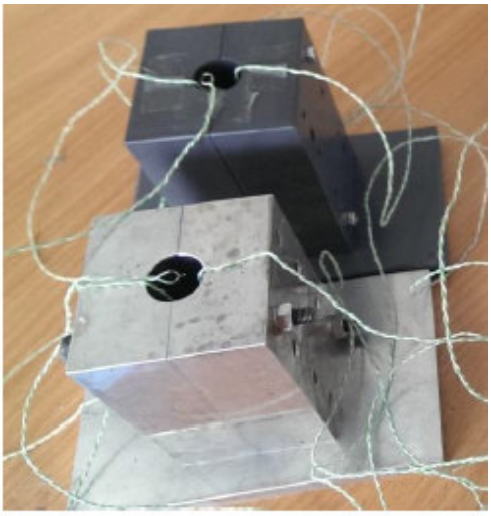

(b)

Figure 120. (a) Thermocouples connected to the internal mould slot, (b)both the moulds ready with the thermocouple connections (mould length 80mm with 15mm internal diameter)

Slurry of 50wt% solid loading and a composition based on the optimised values (see Table 11) was prepared at 60^{o}C. This slurry was poured into both the moulds connected to the data-logger (figure 121) and the temperature variation over the solidification period was monitored.

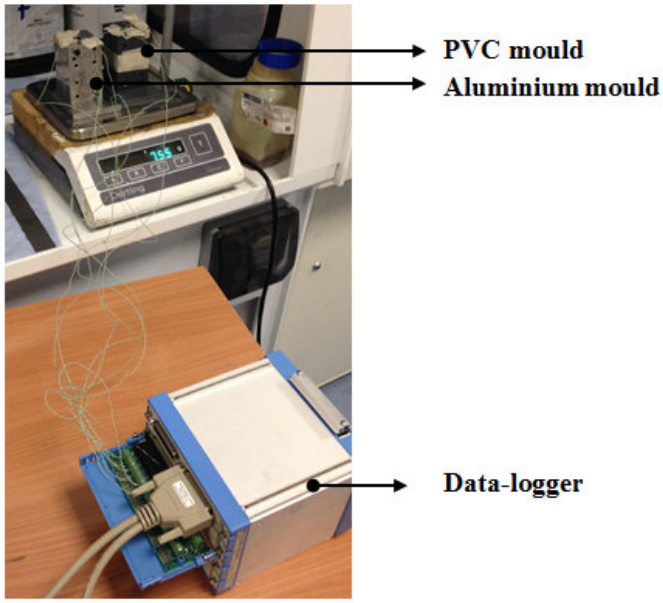

Figure 121. Setup ready for solidification temperature monitoring

The temperature variation during solidification was monitored for 30 minutes as this is the optimised solidification time determined in section 7.22b. From figure 122(a) and 122(d), it is clear that the aluminium mould has a higher heat transfer rate as the slurry cooled down to room temperature within one minute. However, for the PVC mould it took approximately 20minutes to cool down to room temperature (refer figure 122(d)). The higher cooling rate of the aluminium mould has the potential to induce a higher degree of super cooling. According to the free dendrite model framed by Divenuti [104], a higher heat transfer rate results in finer pore structure and the region experiencing lower cooling rate will have larger pores [105]. As a result, we can expect finer pores throughout the samples cast in the aluminium mould as the slurry cools down to room temperature within a minute (122(a), 122(b), 122(c)). For the samples cooled in the PVC mould, we can expect larger pores in the region experiencing slower cooling rates (i.e figure 122(d) towards the lower section of the mould), and finer pores towards the opening of the mould as it experiences lower temperature (figure 122(f)) as majority of the heat exchange takes place through the opening of the mould.

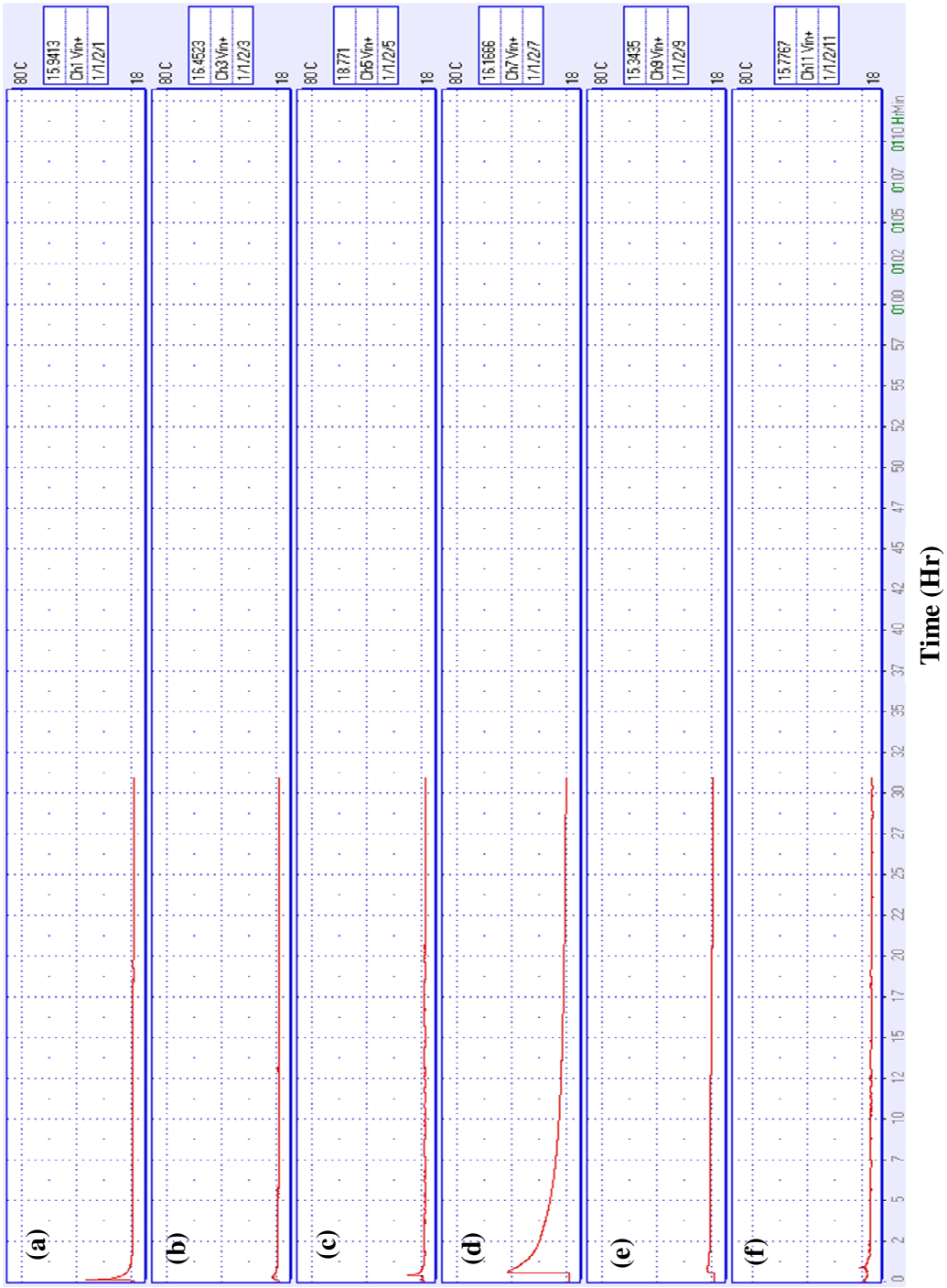

Figure 122. Graph showing temperature variation during solidification of the slurry in both the moulds. (a) temperature reading at the lower section of Al mould as seen in fig 125a, (b) temperature reading at the mid-section of the Al mould as seen in fig 125a, (c) temperature reading at the opening of the Al mould as seen in fig 125a, (d) temperature reading at the lower section of PVC mould as seen in fig 125a, (e) temperature reading at the mid-section of the PVC mould as seen in fig 125a, (c) temperature reading at the opening of the PVC mould as seen in fig 125a

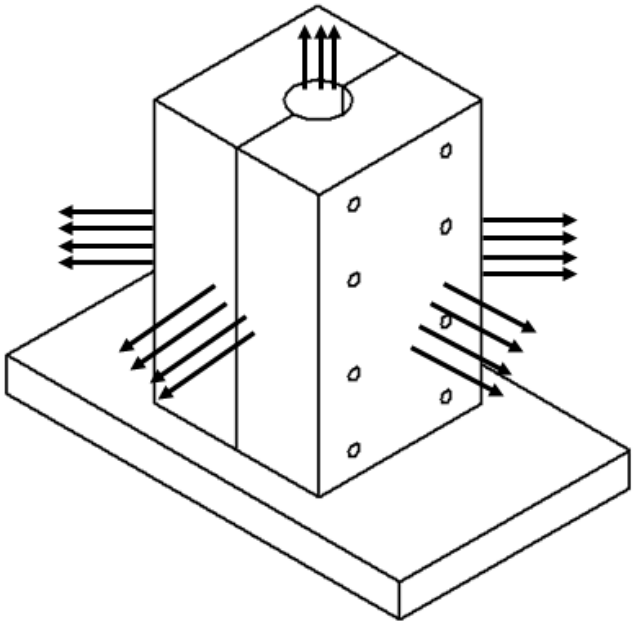

(a)

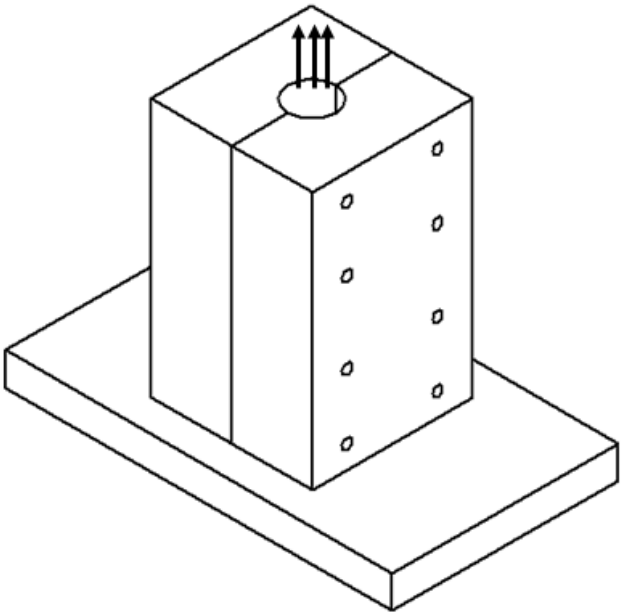

(b)

Figure 123. Schematic representation of heat exchange in (a) aluminium mould and (b) PVC mould with arrows representing the transfer of heat from the system

It can be seen in figure 123(a), in aluminium mould, the heat from the slurry is dissipated to the atmosphere from all the direction. Hence the sample experiences rapid cooling as seen by the sudden drop of temperature in figure 122(a). However, in the PVC mould, figure 123(b), majority of the heat from the slurry is dissipated to the atmosphere through the mould opening since PVC is a good thermal insulator. Hence there is a delay in solidification time; approximately 20 minutes to attain room temperature as seen in figure 122(d). Therefore we can expect more gradient pores in the samples casted in PVC mould than in the Al mould which is explained in the next section.

7.34 Effect of solid loading on porosity, pore size and pore distribution

A study on effect of solid loading on the porosity of the final sintered sample was conducted at 40wt%, 50wt%, 60wt% , 70wt% and 80wt% keeping all the other chemical composition as same as the optimised composition (Table 11, Section 7.22). Other conditions such as room temperature (18 – 22^{o}C), solidification time (30 minutes) and sublimation time (72 hours) were kept constant. Samples (dimensions shown in figure 124) were prepared in both the aluminium and PVC moulds and the porosity and compressive strength of the sintered material was examined. The samples were sintered according to the optimised sintering temperature curve as seen in figure 114.

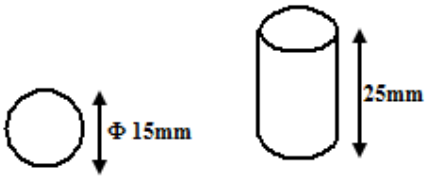

Figure 124. Dimension of the samples prepared for analysis

Samples cast with 40wt% solid loading failed to retain its shape after sintering, the reason being lack of particle integrity due to insufficient ceramic particle throughout the volume of the sample. This was overcome at further solid loadings mention above. Samples with 80wt% solid loading were difficult to prepare as slurry was over saturated due to suspended ceramic particles. Therefore the results discussed below are on the samples freeze cast with 50, 60 and 70wt% solid loading in Al and PVC moulds.

7.34a Porosity measurement

Apparent porosity was measured according to BS EN 623-2:1993 standard discussed in Chapter 1, section 1.53. A minimum of six samples were used for all the following measurements.

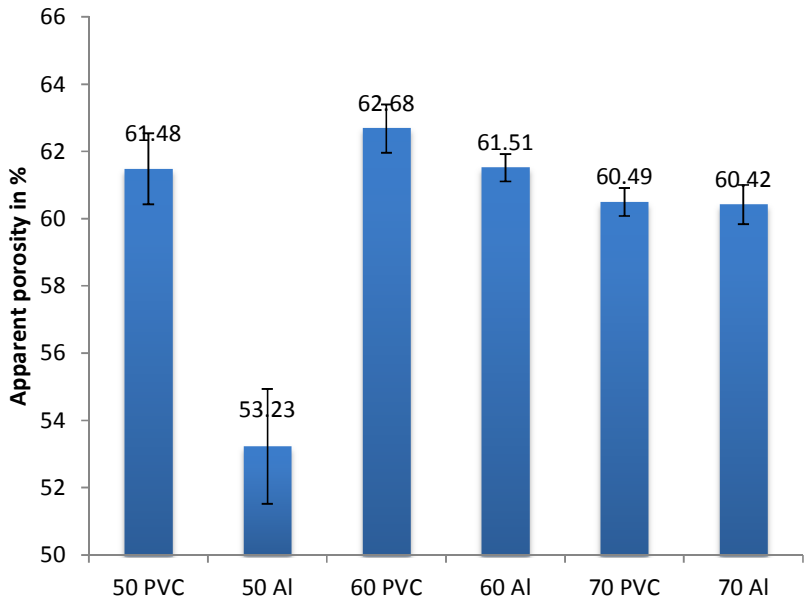

Figure 125. Porosity in % for various solid loadings prepared in Al (aluminium) mould and PVC (poly vinyl chloride) mould

As seen in figure 125, the porosity percent is almost the same in all the samples. However it can be observed that samples prepared in PVC mould are slightly more porous than the samples prepared in the Al mould. The reason is due to the low cooling rate associated with the PVC mould as discussed in section 7.33, results in pores with larger pore size. Koch et al. [105] in his work on freeze casting alumina found that larger pores were produced in the material region which experienced low cooling rate.

It would be expected that the porosity should decrease with an increase in solid loading. We observe similar porosity for 50-70wt% solids loading because the solid loading was measured in weight percent. When the solid loading of 50, 60 and 70wt% is converted to volume percent (vol%), it relates to 55.6, 57.1 and 58.3vol% respectively. As stated earlier weight (and volume) fractions cannot be produced outside the range since at

lower solid loading the materials is not structurally stable on sublimation of camphene and at high loading the slurry in not suitable. Hence there is only a small variation in the volume of ceramic is possible. Therefore from this study it is possible to fabricate gradient porous Ti_2AlC ceramic with a porosity level of approximately 60%.

6.34b Effect on compressive strength

The sintered samples cast in aluminium and PVC moulds with 50, 60 and 70wt% of the solid loading were subjected to uniform compressive load until the maximum failure load. The cross-sectional area of the samples were measured individually and the compressive strength was calculated for 6 -7 samples in each batch. The cross head with the load cell was programmed to move at a constant speed of 2mm/minute. Figure 126 shows how sample was loaded into the testing machine.

Figure 126. Compression test set-up

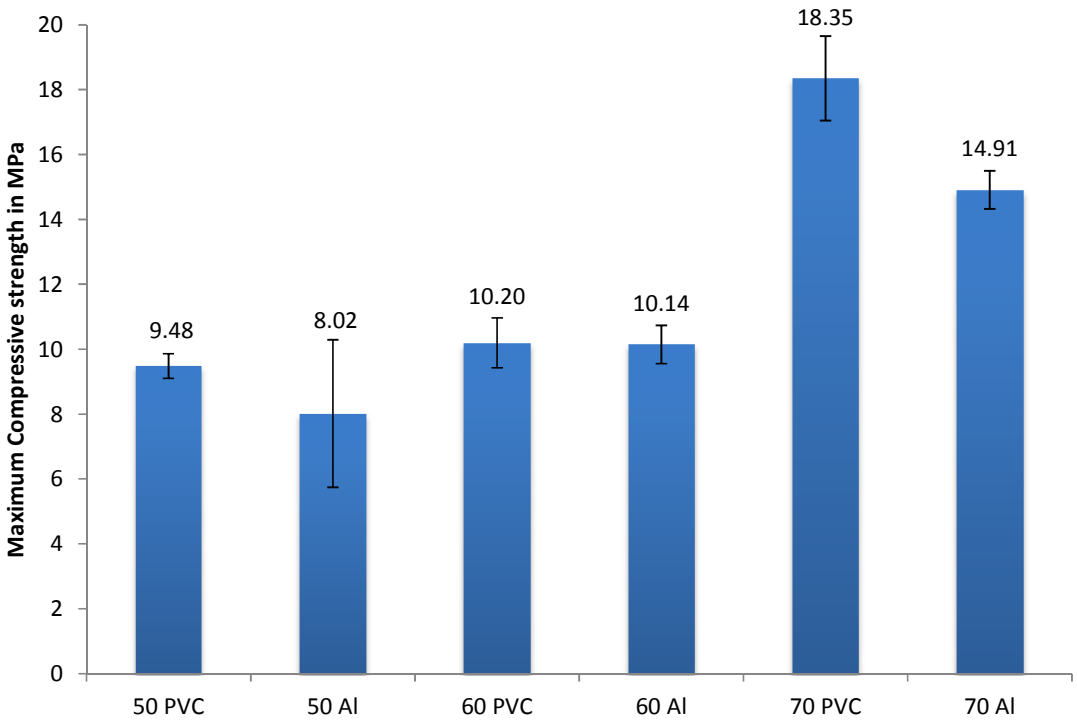

Figure 127. Compression test data conducted on samples casted in Al (aluminium) mould and PVC (poly vinyl chloride) mould with varying solid loading

Figure 127, is the graph showing compressive strength with varying solid loading. There is a small increase in compressive strength with an increase in solid loading. This is due to the increase in the amount of ceramic material. However when the samples of same solid loading but cast in different moulds are compared, the compressive strength is almost the same, because they have similar apparent porosity percent. In addition sample cast in PVC have slightly higher compressive strength when compared to the samples casted in Al mould with the same solid loading. This is due to the directional heat exchange during cooling process as explained in section 7.33 (refer figure 123(b)) which results in aligned pores, increasing the compressive strength.

7.34c Effect of solid loading on pore size and pore distribution

Samples cast in aluminium and PVC moulds with 50, 60 and 70wt% solid loading were sectioned as seen in figure 128. Section A-A is the longitudinal cross-section and section B-B is the transverse cross-section of the sample. SEM was used to analyse the pore morphology and later imageJ application was used to calculate the pore area and pore size as explained in section 7.1. Samples were analysed across the cross-section from top to bottom in the case of longitudinal section and left to right in the case of transverse section and SEM images where taken along this direction as seen in figure 128.

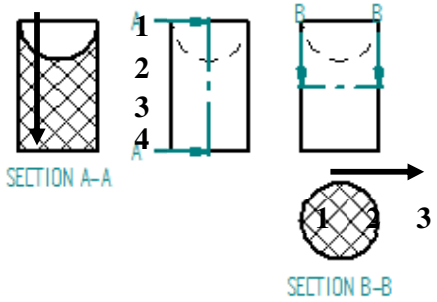

Figure 128. Section view of the samples used for SEM analysis with arrow along the section representing direction of scan and numbers representing region of scan

(**i**) Image analysis of 50wt% solid loaded samples cast in Al mould

Longitudinal cross-section

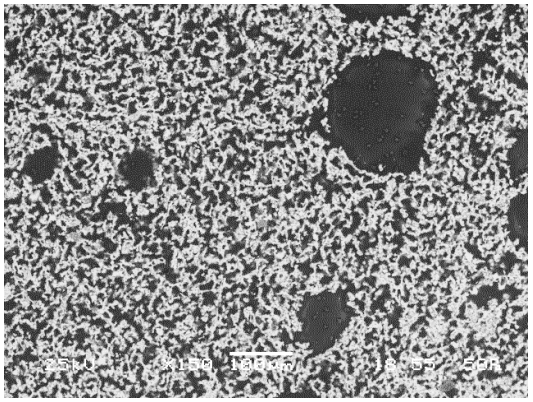

(Region 1 of section A-A)

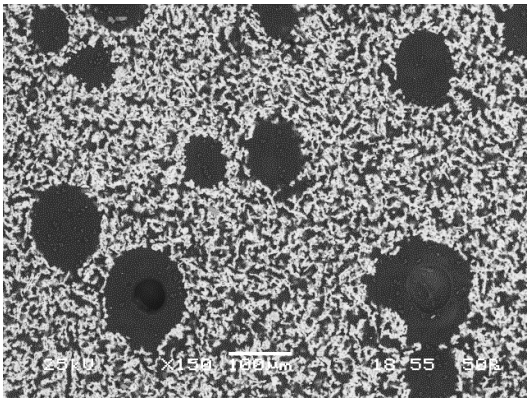

(Region 2 of section A-A)

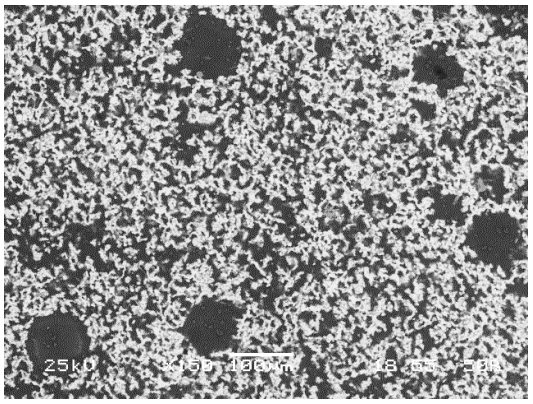

(Region 3 of section A-A)

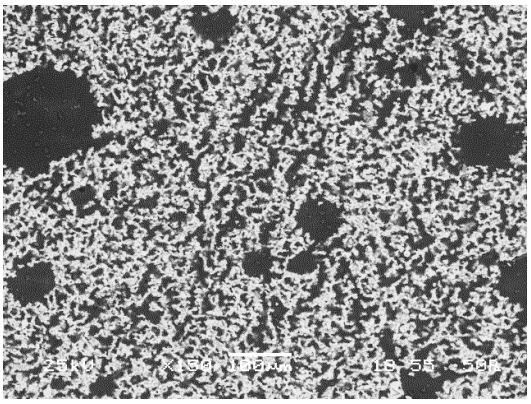

(Region 4 of section A-A)

Figure 129. SEM images of 50wt% solid loaded samples cast in Al mould scanned across the longitudinal cross-section A-A

Figure 129, is the SEM images of the sample cast in Al mould with 50wt% solid loading, scanned along the longitudinal cross-section at regions 1, 2, 3 and 4 as seen in figure 128 (stage was moved approx. 6mm for the consecutive scans). The sample has many pore structures of different shape and size with no specific orientation or pattern in pore formation as expected when camphene is used as a freezing agent.

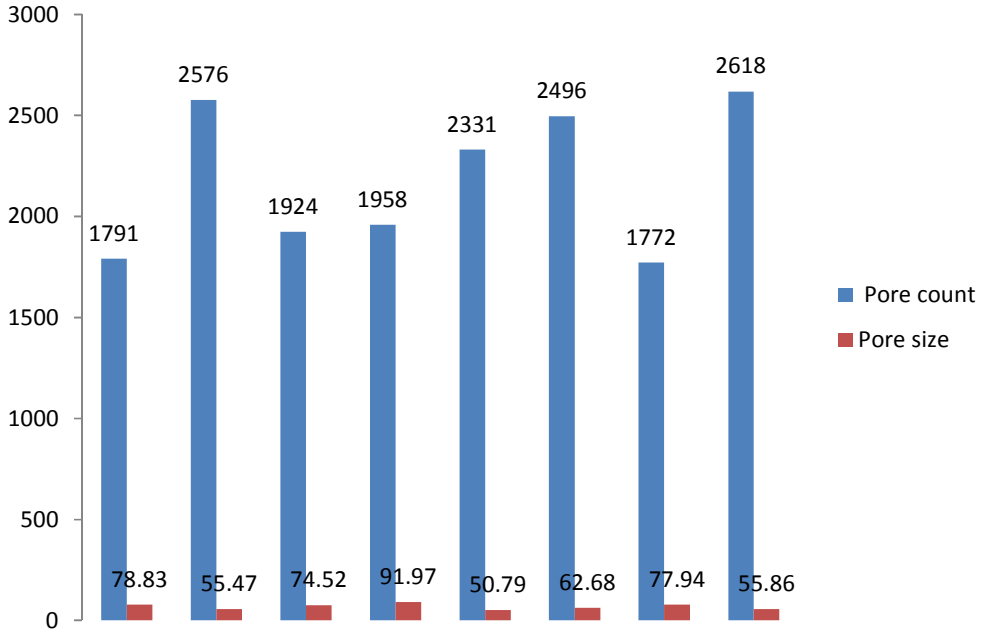

Figure 130. Graph showing the average pore size distribution in µm and number of respective pores in 50wt% solid loaded sample cast in Al mould along the longitudinal cross-section

Figure 130 shows the approximate estimate of the pore size and number of pores of that size formed in the 50wt% solid loaded sample cast in Al mould along the longitudinal cross-section respectively. As seen in the figure 130, it is evident that the pore sizes range from 50 - 80µm with majority of the pore in the size of 55-56µm (refer graph in figure 130).

Transverse cross-section

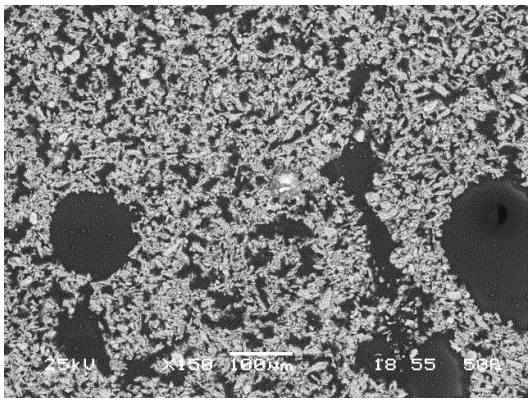

(Region 1 of section B-B)

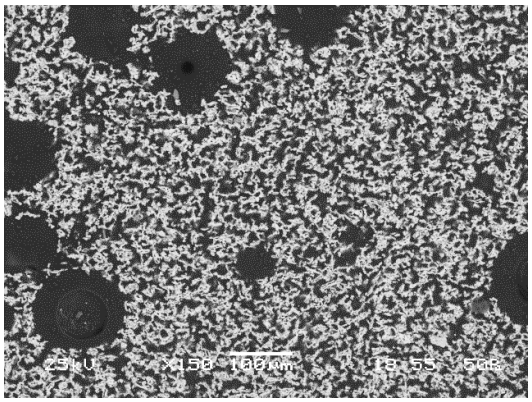

(Region 2 of section B-B)

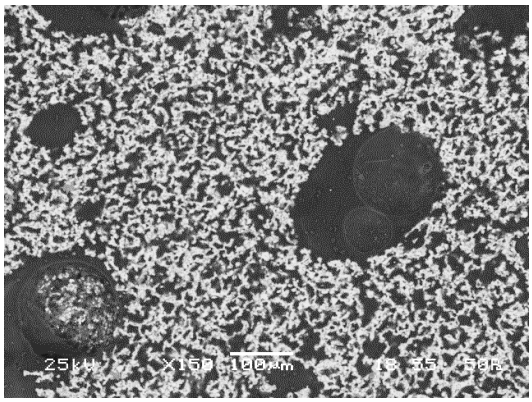

(Region 3 of section B-B)

Figure 131. SEM images of 50wt% solid loaded samples cast in Al mould scanned across the transverse cross-section B-B

Figure 131, is the SEM images of the sample cast in an Al mould with 50wt% solid loading, scanned along the transverse cross-section at regions 1, 2, and 3 (stage was moved approx. 4mm for the consecutive) scans as seen in figure 128. The images look similar to the ones seen in figure 129. It should be noted that the pores seen in above images can be the edge of the pores growing in longitudinal direction as seen in figure 129, as such there can be smaller pores along this plane when compared to the pore size in longitudinal plane. Nevertheless, in this plane we do not observe any pattern in the pore formation or directional growth of the camphene dendrite as camphene fails to form dendritic structure which was also observed in the hot stage microscopy observations in section 7.32.

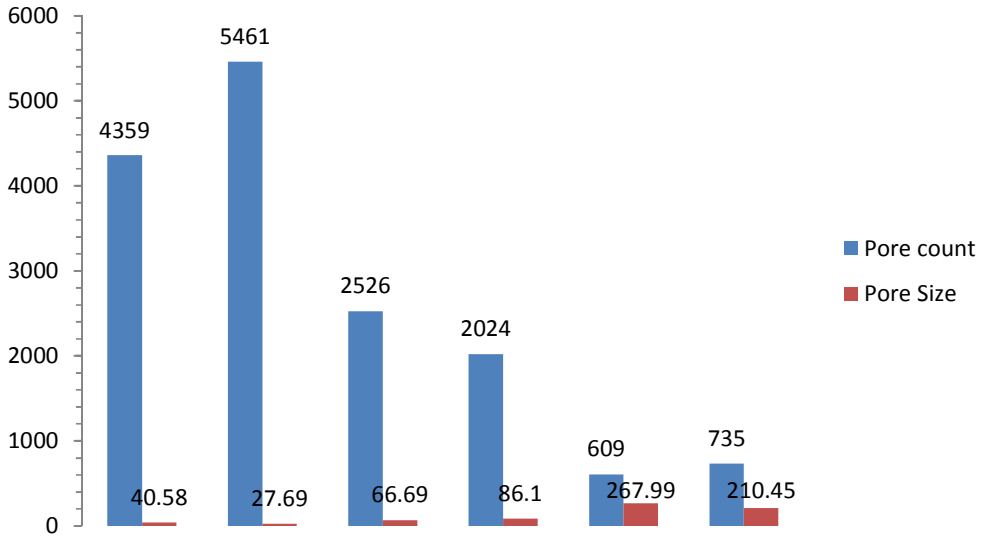

Figure 132. Graph showing the average pore size distribution in µm and number of respective pores in 50wt% solid loaded sample cast in Al mould along the transverse cross-section

Figure 132 shows the approximate estimate of the pore size and number of pores of that size formed in the 50wt% solid loaded sample cast in an Al mould along the transverse cross-section respectively. As seen in the figure 130, there is a large variation in the pore size ranging from 27- 268µm and some of these pores are the edge of the pores growing in longitudinal direction. The majority of the pores formed in this region are between 27 – 86µm (refer graph in figure 132).

(ii) Image analysis of 50wt% solid loaded samples cast in PVC mould

Longitudinal cross section

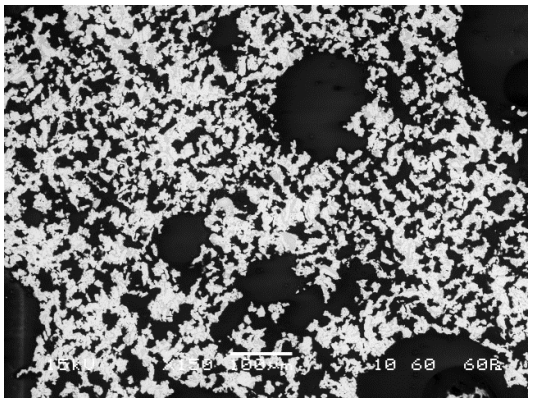

(Region 1 of section A-A)

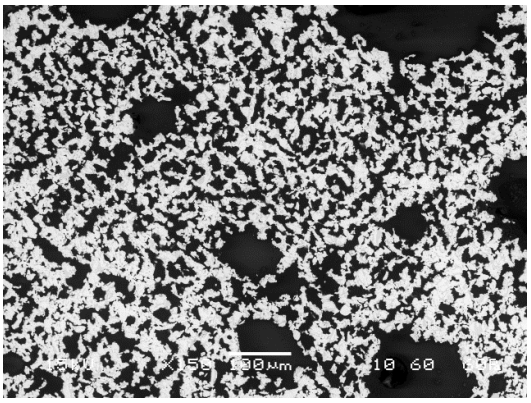

(Region 2 of section A-A)

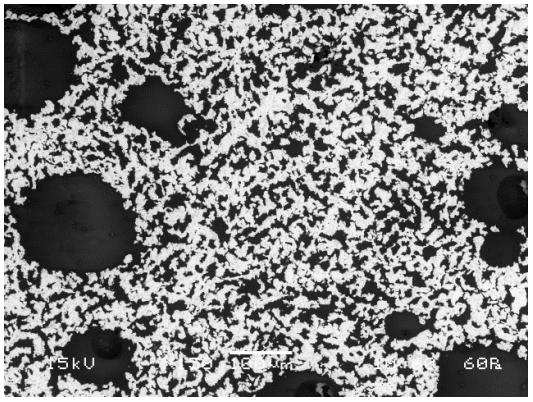

(Region 3 of section A-A)

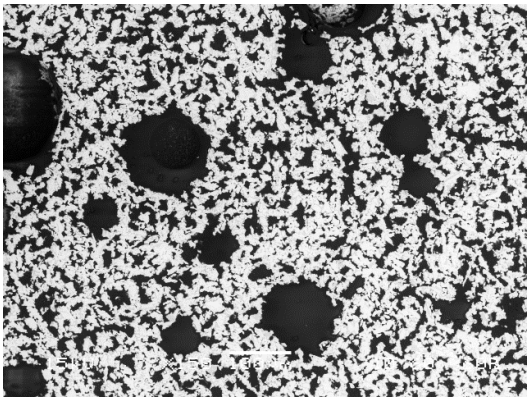

(Region 4 of section A-A)

Figure 133. SEM images of 50wt% solid loaded samples cast in PVC mould scanned across the longitudinal cross-section A-A

Figure 133, is the SEM images of the sample cast in PVC mould with 50wt% solid loading, scanned along the longitudinal cross-section at regions 1, 2, 3 and 4 (stage was moved approx. 6mm for the consecutive scans) as seen in figure 128. The pore morphology looks very similar to the structures seen in figure 129 and 131, however the pore size is slightly larger which is confirmed in the graph shown in figure 134. This is due to the slow cooling effect which takes place in the PVC mould as explained in section 7.33 and observed in figure 122(d). Again, in this sample the pores are not oriented or distributed in any pattern.

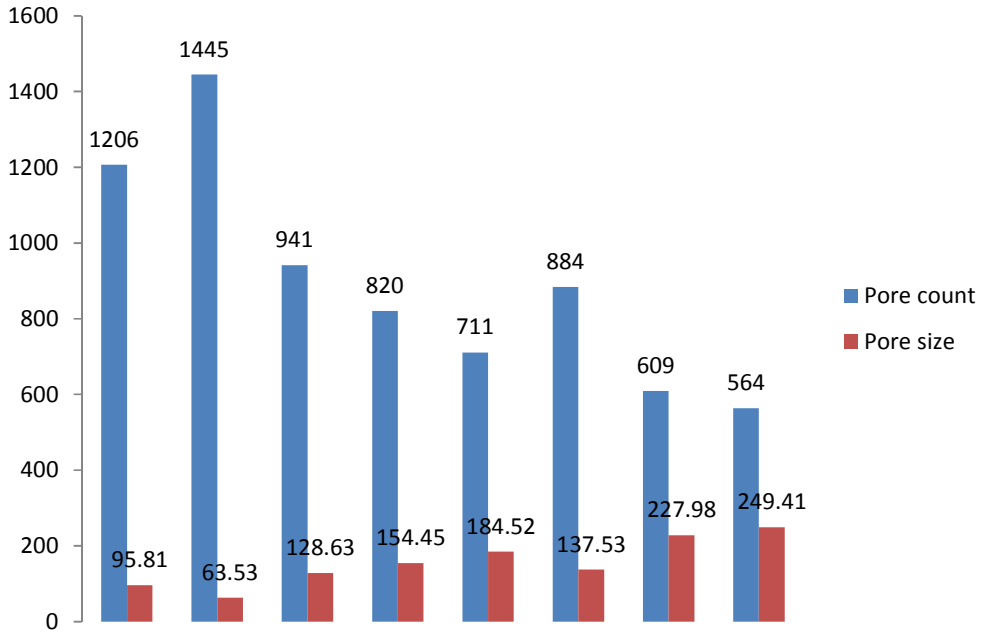

Figure 134. Graph showing the average pore size distribution in µm and number of respective pores in 50wt% solid loaded sample cast in PVC mould along the longitudinal cross-section

Figure 134 shows the approximate estimate of the pore size and number of pores of that size formed in 50wt% solid loaded sample cast in PVC mould along the longitudinal cross-section respectively. As seen in the figure 139, the pore size range from 63-250µm which is bigger than the pores formed in Al mould along this cross-section which ranges from 50 - 80µm (figure 130) with majority of the pore in the size of 63-138µm (refer graph in figure 134). Larger pores are formed due to the slow cooling upon solidification.

Transverse cross-section

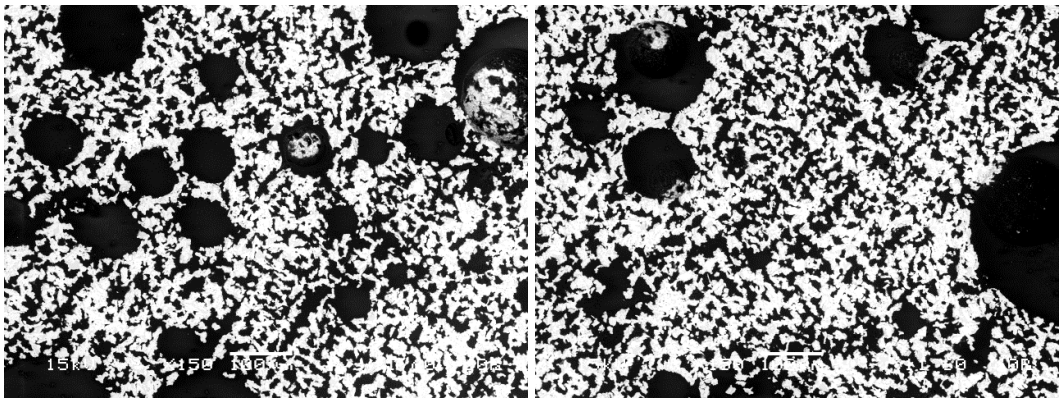

(Region 1 of section B-B) **(Region 2 of section B-B)**

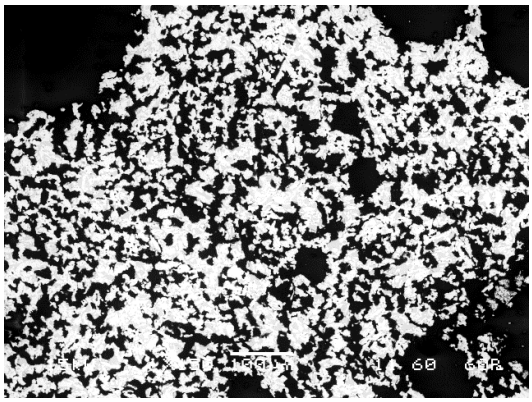

(Region 3 of section B-B)

Figure 135. SEM images of 50wt% solid loaded samples cast in PVC mould scanned across the transverse cross-section B-B

Figure 135, is the SEM images of the sample cast in a PVC mould with 50wt% solid loading, scanned along the transverse cross-section at regions 1, 2, and 3 (stage was moved approx. 4mm for the consecutive scans) as seen in figure 128. The pore structure looks similar to the ones seen in the above SEM images. In this cross-sectional plane, some of the pores can be the edge of the pore formed along the longitudinal direction of the sample so that there can be smaller pores along this plane when compared to the pore size in longitudinal plane (figure 133).

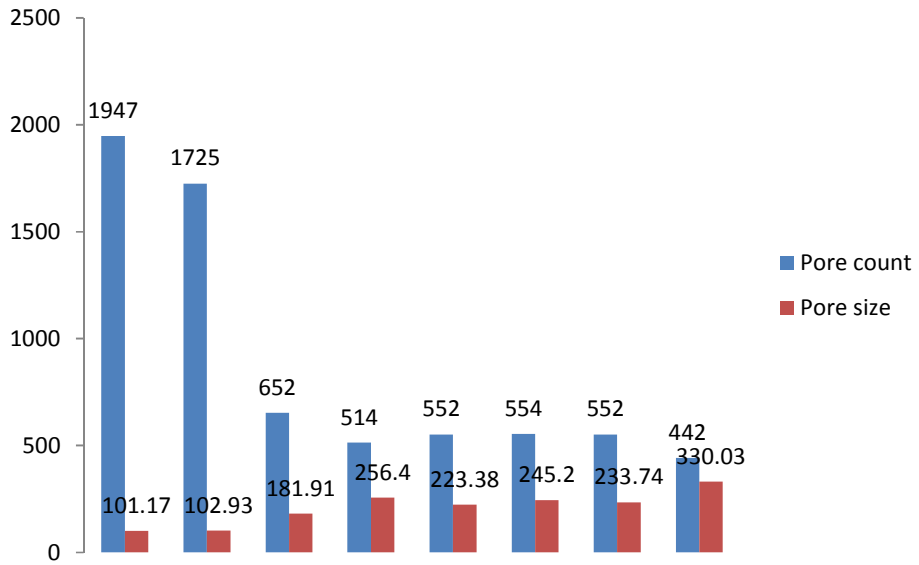

Figure 136. Graph showing the average pore size distribution in µm and number of respective pores in 50wt% solid loaded sample cast in PVC mould along the transverse cross-section

Figure 136 shows the approximate estimate of the pore size and number of pores of that size formed in the 50wt% solid loaded sample cast in PVC mould along the transverse cross-section respectively. The pore size distribution is between 180-330µm which is large compared the pore formed in sample cast in an aluminium mould across the same sectional plane as seen in the figure 132 which is between 27- 268µm due to slow cooling upon solidification. The majority of the pores are of the size 100µm (refer figure 136). Hence it is clear that the use of a thermally conductivity aluminium mould enhances the growth of finer pores and the PVC mould enhances the growth of bigger pores.

(iii) Image analysis of 60wt%, 70wt% solid loaded samples cast in Al mould

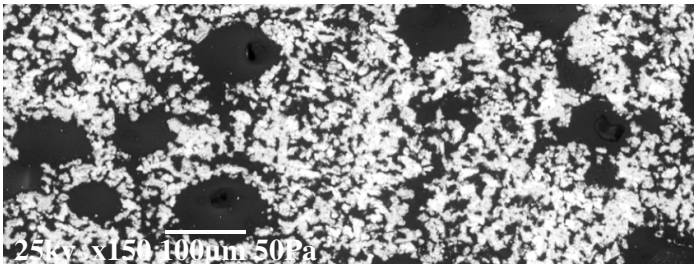

(a)

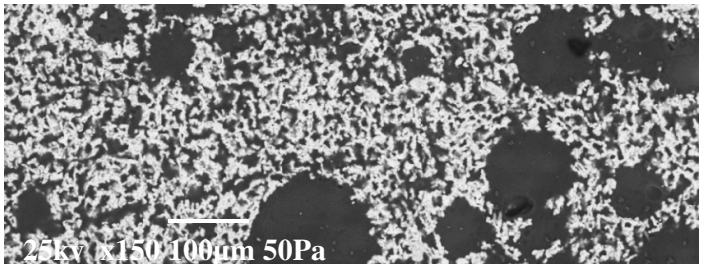

(b)

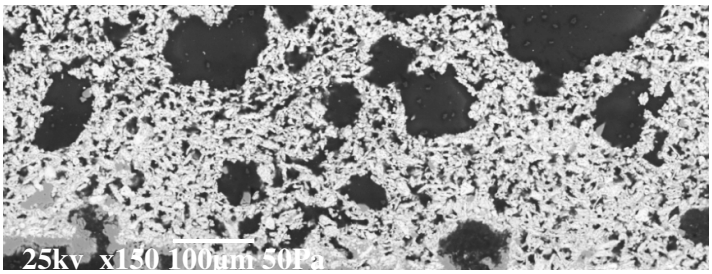

(c)

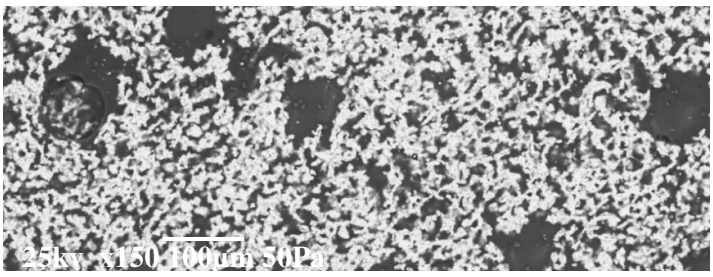

(d)

Figure 137. SEM images of (a) 60wt% (b) 70wt% solid loaded samples cast in Al mould scanned across the longitudinal cross-section A-A and (c) 60wt%, (d) 70wt% 70wt% solid loaded samples cast in Al mould scanned across the transverse cross-section B-B

Figure 137(a) and 137(b) is the SEM images of the 60wt% and 70wt% solid loaded sample cast in an Al mould respectively scanned across the section A-A (refer figure 128). Figure 137(c) and 137(d) are the SEM images of the 60wt% and 70wt% solid loaded sample cast in Al mould respectively scanned across the section B-B (refer figure 128). Images scanned across region 1, 2, 3 and 4 (stage was moved approx. 6mm for the consecutive scans) across the longitudinal plane of the sample (refer figure 128) were stitched together to obtain the above images seen in figure 137(a) and 137(b). Figure 137(c) and 137(d) are the images obtained by stitching the images taken in the region 1, 2 and 3 (stage was moved approx. 4mm for the consecutive scans) across section B-B (refer figure 128). As will the SEM images (figure 129, 131, 133 and 135) the pore structure is similar with no signs of directional pore growth. The possible changes in the pore size and distribution are explained below.

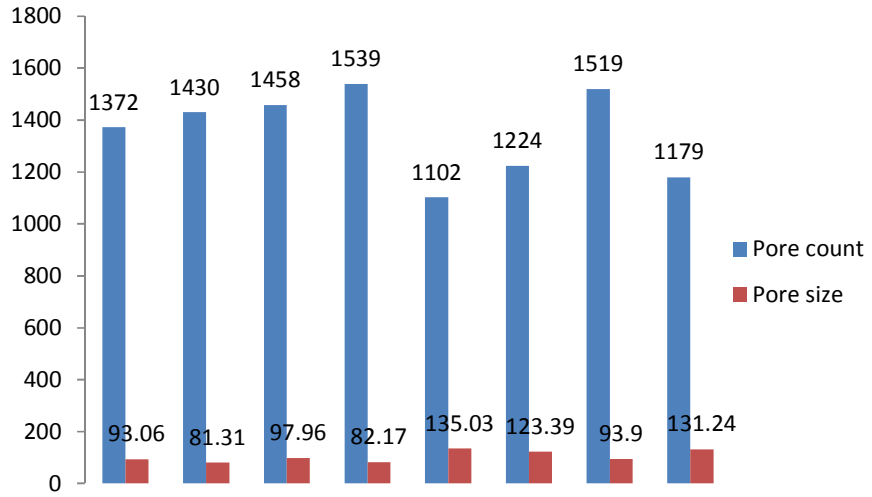

(a)

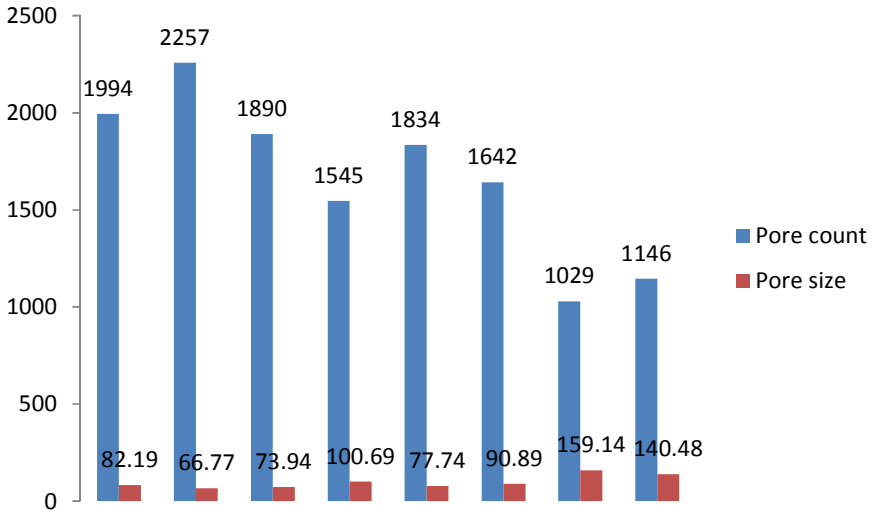

(b)

Figure 138. Graph showing the average pore size distribution in µm and number of respective pores in (a) 60wt% (b) 70wt% solid loaded sample cast in Al mould along the longitudinal cross-section

Figure 138(a) and 138(b) shows the pore size and number of pores of that size formed in the 60wt% and 70wt% solid loaded sample cast in Al mould along the longitudinal cross-section respectively. By comparing the data of this graph in figure 138(a), (b) with figure 130 there is an increase in the average pore size (82 -130µm in 60wt% sample cast in Al mould as seen in figure 138(a) and 82-140µm in 70wt% sample cast in an Al mould as seen in figure 138(b) from 55-91µm in 50wt% solid loaded sample cast in Al mould. The increase in average pore size with the increase in solid loading is due to the fact as the solid loading increases it slightly delays the cooling process due to the presence of increased ceramic content, thus giving time for pore growth.

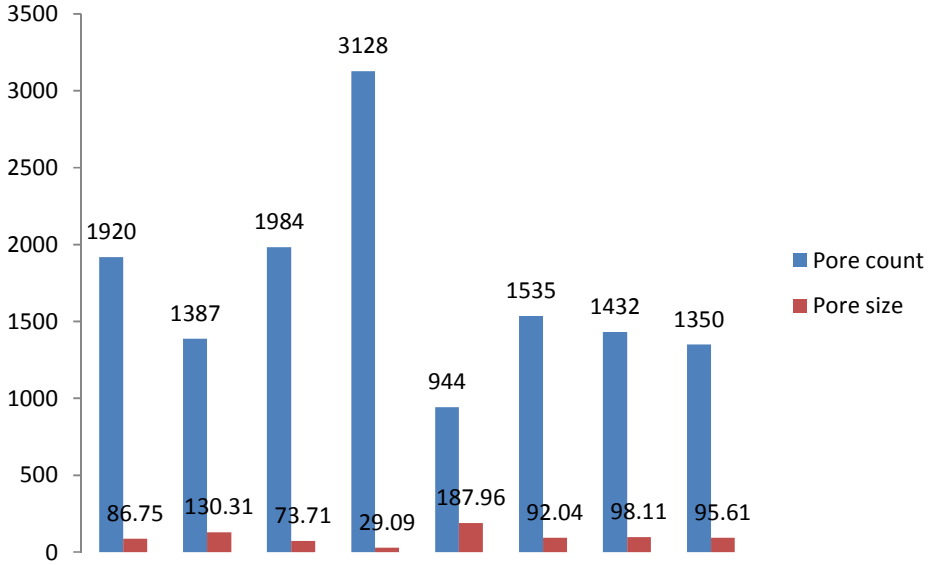

(a)

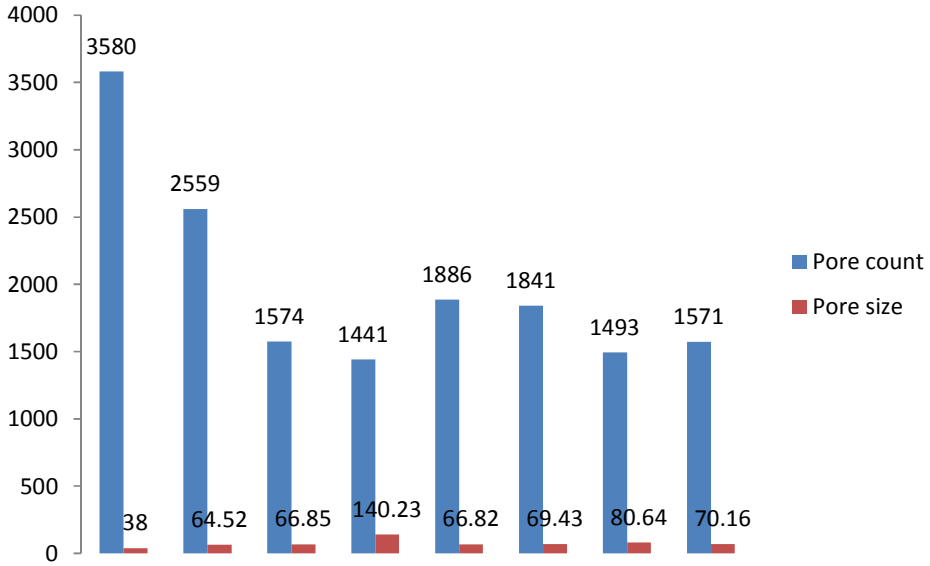

(b)

Figure 139. Graph showing the average pore size distribution in µm and number of respective pores in (a) 60wt% (b) 70wt% solid loaded sample cast in Al mould along the transverse cross-section

Figure 139(a) and 139(b) shows the pore size and number of pores of that size formed in the 60wt% and 70wt% solid loaded sample cast in Al mould along the transverse cross-section respectively. It can be seen that the average pore size range between 29-130µm in 60wt% solid loaded sample (139(a)) and for 70wt% solid loading it is between 38-140.23µm (figure 139(b)). Across this sectional plane the pore size increases with the increase in solid loading.

(iv) Image analysis of 60wt%, 70wt% solid loaded samples cast in PVC mould

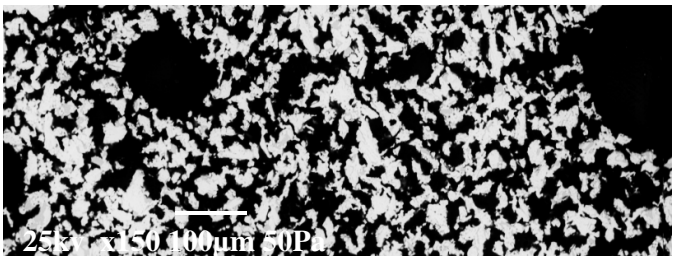

(a)

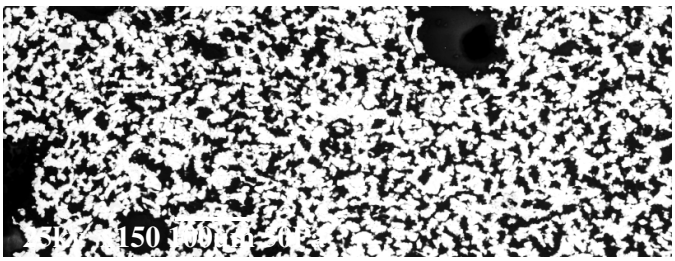

(b)

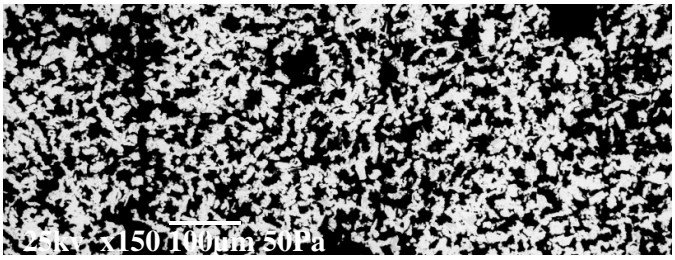

(c)

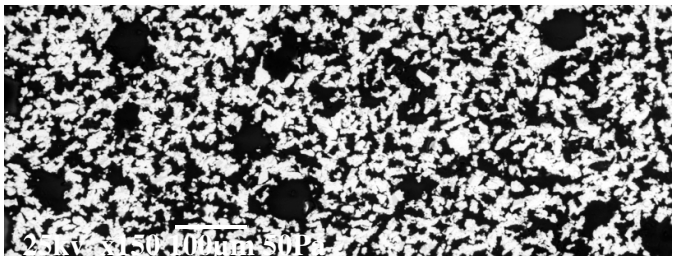

(d)

Figure 140. SEM images of (a) 60wt% (b) 70wt% solid loaded samples cast in PVC mould scanned across the longitudinal cross-section A-A and (c) 60wt%, (d) 70wt% solid loaded samples cast in PVC mould scanned across the transverse cross-section B-B

Figure 140(a) and 140(b) is the SEM images of the 60wt% and 70wt% solid loaded sample cast in a PVC mould respectively and scanned across the section A-A (stage was moved approx. 6mm for the consecutive scans) refer figure 128. Figure 140(c) and 140(d) are the SEM images of the 60wt% and 70wt% solid loaded sample cast in PVC mould respectively scanned across the section B-B (stage was moved approx. 4mm for the consecutive scans) refer figure 128. Images scanned across region 1, 2, 3 and 4 across the longitudinal plane of the sample (refer figure 128) were stitched together to obtain the above images seen in figure 140(a) and 140(b). Figure 140(c) and 140(d) are the images obtained by stitching the images taken in the region 1, 2 and 3 across section B-B (refer figure 128). As with the other SEM images (figure 134, 136, 138, 140 and 142) the pore structure is similar with no signs of directional pore growth. The possible changes in the pore size and distribution are explained below.

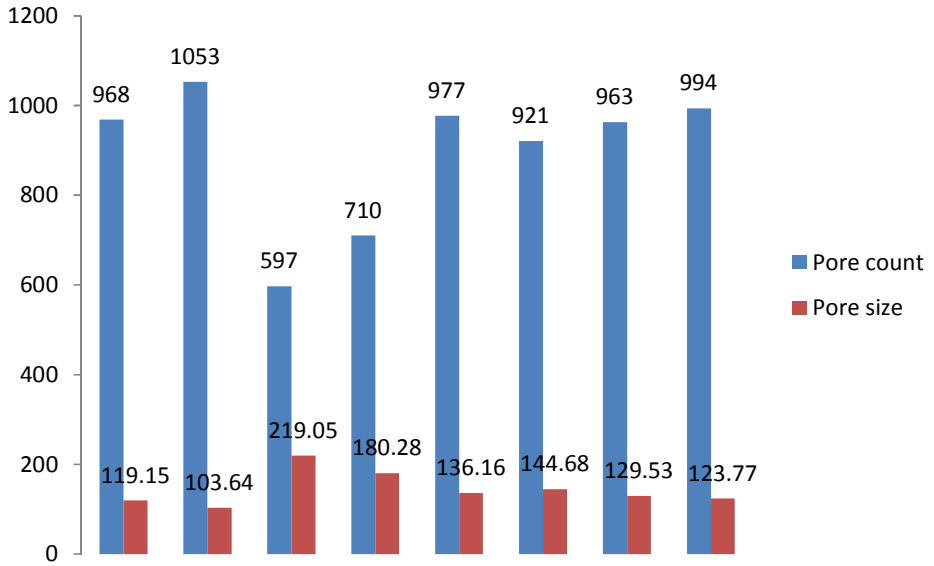

(a)

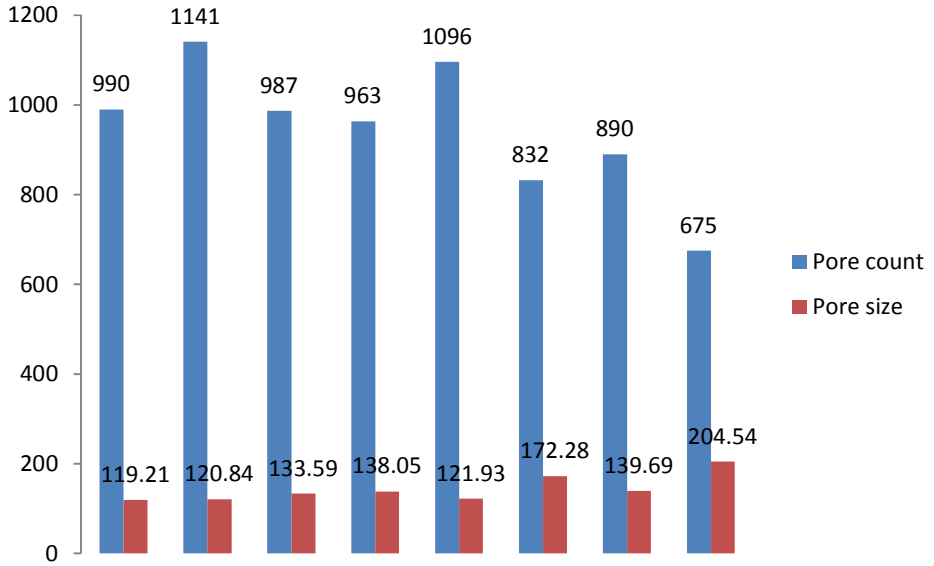

(b)

Figure 141. Graph showing the average pore size distribution in µm and number of respective pores in (a) 60wt% (b) 70wt% solid loaded sample casted in PVC mould along the longitudinal cross-section

Figure 141(a) and 141(b) shows the approximate estimate of the pore size and number of pores of that size formed in the 60wt% and 70wt% solid loaded sample cast in PVC mould along the longitudinal cross-section respectively. Here the pore size in 60wt% solid loaded sample range between 119-219µm (figure 145(a)) whereas in 70wt% solid loaded sample the pore size is in between 119-204µm (figure 145(b)). There is no significant difference in the pore size but has increased 82 -130µm in 60wt% sample cast in Al mould as seen in figure 138(a) and 82-140µm in 70wt% sample cast in Al mould as seen in figure 138(b) and also from 55-91µm in 50wt% solid loaded sample cast in Al mould. Again this confirms that there is an increase in pore size with lower cooling time.

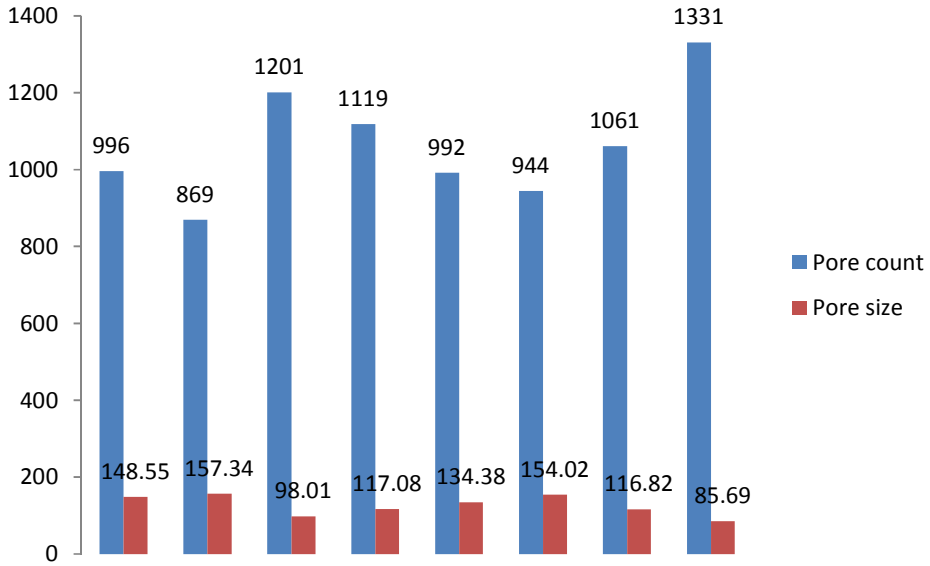

(a)

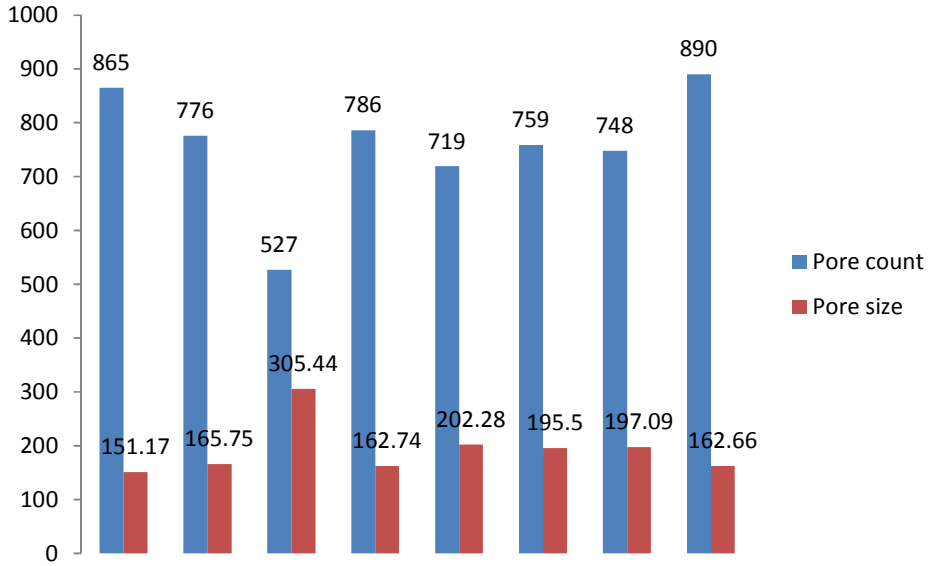

(b)

Figure 142. Graph showing the average pore size distribution in µm and number of respective pores in (a) 60wt% (b) 70wt% solid loaded sample cast in PVC mould along the transverse cross-section

Figure 142(a) and 142(b) shows the pore size and number of pores of that size formed in the 60wt% and 70wt% solid loaded sample cast in PVC mould along the transverse cross-section respectively. It can be seen that the average pore size range between 98-151µm in 60wt% (PVC mould) solid loaded sample (figure 142(a)) whereas the pore size was 29-130µm in 60wt% (Al mould) solid loaded sample (figure 139(a)) and in 70wt% solid loading it's between 150-305µm (figure 142(b)) and it was between 38-140.23µm (figure 144b). From all the above graphs in section 7.34c, it is clear that there is an increase in pore size with the increase in solid loading due to the delay in cooling time upon solidification.

7.35 Summary

It can be concluded that it is possible to fabricate micro porous Ti_2AlC MAX-phase ceramic with the freeze casting process with pores in the range of 27-305µm. With camphene as the freezing vehicle there was no directional growth or dendritic formation of the pores; this is in contrast to previous work on a similar systems for HA/TCP materials. This is likely to be due to the higher density ($4.12g/cm^3$) of the Ti_2AlC material and also the particle size used, compared to HA/TCP (average 6µm particle size and a density $2\text{-}3g/cm^3$) this hinders the propagation of camphene dendrites into the slurry pushing away and enclosing the ceramic particle as explained in Chapter 2 section 2.5 figure 26. As a result it is not possible to obtain highly oriented pores when this technique is used with Ti_2AlC ceramic. Nevertheless the pore size can be controlled by controlling the cooling rate upon solidification and it was observed that metallic mould which has higher heat exchange rate induces finer pores in the ceramic material and plastic mould with comparatively low heat exchange rate induce larger pores in the ceramic material. In addition to tuning the heat transfer characteristics of the mould it is also possible to increase the pore size with the increase in solid loading in the slurry. Table 12, is a summary providing the range of pore sizes that can be achieved with this technique varying the solid loading and mould material.

Table 12. Range of pore sizes obtained with different solid loading, cast in Al and PVC mould along both the cross-sections

Solid loading in wt%	Al mould				PVC mould			
	Longitudinal cross-section µm	**Transverse cross-section** µm	**Porosity %**	**Compressive strength MPa**	**Longitudinal cross-section** µm	**Transverse cross-section** µm	**Porosity %**	**Compressive strength MPa**
50	55-56	27 – 86	53.23	8.02	63-138	180-330	61.48	9.48
60	82 -130	29-130	61.51	10.10	119-219	98-151	62.68	10.20
70	82-140	38-140.23	60.42`	14.91	119-204	150-305	60.49	18.35

Chapter 8. Application of macro-porous Ti_2AlC as a porous electrode in a microbial fuel cell (MFC)

8.1 Introduction to Microbial Fuel Cells (MFCs)

The search for sustainable energy is an important challenge to meet the global energy crisis. This has led to the rise of many research groups considering low cost technologies for harvesting renewable energy. The Microbial Fuel Cell (MFC) is one outcome of such research and is an attempt to harvest renewable energy from micro-organisms [142-145]. MFCs are devices that use a specific type of micro-organism, such as bacteria, to oxidise organic and inorganic matter and therefore generate an electric current [146-149]. Figure 143 is a schematic of the basic working principle of a MFC which shows a dual chamber MFC, the type of fuel cell used in this research application.

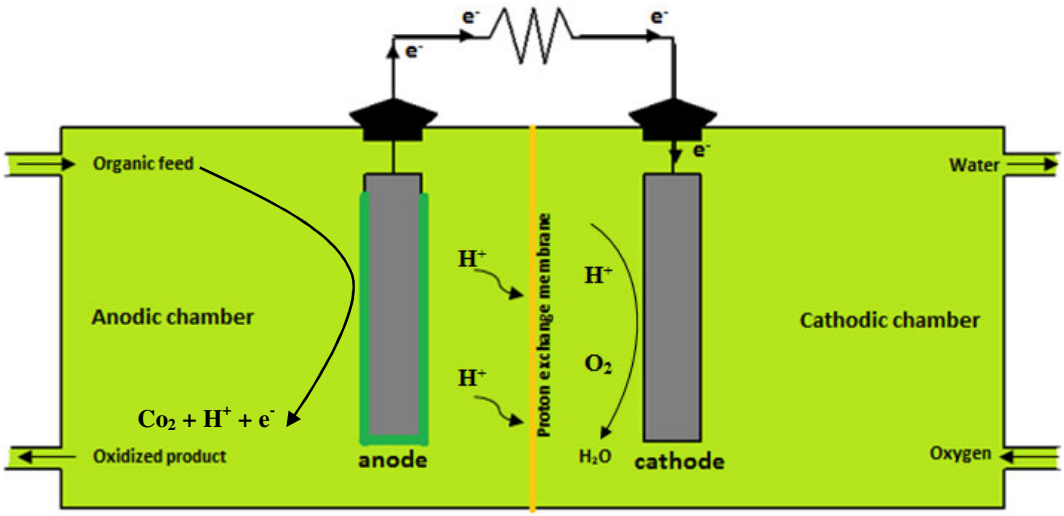

Figure 143. Schematic representation of the working principle of a dual chamber MFC

As seen in figure 143, the MFCs consist of an anaerobic anodic chamber which is separated from a cathodic chamber by a selective membrane. This membrane only allows the diffusion of protons (H^+) and is termed as Proton Exchange Membrane (PEM). In most MFCs, when the proton that reaches the cathode it combines with the electron transferred from the anodic chamber and oxygen from air to form water. The sustainable process of electron liberation by the microbes during metabolism and the subsequent electron consumption at the cathode are the main characteristic feature of a MFC. The other type is the single chambered MFC as seen in figure 144, where both the anode and the cathode are integrated into a single chamber.

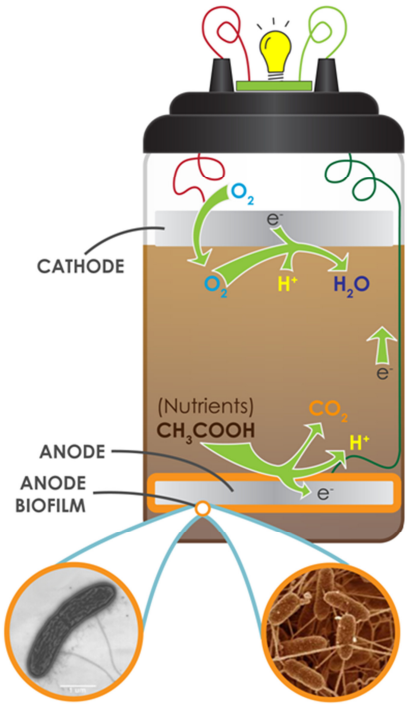

Figure 144. A typical single chamber MFC where both the anode and the cathode are integrated in a single chamber [150]

As an example if a micro-organism consumes sugar as a substrate under aerobic condition (in the presence of oxygen) it will produce carbon dioxide. However in the absence of oxygen, (anaerobic condition), these micro-organisms produce carbon dioxide, protons and electrons [151]. This is the basic reaction that takes place in the anodic chamber in a dual chamber MFC:

$$C_{12}H_{22}O_{11} + 13H_2O \rightarrow 12CO_2 + 48H^+ + 48e^- \textit{ (typical reaction that takes place in anodic chamber)}$$

The protons generated move towards cathodic chamber through a proton selective membrane and combine with oxygen to form water as seen in the following reaction:

$$2e^- + H^+ + \tfrac{1}{2}O_2 \rightarrow H_2O \textit{ (typical reaction that takes place in cathodic chamber)}$$

As seen in figure 143, in a dual chamber MFC, electrons are produced by bacteria at the anode as a result of a metabolic redox reaction that oxidises organic matter in the anodic chamber. These electrons are transferred to an anode which acts as the electron acceptor; the electrons then flow from the anode to the cathode through a conductive material to generate power. The electrons are transferred to the anode directly by nanowires generated by the bacteria as seen in figure 145 or via an electron mediator or shuttles [152, 153].

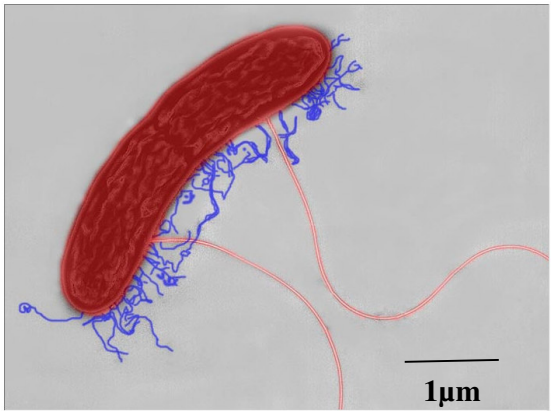

Figure 145. Transmission electron microscopy image of Geobacter bacteria (image courtesy Dr. Derek Lovely, UMASS, Amherst) with blue coloured filament like structure representing the nanowires to transfer electrons

The MFC of interest for this work is a photo-microbial fuel cell (p-MFC) which is a sub-set of the MFCs. In this type of MFC, the anodic chamber comprises of photosynthetic micro-organism (algae or cyanobacteria) which releases electrons during the photosynthetic and respiration process [154-156]. The main advantage of p-MFCs is that the bacteria in a p-MFC do not need to be fed with organic matter because they are able to photosynthesise carbohydrates which can be supplied or obtained by consuming other bacteria in the medium in the presence of light [157]. This type of fuel cell was proposed in the early 1930's by Cohen, in order to enhance the generation of bio-electrochemical current [158]. However this idea was demonstrated in the 1980's by Bennetto and co-workers. Figure 146, is a schematic, showing how the electrons are generated by the cyanobacteria in the anodic chamber of a p-MFC.

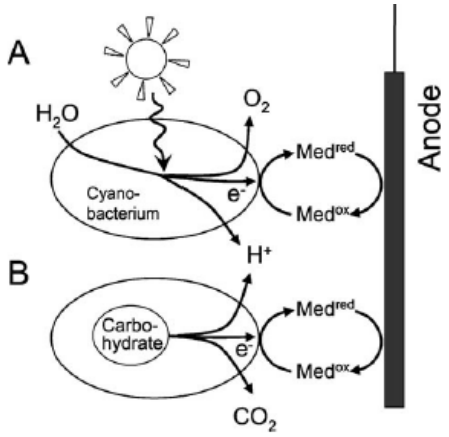

Figure 146. Schematic representation of reactions that take place in the anodic chamber of a p-MFC. (A) Reaction in the presence of light, (B) reaction in the dark [159]

As seen in figure 146, electrons and protons can be generated in the dark, by a respiration process which involves the oxidation of carbohydrates such as glycogen (step B in figure 146) [160]. There is a smaller degree of production of electrons in the presence of light, by photosynthesis, which is restricted due to limited supply of oxygen that is necessary in the reaction process (step A in figure 146).

8.2 Electrode materials used as anode in p-MFC

The greatest advantage of MFCs is its simplicity in construction and the choice of electrode material. Carbon based materials are the common anode material used [153]. Carbon felt or cloths (figure 147) are also used due to its high internal surface area which facilitates the growth of bacteria on it [161, 162].

Figure 147. Carbon felt or cloth which is used as anode material (image courtesy PHYCHEMi) [12x12inch]

Graphite felts and carbon paints are also used as an anode material but there are limited studies showing which of these materials perform the best [163, 164]. There are some studies [154] to improve the anode material by the addition of metallic nanoparticles and even nano-tubes on the electrode material. For example gold and indium doped tin oxide anodes have been examined [154]. The carbon based anode material have achieved good performance (higher power density) in MFC applications, however when they are used in p-MFCs, it has several drawbacks. One of them is the colour of the carbon material itself since the use of a dense black material allows light to fall only on the outer electrode surface and therefore limits the photosynthesis reaction (Path A Figure 146). Thus most of the bacterial growth is concentrated on the electrode surface so that the internal electrode surface area in not used [157]. To overcome this problem, transparent glassy materials coated with a conductive coating of fluorine tin oxide (FTO) was used as an electrode but these materials lacked a high internal surface area [157].

There is one report on the use of TiO_2 scaffolds (10mm in diameter and length) with macro-pores (60 pores per inch) which was used as a substrate for culturing human mesenchymal stem cells [165]. This led to the idea of using macro porous electrodes in p-MFCs, where a healthy biofilm can grow throughout the 3-D matrices of the electrode material and the biofilm can grow on the internal area of the electrode which has easy access to nutrients as there is an easy continuous flow of the medium through the macro electrode pores. Hence the University of Bath developed a porous TiO_2 as the electrode with a conductive coating of FTO (fluorine tin oxide) deposited on the electrode surface using chemical vapour deposition (CVD) technique [157]. This material was promising as an anode initially with a power output of $3.4\mu Wcm^{-2}$ but its performance deteriorated as the FTO coating eroded with time. Coating the porous ceramic with FTO was also an additional complex stage in the manufacturing process.

As a result of this work the fabrication of macro porous conductive Ti_2AlC ceramic was undertaken since the Ti_2AlC MAX-phase ceramic is inherently a good conductor of electricity as seen in figure 148. This would remove the need to coat the materials with a conductor such as FTO and enable high performance over long periods (months or years).

Requirements were as follows:

(i) Sufficient mechanical strength to be handled and attach an electrode (no mechanical load in service) – using information obtained from Chapter 6; This material has a maximum compressive strength of 0.32MPa, which is sufficient for handling

(ii) High porosity for flow of nutrients through the electrode to sustain algae – use of 10ppi foam (3 mm – 5mm typically)

(iii) High electrical conductivity (high Ti_2AlC content) by optimising sintering condition to maximise Ti_2AlC content and density of struts (Chapter 5)

(iv) Bio-compatibility and long term stability (tested over a year); to be assessed in a p-MFC cell.

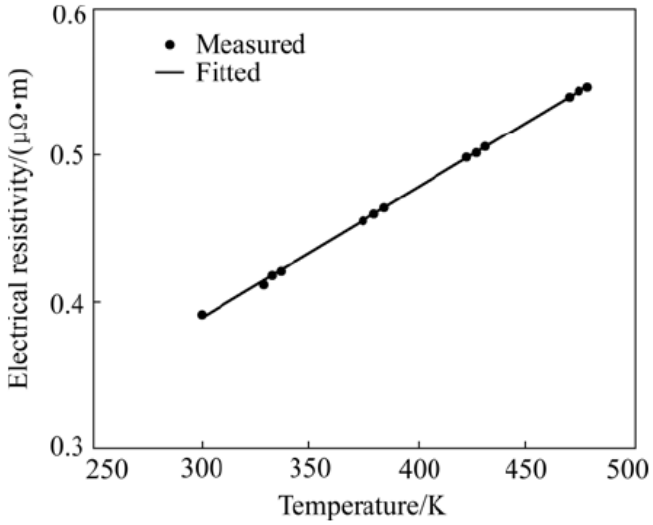

Figure 148. Electrical conductivity of dense Ti_2AlC ceramic [167]

The Ti_2AlC ceramics were prepared and had a bulk electrical resistivity of 9.11Ωcm as measured by a four point probe. This is a much lower resistance than, TiO_2 which has a bulk resistance of 10^{12}Ωcm [170]. With such a low resistance, the development of the macro porous Ti_2AlC ceramic has the potential to replace TiO_2 electrode with an additional FTO coating. The procedure and methods developed to fabricate macro-porous Ti_2AlC ceramics was explained in detail in Chapter 6.

For the manufacture of macro-porous Ti_2AlC for the p-MFC the following chemicals were used in the preparation of slip to be coated on the polyurethane foam:

(i) Ti_2AlC ("Maxthal 211 engineering ceramic material" from Kanthal),
- Particle size distribution: 90% of the powder comprised of 20μm particles, and the rest was a mixture of 2μm and 8μm particles.

(ii) Poly(ethylenglycol) average Mn 380-420 from Sigma Aldrich,

(iii) Dispex GA40 from Ciba AG,

(iv) Methyl cellulose from Sigma Aldrich,

(v) Distilled water with a resistivity of 18.2MΩcm.

The slip was prepared with the optimised composition of the above chemicals explained in detail in Chapter 6, section 6.21 (see Table 8, Composition 3). This pores size was selected since it is necessary that the nutrients flow through the pores of the electrode providing growing environment for the algae.

After the impregnated foam was dried for 24 hours, it was sintered with the optimised heat treatment process as seen in figure 149 to burnout the polyurethane foam and to strengthen the ceramic material as seen in figure 150 which also shows the electrical connectivity to the porous material.

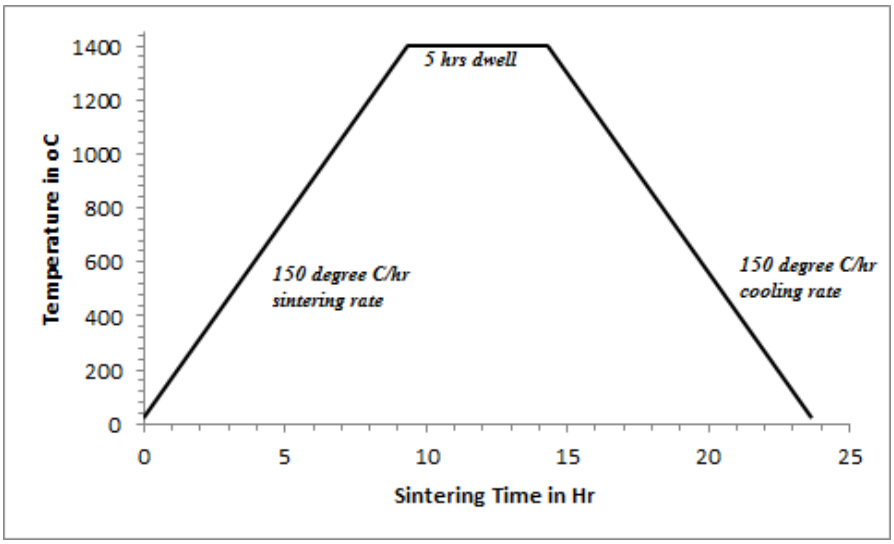

Figure 149. Optimised sintering condition for porous ceramic
(refer Chapter 6, section 6.3)

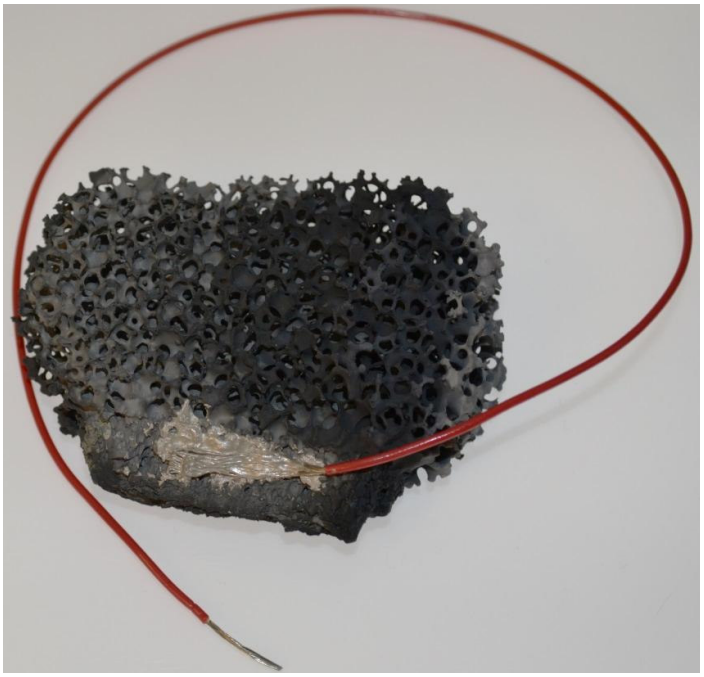

Figure 150. Sintered porous single coated Ti_2AlC ceramic electrode with uniform pore distribution with approx. 5mm pore size

8.3 Macro porous Ti_2AlC used as anode material in a p-MFC

This work on MFCs was in collaboration with Mr Kenneth Schneider from Department of Chemistry, University of Bath [168], whose PhD research topic was improving the efficiency of a self-sustaining p-MFC using porous anode electrodes. My part in this chapter was the fabrication of a tailored macro porous Ti_2AlC based on the required surface area and electrode geometry.

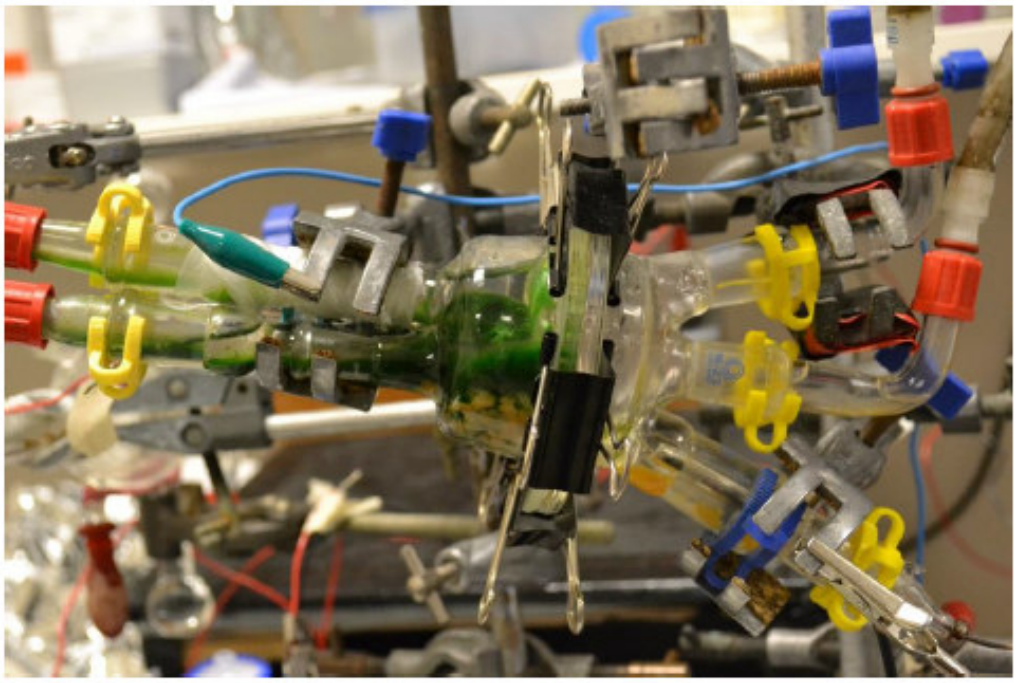

(a)

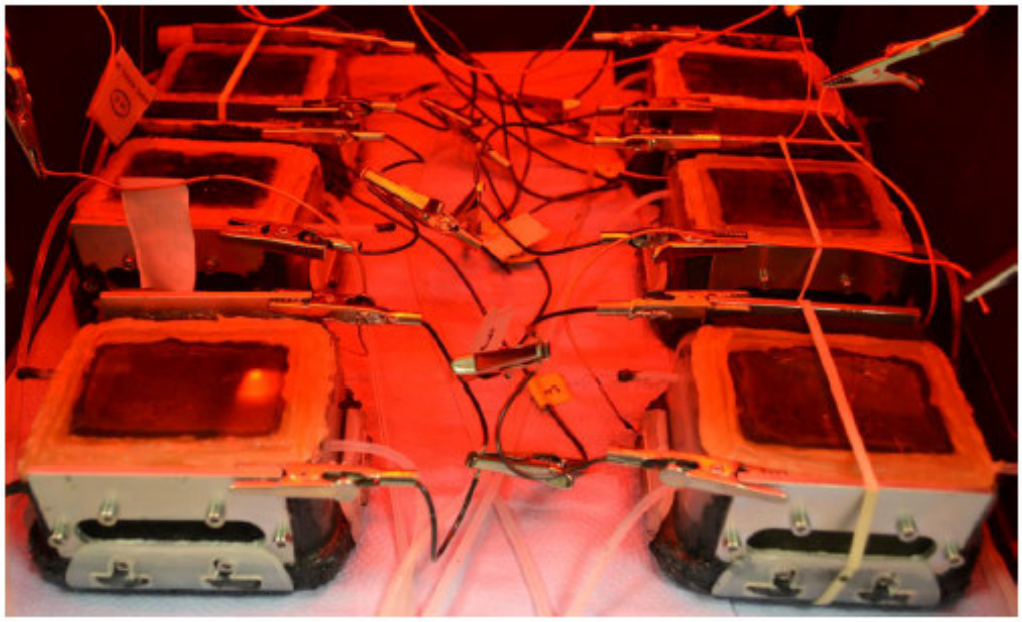

(b)

Figure 151. Set-up of a dual-chamber p-MFC used by the researcher. (a) The anodic chamber, (b) the air cathodic chamber [168]

Figure 151, is the set-up of a dual-chamber p-MFC used by the researcher in his study. A dual chamber MFC is a fuel cell with two separate anode chamber and cathode chamber which is separated by a proton exchange membrane (PEM) (refer to figure 143).

The dual-chamber p-MFC used in this research was a mixed culture of green algae and cyanobacteria, also known as the blue-green algae which was grown in BG-11 medium, which was used to support the growth of blue-green algae and green algae. A bio-reactor was used to support the growth of the bacteria and the medium was pumped into the anodic chamber using a peristaltic pump. Green algae and cyanobacteria are the most common bacteria found in the water bodies and produce oxygen as a by-product of photosynthesis. Cyanobacteria are considered to be important in achieving an oxidising atmosphere on earth, which caused the dramatic changes to the life form on earth by enhancing biodiversity and killing the oxygen intolerant organism [169].

The macro porous Ti_2AlC ceramic with 10 pores per inch (ppi) (figure 151(b)) was used as the anode in the anodic chambers seen in figure 152(a). Platinum foil was used as the cathode in the air cathode flow cell. The system is called an 'air cathode cell' as these cambers were aerated to supply oxygen to support the cathodic reaction. The anode and the cathode chambers were separated by Nafion perfluorinated membrane 115 from Sigma Aldrich as the proton exchange medium. No artificial electron mediators or electron shuttles like thionine, methyl blue, neutral red or bold basal [157] were used since the bacteria directly injects the electrons into the anode via naturally produced mediators or nano-wires as shown in figure 145. Another reason for not using the artificial mediator is because they are toxic to environment and it would therefore not be a sustainable energy technology.

Polarisation curves were measured under constant flow condition and using a low monochromatic light as the source of light for the photosynthesis process (12 Wm^{-2} at 625nm).

8.4 Observation and results

8.41 Microscopic Observation

Figure 152. Figure showing the bio-film grown on the Ti_2AlC electrode [electrode size: 25x25x25mm][168]

Figure 152, shows the growth of thin bio-film on the Ti_2AlC electrode material after an incubation of the culture for three months in the anodic chamber. This indicates that the macro-porous Ti_2AlC as an anode material is biocompatible and a potential material for MFC application. Confocal microscopy was used to observe the bio-film grown on the electrode material. From the confocal micrographs in figure 153, it is possible to observe healthy colonies of green algae and cyanobacteria (blue-green algae) grown on Ti_2AlC macro porous electrode.

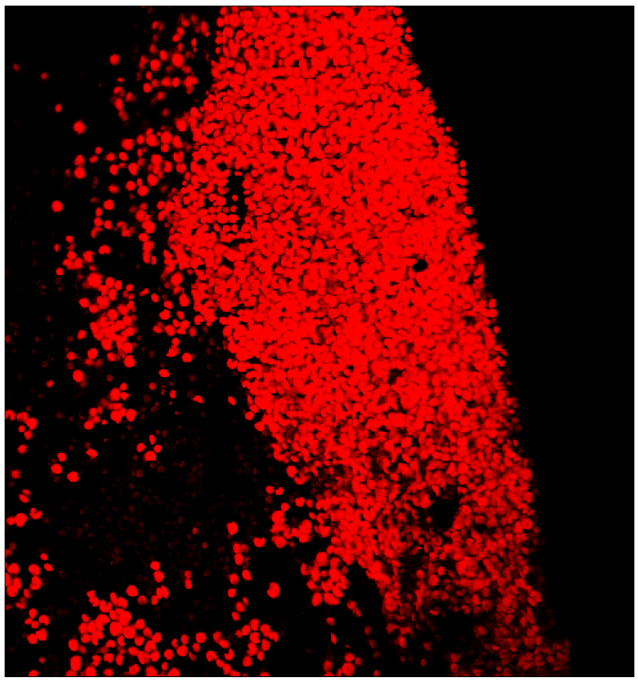

(a)

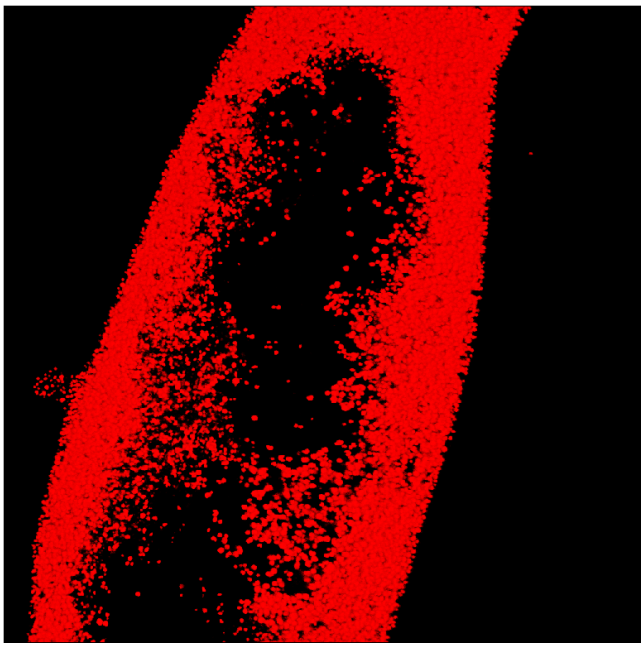

(b)

Figure 153. Confocal micrographs of the bio-film grown on Ti_2AlC. (a) Thin healthy mat of bio-film (225x225µm), (b) Bio-film grown on a single strut of the Ti_2AlC electrode material (450x450µm)

8.42 Polarisation and Power Curves

The polarisation curve, showing the cell voltage against the current density, is the most common way of representing the efficiency of a MFC and indicates the performance of the MFCs (Figure 154(a)). In addition, the power curve dictates the performance of the MFCs, showing the voltage against the power density from the power equation P = IV, where P is the power of cell in Watt, I is the current in amps and V is the voltage in volts (Figure 154(b)). Six samples were tested at a time with specific load resistance. Hence there are six separate chambers in figure 151(b).

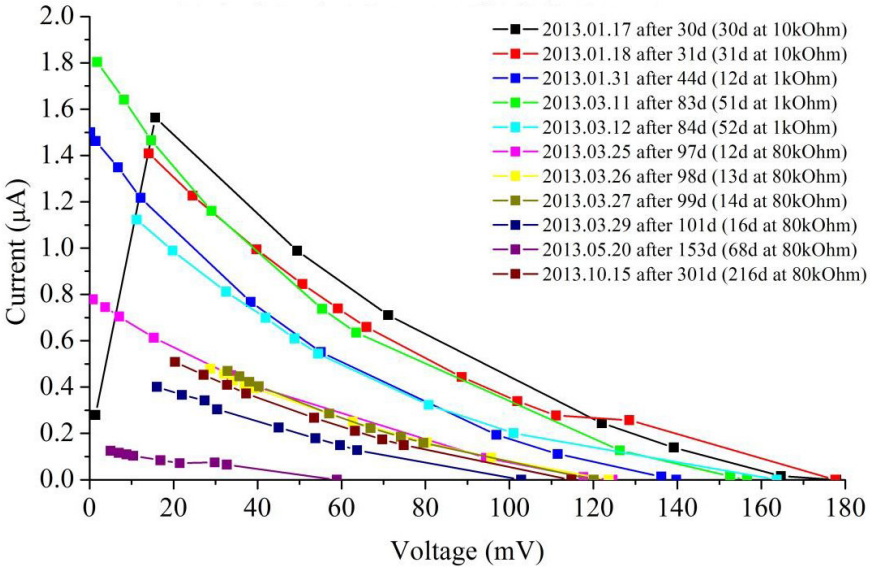

(a)

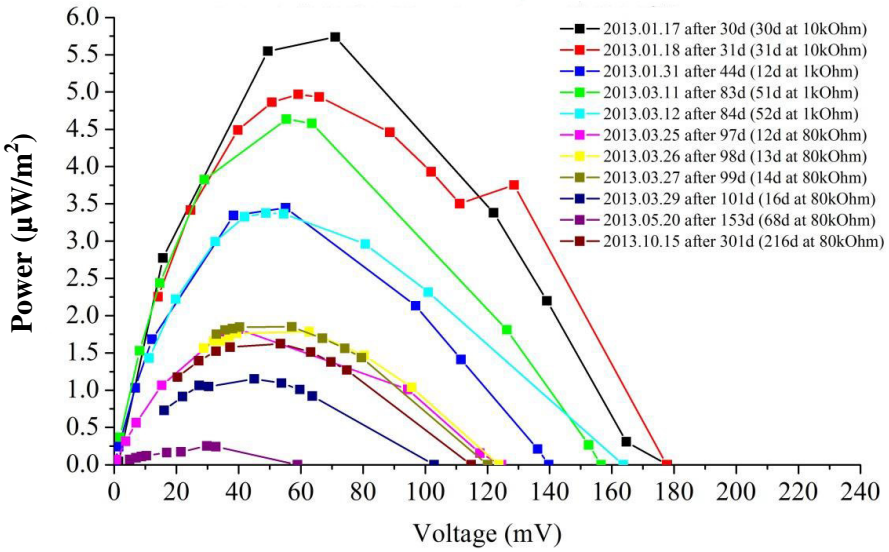

(b)

Figure 154. a) Polarisation curve of mixed culture p-MFC with 10ppi Ti_2AlC electrode and Pt foil as cathode under a light of 625nm, (b) Power curve of mixed culture p-MFC with 10ppi Ti_2AlC electrode and Pt foil as cathode under a light of 625nm [168]

Figure 154(a) and 154(b) are the polarisation curves and power curves of the p-MFC with Ti_2AlC as the anode and Pt foil as the cathode with range of resistors varied between 1kΩ to 80kΩ. The figure represents the current and power generated from day 30 i.e. after the growth of bio-film until almost 10 months (310 days). It can be observed that initially at day 30 the current produced is 1.6µA with a power density up to 6µW/m^2 which increases to 1.8µA with a power density of 4.5µW/m^2 after 83 days. This shows the increase in the growth of bio-film area with time. As the number of days proceed the current and power generation deteriorated with the expiration of the bio-film after 153 days in figure 154(a) and 154(b). However, it can be seen that the current is approximately 1.25µA at day 301 and was 0.25µA at day 153. This shows that the bio-film is re-growing thus showing the possibility of self-sustainable nature of the system and that the Ti_2AlC macro-porous electrode has the potential to operate of a long term p-MFC anode material.

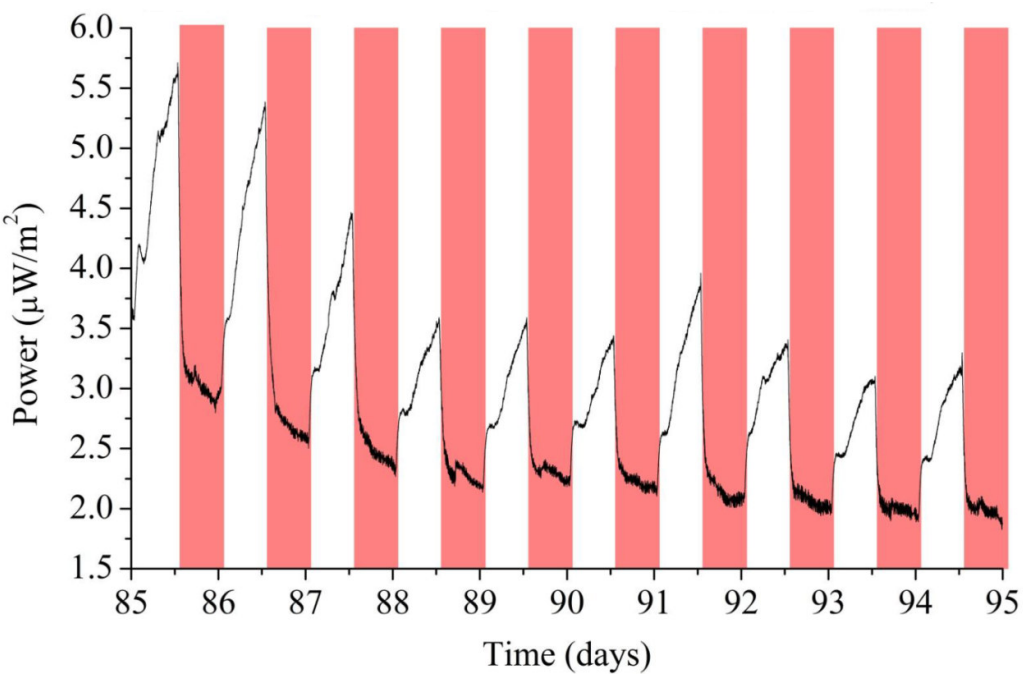

Figure 155. Power output from the p-MFC in the presence of light and in dark [163]

Figure 155, shows the power density generated from a mixed culture of green algae and cyanobacteria, using Ti_2AlC as anode and Pt foil as cathode. The pink bar represents the duration of the presence of light on the system. As seen in figure 155, higher power is generated in the dark during the respiration process when the food is metabolised as explained in figure 146. With the depletion of the bio-film with time the power output minimises.

8.43 Comparison of 10ppi Ti_2AlC electrode with 10ppi reticulated carbon foam electrode

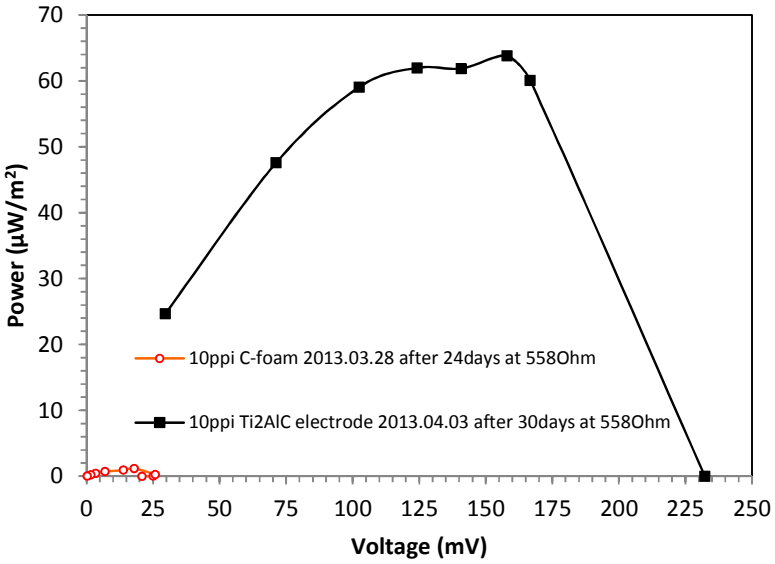

Figure 156. Power curves of p-MFC when different anode electrode material is used [163]

Mr Kenneth Schneider from Dept. of Chemistry, University of bath, conducted a study on the performance of the 10ppi Ti_2AlC electrode (figure 151(a)) with the most commonly used activated carbon foam (FM 10) from Chemviron Carbon with Pt foil as the cathode material. This type of carbon foam is an extensively used anode material in this research field and most of the outstanding results on MFCs were based on this type of carbon foam in the past [161, 162]. As seen in figure 156, the carbon foam for the same applied resistance for a period of 24 days produced a power output of 1.2µW/m^2, whereas the 10ppi porous Ti_2AlC produced a power output of almost 68µW/m^2 which is 58 times better than the carbon foam. This proves that there is a higher population density of green algae and cyanobacteria grown on Ti_2AlC than on activated carbon foam which is the most competitive electrode material sold in the market and Ti_2AlC is more biocompatible than carbon foams. This high performance coupled with the long terms results demonstrated that the macro-porous Ti_2AlC is a highly promising anode material for p-MFC applications.

8.5 Summary

A macro-porous Ti_2AlC ceramic was successfully fabricated for the electrode application purpose in p-MFC. Based on the requirement of the electrode's multifunctional properties such as the need to be conductive while at the same time being sufficiently porous to facilitate the flow of medium through it, a 10 pores per inch porous Ti_2AlC single coated electrode was developed for this application. The foam was also sufficiently strong to be handled and connected to the dual chamber MFC. This electrode has a compressive strength of $0.32N/mm^2$, which was increased from $0.21N/mm^2$ by optimising the heat treatment process (refer Chapter 6, section 6.4). Studies conducted over a period of 1 year by Mr. Kenneth Schneider [168] on this electrode material showed that this material has a potential to be used as anode electrode material to replace the activated carbon foam which is most commonly used anode electrode material. A power density of up to $68\mu W/m^2$ was produced using Ti_2AlC electrode whereas research in the past using porous TiO_2 with FTO coating and carbon foam shows a power density of 3.4 [157] and $1.2\mu W/m^2$ respectively. More research work has to be carried out in order to optimise the design for achieving self-sustaining recognition.

Chapter 9: Conclusion and ideas for future work

9.1 Introduction

This chapter is intended to summarise the outcome of the research study carried out in this PhD. In addition suggestions on possible future work on some of the above chapters which can be useful for augmenting this research have been reported in this chapter.

9.2 SHS to produce Ti_2AlC ceramics

9.21 Thermodynamic study of the reaction

A mathematical thermodynamic model to predict the maximum combustion temperature under adiabatic condition T_{ad}, has been formulated and the predicted T_{ad} of the elemental reaction *3.1* of 2368K (Chapter 3, section 3.13). This was in close agreement with the experimental values of 2073-2110K [26, 115]. This is a complete model incorporating phase changes of all the elements and compounds in the system with the only assumption of no heat loss to the surroundings during the actual reaction. The results also incorporate high temperature thermal analysis of the Ti_2AlC ceramic where limited data has been reported in the literature.

9.22 Thermal explosion

The thermal explosion mode of combustion synthesis was carried out to observe the effect of particle size on the ignition temperature. It can be concluded that the particle size of the elements used in the reaction has no significant effect on the ignition temperature as long as the reaction is sufficiently exothermic to undergo the combustion synthesis process. Generally the reaction, irrespective of the particle size, initiated at a temperature near the melting point of aluminium, which is $660^{o}C$. An important observation made from this study is that even though the reaction mixture is highly exothermic, to initiate the reaction process there should be a sudden rise in the activation temperature to initiate the reaction. Slow and controlled rate of heating is less likely to initiate the reaction (refer Chapter 3, section 3.23).

9.23 Effect of particle size on the formation mechanism of Ti_2AlC by SHS

Aluminium and titanium with a range of particle sizes (refer Chapter 4, section 4.2 for information on size) were mixed according to stoichiometric ratio of 2Ti:1Al:1C and their influence in the phase formation of final product were studied. It can be concluded that the particle size of Al and Ti has no influence on the formation mechanism but the shape of the particles strongly influence the formation mechanism. It was found that as the green body sample is made more porous the less likely it will form Ti_2AlC, resulting in incomplete reaction due to a lower degree of particle to particle contact. By ensuring a high green density and all the elements in the reaction mixture take part in the reaction, the desired product can be achieved. Increasing the particle to particle contact could also be achieved by introducing additional liquid phase into the reaction, which has been demonstrated in the study (refer chapter 4, section 4.24). By using additional liquid phase, the exothermicity of the reaction decreases and as a result it slows down the combustion wave velocity, facilitating the formation of Ti_2AlC.

In this part of the study, a variety of carbon sources were used to see its effect on the final product. Graphite, lamp black and carbon fibres were used as the carbon source. It was concluded that for the formation of Ti_2AlC using SHS, a carbon source with high surface area is required. As the reaction mechanism mainly depends on the formation of TiC, which in turn reacts with the intermediate compounds like Ti_3Al, TiAl to form Ti_2AlC upon the cooling process.

9.24 Suggestion for future work for SHS

Many attempts were made to record the reaction temperature during the SHS process. Type B (Platinum and Rhodium) and Type C (Tungsten and Rhenium) thermocouples for high temperature recording were used for this purpose during the PhD. However, due to the high temperature generated during the reaction, the thermocouples +ve and –ve terminal bonding consistently broke at elevated temperature. Effort has to be made increase the thermal shock resistance of these bonding so that this thermocouple can withstand sudden rise in temperature. For this type of measurement the tip of the thermocouple should be spot welded over some distance (figure 157(b)), rather than at the tip of the thermocouple as seen in the figure 157(a). By doing so, even though the tip of the thermocouple in contact with the green sample breaks upon the reaction, the circuit is still closed and reading can be taken without any interruption. If this technique works then the actual temperature reading can be used to assess the %error compared to the thermodynamic model.

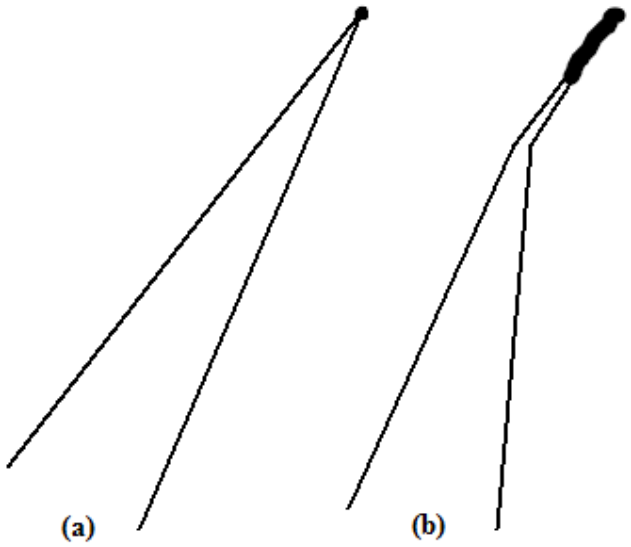

Figure 157. Possible change to be made in thermocouple bonding. (a) Existing spot welded bond. (b) Proposed type of spot welded bond

Another important characterisation will be the study of the combustion wave velocity. Combustion wave velocity of the reaction directly relates to the exothermicity of the reaction. The more exothermic the reaction is, quicker will be the propagation velocity of the combustion wave. Some attempts were made using high speed camera to record the SHS reaction, but due to the exposure of high intensity light emitted from the reaction, the image obtained are over saturated with light and it is very difficult to identify the end point of the reaction. Techniques such as using a thin UV film over the camera lens could possibly overcome this problem and helps in calculating the combustion wave velocity. Acquiring this data can help in understanding the effect of particle size on the combustion wave velocity which in turn will augment the information on the formation mechanism of Ti_2AlC.

9.3 Optimisation of sintering temperature for dense Ti_2AlC

As the second part of the research was associated with the fabrication of macro and micro porous Ti_2AlC ceramic, it was essential to optimise the sintering temperature to obtain dense and pure Ti_2AlC after sintering. Dense Ti_2AlC tablets were cold pressed at 1.77kN/mm^2 for this study and sintering was carried at 1200, 1250, 1300, 1350 and 1400^{0}C and the evolution of compounds were studied along with density measurements (refer Chapter 5, section 5.3). It was found that to obtain high purity Ti_2AlC pellets a sintering temperature of 1400^{0}C for a period of three hours is required and it had a density of 3.85g/cm^3, which is very close the density of 4.11g/cm^3 reported in the literature [9]. From this study the sintering characteristics of Ti_2AlC was well established and it was used as a benchmark to set the sintering temperature for fabricating macro and micro porous Ti_2AlC ceramics with a dense solid structure.

9.4 Fabrication of macro porous Ti_2AlC ceramics

As Ti_2AlC ceramics are relatively new, only handful of applications have been examined using this material (refer Chapter 2, section 2.3). The motivation for fabricating macro porous Ti_2AlC ceramic was a need of highly conductive and highly porous electrode for applications such as a photo-microbial fuel cell (p-MFCs) application (refer Chapter 8). This material has an electrical conductivity of $3x10^6\Omega^{-1}m^{-1}$ [9]. To meet the requirement of the application, there was a need to fabricate a macro porous structure of desired shape, pore size and pore distribution using foam replication technique (refer Chapter 6). A systematic technique was developed to produce

structurally stable interconnected macro porous ceramic (pore size up to 5mm). Different coating techniques were adapted to reduce the defects on the struts on the structure in the ceramic and with these techniques it was possible to minimise the cracks formed and increase the compressive strength from 0.32 to 6.34N/mm^2. Sintering conditions were optimised further to enhance the compressive strength of the porous structure which shows the importance of heat treatment. Based on the level of interconnected pores required, techniques such as coating of the foam before sintering and coating of the foam after sintering were examined. This Ti_2AlC macro porous structure is first of its kind and has a potential of being a good candidate as a substrate with qualities such as high electrical conductivity, chemical inertness and oxidation resistant features.

This porous ceramic has been used as a porous electrode in a p-MFC, and has delivered excellent results compared to other electrodes mainly vitreous reticulated carbon foam, which are generally used in this application. The researcher [168] was able to grow a healthy layer of bio-film on this material and harvest energy up to 68μW/m^2 whereas with carbon foam as the electrode only up to 1.2μW/m^2 of energy was harvested. The difference in the energy output clearly shows how good this material can be for electrode application.

9.41 Suggestion for future Work

A major part of the fabrication technique has been optimised for this material. The only future work can be using this material in various applications such as a high temperature filter, mainly to filter molten Al as the material has a decomposition temperature of 1550^{o}C which was analysed using DTA technique (figure 29). In addition due to the high surface area of the structure, it can be used in high temperature chemical support for gas absorption, catalyst support for various chemical reactions and also as membrane supports for various sensor applications. Its electrical conductivity could also allow for it to be used as an electrode in a corrosive environment.

9.5 Fabrication of graded micro porous Ti_2AlC ceramic

While the foam replication technique is used to produce uniform pore size macro porous ceramic, freezing casting can be used to produce a ceramic with graded structure with porosity in the micron level. This is the first time micro porous Ti_2AlC ceramic was fabricated using freeze casting with camphene as the freezing vehicle (refer Chapter 7). Using this technique, it was possible to control the evolution of pore size by controlling the cooling rate of the slurry, which was demonstrated in this research using two different mould materials with different heat exchange rate (Al and PVC mould). Pore sizes ranging from 27-305µm was observed in the samples fabricated using this technique. However this technique failed to induce directional growth of the pores in this ceramic system. The reason is possibly that the size of the ceramic particles is bigger than the camphene dendrite formed during cooling stage. As a result the dendrites fail to grow upon solidification thus forming gradient pores with no pattern.

Various solid loaded slurries (50, 60 and 70wt %) were prepared to study the effect of solid loading on the density, compressive strength and also pore size. There was no significant change in the density or the compressive strength in the samples cast in both the moulds. However the solid loading affected the growth of pore size in samples cast in both the moulds. Samples cast in an aluminium mould had a finer pore size and structure due to rapid cooling with pore size slightly increasing with increased solid loading. Samples cast in PVC had a larger pore size and structure due to slow rate of cooling with increasing pore size as the solid loading was increased (refer Chapter 7, section 7.33). The motivation to fabricate gradient micro porous Ti_2AlC ceramic was the need of an electrode material, which has a high surface-area contact with a surrounding electrolyte to be used in a micro redox battery for sensing application. Hence this technique was chosen to produce such micro pores on the surface as well as throughout the material (refer Table 12, for information of pore size that can be achieved with this technique).

9.51 Suggestion for future work

As mentioned above, this technique failed to exhibit directional growth of pores due to the geometry and density of the ceramic particle used. It cannot be concluded that the freeze casting technique cannot produce directional growth of pores in Ti_2AlC ceramic system without further research. It can be useful to prepare samples with different particle of homogenous size and see whether this favours the growth of camphene dendrite in the ceramic system. For this purpose various sizes of sieve can be used to separate particles of specific size to conduct this study, which can help in optimisation of particle size to facilitate dendrite growth and in turn induce directional growth of the pores in this ceramic system. Other freezing solutions can be examined other than camphene, for example water has been used to induce lamellar channels in the material [98] and tert-butyl alcohol [102] has been used to induce a prismatic channel in the material.

CT scanning can be used to study the evolution of pores at various time intervals upon the solidification of the slurry. These results from this study can be coupled with a mathematical model to understand the kinetics of camphene growth in this ceramic system. The model can help in better understanding of other parameter, which directly influences the growth of camphene dendrite thus providing more information on how to induce directional growth of pores in this ceramic system.

The micro porous samples obtained from this fabrication technique could be studied as an electrode material and study the performance and compare with other competing electrode materials.

9.6 Fabrication of micron sized Ti_2AlC conductive fibres

Effort has been made to extrude this ceramic material into 500 and 800µm fibres as seen in figure 158 with the help from Dr. Frank Clemens and Mr. Tony Luiola of EMPA-Swiss Federal Laboratory for Material Science and Technology. They successfully extruded Ti_2AlC ceramic mixed with polyethylene oxide binder (50:50vol %), into thin fibres of diameter 500 (figure 158(a)) and 800µm (figure 158(b)) at 105 and 95^{o}C respectively.

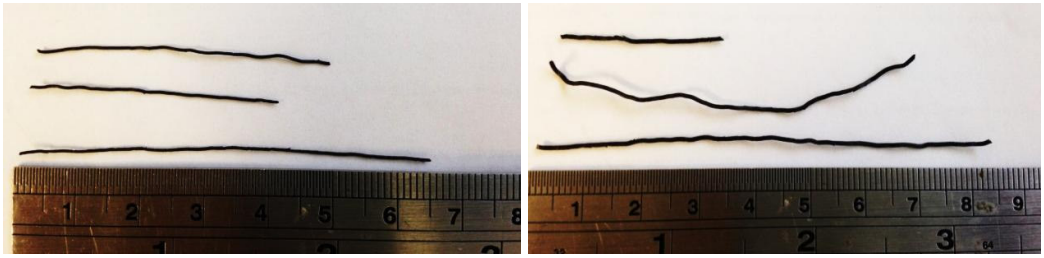

(a) **(b)**

Figure 158. (a) Ti_2AlC micro fibre of diameter 500µm of different length. (b) Ti_2AlC micro fibre of diameter 800µm of different length

As seen in the figure 158, it is possible to extrude Ti_2AlC fibre. However further effort has to be made to extrude straight fibres, so that the intrinsic properties of the material is isotropic throughout the length of the fibre. The fibres seen in the figure 158 are green fibres and hence there is a need to optimise the sintering condition for these fibres and establish mechanical and electrical properties of these Ti_2AlC fibres.

10. References

[1] M. W. Barsoum, Program on Solid State Chemistry, vol 28, page 201, 2000

[2] J. P. Palmqust, S. Li, P. O. A. Persson, J. Emmerlich, O. Wilhelmsson, H. Hogberg and M. I. Katsnelson, Phys. Rev, vol 70, page 13, 2004

[3] Z. J. Lin, M. J. Zhuo, Y. C. Zhou, J. Am. Ceram. Soc., vol 89, page 3765, 2006

[4] X.H. Wang and Y.C. Zhou: Corros. Sci, vol 45, page 891, 2003

[5] X.H. Wang and Y.C. Zhou: Oxid. Met., vol 59, page 303, 2003

[6] W. B. Person, Acta Crystallogr., Sect. A: Cryst. Phys., Diffr.Theor. Gen. Crystallogr., vol A36, page 724, 1980

[7] W. Jeitschko, H. Nowotny, and F. Benesovsky, Monatsch. Chem. vol 94, page 672, 1963

[8] Yanchun Zhou and Zhimei Sun, Phys Rev B, vol 61, page 19, 1999

[9] Z.M. Sun, International Material Reviews, vol 56, pages 143-166, 2011

[10] M.W. Barsoum, M. Ali and T. El-Raghy: Metall. Mater. Trans. A, vol 31, page 1857, 2000

[11] C.J. Gilbert, D.R. Bloyer, M.W. Barsoum, T. El-Raghy, A.P. Tomsial, and R.O. Ritchiel, Scripta Materialia, vol 42, pages 761-767, 2000

[12] M.W. Barsoum, Encyclopedia of Materials: Science and Technology, eds. K.H.J. Buschow, Elsevier, Amsterdam, NY, vol 11, pages 1-16, 2004

[13] F.L. Meng, Y.C. Zhou, and J.Y. Wang, Scripta Materialia, vol 53, pages 1369-1372, 2005

[13] A.G. Merzhanov, Combust Flame, vol 13, pages 143-156, 1969

[14] A.G. Merzhanov, Ceramic International, vol 21, pages 371-379, 1995

[15] J. J. Berzelius, Prog. Ann. vol 4, page 126, 1825

[16] V. Hlavacek, Ceram. Bull, vol 70, pages 240-243, 1991

[17] J. W. McCauley, International Journal of Self-Propagating High-Temperature Synthesis, vol 17[1], pages 58–75, 2008

[18] J. B. Holt and Z. A. Munir, J. Mater. Sci., vol 22, page 251, 1986

[19] A. G. Merzhanov, Int. J. SHS, vol 2, page 113, 1993

[20] J. J. Moore and H. J. Feng, Combustion Synthesis of Advanced Materials, Part 1, vol 39, pages 243-273, 1995

[21] M. Eslamloo-Grami and Z. A. Munir, Material Science Report, vol 3, pages 227-365, 1989

[22] Arvind Varma and Jean Pascal Lebrat, Combustion Synthesis of Advanced Materials, vol 47, pages 2179-2194, 1992

[23] A. Hendaoui, D. Vrel, A. Amara, A. Benaldjia and P. Langlois, Inter. J. Self-Propag. High-Temp. Synth., vol 17, pages 125–128, 2008

[24] A. Hendaoui, D. Vrel, A. Amara, P. Langlois, M. Andasmasa and M. Guerioune, J. Eur. Ceram. Soc., vol 30, pages 1049–1057, 2010

[25] A. Hendaoui, D. Vrel, A. Amara, P. Langlois amd M. Guerioune. Int. J. Self-Propag. High-Temp. Synths., vol 18[4], pages 267-272, 2009

[26] A. M. Stolin, D. Vrel. S. N. Galyshev, A. Hendaoui, P. M. Bazhin, and A. E. Sytschev, Int. J. Self-Propag. High-Temp. Synths., vol 18, pages 194-199, 2009

[27] A. Hendaoui, D. Vrel, A. Amara, A. Benaldjia and P. Langlois, Inter. J. Self-Propag. High-Temp. Synth., vol 17, pages 125-128, 2008

[28] M.W. Barsoum, D. Brodkin and T. El-Raghy: Scripta Mater., vol 36, page 535, 1997

[29] http://www.google.co.uk/imgres?um=1&hl=en&sa=N&tbm=isch&tbnid=40-ZVQOC4vaabM:&imgrefurl=http://www.royalarmouries.org/learning/online, accessed on 10/08/2012

[30] K. Maca1, V. Pouchly, A. R. Boccaccini, Science of Sintering, vol 40, pages 117-122, 2008

[31] W. Jeitschko, H. Nowotny, F. Benesovsky, Monatsh. Chem., vol 94, page 672, 1963

[32] M.W. Barsoum, M. Ali and T. El-Raghy: Metall. Mater. Trans. A, vol 31, page 1857, 2000

[33] M.A. Pietzka and J.C. Schuster: J. Phase Equilib., vol 15, page 392. 1994

[34] N.V. Tzenov and M.W. Barsoum: J. Am. Cearm. Soc., vol 83, page 825, 2000

[35] X.H. Wang and Y.C. Zhou: J. Mater. Chem., vol 12, page 455, 2002

[36] Y.L. Bai, X.D. He, Y.B. Li, C.C. Zhu and S. Zhang: J. Mater. Res., vol 24, page 2528, 2009

[37] S.B. Hashimoto, M. Takeuchi, K. Inoue, S. Honda, H.Awaji, K.C. Fukuda and S.W. Zhang: Mater. Lett., vol 62, page 1480, 2008

[38] X.P. Lu and Y.C. Zhou: Int. J. Appl. Ceram. Tech-nol., vol 7[6], pages 697-703, 2010

[39] C.J. Lee, J.I. Chae and D.J. Kim: J. Eur. Ceram. Soc., vol 20, page 2667, 2000

[40] X.W. Zhu, Y. Zhou and K. Hirao: J. Eur. Ceram. Soc., vol 26, page 711, 2006

[41] M. Lopacinski, J. Puszynski and J. Lis: J. Am. Cearm. Soc., vol 84, page 3051, 2001

[42] Y.C. Zhou, X.H. Wang, Z.M. Sun and S.Q. Chen: J. Mater. Chem., vol 11, page 2335, 2001

[43] C.L. Yeh and Y.G. Shen: J. Alloy. Compd., vol 470, page 424, 2009

[44] C. J. Gilbert, D. R. Bloyer, M. W. Barsoum, T. El-Raghy, A. P. Tomsia and R. O. Ritchie, Scripta Materialia, vol 42 [8], pages761-767, 2000

[45] http://www.google.co.uk/imgres?um=1&hl=en&sa=N&tbm=isch&tbnid=xPBCA accessed on 02/12/2011

[46] H. I. Yoo, M. W. Barsoum and T. El-Raghy, Nature vol 407, pages 581–582, 2000

[47]http://www.google.co.uk/imgres?um=1&hl=en&tbm=isch&tbnid=hAu9g1l5uUXYtM:&imgrefurl=http accessed on 02/12/2011

[48]http://www.google.co.uk/imgres?um=1&hl=en&tbm=isch&tbnid=O6GHYucU91KthM:&imgrefurl, accessed on 2/12/2011

[49] L. M Shepard, Am. Ceram. Soc. Bull., vol 7, pages 1146–1158, 1991

[50] W. Suchnek and M. Yoshimura , J. Mater. Res., vol 13, pages 94–117, 1998

[51] http://allthumbsdiy.com/references/spray-polyurethane-foam/open-vs-closed-cell-foam-insulation, accessed on 12/08/2012

[52] J. Saggio-Woyansky , C. E. Scott and W. P. Minnear, Am. Ceram Soc. Bull., vol 11, pages 1674–1682, 1992

[53] Yu-Hsiu Hsu, Fabrication of porous calcium phoshate bioceramics, PhD thesis, 2005, University of Bath, England, UK.

[54] E. E. McLeary and J. C. Jansen, Topics Catal., vol 1[2], pages 85–92, 2004

[58] S. Guicciardi, C. Galassi , E. Landi , A. Tampieri , K. Satou and G. Pezzotti, J. Mater. Res., vol 1, pages 163–170, 2001

[59] P. Greil, J. Eur. Ceram. Soc., vol 2, pages 105–118, 2001

[60] Will and L. J. Gauckler, ‘‘Ceramic Foams as Current Collector in Solid Oxide Fuel Cells (SOFC): Electrical Conductivity and Mechanical Behaviour’’, in Proceedings of the Fifth International Symposium on Solid Oxide Fuel Cells (SOFCV), Aachen, Germany. Edited by U. Stimming, S. C. Singhal, H. Tagawa, and W. Lehnert. The Electrochemical Society Inc, Pennington, NJ, 1997.

[61] R. Andre, W. Studart, T. Gonzenbach, Elena Tervoort, and J. Ludwig Gauckler, J. Am. Ceram. Soc., vol 89[6], pages 1771–1789, 2006

[62] K. Schwartzwalder and A. V. Somers, Method of Making Porous Ceramic Articles, US Pat. No. 3090094, May 21, 1963.

[63] L. J. Gauckler,M.M. Waeber, C. Conti, and M. Jacobduliere, J. Metals, vol 37 [9], pages 47–50, 1985

[64] X. P. Pu, X. J. Liu, F. G. Qiu, and L. P. Huang, J. Am. Ceram. Soc., vol 87[7], pages 1392–4, 2004

[65] J. M. Tulliani, L. Montanaro, T. J. Bell, and M. V. Swain, J. Am. Ceram. Soc., vol 82[4], page 961, 1999

[66] Saggio-Woyansky, C. E. Scott, and W. P. Minnear, Am. Ceram. Soc. Bull., vol 71[11], page 1674, 1992

[67] M. D. M. Innocentini, P. Sepulveda, V. R. Salvini, V. C. Pandolfelli, and J. R. Coury, J. Am. Ceram. Soc., vol 81[12], pages 3349–3352, 1998

[68] http://www.swri.org/3pubs/brochure/d18/preceram/preceram.htm, accessed on 23/09/2012

[69] R. A. White, E. W. White, and J. N. Weber, Metal and Polymer Prosthetic Materials Science, vol 176 [4037], page 922, 1972

[70] D. M. Roy and S. K. Linnehan, Nature, vol 247[5438], page 220–222, 1974.

[71] E. Vogli, H. Sieber, and P. Greil, J. Eur. Ceram. Soc., vol 22[14–15], pages 2663–8, 2002

[72] P. Greil, J. Eur. Ceram. Soc., vol 21[2], pages 105–18, 2001

[73] T. Ota, M. Takahashi, T. Hibi, M. Ozawa, S. Suzuki, Y. Hikichi, and H.Suzuki, J. Am. Ceram. Soc., vol 78[12], pages 3409–3411, 1995

[74] O. Lyckfeldt and J. M. F. Ferreira, J. Eur. Ceram. Soc., vol 18[2], pages 131–140, 1998

[75] P. Colombo, E. Bernardo, and L. Biasetto, J. Am. Ceram. Soc., vol 87[1], pages 152–4, 2004

[76] T. J. Fitzgerald, V. J. Michaud, and A. Mortensen, J. Mater. Sci., vol 30[4], pages 1037–45, 1995

[77] K. M. Lindqvist and E. Carlstrom, J. Eur. Ceram. Soc., vol 25 [16], pages 3539–45, 2005

[78] A. Imhof and D. J. Pine, Adv.Mater., vol 11[4], pages 311–314, 1999

[79] L. M. Rodriguez-Lorenzo, M. Vallet-Regi, and J. M. F. Ferreira, J. Biomed. Mater. Res., vol 60[2], page 232–40, 2002

[80] S. R. Mukai, H. Nishihara, and H. Tamon, Chem. Commun., vol 7, page 874–5, 2004

[81] A. Macchetta, I. G. Turner and C. R. Bowen, Acta Biomater., vol 5, pages 1319–1327, 2009

[82] S. Deville, Materials, vol 3, pages 1913-1927, 2010

[83] S. Deville, Advanced Engineering Materials, vol 10[3], pages 155-169, 2008

[84] T. Fukasawa, M. Ando, T. Ohji and S. Kanzaki, J. Am. Ceram.Soc., vol 84, page 230, 2001

[85] J. S. Wettlaufer, M. G. Worster and H. E. Huppert, J. Fluid. Mech., vol 344, page 291, 1997

[86] B. H. Yoon, Y. H. Koh, C. S Park and H. E Kim, J. Am. Ceram. Soc., vol 90, pages 1744–1752, 2007

[87] K. H. Zuo, Y. P. Zeng and D. Jiang, Mater. Sci. Eng., vol 30, pages 283–287, 2010

[88] K. K. Mallick, J. Am. Ceram. Soc., vol 92, pages S85–S94, 2009

[89] J. H. Song, Y. H. Koh, H. E. Kim, L. H Li and H. J. Bahn, J. Am. Ceram. Soc., vol 89, pages 2649–2653, 2006

[90] Z. Y. Deng, H. R. Fernandes, J. M. Ventura, S. Kannan and J. M. F. Ferreira, J. Am.Ceram. Soc., vol 90, pages 1265–1268, 2007

[91] J. Han, C. Hong, X. Zhang, J. Du and W. Zhang, J. Eur. Ceram. Soc., vol 30, pages 53–60, 2010

[92] Y. Cao and J. He, Chin. J. Mater. Res., vol 23, pages 518–523, 2009

[93] B. H. Yoon, W. Y. Choi, H. E. Kim, J. H. Kim and Y. H. Koh, Scripta. Mater., vol 58, pages 537–540, 2008

[94] J. Han, L. Hu, Y. Zhang and Y. Zhou, J. Am. Ceram. Soc., vol 92, pages 2165–2167, 2009

[94] E. Landi, F. Valentini and Tampieri, Acta. Biomater., vol 4, pages 1620–1626, 2008

[96] S. Yunoki, T. Ikoma, A. Monkawa, K. Ohta, M. Kikuchi, S. Sotome, K. Shinomiya and J. Tanaka, Mater. Lett., vol 60, pages 999–1002, 2006

[97] V. Maquet, A. R. Boccaccini, L. Pravata, I. Notingher and R. Jerome, Biomaterials, vol 25, pages 4185–4194, 2004

[98] K. Araki and J. W. Halloran, J. Am. Ceram. Soc., vol 87, page 2014, 2004

[99] S. Deville, E. Saiz and A. P. Tomsia, Acta Mater., vol 55, page 1965, 2007

[100] J. W. Moon, H. J. Hwang, M. Awano and K. Maeda, Mater. Lett., vol 57, page 1428, 2003

[101] H. Schoof, J. Apel, I. Heschel and G. Rau, J. Biomed. Mater. Res., vol 58, page 352, 2001

[102] R. Chen, C. A. Wang, Y. Huang, L. Ma and W. Lin, J. Am.Ceram. Soc., vol 90, page 3478, 2007

[103] S. Roy and T. Ando, Materials Science in Semiconductor Processing, vol. 15, pages 722-730, 2012

[104] A. G. Divenuti, Metallurgical and Materials Transactions A: Physical Metallurgy and Materials Science, vol 29, pages 3047-3056, 1998.

[105] D. Koch, L. Andresen, T. Schmedders and G. Grathwohl, Journal of Sol-Gel Science and Technology, vol 26[1-3], pages 149-152, 2003

[106] Z. Hou, F. Ye, L. Liu and Q. Liu, Material Science and Engineering, vol 558, pages 742-746, 2012

[107] Z. Hou, Material Science and Engineering, vol.558, pages 742-746, 2012

[108] J.Li, Z. Y. Fu, J. Y. Zhang, H. Wang, W. Mi. Wang, Y. C. Wang and Y. B. Cheng, Advanced Materials Research, vol 66, pages 258-261, 2009

[109] J. John. Moore and H. J. Feng, Prog. Mater. Sci., vol 39, pages 243-273, 1995

[110] G. Merzhanov, J. Mater. Chem., vol 14, pages 1779-1786, 2004

[111] C.R. Bowen and B. Derby: Acta Metall Mater, vol 43[10], pages 3903-3913, 1995

[112] T. Duong, S. Gibbons, R. Kinra and R.Arróyave, J. App. Phys., vol 110, page 093504, 2011

[113] O. Kubashewski and C. B. Alcock, "Metallurgical Thermochemistry", Pergamon Press, Oxford, 1979

[114] M. W. Barsoum, I. Salama, F. Aldinger, Metallurgical and Material Transactions A, vol 33[A], page 2779, 2002

[115] S. Hashimoto, N. Nishina, K. Hirao, Y. Zhou, H. Hyuga, S. Honda and Y. Iwamoto, Materials Research Bulletin, vol 47, pages 1164–1168, 2012

[116] M. Martinez Pacheco, M. Martinez Pacheco, ISBN 978-90-77172-27-8, 2007

[117] http://www.engineeringtoolbox.com/melting-temperature-metals-d_860.html (accessed on 12/06/12)

[118] L. L. Wang, Z. A. Munir, Y. M. Maximov, ‚J. Mat. Sci. vol 28, pages 3693-3708, 1993

[119] J. A. Rodrigues, V. C. Pandolfelli, W. J. Botta and F., R. Tomasi, J. Mat. Sci. Lett., vol 10, pages 819-823, 1991

[120] M. Bingchu, Y.Ming, Z. Jiaoqun and Z. Weibing, Journal of Wuhan University of Technology - Mater. Sci. Ed., vol 21[2], pages 1-3, 2006

[121] Zhenbin Ge, Kexin Chen, Junming Guo, Heping Zhou and Jose M F, Journal of the European Ceramic Society, vol 23[4], pages 567-574, 2003

[122] W. Ping, M. Bingchu, H. Xiaolin, Z. Jiaoqun and Z. Weibing, Journal of Wuhan University of Technology-Mater. Sci. Ed., vol 22[2], pages 325-328, 2007

[123] S. Hashimoto, N. Nishina, K. Hirao, Y Zhou, H Hyuga, S Honda and Y Iwamoto, Mat. Res. Bull., vol 47, pages 1164-1168, 2012

[124] G. Liu , K. Chen, H. Zhou, J. Guo,K. Ren and J.M.F. Ferreira, Mat. Let., vol 61, pages 779-784, 2007

[125] https://www.memsnet.org/material/titaniumcarbideticbulk/ (accessed on 10/10/2012)

[126] L. Hu, R. Benitez, S. Basu, I. Karaman and M. Radovic, Acta. Materialia., vol 60, pages 6266-6277, 2012

[127] Z. Sun, Y. Liang, M. Li and Y. Zhou, J. Am. Ceram. Soc, vol 93[9], pages 2591-2597, 2010

[128] Y. H. Hsu, I. G. Turner and A. W. Miles, Key Eng Mat, vol 284-286, page 305-308, 2005

[129] http://www.hydramotion.com/pdf/Website_Viscosity_Units_V2.pdf (accessed on 14/08/2012)

[130] X. W. Zhu, D. L. Jiang, S. H. Tan and Z. Q. Zhang, J. Am. Ceram. Soc., vol 84[7], pages 1654–1656, 2001

[131] H. R. Ramay and M. Q. Zhang, Biomaterials, vol 24 [19], pages 3293–3302, 2003

[132] M. R. Nangrejo, X. J. Bao, and M. J. Edirisinghe, J. Eur. Ceram. Soc., vol 20 [11], pages 1777–85. 2000

[133] C.R. Bowen, T.Thomas and V. Adamaki, Manufacture of Porous Electrically Conductive Ceramic, Proceeding of the International conference of mining, material and metallurgical engineering (MMME2014), 2014

[134] O. Bobertag, K. Feist, and H. W. Fischer, Berichte der deutschen chemischen Gesellschaft, vol 41, pages 3675-3679, 1908

[135] H. Handovsky, Zeitschrift für Chemie und Industrie der Kolloide, vol 4, pages 145-145, 1909

[136] A. Lottermoser, Berichte der deutschen chemischen Gesellschaft, vol 41, pages 3976-3979, 1908

[137] S. Deville, Advanced Engineering Materials, vol 10[3], pages 155-169, 2008

[138] W. A. Maxwell, R. S. Gurnick, and A. C. Francisco, "Preliminary investigation of the'freeze-casting'method for forming refractory powders," National Advisory Committee for Aeronautics (NACA), NACA RM E53L21, Washington, 1954

[139] A. Macchetta, "Fabriaction and analysis of highly porous hydroxyapatite/tricalcium phosphare ceramic via the implementation of a novel freeze casting technique", University of Bath, 2008

[140] M. N. Rahaman, Ceramic Processing and Sintering Second Ed. CRC Press. page 45, 2003

[141] B. H. Yoon, W. Y. Choi, H. E. Kim, J. H. Kim and Y. H. Koh, Scripta. Mater., vol 58, pages 537–540, 2008

[142] L. T. Angenent, K. Karim, M. H. Al-Dahhan and R. Domiguez-Espinosa, Trends Biotechnol., vol 22, pages 477–485, 2004

[143] B. E. Logan and J. M. Regan, Environ. Sci. Technol., vol 40, pags 5172–5180, 2006

[144] K. Rabaey and W. Verstraete, Trends Biotechnol., vol 23, pages 291–298, 2005

[145] F. Zhao, R. C. T. Slade and J. R. Varcoe, Chem. Soc. Rev., vol 38, pages 1926–1939, 2009

[146] R. S. Berk and J. H. Canfield, Appl. Microbiol., vol 12, pages 10-12, 1964

[147] J. B. Davis and H. F. Yarbrough, Preliminary experiments on a microbial fuel cell. Science 1962, vol 137, pages 615-616, 1962

[148] B. Cohen, J.Bacteriol., vol 21, pages 18-19, 1931

[149] M. C. Potter, R. Soc. London Ser. B 1911, vol 84, pages 260-276

[150] http://en.wikipedia.org/wiki/Microbial_fuel_cell (accessed on 01/07/2014)

[151] H. P. Bennetto, Biotechnology Education, vol 1 [4], pages 163-168, 1990

[152] K. Rabaey, N. Boon, S. D. Siciliano, M. Verhaege and W. Verstraete, Appl. Environ. Microbiol., vol 70, pages 5373-5382, 2004

[153] K. Rabaey, N. Boon, M. Hofte and W. Verstraete, Environ. Sci. Technol., vol 39, pages 3401-3408, 2005

[154] M. Chiao, K. B. Lam and L. W. Lin, J. Micromech. Microeng., vol 16, pages 2547–2553, 2006

[155] K. Nishio, K. Hashimoto and K. Watanabe, Appl. Microbiol. Biotechnol., vol 86, pages 957–964, 2010

[156] S. Tsujimura, A. Wadano, K. Kano and T. Ikeda, Enzyme Microb. Technol., vol 29, pages 225–231, 2001

[157] R. Thorne, H. Hu, K. Schneider, P. Bombelli, A. Fisher, L. M. Peter, A. Dent and P. J. Cameron, J. Mater. Chem., vol 21, pages 18055-18060, 2011

[158] B. Cohen, J. Bacteriol., vol 21, page 18, 1931

[159] T. Yagishita, S. Sawayama, K.-I. Tsukahara, T. Ogi, Sol. Energy., vol 61, page 347, 1997

[160] K. Tanaka, R. Tamamushi, T. Ogawa, J. Chem. Technol. Biotechnol., vol 35B, page 191, 1985

[161] D. H. Park and J. G. Zeikus, Appl. Environ. Microbiol., vol 66, pages 1292–1297, 2000

[162] Y. Liu, F. Harnisch, K. Fricke, U. Schroder, V. Climent and J. M. Feliu, Biosens. Bioelectron., vol 25, pages 2167–2171, 2010

[163] D. E. Holmes, D. R. Bond and D. R. Lovley, Appl. Environ. Microbiol., vol 70, pages 1234–1237, 2004

[164] B. E. Logan, Nat. Rev. Microbiol., vol 7, pages 375–381, 2009

[165] H. Haugen, R. Sabetrasekh, H. Tiainen, S. P. Lyngstadaas and J. Reseland, J. Biomater. Appl., vol 25, pages 559–580, 2011

[167] W. Ping, M.Bing-chu, H. Xiao-lin and Z. Wei-bing, Trans. Nonferrous Met. Soc. China., vol 17, pages 1001-1004, 2007

[168] Kenneth Schneider, Department of Chemistry, University of Bath, BA2 7AY, England, UK

[169] A. Oren, Int. J. Syst. Evol. Microbol., vol 54[5], pages 1295-1902, 2004

[170] http://www.azom.com/article.aspx?ArticleID=1179 (accessed on 06/06/2014)

11. Appendices

Appendix 1. Design details of mould used for freeze casting

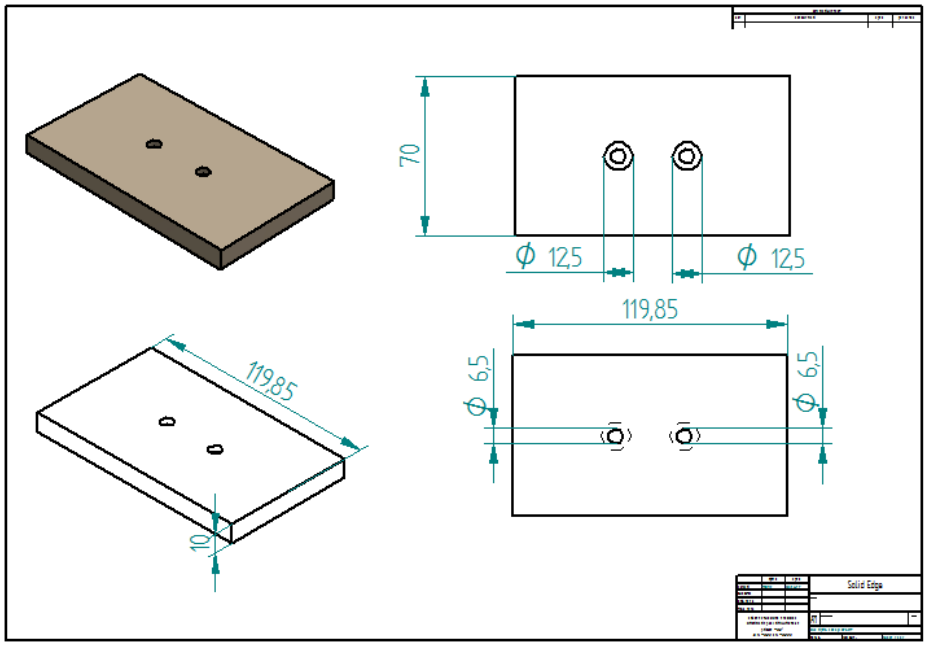

Figure 159. Design details in mm for the base plate of the mould

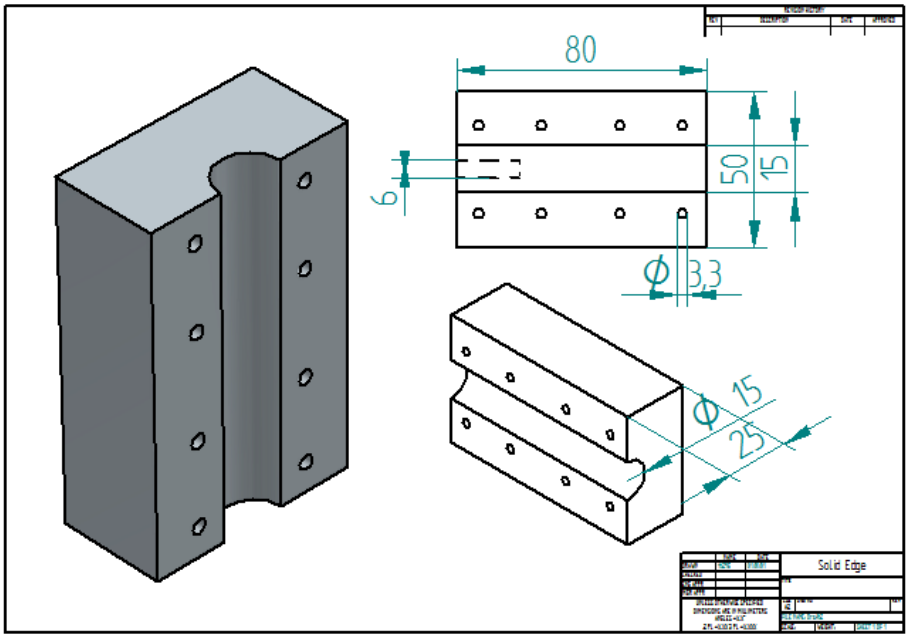

Figure 160. Design details in mm for the half upper mould body

Appendix 2. Posters presented in conferences

Electroceramics XIII, University of Twente, Enschede, Netherlands, June 24th-27th, 2012

Thermodynamic Study for the Manufacture of MAX-phase Ceramic by Combustion Synthesis Process

T. Thomas, C. R. Bowen, Department of Mechanical Engineering, University of Bath, UK

Introduction

MAX phase ceramics are a novel class of ductile material with the general formula $M_{n+1}AX_{n-1}$ (n = 1, 2 or 3), where **M** is a transition metal, **A** is an element often of IIIA or IVA subgroup of the periodic table and **X** is either nitrogen or carbon. These ceramic are attracting significant interest since they are inherently nano-laminated ternary nitrides or carbides and to do date there are up to sixty known phases. Recent research has resulted in the discovery of other ternary compounds such as Ti_2AlC and Ti_3AlC_2 which are known to be low density, high electrical conductivity and oxidation resistant compounds in their category [1] . This poster will provide an overview of thermodynamic model to calculate the adiabatic combustion temperature (T_{ad}) in the synthesis of Ti_2AlC Max-phase ceramic and the effect on the reaction when additional diluents like Al and Ti are added.

Combustion Synthesis

Combustion synthesis or Self-propagating high temperature synthesis (SHS) is related to the ignition of a compact powder mixture in either inert or air atmosphere which provides suitable environment for chemical reaction to produce sufficient heat and this heat (exothermic reaction) becomes self-sustaining in the form of combustion wave (Fig 1). As the combustion wave propagates, the reactants are converted into the desired products [2].

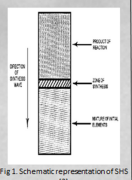

Fig 1. Schematic representation of SHS [2]

Why is Thermodynamic analysis Necessary?

- Thermodynamic analysis of the reactions is important because the control of the temperature and the combustion wave propagation of reacted material ensure the high-quality of the products.
- It also helps in assessing the stability and feasibility to synthesis a compound.
- Hence it is necessary to know the temperatures associated with the combustion reaction for detailed insight. The main temperature involved is the adiabatic combustion temperature (T_{ad}).

Adiabatic combustion temperature (T_{ad})

- It is a very useful parameter that indicates the maximum temperature attained in the reaction when the reaction is self sustaining.
- T_{ad} can be calculated by assuming that the enthalpy of the reaction is used in forming the product without any heat loss to the surroundings [3].
- Therefore only highly exothermic reaction can undergo the combustion synthesis process.

Method

Thermodynamics involved in the SHS process for producing max-phase ceramic composite was analysed using the following exothermic reaction:

$$2Ti + Al + C \rightarrow Ti_2AlC \qquad (1)$$

Later this model was adopted to study the change in the reaction 1, when excess Al and Ti was added according to the following reaction:

$$3Ti + 2Al + C \rightarrow Ti_2AlC + Al + Ti \qquad (2)$$

$$2Ti + 2Al + C \rightarrow Ti_2AlC + Al \qquad (3)$$

Modelling of adiabatic combustion temperature T_{ad}

Let us consider a simple reaction

$M_{To} + X_{To} \rightarrow MX_{To} + \Delta H_r$ (a)

Where ΔH_r is the enthalpy of the reaction at the initial temperature T_o which is usually 298 K.

If we consider that ΔH_r is used in forming the product MX, then the Tad can be calculated using the definition of heat capacity of the product C_p (MX) in reaction (a)

$$-\Delta H_{rTo} = \int_{To}^{Tad} Cp[MX]\,dT \qquad (b)$$

In order to understand the thermodynamics involved in the reaction we have to even consider the energy supplied by initial heating of the whole reactants. i.e. [4]

Enthalpy of the reaction + Energy supplied by heating = Energy required to heat up products

$$-\Delta H_r(298) + \int_{298}^{Tad} Cp[M+X]\,dT = \int_{298}^{Tad} Cp[MX]\,dT \qquad (c)$$

Processing

Reaction initiation → Propagation → Product

Reacted Sample

After Polishing

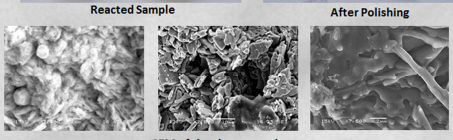

SEM of the above sample

Result

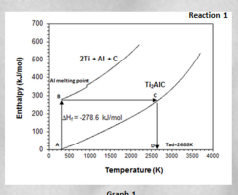

Graph 1

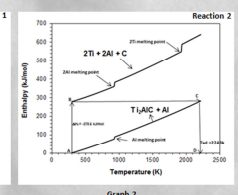

Graph 2

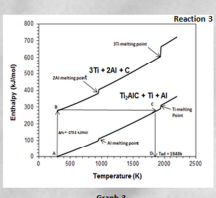

Graph 3

The graph 1, 2 and 3, explain the changes in the enthalpy of the reactants and products at various temperatures. It graphically explains the thermodynamics involved in the reaction 1, 2 and 3 respectively and helps in understanding the model better.

The vertical line (**A → B**) gives the **Tad** from different starting temperatures. It explains the left hand side of the expression (**c**). The horizontal line (**B → C**) to the enthalpy of the products and the Tad value can be found from the vertical line down to x-axis (**C → D**). This explains the right hand side of the expression (**c**).

Conclusion

- Thermodynamic model to calculate the adiabatic combustion temperature to synthesis Ti_2AlC max-phase from high purity Ti, Al and C elemental powders using SHS process is explained.
- The model show that the exothermicity of the reaction can be reduced by adding excess Al and Ti which is shown in the graphs. The Tad is gradually reduced in graph 1, 2 and 3.
- The model can be applicable to other processing reactions to understand the thermodynamics of the process.
- From the graphical data it is evident that the model is sufficient to predict the nature of the reaction.

Reference

[1] M. W. Barsoum, Program on Solid State Chemistry, vol 28, page 201, 2000
[2] Self-Propagating High Temperature Synthesis-A Soviet Method for Producing Ceramic Materials. Joey F. Crider. U.S. Army Foreign Science and Technology Centre, Charlottesville, VA 22906
[3] C. R. Bowen, Manufacture of Multiphase Ceramic Composites by Self-Propagating High-Temperature Synthesis, Worcester College, Oxford, 1993
[4] C. R. Bowen, Selfpropagating high temperature synthesis of ceramic materials

Manufacture of Ti-Al-C Based, Electrically Conductive Micro and Macro Porous MAX-phase Ceramic

T. Thomas, C. R. Bowen, Department of Mechanical Engineering, University of Bath, UK

Introduction

MAX phase ceramics are a novel class of ductile material with the general formula $M_{n+1}AX_{n-1}$ (n = 1, 2 or 3), where **M** is a transition metal, **A** is an element often of IIIA or IVA subgroup of the periodic table and **X** is either nitrogen or carbon. These ceramics are attracting significant interest since they are inherently nano-laminated ternary nitrides or carbides and to date there are up to sixty known phases. Recent research has resulted in the discovery of other ternary compounds such as Ti_2AlC and Ti_3AlC_2 which are known to be low density, high electrical conductivity and oxidation resistant compounds in their category [1] .

Porous ceramics are generally reticulated type of ceramic material which includes variety of structures like foams, interconnected rod, hollow spheres, honey combs and fibres. Until the advent of new porous ceramic techniques the production was limited to metallic and polymeric structures, because ceramics were inherently brittle. . Nowadays porous materials are used excessively, for example, polymeric foams for packing, porous ceramics for water purification [2] and biomaterials, thermal and acoustic insulation, catalyst support, porous burners, gas sensors, electrodes for fuel cells and much more. The main objective of the poster is to highlight the manufacturing techniques to produce Ti-Al-C based porous Ti_3AlC Max-phase ceramic using **Self-propagating high temperature synthesis** (SHS) also known as combustion synthesis, **Reticulated foam casting** techniques and also a brief taster on **Freeze casting** technique.

Combustion Synthesis

Combustion synthesis or Self-propagating high temperature synthesis (SHS) is related to the ignition of a compact powder mixture in either inert or air atmosphere which provides suitable environment for chemical reaction to produce sufficient heat and this heat (exothermic reaction) becomes self-sustaining in the form of combustion wave (Fig 1). As the combustion wave propagates, the reactants are converted into the desired products [3].

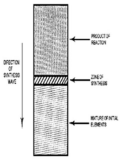

Fig 1. Schematic representation of SHS [3]

Processing

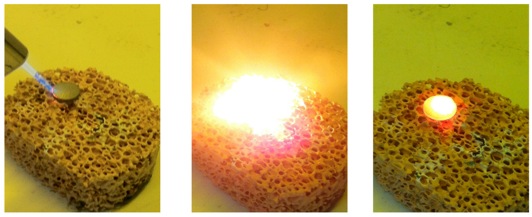


Reacted Sample

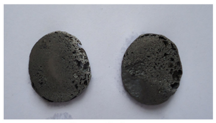
After Polishing

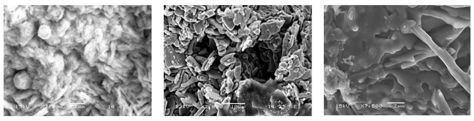
SEM of the above sample

Advantages

- Use of simple equipment for the process
- Energy and time efficient compared to conventional process
- Fabrication of high purity metastable phases as seen in figure 2.
- Any size and shape samples can be prepared.

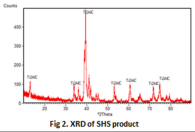
Fig 2. XRD of SHS product

Disadvantage

- The main disadvantage of this technique is controlling the porosity and the high temperature associated with the reaction. By adding diluents and changing the particle size this can be rectified as seen in figure 3.

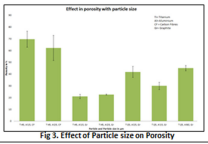
Fig 3. Effect of Particle size on Porosity

Reticulated Foam Replication

The immersion of a cellular substrate or template in a ceramic slip or suspension to produce porous ceramic with the same features as the original ceramic material [2]

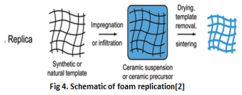

Fig 4. Schematic of foam replication[2]

Based on the template used the number of pores and the pore size can be controlled.

Processing

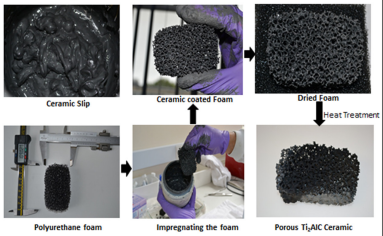

Figure 5.

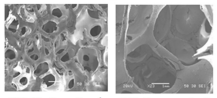

- **Disadvantage** of this process is, when the foam melts during heat treatment ,they burst out of the struts, leaving behind cracks as seen in figure 5.
- This makes the ceramic very friable
- We can over come this defect by coating again after sintering as seen from the data in figure 6.

Figure 6.

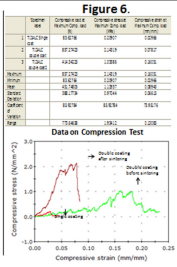

Freeze Casting Technique

- Freeze casting is a versatile process to produce virtually any shaped porous ceramic parts.
- Here a sublimable pore former (Camphene $C_{10}H_{16}$) is mixed with the ceramic to form a sol-gel mixture with suitable dispersant to uniformly suspend the ceramic particle in the mixture.
- Camphene sublime at room temperature leaving behind pores in the form of dendrites(figure 7) in the solid green sample which are later sintered to strengthen.
- The pore size and porosity can be controlled by ceramic loading and even by controlling the cooling temperature and the cooling direction. Heat transfer rate of the mould plays a very important role in this process.

Figure 7

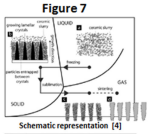

Schematic representation [4]

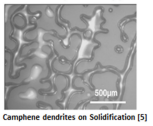

Camphene dendrites on Solidification [5]

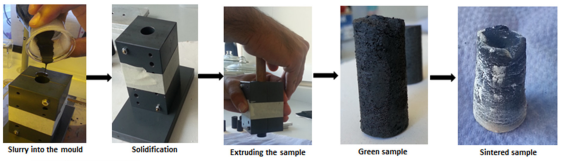

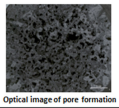
Optical image of pore formation

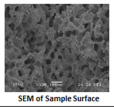
SEM of Sample Surface

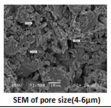
SEM of pore size(4-6µm)

Conclusion

From the above discussion it is evident that Max-phase Ti_2AlC engineering ceramic(produced by Kanthal, maxthal 211) can be easily used in producing macro and micro porous electrically conductive ceramic for any specific application. By studying the process parameters irrespective of the manufacturing process, its possible to tailor the technique for most of the materials.

Reference

[1] M. W. Barsoum, Program on Solid State Chemistry, vol 28, page 201, 2000
[2] R. Andre, w. Studart, T. Gonzenbach, Elena Tervoort, and J. Ludwig Gauckler, J. Am. Ceram. Soc., vol 89 [6], page 1771–1789, 2006
[3] Self-Propagating High Temperature Synthesis-A Soviet Method for Producing Ceramic Materials. Joey F. Crider. U.S. Army Foreign Science and Technology Centre, Charlottesville, VA 22906
[4] Sylvain Deville, Ad Eng Ceram 2008,vol 10(3), page 156-169, 2008
[5] A. Macchetta, I.G. Turner , C.R. Bowen, Acta Biomaterialia, Vol 5(4), page 1319-1327, 2009

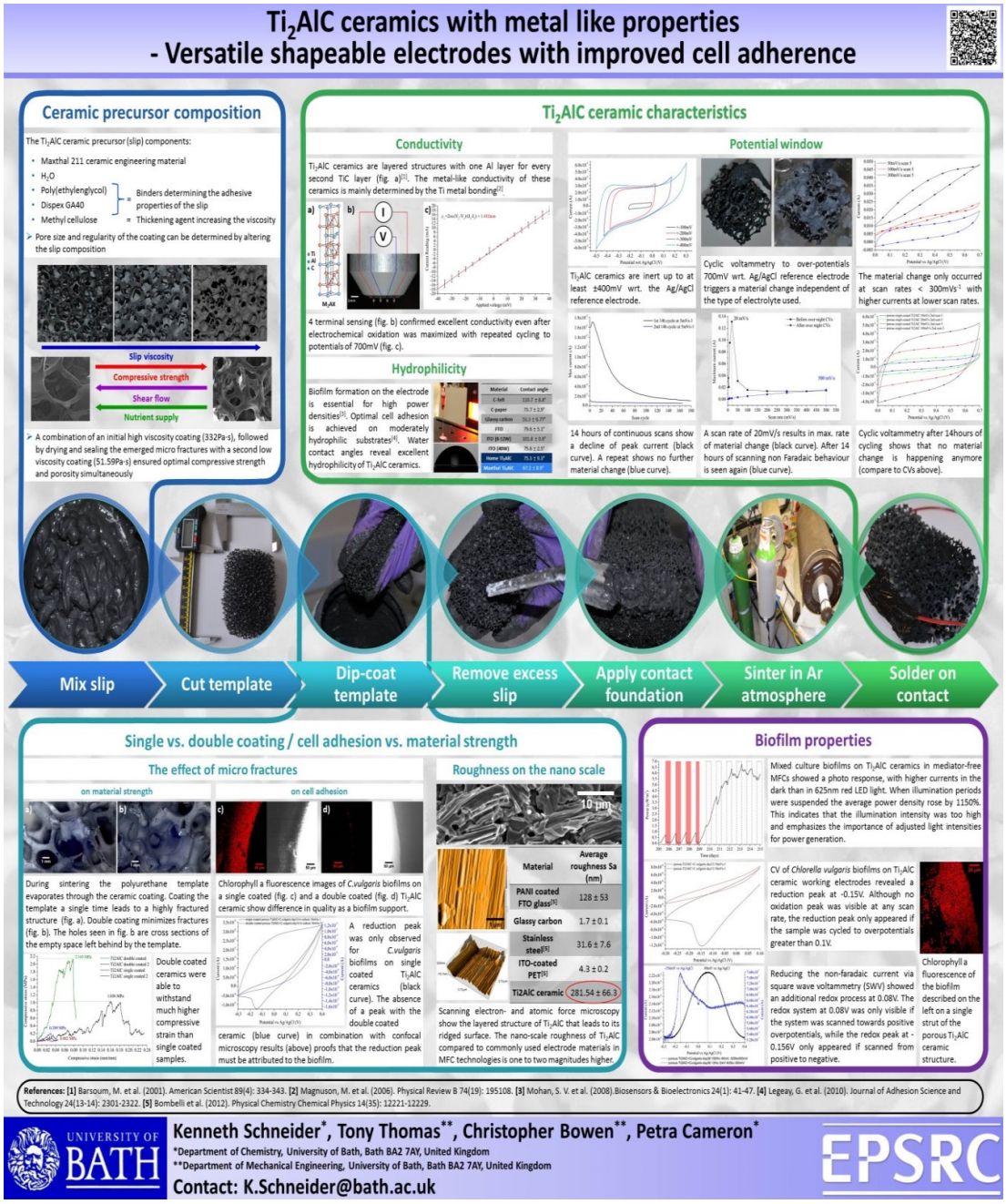
Ti2AlC ceramics with metal like properties
- Versatile shapeable electrodes with improved cell adherence
Ceramic precursor composition
The Ti3AlC ceramic precursor (slip) components:
Maxthal 211 ceramic engineering material
H2O
Poly(ethylenglycol)
Dispex GA40
Binders determining the adhesive properties of the slip
Methyl cellulose
= Thickening agent increasing the viscosity
Pore size and regularity of the coating can be determined by altering the slip composition
Slip viscosity
Compressive strength
Shear flow
Nutrient supply
A combination of an initial high viscosity coating (332Pa-s), followed by drying and sealing the emerged micro fractures with a second low viscosity coating (51.59Pa-s) ensured optimal compressive strength and porosity simultaneously
Ti2AlC ceramic characteristics
Conductivity
Ti2AlC ceramics are layered structures with one Al layer for every second TiC layer (fig. a)[1]. The metal-like conductivity of these ceramics is mainly determined by the Ti metal bonding[2].
4 terminal sensing (fig. b) confirmed excellent conductivity even after electrochemical oxidation was maximized with repeated cycling to potentials of 700mV (fig. c).
Hydrophilicity
Biofilm formation on the electrode is essential for high power densities[3]. Optimal cell adhesion is achieved on moderately hydrophilic substrates[4]. Water contact angles reveal excellent hydrophilicity of Ti3AlC ceramics.
Material
Contact angle
C-felt
C-paper
Glassy carbon
FTO
ITO (R-LOW)
ITO (NRW)
Home TiAlC
Maxthal TiAlC
Potential window
Ti2AlC ceramics are inert up to at least ±400mV wrt. the Ag/AgCl reference electrode.
Cyclic voltammetry to over-potentials 700mV wrt. Ag/AgCl reference electrode triggers a material change independent of the type of electrolyte used.
The material change only occurred at scan rates < 300mVs-1 with higher currents at lower scan rates.
14 hours of continuous scans show a decline of peak current (black curve). A repeat shows no further material change (blue curve).
A scan rate of 20mV/s results in max. rate of material change (black curve). After 14 hours of scanning non Faradaic behaviour is seen again (blue curve).
Cyclic voltammetry after 14hours of cycling shows that no material change is happening anymore (compare to CVs above).
Mix slip
Cut template
Dip-coat template
Remove excess slip
Apply contact foundation
Sinter in Ar atmosphere
Solder on contact
Single vs. double coating / cell adhesion vs. material strength
The effect of micro fractures
on material strength
on cell adhesion
During sintering the polyurethane template evaporates through the ceramic coating. Coating the template a single time leads to a highly fractured structure (fig. a). Double coating minimizes fractures (fig. b). The holes seen in fig. b are cross sections of the empty space left behind by the template.
Chlorophyll a fluorescence images of C.vulgaris biofilms on a single coated (fig. c) and a double coated (fig. d) Ti3AlC ceramic show difference in quality as a biofilm support.
Double coated ceramics were able to withstand much higher compressive strain than single coated samples.
A reduction peak was only observed for C.vulgaris biofilms on single coated Ti3AlC ceramics (black curve). The absence of a peak with the double coated ceramic (blue curve) in combination with confocal microscopy results (above) proofs that the reduction peak must be attributed to the biofilm.
Roughness on the nano scale
10 µm
Material
Average roughness Sa (nm)
PANI coated FTO glass[5]
128 ± 53
Glassy carbon
1.7 ± 0.1
Stainless steel[5]
31.6 ± 7.6
ITO-coated PET[5]
4.3 ± 0.2
Ti2AlC ceramic
281.54 ± 66.3
Scanning electron- and atomic force microscopy show the layered structure of Ti3AlC that leads to its ridged surface. The nano-scale roughness of Ti3AlC compared to commonly used electrode materials in MFC technologies is one to two magnitudes higher.
Biofilm properties
Mixed culture biofilms on Ti3AlC ceramics in mediator-free MFCs showed a photo response, with higher currents in the dark than in 625nm red LED light. When illumination periods were suspended the average power density rose by 1150%. This indicates that the illumination intensity was too high and emphasizes the importance of adjusted light intensities for power generation.
CV of Chlorella vulgaris biofilms on Ti3AlC ceramic working electrodes revealed a reduction peak at -0.15V. Although no oxidation peak was visible at any scan rate, the reduction peak only appeared if the sample was cycled to overpotentials greater than 0.1V.
Reducing the non-faradaic current via square wave voltammetry (SWV) showed an additional redox process at 0.08V. The redox system at 0.08V was only visible if the system was scanned towards positive overpotentials, while the redox peak at -0.156V only appeared if scanned from positive to negative.
Chlorophyll a fluorescence of the biofilm described on the left on a single strut of the porous Ti3AlC ceramic structure.
References: [1] Barsoum, M. et al. (2001). American Scientist 89(4): 334-343. [2] Magnuson, M. et al. (2006). Physical Review B 74(19): 195108. [3] Mohan, S. V. et al. (2008).Biosensors & Bioelectronics 24(1): 41-47. [4] Legeay, G. et al. (2010). Journal of Adhesion Science and Technology 24(13-14): 2301-2322. [5] Bombelli et al. (2012). Physical Chemistry Chemical Physics 14(35): 12221-12229.
UNIVERSITY OF BATH
Kenneth Schneider*, Tony Thomas**, Christopher Bowen**, Petra Cameron*
*Department of Chemistry, University of Bath, Bath BA2 7AY, United Kingdom
**Department of Mechanical Engineering, University of Bath, Bath BA2 7AY, United Kingdom
Contact: K.Schneider@bath.ac.uk
EPSRC